Design and Synthesis of Fluorescent Probes for Applications in Sensors and Modulating Amyloid β Fibrils

A Dissertation Submitted in Partial Fulfillment for the Degree of Doctor of Philosophy

By

B. Muthuraj

Roll No. 10612204

Department of Chemistry

Indian Institute of Technology Guwahati

October - 2015

…Dedicated to My Father M. Balakrishnan, and

My Mothers B. Vellathai (Late) and B. Meenakshi and

My Grandmother M. Chellammal…

INDIAN INSTITUTE OF TECHNOLOGY GUWAHATI

Department of Chemistry

STATEMENT

I do hereby declare that the matter embodied in this thesis is the result of investigations carried out by me in the Department of Chemistry, Indian Institute of Technology Guwahati, India, under the guidance of Professor Parameswar Krishnan Iyer.

In keeping with the general practice of reporting scientific observations, due acknowledgements have been made wherever the work described is based on the findings of the other investigators.

October, 2015.

IIT Guwahati. **B. Muthuraj**

INDIAN INSTITUTE OF TECHNOLOGY GUWAHATI

Department of Chemistry

CERIFICATE

This is to certify that **B. Muthuraj** has been working under my supervision since July, 2010 as a regular registered Ph. D. student. His thesis entitled **"Design and Synthesis of Fluorescent Probes for Applications in Sensors and Modulating Amyloid β Fibrils"** is an authentic record of the results obtained from the research work in the Department of Chemistry, Indian Institute of Technology Guwahati, Assam, India. I am forwarding his thesis for the award of degree of Doctor of Philosophy, from this institute. I certify that he has fulfilled all the requirements according to the rules of this institute regarding the investigations embodied in his thesis and this work has not been submitted elsewhere for a degree.

October, 2015

Guwahati.

Prof. Parameswar Krishnan Iyer

Thesis Supervisor

Department of Chemistry

IIT Guwahati

Guwahati -781 039

Assam, India.

Acknowledgements

There are number of great people to whom I would like to express my gratitude during my Ph.D. journey. Without their help and support, it would not have been possible to complete this task.

First, I would like to express my heartfelt thanks to my father M. Balakrishnan, mothers B. Vellathai (Late, in 1992) & B. Meenakshi and my grandmother M. Chellammal for their love and support towards my ambition.

I would like to express my thanks to my supervisor, Prof. Parameswar Krishnan Iyer for his support and guidance to my Ph.D. dissertation.

Besides my supervisor, I would also like to thank my chairman Prof. Anil Kumar Saikia and committee members Dr. Vishal Trivedi, Dr. Bhubaneswar Mandal, Prof. K. Pakshirajan, and Dr. Sunanda Chatterjee for their precious time, efforts and excellent suggestions on my Ph.D. dissertation.

My Ph.D research projects have involved lots of collaborative work. I am very much grateful to my research collaborators Dr. Vishal Trivedi (Department of Biosciences and Bioengineering, IITG) and his group members, Dr. Rohitas Deshmukh, Mr. Sourav Layek, Mr. S. N. Balaji (Department of Biosciences and Bioengineering, IITG), and Dr. Chittaranjan Patra (CSIR-Indian Institute of Chemical Technology Hyderabad) and his student Mr. Sudip Mukherjee. Their efforts made indispensable contributions to the projects in this dissertation.

I would like to express my thanks to my labmates Dr. Prasanta Jyoti Gautam, Dr. Bolin Chetia, Dr. Gunin Sikia, Dr. Atul Kumar Dwivedi, Radhakrishna Rath, Dr. Jupitara Das and my juniors. I sincerely express my appreciation to their great efforts for helped me.

I am thankful to all faculty members in the Department of Chemistry IIT Guwahati for their help and encouragement and also the non-teaching staff of the Department of Chemistry for their technical support. I am really thankful to the Central Instruments Facility (CIF), IIT Guwahati for different characterization facilities. I also thank Prof. R. Chaturvedi and groups for helping me with Fluorescence Microscopy studies. I express my sincere gratitude and acknowledgement to IIT Guwahati and Department of Science and Technology (DST), New Delhi for financial support.

I take this opportunity to thank all my friends from IIT Guwahati Prasant bhiya, Atul bhiya, Radhakrishna Rath, Ravi anna, Muthusivaramapandi, K. Radhakrishnan, Meenakshi Sharma, Suresh, Bhim for their kindness and support in my difficult time. I

wish to express my special thanks to Prof. B. K. Patel (Department of Chemistry, IITG), and Prof. Ramesh (Department of Biosciences and Bioengineering, IITG) for their support in my personal event. I would like to thank my M. Sc senior Dr. Yogapriya and my batchmates in PhD especially Prithiviraj, Sukhamoy, Nilufa, Manish, Somesh and juniors R. Suresh, Ganesh, Rituparna, and others for their support in different aspects.

I would like to thank my childhood friends Murugan, Nehru, Rengaraj, Malaiyammal, Dhanalakshmi, Sathiya and P. Chandra for their love and support in every aspect.

My heartfelt thanks to my M. Sc and M. Phil friends who are shared their positive thoughts with me to get confidence and motivations in my journey.

No words would suffice to express my feelings for my school (Manimuthu middle school, Ramalingapuram) and college teachers to whom I owe my obligations for all their great teaching and philosophy to be a good human; Mrs. Ramalakshmi teacher, Mrs. Sathiyabama teacher, Mr. Lakshminarayanan sir, Mr. Natarajan Sir, Mr. Raja sir and the entire fraternity from my school, college and university who gave me the direction and insightful information to march forward in this field.

Finally, I would like to thank my family members for their unconditional love, support, encouragements and understanding me for this five and half year Ph.D. study. Particularly, a million words could be too short to say how grateful I am to my beloved father M. Balakrishnan, my mothers B. Vellathai (Late, in 1992) and B. Meenakshi, my grandmother M. Chellammal, my sister B. Murugeshwari, my brothers B. Selvakumar, B. Muthukumar, my cousins Manikumar, Jodhi, M. Malliha, my brother-in-law Mr. Elangovan and my uncle as well as my friend C. Kaliraj. They have been supporting me always in every aspect and shared my happiness or sadness to get me confidence and motivations. Without their support, I could imagine how pale and struggle my study life would be. Finally I would like to thank my niece E. Pradeepa and nephew E. Vasanthabalan for their smile and love. So, I really want to say a Big Thanks to my dear family members!

Ph.D. study is an incredible journey and I am so grateful to all of the amazing people who have helped me along the way.

B. Muthuraj

Synopsis

The content of this thesis report entitled **"Design and Synthesis of Fluorescent Probes for Applications in Sensors and Modulating Amyloid β Fibrils"** is divided into 5 chapters and the chapters 2 to 5 having subdivisions based on the results of experimental research work.

* Chapter 1 is the introductory explanation to the respective research areas of ***"Design and Synthesis of Fluorescent Probes for Applications in Sensors and Modulating Amyloid β Fibrils"*** where the scope and relevance of the subsequent chapters are described highlighting the existing literature knowledge.

* Chapter 2a discusses about the synthesis of new conjugated polymer PHQ followed by monitoring its binding ability with inorganic salts of Fe^{2+}/Fe^{3+} ions, non–heme metalloprotein ferritin via photoluminescence quenching study.

* Chapter 2b discusses about disruption or modulation of aggregated amyloid–β (Aβ) fibrils using fluorescent conjugated polymer PHQ.

* Chapter 3a discusses about synthesis of a new conjugated polymer PF–DPA followed by its selective sensing ability of Co^{2+} ion and vitamin B_{12} via photoluminescence quenching. PF–DPA, exhibits a large and unique red shifted enhanced emission at 556 nm in higher water ratio around 1:9 (THF: H_2O) due to the formation of polymer nanoparticles or PDots by intra and intermolecular self–assembly induced aggregation phenomenon (AIEE). Further, PF–DPA utilized for cell imaging that showed high biocompatibility up to 1.6 mg/mL in normal cells but shows potent cytotoxicity against cancer cell in higher doses (>80 µg/mL).

* Chapter 3b discusses about inhibition of Aβ fibrillation and modulation effect on preformed Aβ oligomers and fibrils by the influence of AIEE luminogen of PF–DPA PDots.

* Chapter 4a discusses about the synthesis of new indole–3–carboxaldehyde functionalized fluorescein hydrazone (FI) molecule followed by its selective "turn–on" sensing ability with Cu^{2+} ion and "turn–off" sensor with nitric oxide (NO) were studied by photoluminescence properties. Further, we utilized FI to detect Cu^{2+} ion and endogenous NO gas in living cells.

* Chapter 4b discusses about the extension of this nontoxic indole–3–carboxaldehyde fluorescein hydrazone (FI) probe to perform multiple tasks of disaggregating Aβ aggregates in different biomarker environment such as cerebrospinal fluid (CSF), Aβ1–40, Aβ lysozyme aggregates (LA) and U87 MG Human astrocytes cells.

* Chapter 5a discusses about the synthesis of highly water–soluble fluorescent perylene diimide (PDI–HIS) molecule followed by its selective "turn–off" sensing ability with Cu^{2+} ion and "turn–on" sensor for ATP were studied by photoluminescence properties.

* Chapter 5b discusses about the synthesis of highly water-soluble biocompatible nanocomposite with graphene oxide (GO) probe for the exclusive detection of pyrophosphate (PPi) in physiological conditions and *in vitro* live melanoma cancer cells (B16F10).

* Chapter 5c discusses about modulation of Aβ fibrils into mature micro rod–shaped coassembly structure by histidine functionalized perylene diimide (PDI–HIS).

Chapter 1: Introduction

Novel fluorescent materials, namely, polymer and small molecules are significant sensor elements and provide very promising direction in interdisciplinary areas of chemistry, material sciences, biological sciences and medicine. These fluorescent materials are well demonstrated to detect specific chemical and biological targets in selective and sensitive manner. Fluorescent chemosensors, in general, are able to selectively recognize a guest species, which, in recent times have received significant attention in supramolecular chemistry because of their potential applications in environmental detection, molecular catalysis, biological fluorescence imaging, etc. According to their high selectivity and sensitivity, together with the advantages of spatial and temporal resolution, fluorescent chemosensors can be conveniently used to analyze, quantify and separate the guest species as well as sense biologically important species *in vitro* and *in vivo* to elucidate their function in living systems.

The construction of a fluorescent chemosensor usually involves two integrated components. One is a signalling fluorophore and another is a guest receptor that possesses a recognition capability, both are connected by a spacer to form a fluorophore–spacer–receptor scaffold system. When a guest species is bound to the receptor, the photophysical characteristics of the fluorophore, such as fluorescence intensity, emission wavelength and fluorescence lifetime, changes via different mechanisms and such a change provides a signal that indicates guest binding. Since chemosensors are applied in food analysis, process control, environmental monitoring, medical diagnosis and many other disciplines, a thorough understanding of the available constructions at the molecular level can help elucidate and improve the design of fluorescent chemosensors to develop sophisticated sensing systems. Moreover, this chapter will describe the basic concept of sensors using novel conjugated polymers and small molecules, their electronic and signaling properties. These essential concepts have helped to shape this dissertation that involved the development of highly sensitive and selective conjugated polymer and small molecule based sensors. Thus, the fluorescent materials such as small molecules and polymers are employed in different sensing

applications particularly, a sensitive detection of metal ions, anions and biomolecules. Importantly, the detection of biologically important metal ions such as iron, copper and zinc has gained significant interest. Although these metal ions are essential for the proper functioning of all living cells, their excessive concentrations in body are toxic that leading to various neurodegenerative diseases such as Alzheimer's (AD), Parkinson's (PD) and Huntington's diseases (HD). There are millions of people worldwide, who suffer from neurodegenerative disorders and most of these diseases manifest themselves later in life. Therefore, the main objective of this thesis was to design and synthesize novel fluorescent materials viz. small molecule and polymers for selective detection of biologically important metal ions such as iron and copper; further, we had plans to utilize these small molecules and polymers as modulators to target misfolded proteins of self-assembled Aβ fibrils and metal induced Aβ fibrils into disaggregated forms. The focus of the thesis work is given below in chapter format.

Chapter 2a: A Rapid and Sensitive Detection of Ferritin in Nanomolar Level using Fluorescent Conjugated Polymer

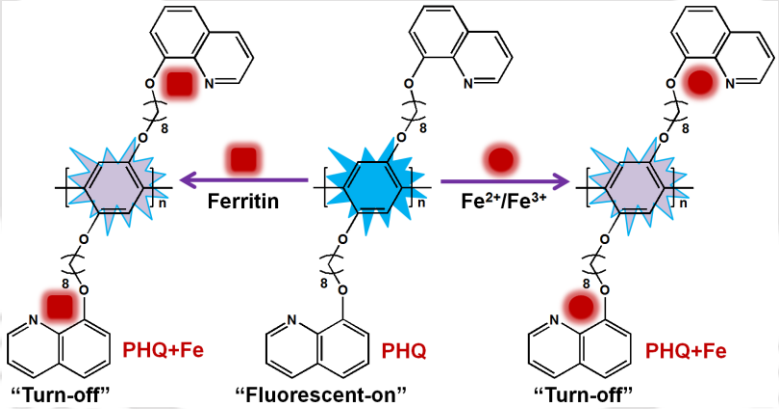

Scheme 1. PHQ selectively detects Fe^{2+}/Fe^{3+} ion and non–heme metalloprotein ferritin in THF: H_2O (4:1) (HEPES buffer, pH 7.4) by "turn–off" mechanism. λ_{ex} 332 nm, and λ_{em} 401 nm.

A neutral conjugated polymer poly-p-phenylene (PPP) derivative, poly(1,4-bis-(8-(8-hydroxyquinoline)-octyloxy)-benzene) (PHQ), was prepared using a simple and economical method of oxidative polymerization reaction. This newly synthesized polymer PHQ has absorption maximum at 327 nm and emission at 401 nm in aqueous conditions. Moreover, PHQ displays fluorescence "turn-off" characteristic with metal ion and selectively detects Fe^{2+}, Fe^{3+} and non-heme metalloprotein ferritin compared to other metallo and non-metalloproteins in physiological conditions (Scheme 1). The Stern−Volmer constant (K_{SV})

value obtained for the detection of ferritin is 0.84×10^7 M^{-1}, confirming high sensitivity of this polymer for ferritin among other proteins.

Chapter 2b: Modulation of Aβ Fibrils using Fluorescent Conjugated Polymer

This chapter describes the use of non–toxic conjugated polymer PHQ to interact with the bound iron containing Aβ fibril aggregates and diminishes their accumulation via metal chelation method (Scheme 2). The enhanced levels of toxic metals, especially iron, from the labile iron pool in brain are primarily responsible for the pathogenesis of several neurological disorders such as AD. They are the major source for generating the highly toxic reactive oxygen species (ROS), accelerating the Aβ peptide aggregation in the brain of AD patients. The anti–AD activity of PHQ was confirmed via *in vitro* control studies by cerebrospinal fluid (CSF Aβ fibrils) and Aβ1–40 fibrils with and without iron using Thioflavin T (ThT) binding assay test and electron microscopy analysis. Conceptually, this new strategy to clear the cerebral deposits in CSF and Aβ1–40 fibrils using PHQ was confirmed successfully under physiological conditions.

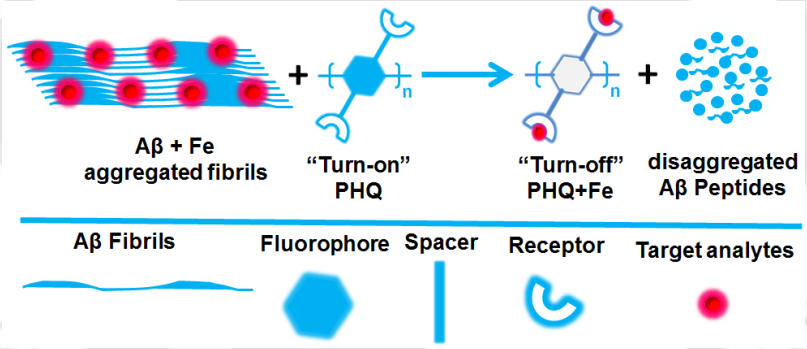

Scheme 2. Modulating effect on Aβ+Fe aggregated fibrils by PHQ via metal chelation method.

Chapter 3a: Amplified Fluorescence from Polyfluorene Nanoparticles with Aggregation–Induced Enhanced Emission: Multifunctional Role as Cobalt, Vitamin B_{12} Sensor and Living Cell Imaging

This chapter describes a new polyfluorene derivative comprising pendant di (2–picolyl)amine (PF–DPA) that was designed and utilized for the detection of Co^{2+} and Vitamin B_{12}. Further this polymer was also used for cell imaging and cancer theranostics via aggregation induced enhanced emission (AIEE) behavior of PF–DPA PDots luminogen. Upon coordination with Co^{2+}, the fluorescence of PF–DPA was quenched by ~98% at low concentrations (0.33 μM) in the solvent ratio of THF: H_2O (9:1) (HEPES buffer, pH 7.4) (Scheme 3). Further, the PF–

DPA was utilized for the selective detection of vitamin B_{12}, a cobalt containing biological macrocycle. The limit of detection (LOD) was calculated for Co^{2+} and VB_{12} from the 3σ/k equation as 3.83×10^{-7} M and 4.9×10^{-6} M respectively.

PF–DPA is highly biocompatible upto 1.6 mg/mL in normal cells but shows potent cytotoxicity against cancer cells in higher doses (>80 µg/mL) enhancing its utility for cancer theranostics. PF–DPA, exhibits a large and unique red shifted enhanced emission at 556 nm in higher water ratio of THF: H_2O (1:9) due to the formation of polymer nanoparticles or PDots by intra and intermolecular self–assembly induced aggregation phenomenon. AIEE in PF–DPA homopolymer nanoparticles is fundamentally very unique and attributed to the combined effect of intramolecular planarization and J–type aggregate formation in the nanoparticles (20±5 nm). Therefore, the PF–DPA PDots showed exceptional live cell imaging applications, exhibiting bright green and red fluorescence.

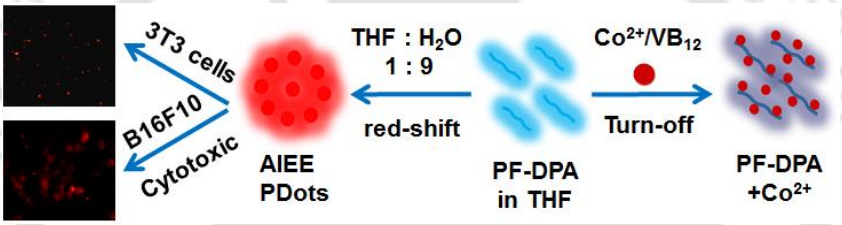

Scheme 3. PF-DPA selectively detects Co^{2+} and VB_{12} in THF: H_2O (9:1) (HEPES buffer, pH 7.4), by "turn–off" mechanism. PF–DPA forms PF–DPA PDots in THF: H_2O (1:9) (HEPES buffer, pH 7.4) by AIEE phenomenon and it could be applied for cell imaging, delivery of anticancer drugs in cells and for cancer theranostics.

Chapter 3b: Inhibition of Aβ Fibrillation and Modulation Effect on Preformed Aβ Oligomers and Fibrils by an Influence of Aggregation Induced Enhanced Emission luminogen of PF–DPA PDots

This chapter describes the utility of a conjugated polyfluorene derivative of PF–DPA which displays AIEE phenomenon in the nanoparticle/polymer dots (PDots) form and is reported for its inhibition of Aβ fibrillization and modulating effect on Aβ1–40 oligomers and fibrils (Scheme 4). It is established that PF-DPA PDots (5 µM) inhibited Aβ1-40 fibrillation to form spherical oligomers into Aβ1-40 aggregates. Furthermore, in presence of PF-DPA PDots (5 µM) preformed Aβ1-40 oligomers, Aβ1-40 fibrils and CSF Aβ aggregates, showed an exceptional modulation effect due to the formation of coassembly between the PF-DPA PDots and Aβ aggregates. Consequently, the formation of coassembly between PF-DPA PDots and Aβ aggregates is due to the formation of face-to-face arrangements by

hydrophobic interactions resulting in modulation of the aggregated peptides which may likely lead to the prevention or treatment for AD.

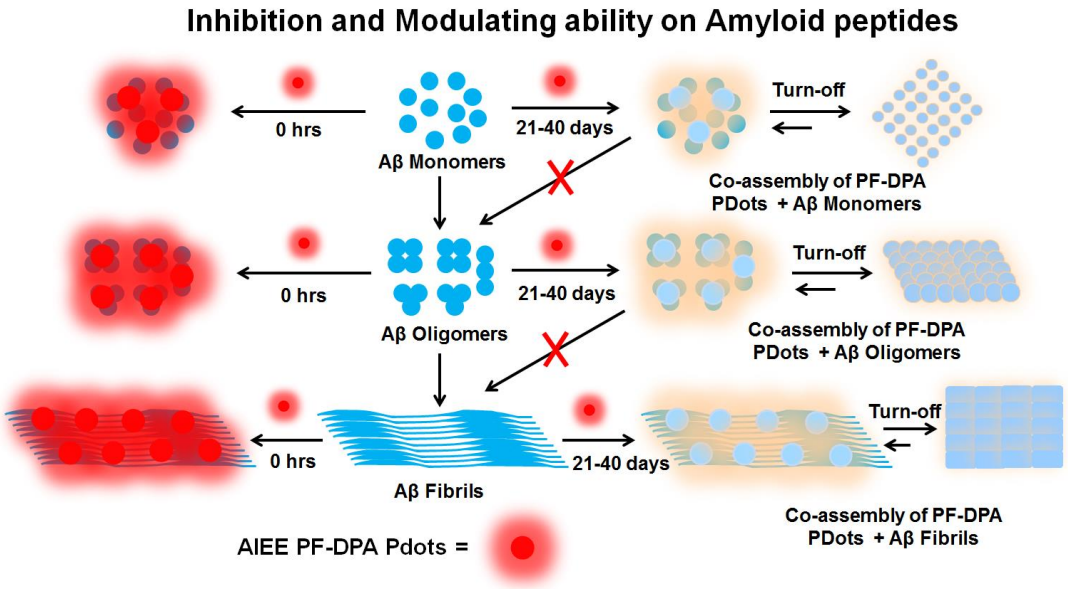

Scheme 4. Schematic representation for inhibition of Aβ fibrillation and modulating effect on Aβ oligomers and fibrils by AIEE luminogens of PF–DPA PDots.

Chapter 4a: Highly Selective Probe Detects Cu^{2+} and Endogenous NO Gas in Living Cells

This chapter describes the synthesis of a new indole–3–carboxaldehyde functionalized fluorescein hydrazone FI, which can selectively detect Cu^{2+} *in vitro* by the "turn–on" mechanism followed by fluorescence "turn–off" with nitric oxide (NO) (Scheme 5). FI demonstrates characteristic "turn–on" behavior in the presence of Cu^{2+} ion via spirolactom ring–opening, while other metals such as Na^{+}, K^{+}, Ca^{2+}, Cr^{3+}, Mn^{2+}, Fe^{2+}, Fe^{3+}, Co^{2+}, Ni^{2+}, Zn^{2+}, Cd^{2+}, Hg^{2+} and Ag^{+} did not influence FI fluorescence even at very high concentration. Further, the FI−Cu^{2+} complex fluorescence was not quenched with any anions or amino acids but was completely quenched by NO and the paramagnetic nature of Cu^{2+} ion converted into the diamagnetic nature when reduced to Cu^{+}. The experiment performed in the cellular system indicates that FI loaded RAW264.7 cells showed bright fluorescence in the presence of Cu^{2+}, while other metals did not influence the FI fluorescence. In addition, the fluorescence of FI−Cu^{2+} was efficiently quenched by NO generated in macrophages through LPS stimulation.

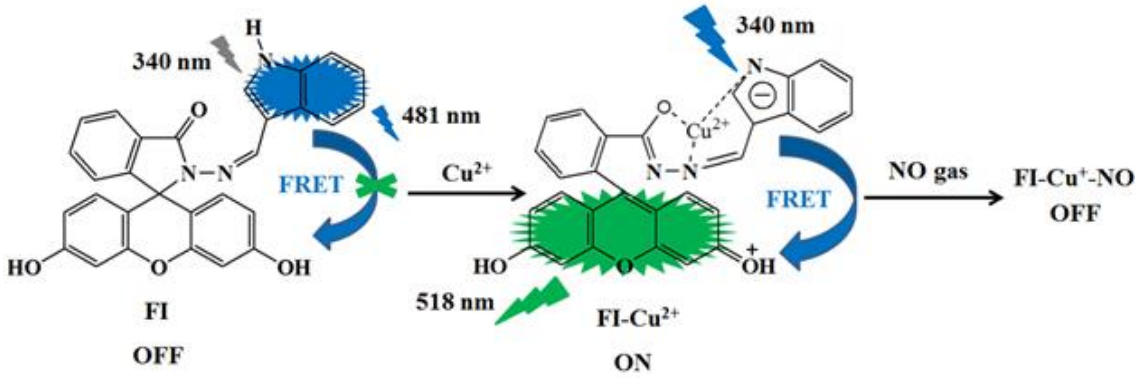

Scheme 5. Indole–3–carboxaldehyde functionalized fluorescein hydrazone (FI) selectively detects Cu^{2+} by the "turn–on" mechanism followed by fluorescence "turn–off" with NO gas *in vitro*.

Chapter 4b: Multiple Function Fluorescein Probe Performs Metal Chelation, Disaggregation and Modulation of Aggregated Aβ fibrils and Aβ-Cu Complex

This chapter describes an exceptional nontoxic indole-3-carboxaldehyde fluorescein hydrazone (FI) performs multiple tasks, namely, disaggregating amyloid β (Aβ) aggregates in different biomarker environments such as cerebrospinal fluid (CSF Aβ fibrils), Aβ1-40 fibrils, β-amyloid lysozyme aggregates (LA) and U87 MG Human astrocytes cells. Additionally, the probe FI binds with Cu^{2+} ions selectively, disrupts the Aβ aggregates into disaggregated forms and prevents their reaggregation, thereby performing disaggregation and modulation of amyloid-β in the presence as well as absence of Cu^{2+} ion. The excellent selectivity of probe FI for Cu^{2+} was effectively utilized to modulate the assembly of metal-induced Aβ aggregates by metal chelation with the "turn-on" fluorescence via spirolactam ring opening of FI as well as the metal-free Aβ fibrils by noncovalent interactions (Scheme 6). These results confirm that FI has exceptional ability to perform multifaceted tasks such as metal chelation in intracellular conditions using Aβ lysozyme aggregates in cellular environments by the disruption of β-sheet rich Aβ fibrils into disaggregated forms. Subsequently, it was confirmed that FI had the ability to cross the blood brain barrier (BBB) and it also modulated the metal induced Aβ fibrils in cellular environments by "turn-on" fluorescence, which are the most vital properties of a probe or a therapeutic agent. Furthermore, the morphology changes were examined by atomic force microscopy (AFM), polarizable optical microscopy (POM), fluorescence microscopy and dynamic light scattering (DLS) studies. These results provide very valuable clues on the Aβ (CSF Aβ fibrils, Aβ1-40

fibrils, Aβ lysozyme aggregates) disaggregation behavior via *in vitro* studies, which constitute the first insights into intracellular disaggregation of Aβ by "turn-on" probe method thereby influencing amyloidogenesis.

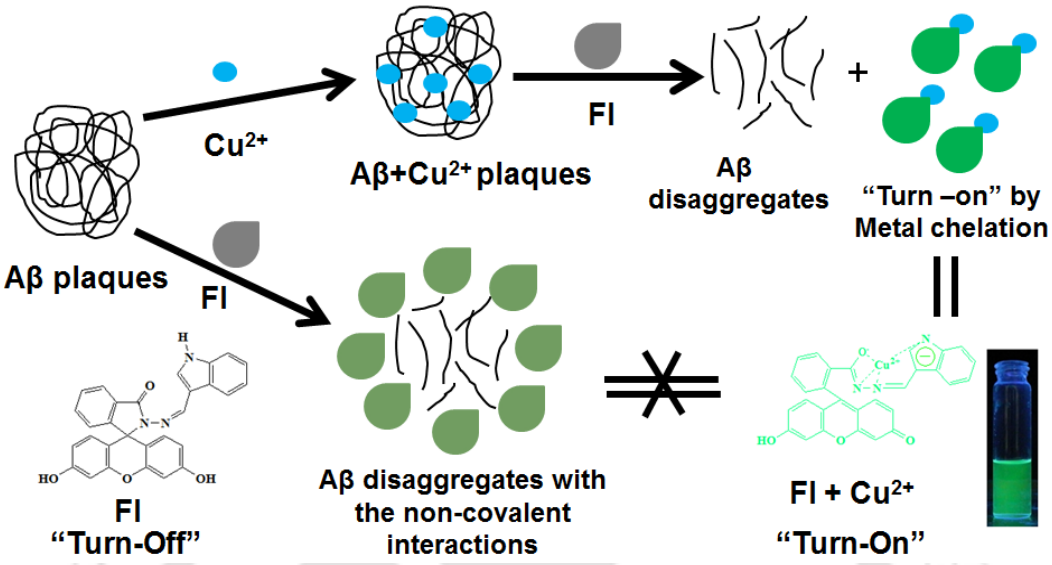

Scheme 6. Modulating effect on Aβ aggregated fibrils in the presence and absence of Cu^{2+} ion by FI via turn "on–off" method.

Chapter 5a: Aggregation Deaggregation Influenced Selective and Sensitive Detection of Cu^{2+} and ATP by Histidine Functionalized Water Soluble Fluorescent Perylene Diimide under Physiological Conditions and in Living Cells

This chapter describes the synthesis of highly water–soluble fluorescent perylene diimide (PDI–HIS), functionalized with histidine amino acid and utilized as a rapid "turn–off" fluorescence and colorimetric probe for the detection of Cu^{2+} and ATP under physiological conditions and in A549 cells (Scheme 7). The emission of PDI–HIS gets completely quenched upon formation of PDI–HIS+Cu^{2+} complex, primarily caused by metal coordination induced molecular aggregation with a K_{SV} value of 7.1×10^{6} M^{-1}. The PDI–HIS+Cu^{2+} complex was highly selective for ATP due to the disaggregation of this complex with a very low limit of detection of 0.58×10^{-6} M. The low toxicity of PDI–HIS probe allowed its use for the detection and imaging of both Cu^{2+} and ATP in A549 living cells.

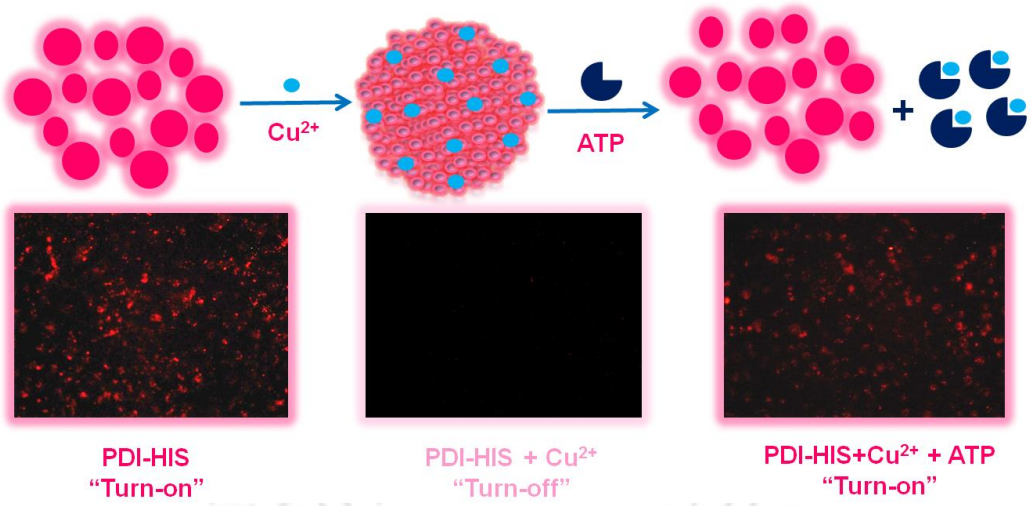

Scheme 7. Histidine functionalized perylene diimide (PDI–HIS) selectively detects Cu^{2+} by the "turn–off" metal induced aggregation mechanism followed by fluorescence "turn–on" disaggregation of PDI–HIS+Cu^{2+} complex with ATP *in vitro.*

Chapter 5b: An Efficient Strategy to Assemble Water Soluble Histidine–Perylene Diimide and Graphene Oxide for the Highly Selective and Sensitive Detection of PPi in Physiological Conditions and *in vitro*

This chapter describes a novel strategy to self–assemble multiple dimension materials interconnected into aggregated networks that resulted in the development of water soluble, biocompatible nanocomposite probe for the exclusive detection of pyrophosphate (PPi) in physiological conditions and *in vitro* live melanoma cancer cells (B16F10). The water soluble materials studied here comprised of amino acid (histidine) functionalized perylenediimide (PDI–HIS), copper and graphene oxide (GO) that could self–assemble, and could be utilized as a highly effective sensing platform in biological medium and cellular environment *via* fluorescence "turn–on" method for PPi detection. This PDI–HIS–Cu–GO (PCG) nanocomposite sensor provides a unique platform for the fluorogenic detection of PPi having a very low limit of detection of 0.60×10^{-7} M (LOD) based on the strong affinity between the copper complex of PDI–HIS receptor and PPi. The intracellular detection of PPi using PCG was also carried out in B16F10 cells where >10 times sensitively was observed as compared to the PDI–HIS+Cu^{2+} probe. This confirms the utility of this biocompatible nanocomposite for early cancer detection *via* PPi recognition in physiological conditions and in live cells. Furthermore, the fabrication of PDI–HIS and PCG with PVA hydrogel films and on thin layer chromatography plates demonstrated the practical utility for the detection of PPi anions by "off–on" response rapidly in a label free manner (Scheme 8).

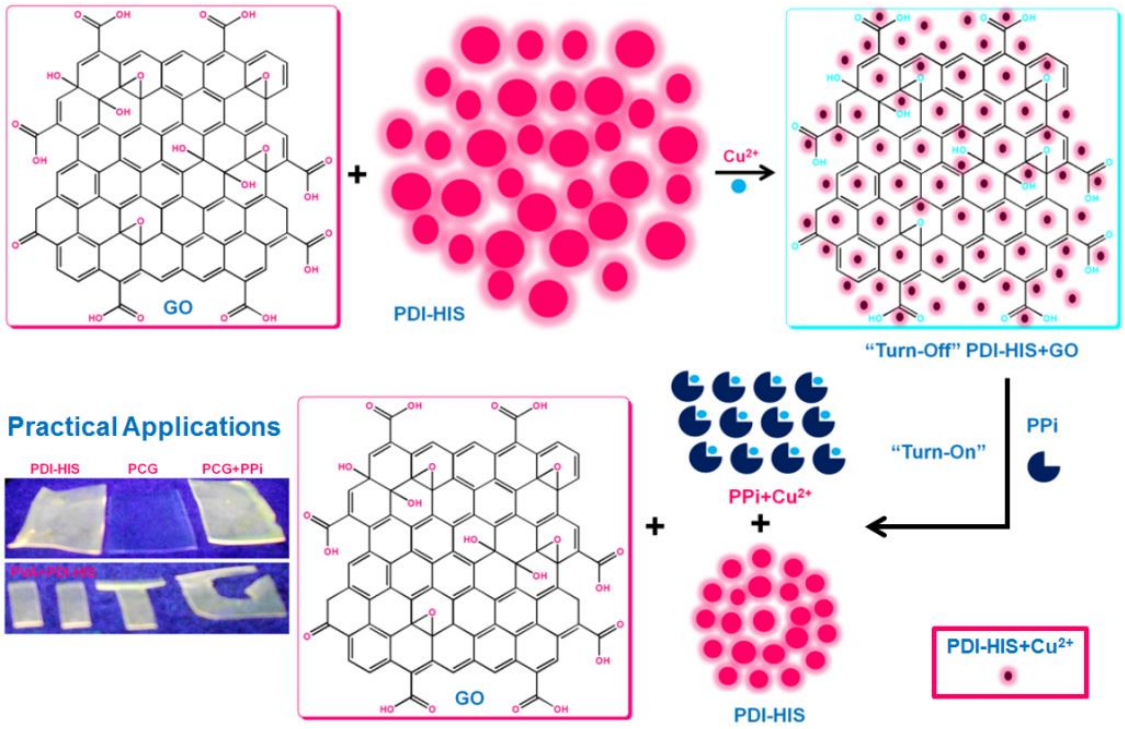

Scheme 8. The formation of PCG nanoaggregates from the mixture of PDI–HIS, GO and Cu^{2+} and the detection of PPi at very low limit of detection of 0.60×10^{-7} M (LOD). The fabrication of PDI–HIS and PCG with PVA hydrogel films in practical applications for the detection of PPi anions by "off–on" response.

Chapter 5c: Modulation of Aβ Fibrils into Mature Micro Rod shaped Hybrid Structure by Histidine Functionalized Water soluble Perylene Diimide

This chapter describes a unique approach towards transforming the aggregated amyloidogenic peptides using an amino acid functionalized perylene diimide as a molecular modulator, which is a different nondestructive approach as compared to inhibiting the aggregation of peptides. The histidine functionalized perylenediimide (PDI-HIS) molecule could coassemble with Aβ peptides via hydrogen bonding that leads to the enhancement in the π-π interactions between Aβ and PDI-HIS moieties (Scheme 9). The ThT assay and various spectroscopic and microscopic techniques establish that the PDI-HIS molecules accelerate the Aβ1-40 and the Aβ aggregates in CSF into micro size coassembled structures. These results give rise to a new and unique complementary approach for modulating the biological effects of the aggregates in amyloidogenic peptides.

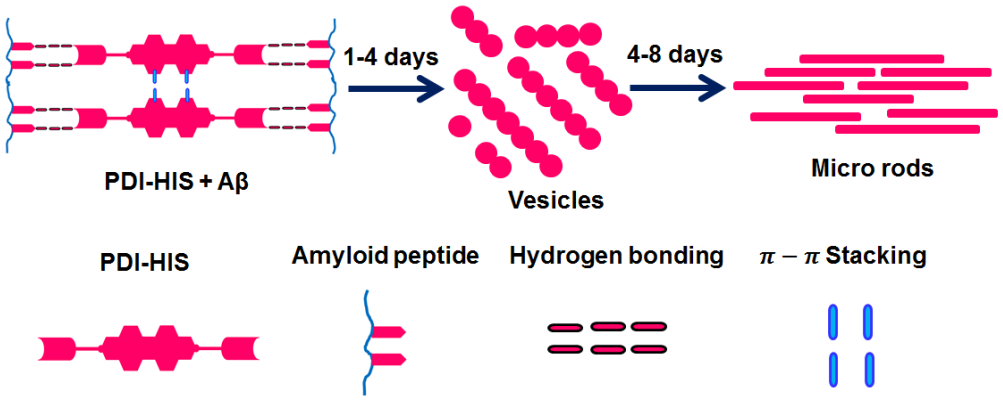

Scheme 9. Modulating effect on Aβ aggregated fibrils by PDI–HIS. Schematic representation of coassembly micro rods formation between Aβ fibrils and PDI–HIS via noncovalent interactions.

Conclusion and thesis overview

In conclusion, we designed and synthesized new fluorescent conjugated polymers (PHQ and PF–DPA) and small molecules (FI and PDI–HIS) and successfully utilized them for various applications in sensors to detect cations (Fe^{2+}/Fe^{3+}, Co^{2+} and Cu^{2+}) and anions (ATP, PPi and NO) respectively. Furthermore, the same conjugated polymers (PHQ and PF–DPA) and small molecules (FI and PDI–HIS) were also successfully utilized for modulating Aβ fibrils and metal–associated Aβ aggregates by different mechanisms.

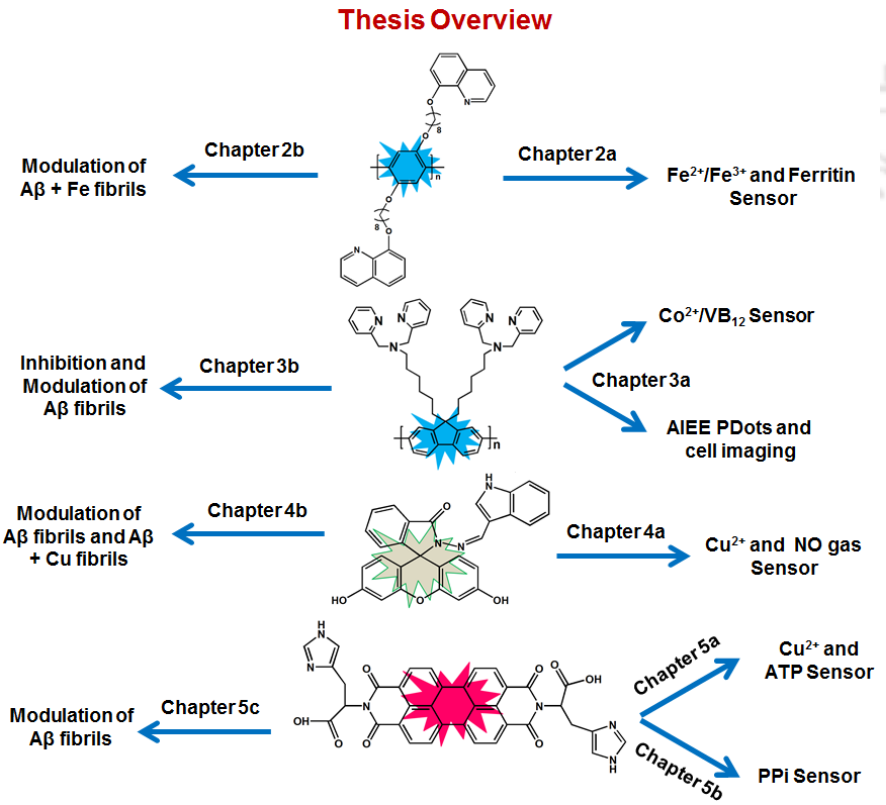

Scheme 10. Thesis overview.

Contents

Chapter 5c: Modulation of Aβ Fibrils into Mature Micro Rod shaped Hybrid Structure by Histidine Functionalized Water soluble Perylene Diimide

1.1. Introduction

Novel fluorescent materials, namely, polymer and small molecules are significant sensor elements and provide very promising direction in interdisciplinary areas of chemistry, material sciences, biological sciences and medicine. These fluorescent materials are well demonstrated to detect specific chemical and biological targets in selective and sensitive manner. Fluorescent chemosensors, in general, are able to selectively recognize a guest species, which, in recent times have received significant attention in supramolecular chemistry because of their potential applications in environmental detection, molecular catalysis, biological fluorescence imaging, etc.[1,2] According to their high selectivity and sensitivity, together with the advantages of spatial and temporal resolution, fluorescent chemosensors can be conveniently used to analyse, quantify and separate the guest species as well as sense biologically important species *in vitro* and *in vivo* to elucidate their function in living systems.[3,4]

The construction of a fluorescent chemosensor usually involves two integrated components. One is a signalling fluorophore and another is a guest receptor that possesses a recognition capability, both are connected by a spacer to form a fluorophore–spacer–receptor scaffold system.[5] When a guest species is bound to the receptor, the photophysical characteristics of the fluorophore, such as fluorescence intensity, emission wavelength and fluorescence lifetime, will change via different mechanisms, and such a change provides a signal that indicates guest binding. Since chemosensors are applied in food analysis, process control, environmental monitoring, medical diagnosis and many other disciplines, a thorough understanding of the available constructions at the molecular level can help elucidate and improve the design of fluorescent chemosensors to develop sophisticated sensing systems.[6-8] Moreover, this chapter will describe the basic concept of sensors using novel conjugated polymers and small molecules, their electronic and signaling properties. These essential concepts have helped to shape this dissertation that involved the development of highly sensitive and selective conjugated polymer and small molecule based sensors.

1.2. Small Molecule based Sensors

The development of small molecule probes are fascinating, which hold attractive potential applications in *in vivo* experiments because of their low molecular weight, high chemical stability, and relatively good cell permeability.[9] Most of the small molecules mainly focused on the derivatives of known recognition elements (e.g., crown ethers, polyamines,

macrocyclic amines, pyridines, and acetates),[10] and the discovery of new recognition elements remains challenging.

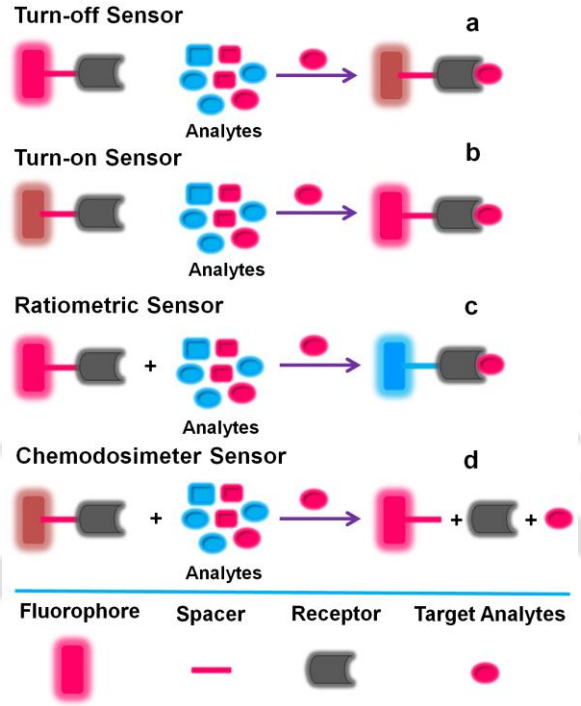

Scheme 1.1 Schematic representation of various types of small molecular fluorescent sensors.

There are various small molecule based fluorescent sensors that have been developed in recent years for the selective detection of metals and anions. These fluorescent sensors are classified into four different types according to their fluorescence signaling process for example: (a) Turn–Off, (b) Turn–On, (c) ratiometric and (d) chemodosimeters. The fluorescence of 'Turn–Off', 'Turn–On' and ratiometric sensors is, in general, quenched, enhanced and shifted upon recognition of the target analyte and the process is usually reversible (Scheme 1.1). However, the fluorescent chemodosimeters are molecular systems that allow analyte detection through a highly selective and usually irreversible chemical reaction between the dosimeter molecule and the target analyte leading to an observable signal or some physical change, in which an accumulative effect is directly related to the analyte concentration (Scheme 1.1).

So far, various small molecule fluorophores with different excitation and emission wavelengths have been employed as signal reporters of chemosensors (Figure 1.1), such as anthracene, coumarin, boron dipyrromethene difluoride (BODIPY), xanthenes, cyanine, naphthalenedimide (NDI), perylenediimide (PDI) etc.[10,11-21]

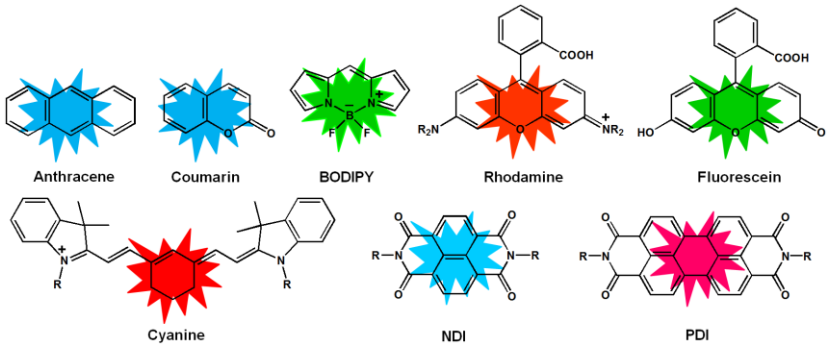

Figure 1.1 Common small molecule fluorescent probes for chemosensor.

1.2.1. Fluorescein based Sensors

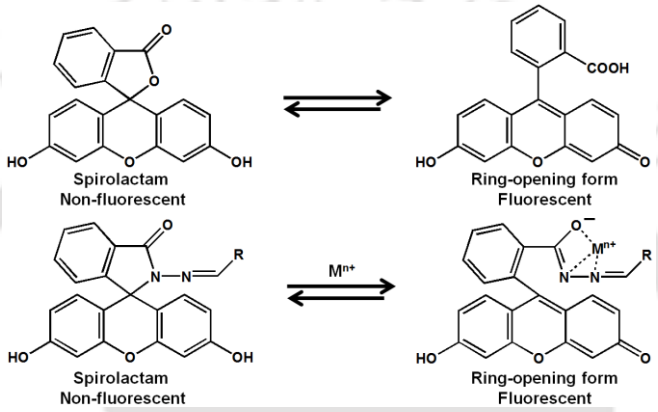

Figure 1.2 Ring-opening of spirocyclic xanthene derivatives of fluorescein.

Xanthene derivatives of fluorescein and rhodamines are highly favourable molecules because of their excellent photophysical properties, such as high extinction coefficients, excellent quantum yields, great photostability and relatively long emission wavelengths. Fluorescein was first synthesized by von Bayer in 1871 with resorcinol and phthalic anhydride via Friedel–Crafts acylation/cyclodehydration.[22] Some of the advantageous of the fluorescein fluorophores are good water solubility, visible excitation and emission (an absorption maximum at 494 nm and emission maximum of 521 nm in water), and highly bright fluorescence at physiological pH.[23] The fluorescein derivatives are nonfluorescent when they exist in the lactone form, and the ring opened form can induce color changes and fluorescence enhancements (Figure 1.2). As another typical xanthene dye, rhodamine was first synthesized by Noelting and Dziewonsky[24] in 1905 and has been widely used in many research fields, including the lasing medium in dye lasers and fluorescent markers in biological studies (Figure 1.3).[25,26]

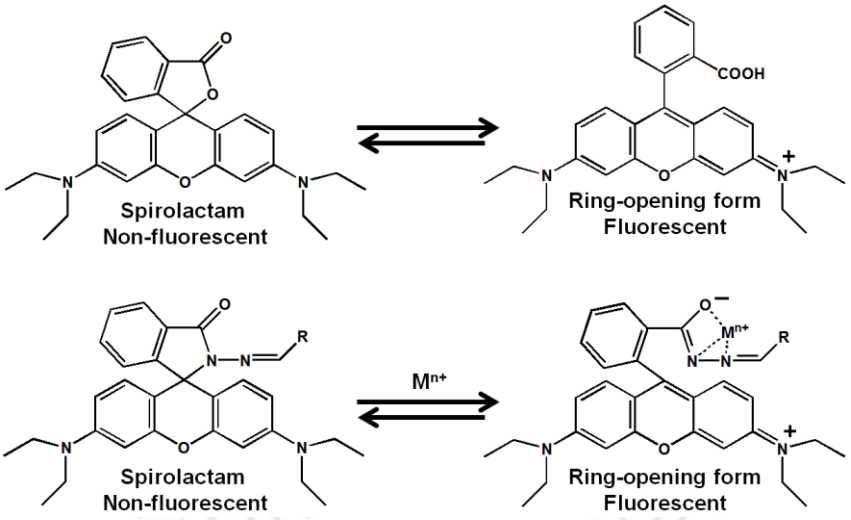

Figure 1.3 Ring-opening of spirocyclic xanthene derivatives of Rhodamine B.

The spirocyclic derivatives of fluorescein and rhodamine dyes are useful sensing platforms because the ring-opening process leads to a "turn-on" fluorescence change. This "turn-on" fluorescence change occurred via conversion of the weakly fluorescent form to the ring-open fluorescent amide form which is designed to bind metal ions via the carbonyl O, enamine N and hydroxyl groups as donors. In 1997, Anthony W. Czarnik was first reported a rhodamine-based fluorescent chemosensor for Cu^{2+} ion,[27] afterwards, a large number of papers have been published based on fluorescent chemosensors via spiro ring-opening processes by various metal ions (Cu^{2+}, Hg^{2+}, Fe^{3+}, Zn^{2+}, Cr^{3+}, Ag^{+}, Au^{+}, Pb^{2+}, Pd^{2+}, and Pt^{2+}), anions (cyanide and pyrophosphate), and reactive oxygen species.[25] Toward this end, novel fluorescein based probes have been developed using different receptors and utilized for sensor applications, as discussed in detail below.

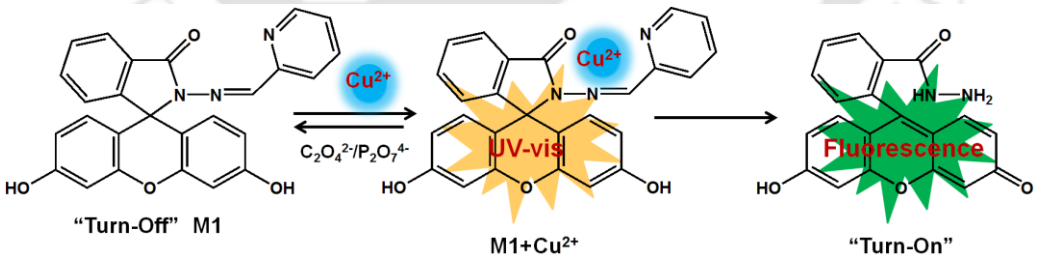

Figure 1.4 The 2-pyridylaldehyde fluorescein hydrazone chemosensor (Molecule 1 (M1)) for copper and PPi/$C_2O_4^{2-}$ anions.

Huo et al,[28] synthesized and developed a 2-pyridylaldehyde fluorescein hydrazine of M1 for the detection of copper by an UV−vis reversible but fluorescence irreversible chemosensor. The coordination complex of M1−Cu^{2+} gave UV−vis response by PPi/$C_2O_4^{2-}$, which makes the probe response reversible and the storage of the M1−Cu^{2+} complex resulted in hydrolytic

cleavage of the N=C bond, which released the fluorophore (ring-opened fluorescein hydrazine) and gave irreversible fluorescence (Figure 1.4).

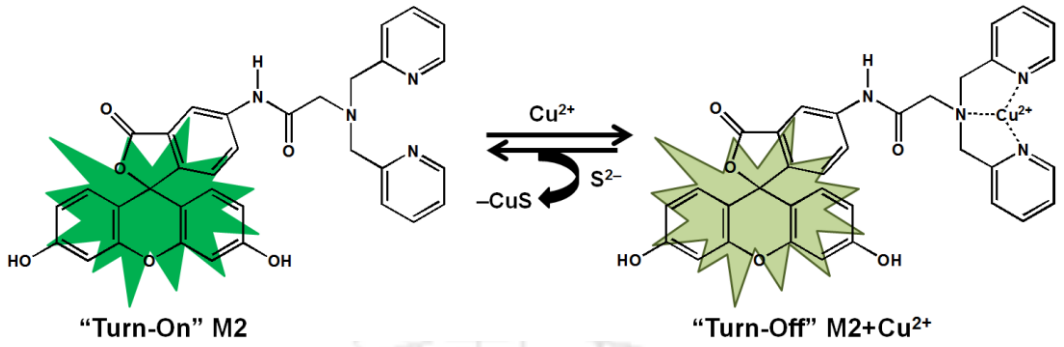

Figure 1.5 The structure of the fluorescein–DPA chemosensor of M2 for copper and S^{2-} and the possible mechanism.

Chang et al,[29] synthesized a very simple fluorophore which consisted of a fluorescein signaling moiety and a DPA binding unit (M2) for the selective sensing of sulfide ion (Figure 1.5). The dipicolylamine appended fluorescein probe exhibited a selective "on–off" sensor for copper ion which is further used for "off–on" type signaling behavior towards sulfide ion in 100% aqueous solution, with a detection limit of 420 nM.

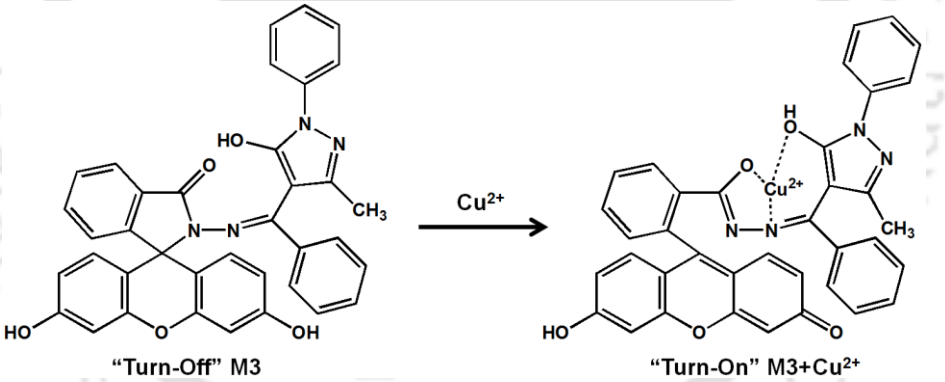

Figure 1.6 The fluorescein–1-phenyl-3-methyl-4-benzoyl-5-pyrazolone chemosensor (M3) for copper.

Yang et al,[30] designed and synthesized a novel fluorescein derivative of M3, by the reaction of fluorescein hydrazide with 1-phenyl-3-methyl-4-benzoyl-5-pyrazolone, and evaluated it as a chemoselective Cu^{2+} ion sensor (Figure 1.6). Addition of Cu^{2+} to an aqueous solution of the fluorescein derivative resulted in a rapid color change from colorless to deep yellow together with a distinctive change in UV-vis absorption spectrum. This observed results indicate that the fluorescein derivative could provide a rapid, selective and sensitive response to Cu^{2+} and could be used as a potential Cu^{2+} colorimetric chemosensor in aqueous solution.

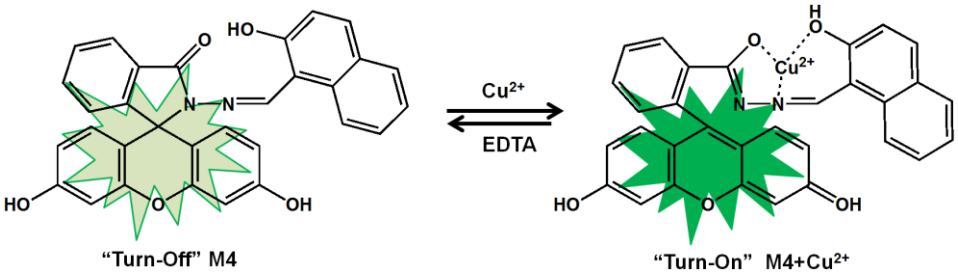

Figure 1.7 The structure of new fluorescein-based chemosensors (M4) for Cu^{2+} ion with highly selective ''off–on'' behavior.

Sinn et al,[31] designed and synthesized a new fluorescein-based chemosensor (M4) for Cu^{2+} ion with highly selective ''off–on'' behavior (Figure 1.7). This probe M4 displayed reversible absorption and fluorescence-enhanced responses to Cu^{2+} via a 1:1 complex. The selectivity towards Cu^{2+} ion is very high over other metals upon addition of Cu^{2+} to M4 in aqueous solution.

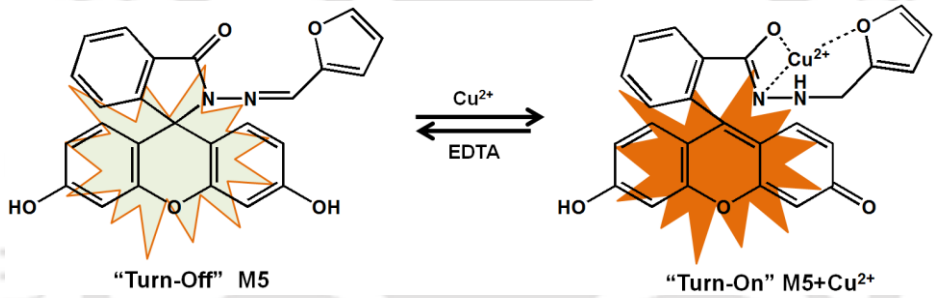

Figure 1.8 A novel furfuraldehyde fluorescein hydrazone (M5) chemosensors for Cu^{2+} with highly selective ''off–on'' behavior.

Dong et al,[32] demonstrated a novel fluorescein derivative furfuraldehyde fluorescein hydrazone (M5), synthesized successfully by simple two-steps and its sensing characteristics to Cu^{2+} were investigated using UV–vis spectroscopy. In the presence of Cu^{2+}, the M5 displayed an obvious color change from colorless to yellow together with UV–vis absorption spectra change in a very short time and their ring-opening reaction mechanisms were proposed for M5 bound Cu^{2+} ion in a 1:1 stoichiometric ratio (Figure 1.8).

1.2.2. Perylene Diimide based Sensors

Molecular self-assembly plays a crucial role in the design and construction of small organic molecule based functional novel materials[33,34] with interesting applications. Perylene-3,4,9,10-tetracarboxylic dianhydride (PTCDA) is a parent compound of this class of materials, first described in 1912.[35] As shown in figure 1.9, various perylene diimide (PDI) materials with different chemical and physical properties could be obtained via modification of the substituents on the imide positions by the R groups (alkyl chains or receptor groups). Last few years, small molecule probes based on PDI derivatives in aqueous medium have

attracted much attention because of their several advantageous properties such as thermal stability, photochemical stability, chemical inertness, and high fluorescence.[36-42] Having such excellent properties, PDI derivatives have been considered as optimal fluorescent dyes and utilized in a wide variety of applications such as laser dyes, photovoltaic cells, fluorescence switches, molecular wires, molecular transistors, sensors and especially molecular fluorescence imaging.[43-48] However, the PDI molecule and its planar π-electron deficient aromatic nature are known to promote strongly the formation of aggregates through stacking interactions between the π-conjugated core[36] and this strong aggregation tendency in aqueous media results in fluorescence quenching.[49,50] In spite of the aggregation and resultant low fluorescence, PDI derivatives have been considered to be excellent fluorophores in sensor design because of their excellent electron accepting ability and high fluorescence in the disassembled state.[51,52]

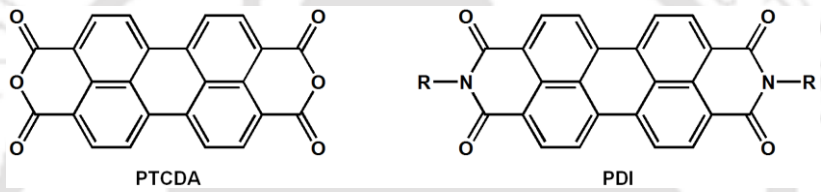

Figure 1.9 The structure of PTCDA and PDI.

The applications in molecular imaging, especially fluorescence imaging, has been proven to be useful in clinical diagnosis and drug discovery[53-56] because it has fine temporal and spatial resolution and can be safely performed with simple instruments and facilities.[57] There are several characteristics of a successful optical molecular probe for medical imaging including water solubility, brightness, photostability and low cytotoxicity.[3] Although, there are variety of water soluble chromophores commercially available today, each optical molecular probe has its own disadvantage, such as low fluorescence quantum yields, photobleaching, or high cytotoxicity. To overcome these problems, PDI derivatives were improved by incorporating hydrophilic substituents at the diimide positions.[38,58-63] However, PDI derivatives with hydrophilic substituents such as carboxylic, sulfonic and other ionic functionalities generally show low fluorescence emission due to predominant π−π stacking and especially in case of ionic functionalities π−π stacking was supposed to be suppressed by the complexation with oppositely charged moieties.[64]

However, the detection of biologically important metal ions such as iron, copper and zinc has gained significant interest since these metal ions are essential for the proper functioning of all living cells and their excessive concentrations in body are toxic leading to various biological disorders.[65-69] However, peptides and/or amino acids are interesting candidates for making

supramolecular structures and advanced soft materials due to their ability of specific molecular recognition, availability, functional flexibility and biodegradability.[70,71] In this context, biomolecules such as amino acids and their derivatives are particularly appealing due to their remarkable metal chelating nature, aqueous solubility, specific molecular recognition, and ability to self-assemble into functional, complex and highly ordered molecular systems and nanomaterials through various noncovalent interactions.[72-77] Toward this end, novel PDI based probes have been developed using different receptors and utilized for sensor applications, which will be discussed in detail below.

In 2012 Li et al,[48] designed and synthesized a water-soluble PDI derivative of M6, through a simple one-step reaction in high yield and developed a simple "turn-on" fluorescent sensor for PPi in 100% aqueous solution based on Cu^{2+}-mediated M6 aggregates (Figure 1.10). In aqueous solution, M6 exhibited strong monomer fluorescence, which was effectively quenched by the addition of Cu^{2+} ions due to the formation of M6/Cu^{2+} aggregates. Upon addition of PPi, fluorescence recovery was observed due to the competitive binding of PPi with Cu^{2+} and the dissociation of the M6/Cu^{2+} aggregates.

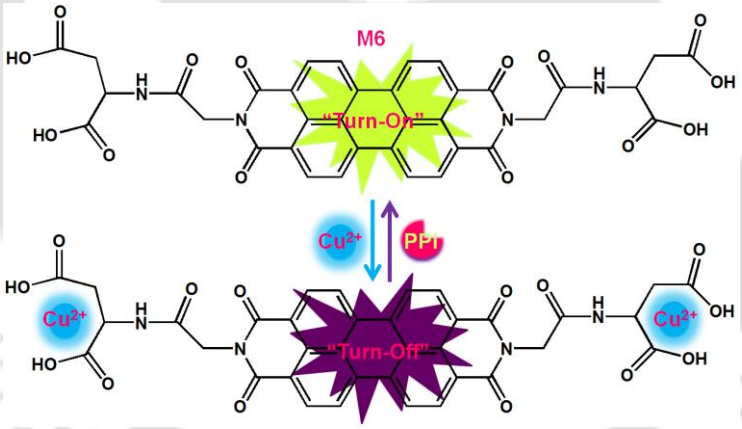

Figure 1.10 A novel PDI derivative of chemosensors M6 for Cu^{2+} and "turn-on" fluorescent sensor for PPi in 100% aqueous solution.

In 2013 Zhu et al,[78] designed and synthesized an aspartic acid functionalized water-soluble perylene diimide (M7). M7 could selectively coordinate to Cu^{2+} in the presence of other competing metal ions in pure aqueous solution. Fluorescence of M7 was completely quenched upon formation of Cu^{2+} complex, thus M7 could act as ''turn-off'' sensor to detect Cu^{2+} ion selectively. The lowest limit of detection for Cu^{2+} was found to be 0.3 μM in HEPES buffer solution. Further, M7+Cu^{2+} complex selectively detected ATP via ''turn-on'' sensor method by metal chelation mechanism (Figure 1.11).

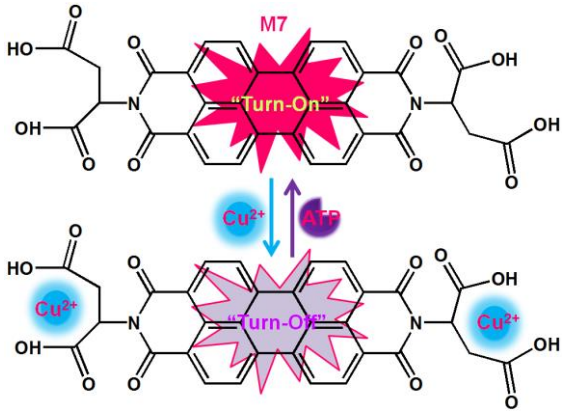

Figure 1.11 A novel aspartic acid functionalized water-soluble perylene diimide (M7) chemosensors for Cu^{2+} and "turn-on" fluorescent sensor for ATP in HEPES buffer solution.

In 2014 Govindaraju et al,[79] developed the amphiphilic L-DOPA functionalized PDI derivative M8 (Figure 1.12) and investigated photophysical properties to achieve its disassembled (molecularly dissolved) state in aqueous media using cationic micellar conditions. Assembly−disassembly modulation of M8 was established as a supramolecular fluorescent probe (switch off−on probe) for metal ions Fe^{3+} and Cu^{2+} in the micellar media of cationic surfactant solution.

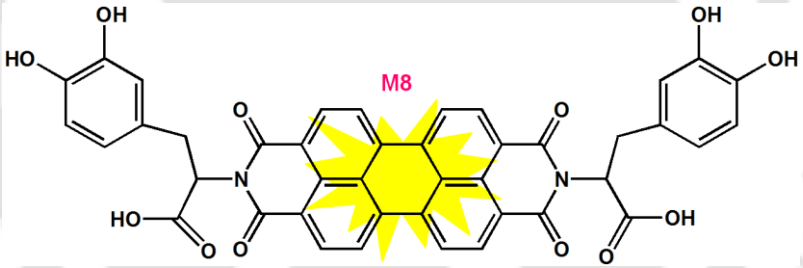

Figure 1.12 A novel amphiphilic L-DOPA functionalized PDI derivative of M8.

In 2009 Yoon et al,[80] demonstrated a new fluorescent sensor (M9) based on a perylene-DPA-Zn^{2+} platform (M9+Zn^{2+}) which could selectively sense UTP and UDP in aqueous solution at physiological pH by "Off-On" fluorescence sensor method (Figure 1.13).

In 2012 Yan et al,[81] demonstrated a new PDI ligand (M9) functionalized with a Zn^{2+} dipicolylethylenediamine (M9+Zn^{2+}) moiety that was synthesized and first used as a fluorometric chemosensor to specifically detect ATP over other phosphate anions in aqueous solution. Secondly, the solution of M9+Zn^{2+} complex upon addition of ATP displayed a remarkable absorption decrease compared with other anions, indicating that the M9+Zn^{2+} complex highly selective toward ATP.

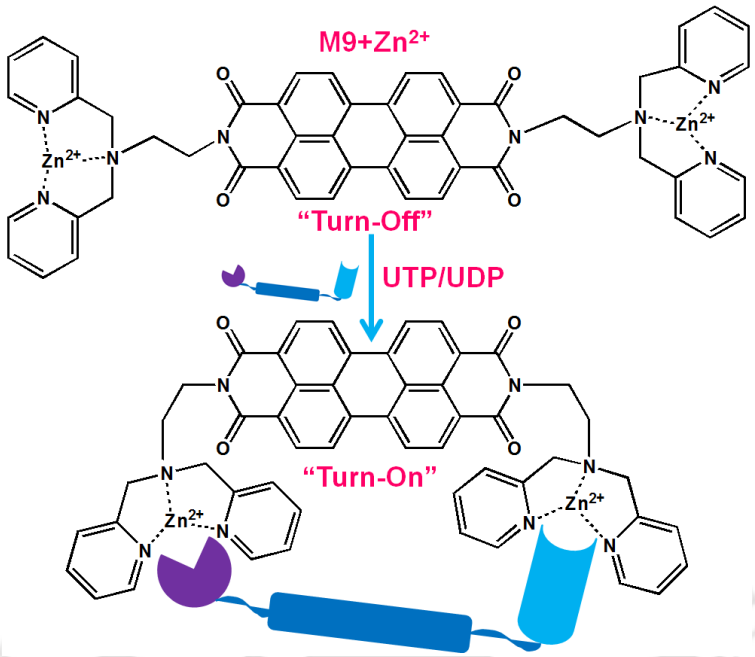

Figure 1.13 PDI derivatives of M9 based Zn^{2+} complex (M9+Zn^{2+}) which can selectively sense UTP and UDP in aqueous solution at physiological pH by "Off-On" fluorescence sensor type.

In 2014 George et al,[82] demonstrated a new allosteric regulation design (M9+Zn^{2+}) for modulating the supramolecular chirality of helical receptor assemblies, by the homotropic and heterotropic binding of adenosine phosphate guest molecules.

In 2008 Zang et al,[38] developed fluorescent sensor from a perylene based molecule, N,N'-dideoxythymidine-3,4,9,10-perylene-tetracarboxylic diimide (M10), which showed strong and highly selective binding between the thymine ligand (T) and Hg^{2+} ion facilitates efficient sensing of Hg^{2+} ions based on a fluorescence quenching mechanism, which is primarily caused by metal coordination induced molecular aggregation (Figure 1.14).

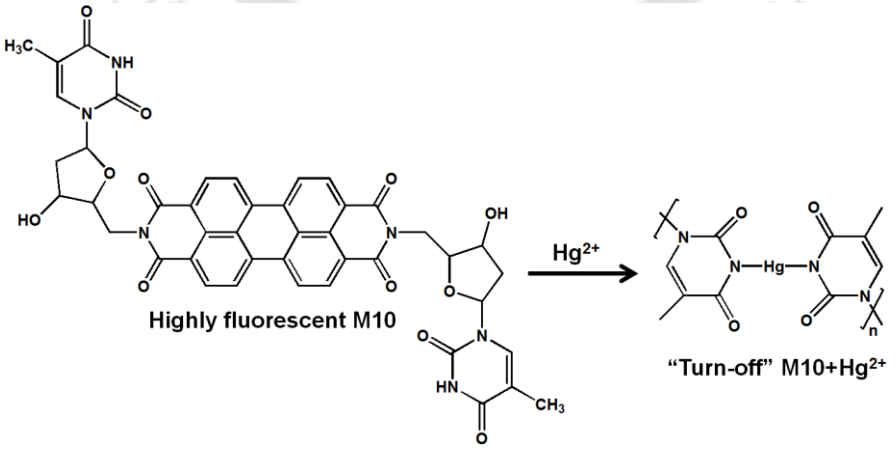

Figure 1.14 A perylene based small molecule of M10 selectively sense Hg^{2+} ions by fluorescence quenching mechanism.

1.3. Conjugated Polymers

Conjugated polymers (CPs) have alternate saturated and unsaturated bonds along the main chain backbone. The saturated single bonds are σ–bonds while unsaturated double bonds are combination of σ–bond and a π–bond. All CPs consist of σ–bond through the overlapping sp^2 hybrid orbitals and the remaining out–of plane p_z orbitals which overlaps with neighboring p_z orbitals and forms π–bonds. Therefore, the electrons that constitute the π–bonds are delocalized over the entire polymer backbone even though the chemical structures of CPs are presented as alternating single and double bonds. This continuous delocalized π–bond along the backbone is the origin of the emissive and conductive property of CPs. It was firstly discovered by Shirakawa, MacDiarmid and Heeger that chemical doping of polyacetylenes caused increase in electronic conductivity over several orders of magnitude then this finding and their life–time contribution to the CP development lead them to the 2000 Nobel Prize in chemistry.[83,84] The CPs are emerging active materials in various applications such as light–emitting diodes (LEDs),[85-87] field effect transistors (FETs),[88] plastic lasers,[89,90] batteries,[91,92] photovoltaic cells,[93] biomaterials[94,95] and sensors.[96,97] There are many different conjugated backbones of CPs that have been developed for above applications, such as poly(para–phenylenes) (PPP),[98] poly(para–phenylene vinylene) (PPV),[85] poly(para–phenylene ethynylene) (PPE),[99] polythiophene (PT),[100] polypyrrole (PPy),[101] polyaniline (PANI)[102] and polyfluorene (PF)[103] (figure 1.15) and many more structures are under development.

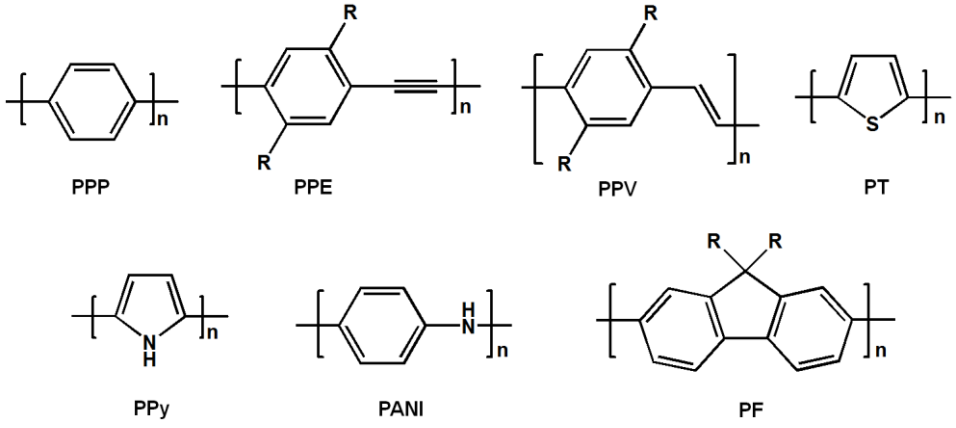

Figure 1.15 Common fluorescent polymers.

1.3.1. Sensory Signal Amplification of Conjugated Polymers

The design and development of chemosensors for sensing various analytes (like cations, anions and biomolecules) utilizing color and/or fluorescence intensity has been a field of great interest in recent decades.[16] A typical fluorescent chemosensor contains a receptor (the recognition site), linked to a fluorophore (the signal source), which translates the recognition

event into the fluorescence signal.[18] The main difference and/or advantageous of CPs over small molecular sensors is that they are able to amplify the signal from a binding event. The signal amplification is one of the most important advantages of polymer–based sensors and this signal amplifying model of CPs was proposed by Swager group in 1995.[104]

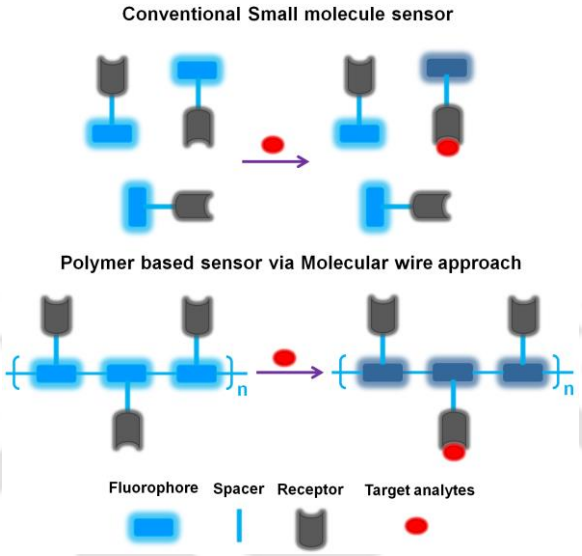

Scheme 1.2 Schematic diagram illustrates the conventional small molecule sensor and signal amplification of CPs sensor.

Scheme 1.2 illustrates the conceptual basis of the signal amplification of the fluorescence sensor signal generated by CPs upon binding with a target analyte. When an analyte binds locally to a receptor on a CPs repeat unit the entire conjugated backbone or the effective conjugation length is affected due to its 1–dimensional wire–like property and the fluorescence of the entire polymer chain is altered. This signal amplification is massive when compared to small molecule sensors. The small molecule only causes a single chromophore to change its fluorescence, whereas a CPs binding event affects the fluorescence of an entire chain of chromophores by energy or electron migration through the conducting polymer backbone.[105] This signal amplification is provided by CPs which is very important for biosensing applications because the molecules being analyzed are often present in extremely dilute concentrations. Toward this end, different novel polymer based chemosensors have been developed using different receptors and utilized for sensor applications, which will be discussed in detail below.

1.3.2. Cation and Anion Sensors

Fluorescent CPs have been employed in different sensing applications and particularly as sensitive probes for the detection of metal ions and anions.[106] Importantly, CP chemosensors

should contain in their structure some acceptor units to bind metal ions such as bipyridyl, terpyridyne, quinoline or imidazole units and others.

1.3.2.1. Imidazole as a Receptor

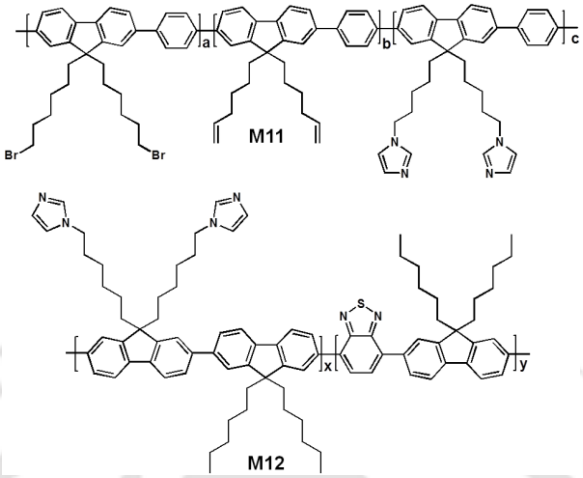

Figure 1.16 Polymer based chemosensor of M11 and M12.

The polyfluorene copolymers with imidazole ring as a receptor unit in the pendent side chains have been used in the field of chemosensors. These systems take advantage of the effective π-conjugation and strong luminescence properties of the polyfluorene and metal ion-recognition ability of imidazole to develop novel classes of highly selective and sensitive detection of metal ion sensors. However, the imidazole units appended to the conjugated polymers selectively recognize Cu^{2+} by the "turn-off" fluorescence method which is recovered by the addition of cyanide ions. Finally, the results of these polymers have been reported for the selective detection of Cu^{2+} metal ions and cyanide (i.e. M11 and M12 (Figure 1.16), by using a fluorescence "turn off–turn on" strategy.[107-109]

In 2004, Pei and co-workers[110] reported the metal-sensing properties of imidazole-substituted polyfluorene (M13) (Figure 1.17), which was synthesized by Suzuki coupling reaction. This polymer could be completely quenched by Cu^{2+} ion in THF with a K_{SV} value of 1.2×10^7 M^{-1}, but showed no absorption or fluorescence response to alkali or alkaline earth metal ions.

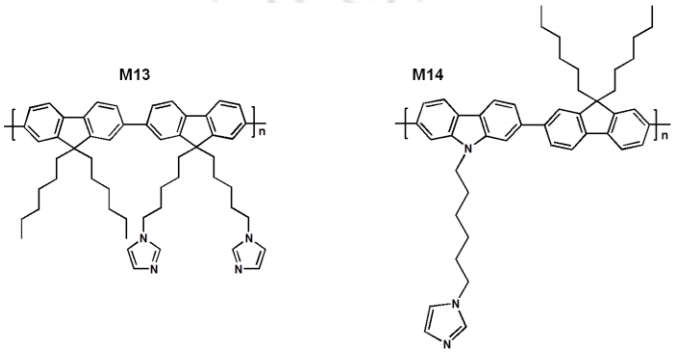

Figure 1.17 Polymer based chemosensor of M13 and M14.

In 2008, Li and co-workers[111] developed a sensitive and selective CN^- chemosensor based on imidazole-functionalized polyfluorene (M14) (Figure 1.17 and 1.18), the fluorescence of M14 could be completely quenched by Cu^{2+} ions at the concentration as low as 0.2 ppm in diluted solutions. The quenched fluorescence of the polymer by Cu^{2+} ions could recover upon the addition of trace CN^- anions, with the detection limit of 0.31 ppm.

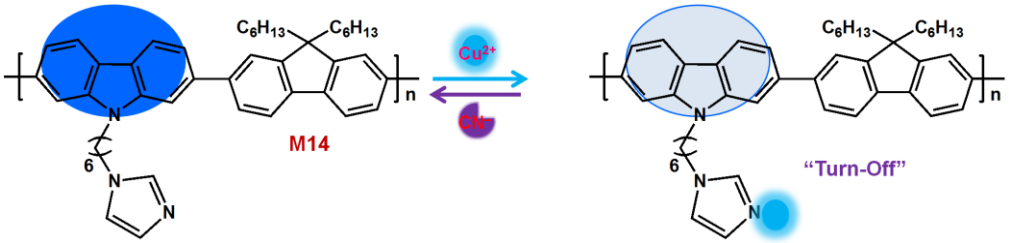

Figure 1.18 Polymer based chemosensor of M14 selectively detects Cu^{2+} and CN^-.

In 2009 same group demonstrated,[112] a fluorescent conjugated polymer (M14) utilized to probe R-amino acids, sensitively and selectively, through a new approach. The strong fluorescence of the prepared polyfluorene was quenched by trace amount of copper ions and then the quenched fluorescence was recovered upon the addition of R-amino acids. This experimental result demonstrated that polymer M14 can selectively sense R-amino acid over other analytes which is relatively good (Figure 1.17) result.

In 2012 Iyer et al, synthesized a neutral polymer, poly(1,4-bis-(8-imidazole-octyloxy)-benzene) (M15) which selectively detects Cu^{2+} and F^- ions (Figure 1.19).[113] This polymer PPI could selectively bind with Cu^{2+} ion and showed highly fluorescence quenching, resulting in >97% reduction in the fluorescence intensity. Furthermore, the fluorescence of M15–Cu^{2+} complex showed 81% fluorescence enhancement on selectively binding F^- anions in contaminated water in the presence of other competing anions. The LOD of fluoride ion was calculated to be very low in the range of 2.5–10.0 ppb by TLC plate and membrane methods.

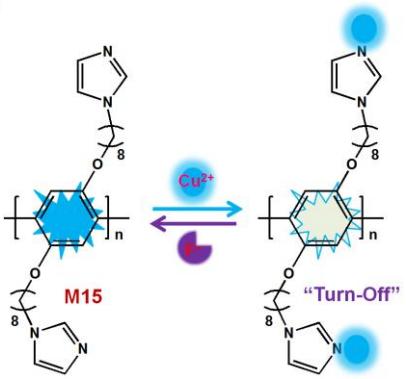

Figure 1.19 Polymer based chemosensor of M15 selectively detects Cu^{2+} and F^- ions.

1.3.2.2. Benzimidazole as a Receptor

Benzimidazole is also a commonly used receptor in molecular recognition of cations, anions and neutral molecules due to the emissive properties of this aromatic ring. As a result, this moiety has been used not only as a binding unit for cations and anions, as the imidazole derivatives do, but also as a fluorogenic antenna. Apart from its photochemical properties it is also worth noting another difference with the imidazole ring which involves the different acidity of the NH proton caused by the electronic effect of the benzene ring.

As already mentioned in the above section concerning the imidazole receptors, conjugated polymers (CPs) have also been used as receptors for different species. Thus, Iyer et al synthesized a polymer which connects benzimidazole moiety to a polyfluorene-alt-1,4-phenylene backbone (M16) (Figure 1.20).[114] This polymer M16, was able to coordinate selectively Fe^{3+} in THF: Water (4 : 1) at pH = 7.4 that originates a strong static quenching of the emission in μM concentrations. Besides, the iron complex fully recovers its original fluorescence emission when it is treated with $H_2PO_4^-/HPO_4^{2-}$ or $HP_2O_7^{3-}$ at low concentration but no significant emission changes observed by other anions. In fact, recovery of the initial fluorescence is caused by the decomplexation of Fe^{3+} induced by the different phosphate species in solution. The selectivity of these processes has successfully been applied to the detection of phosphate in saliva and blood serum, which showed excellent results when they were compared to commonly use analytical techniques.

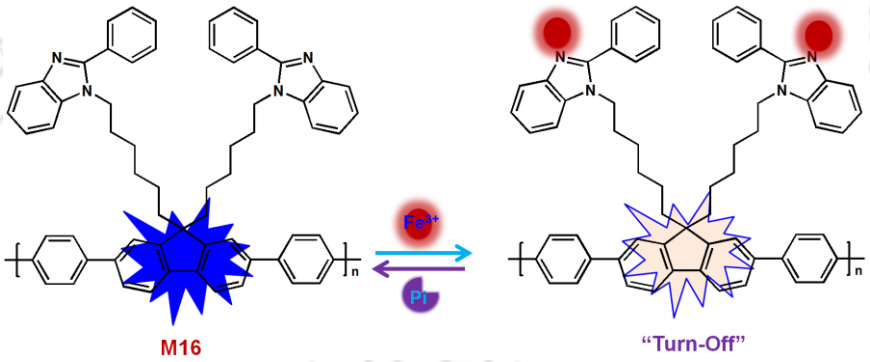

Figure 1.20 Polymer based chemosensor of M16 selectively detects Fe^{3+} and Pi.

1.3.2.3. Dipicolylamine as a Receptor

Di-(2-picolyl)amine (DPA) has been used as the most prevalent receptor to construct Zn^{2+} chemosensors after the first incorporation to fluorescein in 1996.[115] DPA is a derivative of N,N,N',N'-tetrakis(2-pyridylmethyl)- ethylenediamine (TPEN) which is a classical membrane-permeable Zn^{2+} chelator with high selectivity for Zn^{2+} over alkali and alkaline-

earth metal ions that occur in much higher concentrations in biological samples, such as Ca^{2+}, Mg^{2+}, K^{+}, Na^{+}.[116]

Several DPA based chemosensors have been developed with the direct connection of DPA to various fluorophores. The secondary amine nitrogen atom of DPA serves as a good reaction site to be linked to various fluorophores and an effective signal transduction sponsor to response the binding events through PET or ICT mechanisms. Generally, the best spacer length between the fluorophore and receptor is less than a three-carbon linker, which can guarantee the maximum efficiency for PET. Most of the PET type chemosensors sense Zn^{2+} with a fluorescence enhancement signal. Usually, for example if the spacer length is too short that could be a typical PET chemosensor for post-transition metal ions like Zn^{2+} with DPA conjugated to fluorophore. The spacer methylene group allows a PET process from the aliphatic amine nitrogen of DPA to the excited fluorophore which quenches the fluorescence. When the Zn^{2+} metal ion binds to the receptor of DPA, the PET process is completely prevented in fluorophore, which resulted in a significant enhancement of fluorescence.[116]

In 2012 Li and co-workers,[117] developed a sensitive and selective detection of CN^{-} ion sensor by a new polyfluorene bearing pyridine moieties (M17). As shown in figure 1.21, M17 was designed and obtained conveniently, the fluorescence of which could be completely quenched by Cu^{2+} ions at the concentration of 5.67×10^{-7} mol L^{-1} in diluted solutions. Moreover, the quenched fluorescence of the polymer by Cu^{2+} ions could recover upon the addition of CN^{-} anions, with the detection limit of 3.3×10^{-7} mol L^{-1}.

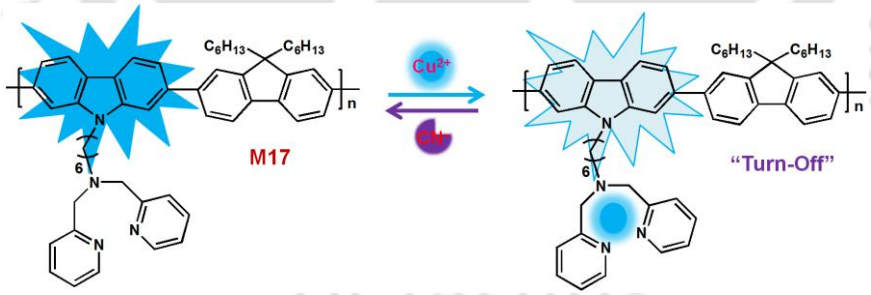

Figure 1.21 Polymer based chemosensor of M17 selectively detects Cu^{2+} and CN^{-}.

1.3.3. Polymer based Biosensing Applications

In 2002, Bazan and co-workers[118] used the cationic polyfluorene copolymer (M18) (Figure 1.22) to optically amplify fluorescent DNA assays (Figure 1.22). In 2003, the same group[119] replaced PNA-FI with more readily available ssDNA-FI as the higher local charge density of the double strand results in a stronger electrostatic attraction between the dsDNA-FI and the conjugated polyelectrolyte (M18) relative to the situation with ssDNA, upon adding a complementary strand ssDNA, the hybridized strand will result an efficient fluorescence or

förster resonance energy transfer (FRET) from polymer (M18) (Figure 1.22) to FI. In 2005, same group[120] modified the above strategy by adding S1 nuclease enzyme to detect single nucleotide polymorphisms.

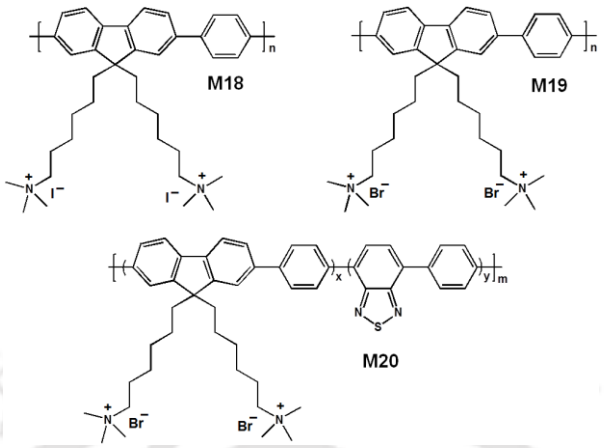

Figure 1.22 Polymer based chemosensors of M18, M19 and M20.

In 2005, Zhu et al,[121] detected G-quadruplex structure efficiently using the same polyfluorene copolymer M19 (Figure 1.22). On the other hand, that technique is able to detect potassium ion in aqueous solution with high sensitivity and selectivity. Finally, the technique showed that highly possible to detect G-rich aptamer-binding proteins.

In 2004, Liu and Bazan[122] demonstrated DNA biosensors using aggregate-induced interchain energy transfer in typical poly (fluorene-co-phenylene) structure substituted with BT unit (M20). The emission is predominantly blue in dilute solution but concentrated solutions emit green light. Therefore, authors used this polymer (M20) (Figure 1.22) to detect noncomplementary DNA and complementary ssDNA by changing green and red color fluorescence respectively due to intramolecular FRET characteristics.

In 2011, Xu and co-workers[123] improved the 2P optical cross sections of conjugate polymers at 800 nm by incorporating ethynylene (M21) (Figure 1.23) and vinylene (M22) (Figure 1.23) bridges into the backbone of polyfluorene. Facilitated by the efficient two-photon excitation fluorescence resonance energy transfer (TPE-FRET) from the polymer to photosensitizer Rose Bengal, up to 85-fold enhanced 2P-excitation emission of Rose Bengal was demonstrated. These studies are expected to provide insight on designing systems with further improved performance for potential applications in two-photon photodynamic therapy, sensing and imaging.

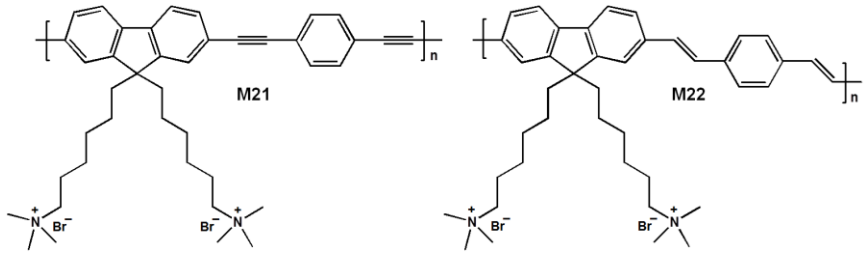

Figure 1.23 Polymer based chemosensor of M21 and 22.

In 2013, Li and co-workers[124] showed the sodium citrate induced efficient interpolymer π-stacking aggregation of the planar cationic conjugated polymer (M21) (Figure 1.23) in aqueous solution, which resulted in the self-quenching of fluorescence. Hence, authors reported a selective and sensitive detection of Al^{3+} in aqueous solution by using the citrate induced aggregation properties of M21.

1.4. Introduction to Alzheimer's Disease

Alzheimer's disease (AD) is the most common form of dementia in humans which is called as a Senile Dementia. AD is an irreversible progressive neurodegenerative disease which gradually leads to the loss of memory, thinking capability and the ability to carry out daily activities. According to the World Alzheimer Report on 2009,[125,126] the global prevalence of dementia is estimated to double every 20 years, increasing from 35 million in 2010 to 115.4 million in 2050 due to the rapid growth mainly of the elderly population in developing countries. Therefore, research should be initiated to develop a cure or a long-term effective treatment for AD on an urgent healthcare priority.

There has been significant progress in defining the main pathology of AD, while the progression is better understood; the underlying cause of AD remains indefinable. One of the most widely accepted characteristic hallmarks of AD is the accumulation/aggregation of insoluble amyloid beta (Aβ) peptides in the brain. These Aβ peptides are produced in a soluble form from the amyloid precursor protein (APP) and form aggregates of various sizes and levels of solubility. Over time they fibrillize to form large linear aggregates by misfolded (i.e. toxic folding) proteins.[127] Afterward, these aggregates turn to form insoluble protein fibrils that go on to form senile plaques and contribute to neuronal cell death.

1.4.1. History of Alzheimer's Disease

Alzheimer's disease was first discovered in 1906 by Alois Alzheimer, a Bavarian psychiatrist.[128] When, Alois examined the brain tissues of a woman who died by an unusual mental illness, he found many abnormal clumps and tangled bundles of fibers, which was later called amyloid/senile plaques and neurofibrillary tangles, respectively. Since then, these

two classical brain lesions have become the major neuropathological features of Alzheimer's disease. In 1960's, the use of electron microscopy allowed the ultrastructures of these plaques and tangles to be studied, revealing the fine fibrillary structures of that brain lesions.[129-132] With the advances in biochemical pathology, the compositions of the plaques and tangles were identified in the 1980's. It was found that the amyloid plaques mainly contain extracellular deposits of β-amyloid peptides,[133-136] while the neurofibrillary tangles are mainly composed of hyperphosphorylated tau (τ) proteins.[137-140] Both β-amyloid peptides and tau proteins are present in a highly ordered and aggregated form in the plaques and tangles. Due to the fact that amyloid plaques and neurofibrillary tangles can occur independently of each other and that neurofibrillary tangles are also present in many less common neurodegenerative diseases in the absence of β-amyloid deposition, it has been suggested that the tangles are likely to occur as a secondary response to the injury of neuronal cells.[141,142] Therefore, Alzheimer's disease studies have primarily focused on Aβ peptides.

According to the USA national statistics from the Aging, Demographics and Memory Study (ADAMS),[143] there were well over 2 million people over the age of 71 suffering with this disease. This number is likely to reach 7.7 million people in 2030 and may increase to 16 million people in 2050 according to some estimates.[144] In terms of mortality, AD was the fifth leading cause of death in the United States in 2006 for those older than 65 years.[145,146] However, most of the current treatments only provide temporary alleviation of the disease symptoms but some also induce undesirable side effects. In the absence of a cure, AD will continue to serve as a current and future major public health problem.

1.4.2. Alzheimer's Disease Hypothesis

Alzheimer's disease occurs mostly late in life to approximately 70% of people, which is called as late-onset dementia, however, it occurs ~5% patients under 60 years old which is termed early-onset familial Alzheimer's disease (FAD).[147-149] AD is the most common cause of dementia[148,150] and the estimation of worldwide affected people by the dementia is around 40-44 million at present according to the WHO.[151] There is no cure for this neurodegenerative disease, due to the difficulty of determining disease etiology.[148,152,153] This is a consequence of the multiple factors, operating either individually or mutually, which are proposed to contribute to disease development.[154,155] One recent approach examines several hypotheses (Scheme 1.3) to further understanding of AD etiology: the amyloid cascade hypothesis,[148,152] the metal ion hypothesis,[156] and the oxidative stress hypothesis.[156,157]

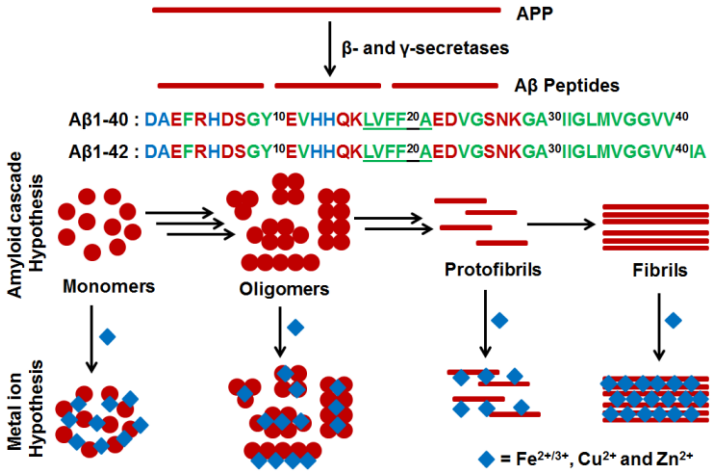

Scheme 1.3 Schematic representation of the amyloid cascade hypothesis, and the metal ion hypothesis. The amino acid sequences of Aβ1-40/Aβ1-42 are shown: metal binding residues (blue); hydrophilic and hydrophobic residues (brown and green, respectively); self-recognition sequence (underlined).

1.4.2.1. Amyloid Cascade Hypothesis

Alzheimer's disease is characterized by two main hallmarks, the first one is extracellular senile plaques and the second one is intracellular neurofibrillary tangles (NFTs) of hyperphosphorylated tau (τ) protein. However, this section will discuss about amyloid plaques which are mainly made up of aggregated forms of amyloid-β peptides (Aβ).[158]

According to the amyloid cascade hypothesis, senile plaques or amyloid plaques and/or their precursors (small Aβ aggregates) induce the formation of NFTs. This senile plaque can be detected before the observation of psychological and behavioral symptoms, placing the formation of plaques at an early stage of AD development.[158] However, healthy individuals can also have amyloid plaques, indicating that plaques are not the only factor in AD. The Aβ peptides are obtained by the cleavage of trans-membrane amyloid precursor protein (APP) by β- and γ-secretases. The most abundant Aβ species of Aβ1-40 and a lesser extent Aβ1-42 are produced in the brain and are present in the cerebrospinal fluid (CSF). Whereas the Aβ1-40/Aβ1-42 ratio in the soluble fractions is approximately 1:9, also Aβ1-42 is considered to be the most toxic peptide in line with a higher propensity to aggregate and thus to initiate Aβ aggregation.[159,160]

1.4.2.2. Metal ion Hypothesis

Remarkably, high concentrations (in the millimolar range) of several transition-metal ions (mainly Cu^{2+}, Zn^{2+}, and $Fe^{2+/3+}$) are found in senile plaques.[161-163] In AD post-mortem brains, the Aβ plaques can be imaged by light microscopy using specific dyes, e.g., Congo red and

thioflavin T (ThT), to stains characteristic of β-sheet structure confirmation.[164] Since, monomeric soluble Aβ are found in healthy persons, they later form Aβ aggregates by different paths which is the main key for the etiology of AD. Moreover, metal ions can also intervene in this process, via different routes, mainly by modulating Aβ aggregation.[165,169] The redox metal ions are mainly involved via reactive oxygen species (ROS) production,[170] according to the main two processes, namely, Aβ aggregation and ROS production can be linked together by oxidative damage on the Aβ peptide itself, which is more prone to form Aβ aggregation such as for instance, cross-linked dimeric species of Tyr10. [171]

1.4.3. Dye Binding Assays to Study the Formation of Amyloid Aggregation

The use of small molecular probes or dyes to monitor biological processes is well established as fluorescent dye binding assays considerably for *in vitro* recognition of protein misfolding,[172-174] and most importantly, practical implications for the understanding of the many human diseases that involve protein aggregation.

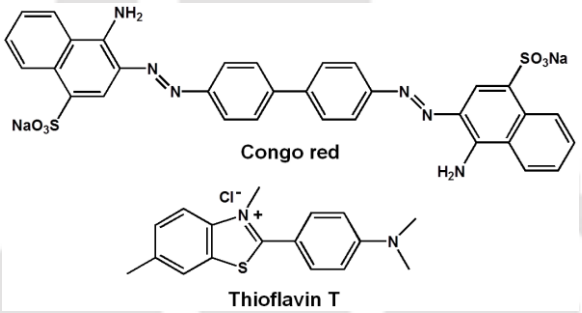

Figure 1.24 Structures of Congo red and Thioflavin T (ThT) dyes used for monitoring amyloid aggregation.

In particular, dye-binding assays are often used to examine the Aβ self-assembly processes. Congo red (CR) and thioflavin T (ThT) as shown in figure 1.24, are the most commonly used dyes to study amyloid aggregation and fibril formation.[175-177] Upon binding to the peptide assemblies, these dyes exhibit distinct spectral properties (spectral shift and/or intensity change) as compared to their unbound state of peptide aggregation processes.

1.4.3.1. Congo Red Dye

The CR (Figure 1.24), spectral shift assays are routinely employed as a technique to quantify fibril content and inhibitory ability of small molecules toward amyloids. On the structural level, it is known that CR has two binding sites in Aβ, parallel to the β-sheet and antiparallel to the β-sheet and the binding ratio may depend on the type of Aβ peptide.[178-181] CR binding to the extensive β-sheet structure results in an enhanced absorption as well as a bathochromic shift in its absorption spectrum (from approximately 480 nm unbound to 540 nm bound),

which is accompanied by a change in color from orange-red to rose in color and depends on the aggregation state of the proteins.[176] Most importantly, green birefringence is observed in polarized light upon binding to the fibrils and it has been typically used as a qualitative measure of fibril formation.[172,177] On the contrary, analysis of the absorption spectra of the unbound CR, fibrils and the bound CR can provide a quantification of fibril concentration.[176]

1.4.3.2. Thioflavin T Dye

The benzothiazole dye, ThT (Figure 1.24), is widely used for the identification and quantification of Aβ fibrils as well as for the exploration of fibrillation kinetics of Aβ using fluorescence spectroscopy. Specific interactions of ThT with amyloid fibrils have been the subject of numerous studies,[182-184] although the exact binding mechanism, stoichiometry, and binding location are still debated. This dye is only weakly fluorescent in an aqueous environment, with excitation and emission maxima at approximately 350 and 440 nm, respectively. However, upon interacting with β-sheet-rich amyloid fibrils, a bathochromic shift of both excitation and emission maxima at 440 and 490 nm are observed respectively. The observed emission at 490 nm is assumed to be directly proportional to the quantity of amyloid fibrils present, therefore, the kinetics of fibril formation can easily be followed by measuring the time-dependent increase in fluorescence. On the other hand, a reduction in the ThT fluorescence is often taken as an indication of inhibition of the macromolecular amyloid self-assembly process.[173] However, it was shown that in some cases even the kinetics of the amyloid aggregation might not be clearly accessed by ThT fluorescence.[185] Specifically, after few hours, ThT fluorescence reached a plateau and remained unchanged up to some extent, which is indicative of a constant β-sheet content.

1.4.4. Aggregation Mechanism for Aβ Fibril Formation

The Aβ monomers are self-assembled into highly ordered fibrils by a complex and dynamic process that involves multiple self-assembly steps (Figure 1.25). Particularly, Aβ peptides undergo complex conformational changes, aggregation and reorganization to form characteristic cross-β-sheet fibrils.[186] However, there are both thermodynamic and kinetic factors that are mainly involved to form Aβ aggregation and distinct intermediate which can coexist at each stage of the process.[187] These transient intermediates are formed by two different paths either ordered or disordered hypothesized mechanism. Also, a general method is needed to understand the aggregation mechanism for the formation of Aβ fibrils by two successive key parameters viz. nucleation (k_n) and elongation (k_e) rate constant steps.[188-190]

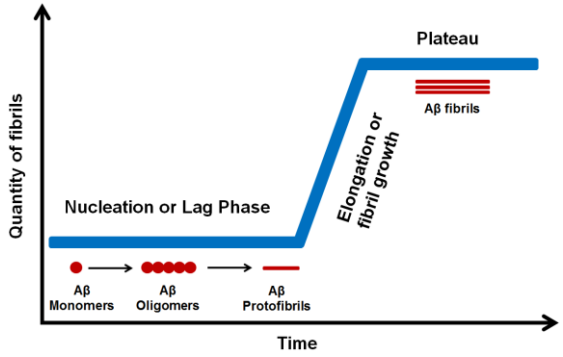

Figure 1.25 Schematic representations of amyloid aggregation paths.

According to the generally accepted model, the unstructured monomers form thermodynamically unfavorable nuclei in "nucleation phase" or "lag phase".[191] Then, these nuclei behave as a template for binding and conformational transitions of monomeric or oligomeric proteins into the formation of fibrillary assemblies in elongation phase (Figure 1.25).[192] In this phase the formation of β-sheet secondary structures can be regularly monitored by fluorescent dye-binding assays, particularly the ThT binding assay monitored upto reaching a plateau (Figure 1.25).[193] Furthermore, the increased β-sheet secondary structure can be measured by circular dichroism spectroscopy (CD), fourier transform infrared spectroscopy (FT-IR) and the peptide morphology by atomic force microscopy (AFM), field emission scanning electron microscopy (FE-SEM) and transmission electron microscopy (TEM).

However, to solve AD problems, the development of materials for inhibition of Aβ self–assembly aggregation, modulation of preformed Aβ fibrils and metal–associated Aβ species by chelation has been considered as the primary therapeutic strategy for neurodegenerative diseases. Hence, various approaches have been explored with significant efforts to inhibit Aβ fibrillation, including small organic molecules,[194] functional polymers,[195] peptide mimetics[196] and nanoparticles.[197-199] Toward this end, in recent literatures different novel inhibitors or modulators have been developed using different design strategy and utilized to study Aβ peptides or fibrils, which is discussed in detail below.

1.4.5. Bifunctional or Multifunctional Small Molecule Probe for Modulating Aβ Aggregates

It is well-known that excess amount of metal ions (Fe, Cu and Zn) have been found in Aβ plaques of AD brains[152,200] particularly, Cu and Zn bind to Aβ peptides facilitating their aggregation. To overcome this problem, several studies report that metal chelators could reduce the metal-induced Aβ aggregation, ROS formation and neurotoxicity *in vitro*.[201] For

example, the nonspecific chelator clioquinol (CQ) showed decreased Aβ aggregate formation that resulted in improved cognition in clinical trials.[201,202] However, use of nonspecific chelators (i.e., CQ) that do not interact selectively with the Aβ−metal species exhibit adverse side effects that will likely limit their long-term clinical use.[152,201,203-205]

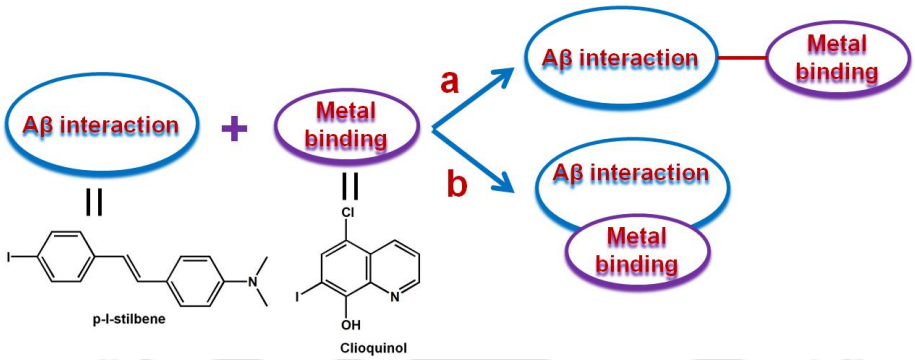

Scheme 1.4 Rational structure-based design by incorporation approach.

To study the relation of metal−Aβ to AD pathology, bifunctional or multifunctional molecules have been prepared via a rational structure-based design strategy by the incorporation approach (Scheme 1.4).[155] In this context, two approaches have been pursued in bifunctional or multifunctional molecule design.[206,207] One strategy is based on the direct incorporation of metal-binding donor atom (Clioquinol) into the structural framework of an Aβ-interacting compound (p-I-stilbene) (Scheme 1.4, approach a), and the other involves linking the metal-chelating and Aβ-binding molecular fragments (Scheme 1.4, approach b). In this approach, bifunctional or multifunctional molecules can interact with the Aβ peptides and also bind the metal ions from the Aβ−metal species and this could potentially lead to more effective therapeutic agents, as well as provide an increased understanding of the metal−Aβ associated neuropathology. Therefore, these type of compounds (for metal chelation and Aβ interaction) target metal−Aβ species and form ternary Aβ−metal−ligand complexes, which are believed to redirect the aggregation pathway into off-pathway, nontoxic or less toxic conformations.

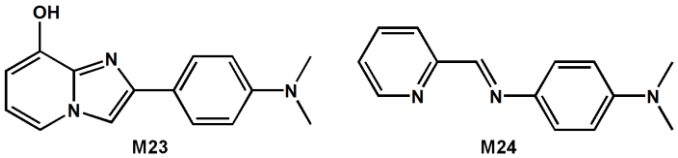

Figure 1.26 Bifunctional small molecules of M23 and M24 by incorporation approach.

In 2009 Lim et al,[208] prepared two bifunctional small molecules M23 and M24 which specifically targeted divalent metal ions in Aβ aggregates (Figure 1.26). These bifunctional

molecules modulate the generation of Cu^{2+}-induced Aβ aggregates and promote their disaggregation which was confirmed by spectroscopic investigations.

In 2011 Lim et al,[209] designed and synthesized a new bifunctional small molecules-M25 and M26 (Figure 1.27). These bifunctional small molecules showed significant reactivity toward metal-induced Aβ aggregation over metal-free conditions in both *in vitro* inhibition and disaggregation experiments which was confirmed by UV-vis and high-resolution two-dimensional (2D) NMR spectroscopy. Subsequently, this study provides another example of a bifunctional small molecule framework that targeted metal ions associated with Aβ species.

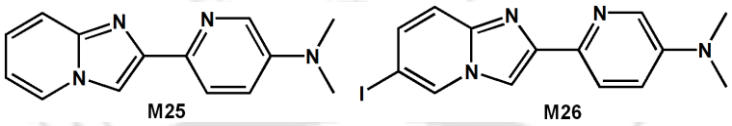

Figure 1.27 Bifunctional small molecules of M25 and M26 by incorporation approach.

Further, in 2011 Lim et al,[210] have developed bifunctional small molecules that can specifically target and modulate metal-Aβ species, which could serve as suitable chemical tool for investigating metal-Aβ-associated events in AD. They developed stilbene derivatives of M24 and M27 (Figure 1.28) and demonstrated their reactivity toward metal-Aβ species. The enhanced bifunctionality of M24 and M27 provided greater effects on metal-induced Aβ aggregation and neurotoxicity *in vitro* and in living cells. Later, this group developed various bifunctional chelators like flavonoid derivatives,[211] diphenylpropynone derivatives,[212,213] triazole–pyridine ligands[214] to inhibit or modulate the Aβ aggregates.

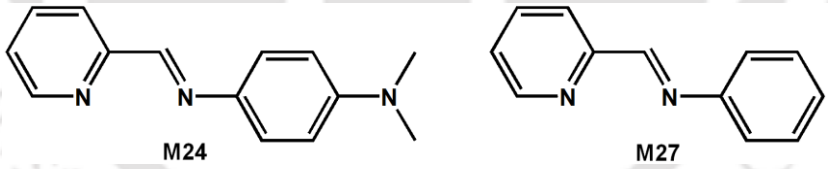

Figure 1.28 Bifunctional small molecules of M24 and M27 by incorporation approach.

Very recently the same group,[200] developed a rationally designed small molecule of M28 for Aβ aggregation control, metal chelation, reactive oxygen species (ROS) regulation, and antioxidant activity (Figure 1.29). The confirmation studies indicated that the compound M28 targets metal free and metal-bound Aβ species and that suppresses Aβ aggregation *in vitro* and diminishes toxicity induced by Aβ and metal-treated Aβ in living cells. Overall, they demonstrated that a rational structure-based design strategy can generate a probe that can target and modulate multiple factors, providing a tool to reveal and address AD complexity.

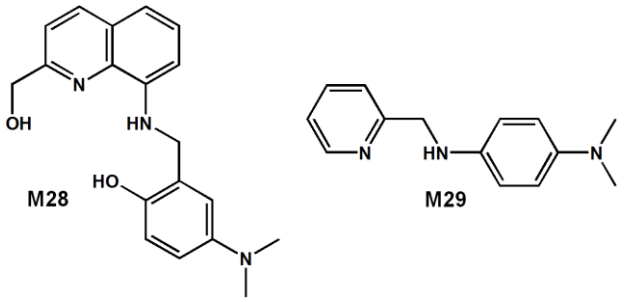

Figure 1.29 Multifunctional small molecules of M28 and M29 by incorporation approach.

To solve AD uncertainty, recently in 2015 Lim et al,[215] have developed a molecule M29 that specifically targets metal–Aβ complexes and modulates their reactivity (Figure 1.29). It was demonstrated that M29 is able to specifically interact with metal–Aβ complexes over metal-free Aβ analogues, redirect metal–Aβ aggregation into off-pathway; nontoxic Aβ aggregates, and diminish metal– Aβ-induced ROS production.

In 2012 Mirica et al,[207] developed two small molecule bifunctional compounds M30 and M31 that contain both Aβ-binding and metal-chelating molecular structures (Figure 1.30). The bifunctional small molecules of M30 and M31 exhibit high stability constants for Cu^{2+} and Zn^{2+} ion and shows good chelation for these metal ions. Moreover, these compounds are efficient inhibitors of the metal-mediated aggregation of the Aβ1-42 peptide and promote disaggregation of Aβ fibrils, as observed by ThT fluorescence, native gel electrophoresis and etc. Remarkably, the ability of the M30 and M31 to inhibit Aβ fibril formation and promote fibril disaggregation leads to increased cellular toxicity, especially for M31, which is likely due to the formation of soluble Aβ42 oligomers of various sizes.

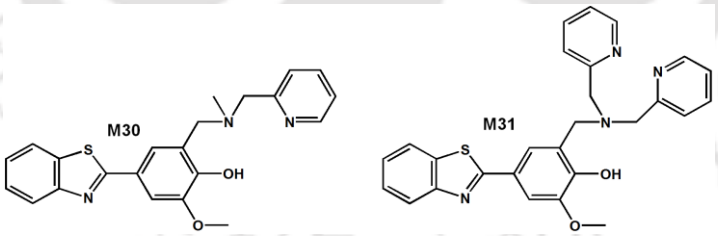

Figure 1.30 Bifunctional small molecules of M30 and M31 by incorporation approach.

In 2014 Mirica et al,[216] developed two novel bifunctional chelators, M32 and M33, by incorporation approach (Figure 1.31). The Aβ binding properties of M32 and M33 were investigated by fluorescence titrations and ThT competition assays. Interestingly, M32 and M33 do not lead to the formation of neurotoxic Aβ42 oligomers in the presence or absence of metal ions, as observed by native gel electrophoresis, western blotting and transmission electron microscopy. Moreover, M32 and M33 were able to reduce the cell toxicity of preformed Aβ42 oligomers and the copper-induced Aβ42 oligomers.

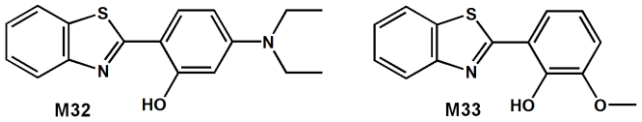

Figure 1.31 Bifunctional small molecules of M32 and M33 by incorporation approach.

1.4.6. Peptide based Inhibitors or Modulators for Aβ Aggregates

The main pathogenic event in Alzheimer's disease is believed to be the aggregation of the Aβ peptides into toxic aggregates. Molecules that interfere with this process may act as therapeutic agents for the treatment of the disease. The recognition unit of peptide based peptidomimetics as inhibitors are a promising approach, as they exhibit greater protease stability compared to natural peptides.

In 2015 Govindaraju et al,[196] presented peptidomimetic inhibitors of Aβ aggregation based on the KLVFF (M34) sequence that are known to bind Aβ aggregates (Figure 1.32). Further they improved inhibition efficiency of M34 by introducing multiple hydrogen bond donor-acceptor moieties at the N-terminal (M35 and M36), and blood serum stability by modifying the backbone by incorporating sarcosine (N-methylglycine) units at alternate positions (M37 and M38). The peptidomimetics showed moderate to good activity in both inhibition and dissolution of Aβ aggregates as depicted by thioflavin assay, circular dichroism (CD) measurements and microscopy (TEM).

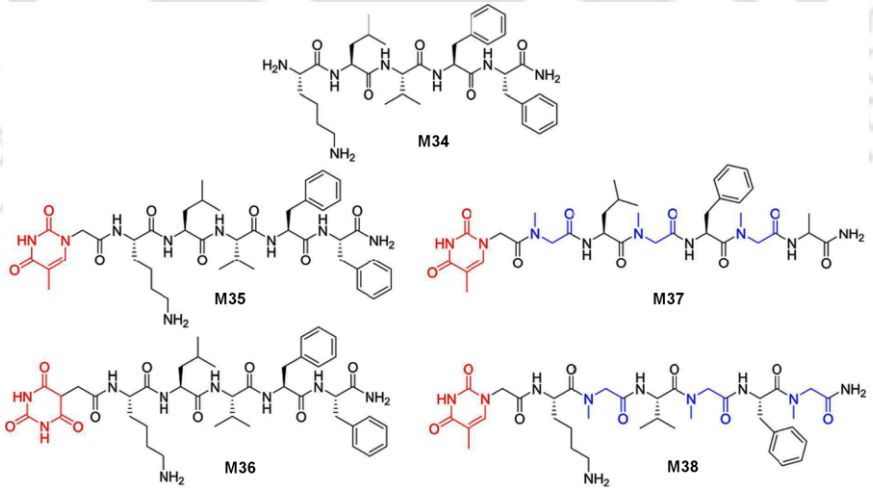

Figure 1.32 Peptidomimetic inhibitors for Aβ aggregation.

In 2015 Yuan et al,[217] developed an active Aβ inhibitor decapeptide RR to transform mature Aβ fibrils into nanorod-like Aβ assemblies which loosen the β-structure assemblies. Thus, this group studied and demonstrated the potential application of RR in Aβ fibrils clearance by a cell-participated and enzyme-mediated pathway.

1.4.7. Nano Particle based Inhibitors or Modulators for Aβ Aggregates

Amyloid protein fibrillation is responsible for a variety of neurological disorders and thus inhibition of fibrillation is a potential therapeutic strategy for AD. Recent literature study shows that nanoparticles can significantly influence the kinetics of Aβ fibrillation, depending on their surface chemistry. In this strategy nanomaterials show promising diagnostic and therapeutic effect on Aβ aggregated fibrils because of their unique physicochemical properties such as small size, large surface area and high reactivity. In recent times, research has found that single-walled carbon nanotubes,[218] quantum dots[219] and other nanomaterials have the ability to cross the BBB. Moreover, the interactions between nanoparticles and peptides induce the formation of coassembly structure by noncovalent interactions (e.g., hydrogen bonding, electrostatic interactions, hydrophobic, and van der Waals forces).[220]

In 2008 Linse et al,[221] developed the copolymeric NiPAM:BAM nanoparticles to inhibit Aβ fibrillation and retard fibrillation of the Alzheimer's disease-associated Aβ fibrils. In 2014 Liu et al,[222] synthesized an L-Cys modified SeNPs, RuNPs and Se/RuNPs. Subsequently, Se/RuNPs exhibited effective inhibition of the metal-induced Aβ1-40 fibrillization or Aβ1-40 self assembly, ROS formation and also decreased the intracellular Aβ40 aggregation.

In 2014 Jana et al,[223] designed nanoparticles which were essential for inhibiting the amyloid fibrillation processes. Using nanoparticles they demonstrated that amyloid fibril formation was completely inhibited by nanoparticles coated with histidine-based polymer.

1.4.8. Small Molecule Probe for Modulating Aβ Self-aggregates

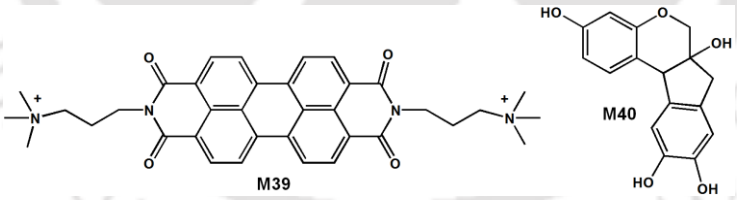

Figure 1.33 Bifunctional small molecules of M32 and M33 by incorporation approach.

In 2013 Qu et al,[224] demonstrated a potential cationic derivative of M39 used as a probe for *in situ* monitoring of Aβ aggregation and screening of Aβ inhibitors (Figure 1.33). The assay is based on the observation of fluorescence changes through the assemblies of compound M39 with Aβ aggregation. Compound M39 emits strongly in the absence of Aβ aggregates but in presence of Aβ aggregates it shows weak fluorescence which supports kinetic monitoring of protein fibrillogenesis and the screening of Aβ inhibitors. Importantly, this probe M39 is more sensitive to Aβ oligomer compared to ThT, which plays a crucial role in the early

events of AD. Therefore, these results shed light on the design of new diagnostic reagents for monitoring or treatment of the diseases associated with conformational disorders of proteins.

The soluble Aβ oligomers are leading neurotoxic species, which are predominantly formed from monomers through a fibril-catalyzed secondary nucleation. In 2015 Sun et al,[225] have developed brazilin natural compound of M40 as a dual functional compound in both Aβ1-42 fibrillogenesis inhibition and mature fibril remodeling, leading to significant reduction in Aβ1-42 cytotoxicity (Figure 1.33).

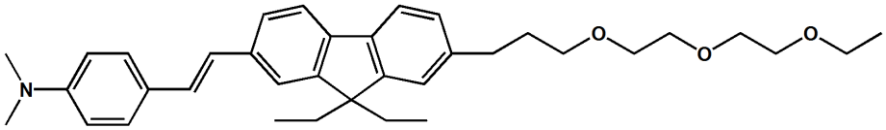

M41

Figure 1.34 The structure of Aβ binding fluorescence probe M41.

In 2013 Ran et al,[226] designed and synthesized a fluorescence probe M41 capable of detecting water-soluble Aβ oligomers and Aβ fibrils (Figure 1.34). The probe M41 showed significant fluorescence enhancement upon binding Aβ oligomers, which is attributed to the viscous environment of Aβ1-42 oligomers. Upon injection into Aβ1-42-challenged mouse brain, probe M41 shows increased fluorescence intensity, indicating its facile binding to extracellular Aβ fibrils in brain tissues. This new strategy opens opportunities for the development of small molecules that are able to detect water-soluble Aβ oligomers as well as Aβ fibrils mostly found in AD patients.

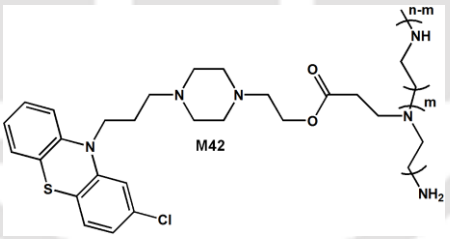

M42

Figure 1.35 The dual modulation effect (“acceleration−inhibition”) fluorescence probe of M42.

The modulation of protein self-assembly has been a powerful strategy for controlling and understanding Aβ protein aggregation. Mostly, the modulators of Aβ aggregation only involve simple inhibition or acceleration but, in 2015 Moore et al,[227] have developed a new multivalent molecular motif, the polyethylenimine-perphenazine derivative of M42 which shows dual “acceleration−inhibition” modulation effect on Aβ aggregation (Figure 1.35). The dose dependent results from Thioflavin T fluorescence assays, circular dichroism, and atomic force microscopy shows that M42 accelerates the formation of Aβ prefibrillar intermediates

and inhibit Aβ fibrillation. Furthermore, the cell viability assays also indicate that the M42 reduces the cytotoxicity of Aβ aggregates in a dose-dependent manner.

1.4.9. Near-infrared molecules for Aβ imaging and Modulation

In 2013 Ran et al,[228] designed and synthesized curcumin-based near-infrared (NIR) fluorescence imaging probes M43 and mainly M44 for detecting both soluble and insoluble Aβ species and then inhibit the formation of cross-linked Aβ which induced by copper (Figure 1.36). The obtained results from SDS-PAGE gel and western blot indicated that M44 was capable of inhibiting Aβ1-42 cross-linking which was induced by copper.

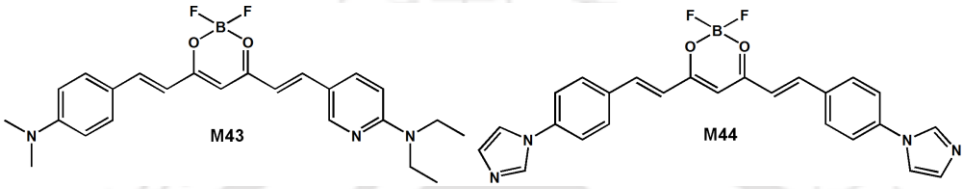

Figure 1.36 Near-infrared molecules of M43 and M44 for modulating Aβ aggregation.

In 2014 Saji et al,[229] have designed, synthesized and evaluated a series of smart near-infrared fluorescence (NIRF) imaging probes (M45-M47) with donor−acceptor architecture bridged by a conjugated π-electron chain for Aβ plaques (Figure 1.37). Probes with extended π-conjugated system displayed maximum emission in PBS (>650 nm), falling in the best range of NIRF probes. M47 proved to have affinity to Aβ plaques in fluorescent staining of brain sections from an AD patient and double transgenic mice, as well as in an *in vitro* binding assay using Aβ1−42 aggregates. Finally, this NIRF probe fulfilled most of the requirements for a NIRF contrast agent for the detection of Aβ plaques both *in vitro* and *in vivo*.

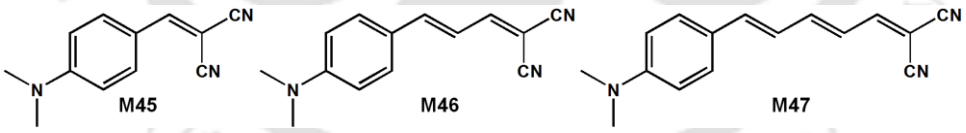

Figure 1.37 Near-infrared molecules of M45 to M47 for modulating Aβ aggregation.

In 2014 Liu et al,[230] designed and synthesized a novel class of near-infrared molecules based on the donor–acceptor architecture (M48-M59) and evaluated as Aβ imaging probes (Figure 1.38). Four probes with the longest conjugated double bond systems displayed moderate binding affinity to Aβ1–42 aggregates and rational optical properties upon association with Aβ1–42 aggregates. *In vivo* imaging studies suggested that M56 could penetrate the BBB and label Aβ plaques in the brains of transgenic mice and could be an optimal NIR probe for the detection of Aβ plaques both *in vitro* and *in vivo*. Moreover, computational studies also confirm the binding sites of probes on the Aβ fibrils which open a new promising generation of Aβ-targeting molecules for diagnostic applications.

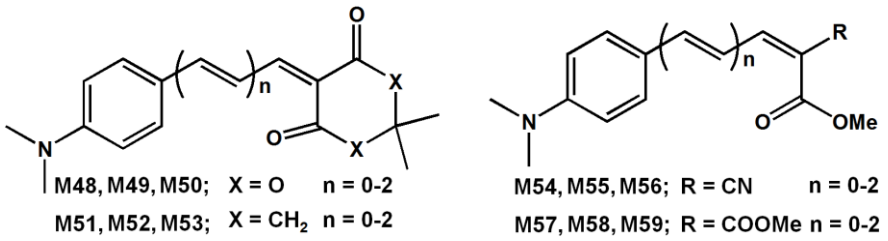

Figure 1.38 Near-infrared molecules of M48 to M59 for modulating Aβ aggregation.

1.5. Conclusion and Objective of Thesis Work

This discussion concludes the brief introduction to fluorescent sensing molecules, Alzheimer's diseases and about inhibitors or modulators for amyloidosis. The intention was to provide a conceptual introduction and reveal few selected examples of both the fields in a comprehensive manner. Thus, the fluorescent materials such as small molecules and polymers are employed in different sensing applications particularly, a sensitive probe for the detection of metal ions, anions and biomolecules. Importantly, the detection of biologically important metal ions such as iron, copper and zinc has gained significant interest, on the other hand these metal ions are essential for the proper functioning of all living cells, in contrast, their excessive concentrations in body are toxic that leading to various neurodegenerative diseases such as Alzheimer's, Parkinson's and Huntington's diseases. There are millions of people worldwide, who suffer from neurodegenerative disorders and most of these diseases manifest themselves later in life. Therefore, the main objective of this thesis was to design and synthesize novel fluorescent materials viz. small molecule and polymers for selective detection of biologically important metal ions such as iron and copper; further, we had plans to utilize these small molecules and polymers as modulators to target misfolded proteins of self-assembled Aβ fibrils and metal induced Aβ fibrils into disaggregated forms.

In addition, the focus of the thesis work is given below as chapterwise,

- Chapter 1 is the introductory explanation to the respective research areas of "Design and Synthesis of Fluorescent Probes for Applications in Sensors and Modulating Aβ Fibrils" where the scope and relevance of the subsequent chapters are described.

- Chapter 2a discusses about the synthesis of new conjugated polymer PHQ followed by its sensing ability with inorganic salts of Fe^{2+}/Fe^{3+} ions and non–heme metalloprotein ferritin by photoluminescence quenching study.

- Chapter 2b discusses about disruption or modulation of aggregated Aβ fibrils using fluorescent conjugated polymer PHQ.

- Chapter 3a discusses about synthesis of a new conjugated polymer PF–DPA followed by its selective sensing ability with Co^{2+} ion and vitamin B_{12} by photoluminescence quenching study. Moreover, PF–DPA exhibits a large and unique red shifted enhanced emission at 556 nm in higher water ratio around 1:9 (THF: H_2O) due to the formation of polymer nanoparticles or PDots by intra and intermolecular self–assembly induced aggregation phenomenon (AIEE). Furthermore, PF–DPA utilized for imaging and shows high biocompatiblity up to 1.6 mg/mL in normal cells but shows potent cytotoxicity against cancer cell in higher doses (>80 µg/mL).

- Chapter 3b discusses about inhibition of Aβ fibrillation and modulation effect on preformed Aβ fibrils by an influence of aggregation induced enhanced emission (AIEE) luminogen of PF–DPA PDots.

- Chapter 4a discusses about the synthesis of new indole–3–carboxaldehyde functionalized fluorescein hydrazone (FI) molecule followed by its selective "turn–on" sensing ability with Cu^{2+} ion and "turn–off" sensor observed in presence of nitric oxide (NO). Furthermore, FI was utilized to detect Cu^{2+} ion and endogenous NO gas in living cells.

- Chapter 4b discusses the use of this nontoxic indole–3–carboxaldehyde fluorescein hydrazone (FI) probe to perform multiple tasks of disaggregating Aβ aggregates in different biomarker environment such as cerebrospinal fluid (CSF Aβ fibrils), Aβ1–40 fibrils, β–amyloid lysozyme aggregates (LA) and U87 MG Human astrocytes cells.

- Chapter 5a discusses about the synthesis of highly water–soluble fluorescent perylene diimide (PDI–HIS) molecule followed by its selective "turn–off" sensing ability for Cu^{2+} ion and "turn–on" sensor for ATP.

- Chapter 5b discusses about preparation of PDI-HIS+Cu^{2+}+graphene oxide (GO) nanocomposite probe for the detection of pyrophosphate (PPi) in physiological conditions and *in vitro* live melanoma cancer cells (B16F10).

- Chapter 5c discusses about modulation of Aβ fibrils into mature microrod shaped coassembly structure by this PDI–HIS molecule.

References

(1) Wright, A. T.; Anslyn, E. V. *Chem. Soc. Rev.*, **2006,** *35*, 14.

(2) Wu, J. S.; Liu, W. M.; Ge, J. C.; Zhang, H. Y.; Wang, P. F. *Chem. Soc. Rev.*, **2011,** *40*, 3483.

(3) Kobayashi, H.; Ogawa, M.; Alford, R.; Choyke, P. L.; Urano, Y. *Chem. Rev.* **2010,** *110*, 2620.

(4) Sinkeldam, R. W.; Greco, N. J.; Tor, Y. *Chem. Rev.* **2010,** *110*, 2579.

(5) Lodeiro, C.; Capelo, J. L.; Mejuto, J. C.; Oliveira, E.; Santos, H. M.; Pedras, B.; Nunez, C. *Chem. Soc. Rev.*, **2010,** *39*, 2948.

(6) Gunnlaugsson, T.; Glynn, M.; Tocci, G. M.; Kruger, P. E.; Pfeffer, F. M. *Coord. Chem. Rev.* **2006,** *250*, 3094.

(7) Jiang, P. J.; Guo, Z. J. *Coord. Chem. Rev.* **2004,** *248*, 205.

(8) Bell, J. W.; Hext, N. M. *Chem. Soc. Rev.*, **2004,** *33*, 589.

(9) Vendrell, M.; Zhai, D. T.; Er, J. C.; Chang, Y. T. *Chem. Rev.* **2012,** *112*, 4391.

(10) Martinez–Manez, R. *Chem. Rev.* **2003,** *103*, 4419.

(11) Quang, D. T.; Kim, J. S. *Chem. Rev.* **2010,** *110*, 6280.

(12) Kim, J. S.; Quang, D. T. *Chem. Rev.* **2007,** *107*, 3780.

(13) Nolan, E. M.; Lippard, S. J. *Chem. Rev.* **2008,** *108*, 3443.

(14) Chen, X.; Zhou, Y.; Peng, X.; Yoon, J. *Chem. Soc. Rev.*, **2010,** *39*, 2120.

(15) Zhou, Y.; Xu, Z.; Yoon, J. *Chem. Soc. Rev.*, **2011,** *40*, 2222.

(16) Kim, H. N.; Guo, Z.; Zhu, W.; Yoon, J.; Tian, H. *Chem. Soc. Rev.*, **2011,** *40*, 79.

(17) Xu, Z.; Kim, S. K.; Yoon, J. *Chem. Soc. Rev.*, **2010,** *39*, 1457.

(18) de Silva, A. P.; Gunaratne, H. Q. N.; Gunnlaugsson, T.; Huxley, A. J. M.; McCoy, C. P.; Rademacher, J. T.; Rice, T. E. *Chem. Rev.* **1997,** *97*, 1515.

(19) Chen, X.; Tian, X.; Shin, I.; Yoon, J. *Chem. Soc. Rev.*, **2011,** *40*, 4783.

(20) Duke, R. M.; Veale, E. B.; Pfeffer, F. M.; Kruger, P. E.; Gunnlaugsson, T. *Chem. Soc. Rev.*, **2010,** *39*, 3936.

(21) Beija, M.; Afonso, C. A. M.; Martinho, J. M. G. *Chem. Soc. Rev.*, **2009,** *38*, 2410.

(22) Bayer, A. V. *Chem. Ber.* **1871,** *5*, 255.

(23) Gonc-alves, M.; Sameiro, T. *Chem. Rev.* **2009,** *109*, 190.

(24) Noelting, E.; Dziewonsky, K. *Ber. Dtsch. Chem. Ges.* **1905,** *38*, 3516.

(25) Chen, X.; Pradhan, T.; Wang, F.; Kim, J. S.; Yoon, J. *Chem. Rev.* **2012,** *112*, 1910.

(26) Amat-Guerri, F.; Costela, A.; Figuera, J. M.; Florido, F.; Sastre, R. *Chem. Phys. Lett.* **1993,** *209,* 352.

(27) Dujols, V.; Ford, F.; Czarnik, A. W. *J. Am. Chem. Soc.* **1997,** *119,* 7386.

(28) Huo, F-J.; Yin, C-X.; Yang, Y-T.; Su, J.; Chao, J. B.; Liu, D. S. *Anal. Chem.* **2012,** *84,* 2219.

(29) Choi, M. G.; Cha, S.; Lee, H.; Jeon, H. L.; Chang, S.-K. *Chem. Commun.,* **2009,** 7390.

(30) Li, T.; Yang, Z.; Li, Y.; Liu, Z.; Qi, G.; Wang, B. *Dyes and Pigments,* **2011,** *88,* 103.

(31) Abebe, F. A.; Sinn, E. *Tetrahedron Lett.* **2011,** *52,* 5234.

(32) Zhang, J.; Zhang, L.; Wei, Y.; Maa, J.; Shuang, S.; Cai, Z.; Dong, C. *Spectrochim. Acta Mol. Biomol. Spectrosc.* **2014,** *122,* 731.

(33) Fry, H. C.; Garcia, J. M.; Medina, M. J.; Ricoy, U. M.; Gosztola, D. J.; Nikiforov, M. P.; Palmer, L. C.; Stupp, S. I. *J. Am. Chem. Soc.,* **2012,** *134,* 14646.

(34) Vemula, P. K. John, G. *Acc. Chem. Res.,* **2008,** *41,* 769.

(35) Herbst, W.; Hunger, K. Industrial Organic Pigments: Production, Properties, Applications, 2nd edn., WILEY-VCH, Weinheim, 1997.

(36) Wuerthner, F. *Chem. Commun.,* **2004,** *14,* 1564.

(37) Avinash, M. B.; Govindaraju, T. *Adv. Mater.* **2012,** *24,* 3905.

(38) Che, Y.; Yang, X.; Zang, L. *Chem. Commun.,* **2008,** *12,* 1413.

(39) Peneva, K.; Mihov, G.; Herrmann, A.; Zarrabi, N.; Börsch, M.; Duncan, T. M.; Müllen, K. *J. Am. Chem. Soc.* **2008,** *130,* 5398.

(40) Wang, B.; Yu, C. *Angew. Chem., Int. Ed.* **2010,** *49,* 1485.

(41) Szekle, H.; Schübel, S.; Harenberg, J.; Krämer, R. A. *Chem. Commun.,* **2010,** *46,* 1667.

(42) Demmig, S. Langhals, H. *Chem. Ber.,* **1988,** *121,* 225.

(43) Ford, W. E.; Kamat, P. V. *J. Phys. Chem.* **1987,** *91,* 6373.

(44) Schmidt-Mende, L.; Fechtenkotter, A.; Müllen, K.; Moons, E.; Friend, R. H.; MacKenzie, J. D. *Science* **2001,** *293,* 1119.

(45) Li, J. L.; Dierschke, F.; Wu, J. S.; Grimsdale, A. C.; Mullen, K. *J. Mater. Chem.,* **2006,** *16,* 96.

(46) Ye, T.; Singh, R.; Butt, H.-J.; Floudas, G.; Keivanidis, P. E. *ACS Appl. Mater. Interfaces* **2013,** *5,* 11844.

(47) Liu, Y.; Wang, N.; Li, Y.; Liu, H.; Li, Y.; Xiao, J.; Xu, X.; Huang, C.; Cui, S.; Zhu, D. *Macromolecules* **2005,** *38,* 4880.

(48) Feng, X.; An, Y.; Yao, Z.; Li, C.; Shi, G. *ACS Appl. Mater. Interfaces* **2012,** *4,* 614.

(49) Tang, T.; Peneva, K.; Mullen, K.; Webber, S. E. *J. Phys. Chem. A* **2007,** *111,* 10609.

(50) Zheng, Y.; Long, H.; Schatz, G. C.; Lewis, F. D. *Chem. Commun.*, **2005,** *38*, 4795.

(51) Jones, B. A.; Ahrens, M. J.; Yoon, M. H.; Facchetti, A.; Marks, T. J.; Wasielewski, M. R. *Angew. Chem., Int. Ed.* **2004,** *43*, 6363.

(52) Zhao, C.; Zhang, Y.; Li, R.; Li, X.; Jiang, J. *J. Org. Chem.* **2007,** *72*, 2402.

(53) Rudin, M.; Weissleder, R. *Nat. Rev. Drug Discovery*, **2003,** *2*, 123.

(54) Lippincott-Schwartz, J.; Snapp, E.; Kenworthy, A. *Nat. Rev. Mol. Cell Biol.*, **2001,** *2*, 444.

(55) Seisenberger, G.; Ried, M. U.; Endress, T.; Büning, H.; Hallek, M.; Bräuchle, C. *Science*, **2001,** *294*, 1929.

(56) Bräuchle, C.; Seisenberger, G.; Endress, T.; Ried, M. U.; Büning, H.; Hallek, M. *ChemPhysChem*, **2002,** *3*, 299.

(57) Ballou, B.; Ernst, L. A.; Waggoner, A. S. *Curr. Med. Chem.*, **2005,** *12*, 795.

(58) Wang, H.; Wang, D.; Wang, Q.; Li, X.; Schalley, C. A. *Org. Biomol. Chem.* **2010,** *8*, 1017.

(59) He, X.; Liu, H.; Li, Y.; Wang, S.; Li, Y.; Wang, N.; Xiao, J.; Xu, X.; Zhu, D. *Adv. Mater.* **2005,** *17*, 2811.

(60) Ehli, C.; Oelsner, C.; Guldi, D. M.; Mateo-Alonso, A.; Prato, M.; Schmidt, C.; Backes, C.; Hauke, F.; Hirsch, A. *Nat. Chem.* **2009,** *1*, 243.

(61) Backes, C.; Schmidt, C. D.; Hauke, F.; Bçttcher, C.; Hirsch, A. *J. Am. Chem. Soc.* **2009,** *131*, 2172.

(62) Baram, J.; Shirman, E.; Ben-Shitrit, N.; Ustinov, A.; Weissman, H.; Pinkas, I.; Wolf, S. G.; Rybtchinski, B. *J. Am. Chem. Soc.* **2008,** *130*, 14966.

(63) Zhang, X.; Rehm, S.; Safont-Sempere, M. M.; Wurthner, F. *Nat. Chem.* **2009,** *1*, 623.

(64) Biedermann, F.; Elmalem, E.; Ghosh, I.; Nau, W. M.; Scherman, O. A. *Angew. Chem., Int. Ed.* **2012,** 5*1*, 7739.

(65) Maity, D.; Govindaraju, T. *Chem. Eur. J.* **2011,** *17*, 1410.

(66) Narayanaswamy, N.; Govindaraju, T. *Sens. Actuators, B* **2012,** *161*, 304.

(67) Sahoo, S. K.; Sharma, D.; Bera, R. K.; Crisponi, G.; Callan, J. F *Chem. Soc. Rev.*, **2012,** *41*, 7195.

(68) Maitya, D.; Karthigeyan, D.; Kundu, T. K.; Govindaraju, T. *Sens. Actuators, B* **2013,** *162*, 831.

(69) Barnham, K. J.; Bush, A. I. *Chem. Soc. Rev.*, **2014,** *43*, 6727.

(70) Rica, R. D. L.; Matsui, H. *Chem. Soc. Rev.*, **2010,** *39*, 3499.

(71) Ulijn, R. V. *J. Mater. Chem.*, **2006,** *16*, 2217.

(72) Lemouchi, C.; Simonov, S.; Zorina, L.; Gautier, C.; Hudhomme, P.; Batail, P. *Org. Biomol. Chem.* **2011,** *9*, 8096.

(73) Ponnuswamy, N.; Pantos, G. D.; Smulders, M. M. J.; Sanders, J. K. M. *J. Am. Chem. Soc.* **2012,** *134*, 566.

(74) Pandeeswar, M.; Avinash, M. B.; Govindaraju, T. *Chem. Eur. J.* **2012,** *18*, 4818.

(75) Pandeeswar, M.; Govindaraju, T. *RSC Adv.* **2013,** *3*, 11459.

(76) Pandeeswar, M.; Khare, H.; Ramakumar, S.; Govindaraju, T. *RSC Adv.* **2014,** *4*, 20154.

(77) Bai, S.; Debnath, S.; Javid, N.; Frederix, P. W. J. M.; Fleming, S.; Pappas, C.; Ulijn, R. V. *Langmuir* **2014,** *30*, 7576.

(78) Zhong, L.; Xing, F.; Bai, Y.; Zhao, Y.; Zhu, S. *Spectrochim. Acta Mol. Biomol. Spectrosc.* **2013,** *115*, 370.

(79) Dwivedi, A. K.; Pandeeswar, M.; Govindaraju, T. *ACS Appl. Mater. Interfaces* **2014,** *6*, 21369.

(80) Chen, X.; Jou, M. J.; Yoon, J. *Org. Lett.*, **2009,** *11*, 2181.

(81) Yan, L.; Ye, Z.; Peng, C.; Zhang, S. *Tetrahedron* **2012,** *68*, 2725.

(82) Kumar, M.; George, S. J. *Chem. Sci.*, **2014,** *5*, 3025.

(83) Shirakawa, H.; Louis, E. J.; MacDiarmid, A. G.; Chiang, C. K.; Heeger, A. J. *J. Chem. Soc., Chem. Commun.*, **1977**, 578.

(84) Service, R. F. *Science* **2000,** *290*, 425.

(85) Kraft, A.; Grimsdale, A. C.; Holmes, A. B. *Angew. Chem., Int. Ed.* **1998,** *37*, 402.

(86) Montali, A.; Smith, P.; Weder, C. *Synthetic Met* **1998,** *97*, 123.

(87) Gustafsson, G.; Cao, Y.; Treacy, G. M.; Klavetter, F.; Colaneri, N.; Heeger, A. J. *Nature* **1992,** *357*, 477.

(88) Stutzmann, N.; Friend, R. H.; Sirringhaus, H. *Science* **2003,** *299*, 1881.

(89) Hide, F.; DiazGarcia, M. A.; Schwartz, B. J.; Heeger, A. J. *Accounts Chem Res* **1997,** *30*, 430.

(90) McGehee, M. D.; Heeger, A. J. *Adv Mater* **2000,** *12*, 1655.

(91) Torsi, L.; Dodabalapur, A.; Rothberg, L. J.; Fung, A. W. P.; Katz, H. E. *Science* **1996,** *272*, 1462.

(92) Novak, P.; Muller, K.; Santhanam, K. S. V.; Haas, O. *Chem. Rev.* **1997,** *97*, 207.

(93) Alam, M. M.; Jenekhe, S. A. *Chem. Mater.* **2004,** *16*, 4647.

(94) Mcginnes.J; Corry, P.; Proctor, P. *Science* **1974,** *183*, 853.

(95) Vogel, A.; Venugopalan, V. *Chem. Rev.* **2003,** *103*, 577.

(96) Thomas, S. W.; Joly, G. D.; Swager, T. M. *Chem. Rev.* **2007,** *107*, 1339.

(97) McQuade, D. T.; Pullen, A. E.; Swager, T. M. *Chem. Rev.* **2000,** *100*, 2537.

(98) Grimsdale, A. C.; Mullen, K. *In Emiss. Mater. Nanomater*. **2006,** *199*, 1.

(99) Bunz, U. H. F. *Chem. Rev*. **2000,** *100*, 1605.

(100) Perepichka, I. F.; Perepichka, D. F.; Meng, H.; Wudl, F. *Adv. Mater*. **2005,** *17*, 2281.

(101) Patil, A. O.; Heeger, A. J.; Wudl, F. *Chem. Rev*. **1988,** *88*, 183.

(102) MacDiarmid, A. G. *Angew. Chem., Int. Ed*. **2001,** *40*, 2581.

(103) Scherf, U.; List, E. J. W. *Adv. Mater*. **2002,** *14*, 477.

(104) Zhou, Q.; Swager, T. M. *J. Am. Chem. Soc.* **1995,** *117*, 12593.

(105) Swager, T. M. *Acc. Chem. Res.*, **1998,** *31*, 201.

(106) Fan, L. J.; Zhang, Y.; Murphy, C. B.; Angell, S. E.; Parker, M. F. L.; Flynn, B. R.; Jones Jr., W. E. *Coord. Chem. Rev.*, **2009,** *253*, 410.

(107) Salinas-Castillo, A.; Camprubí-Robles, M.; Mallavia, R. *Chem. Commun.*, **2010,** *46*, 1263.

(108) Alvarez-Díaz, A.; Salinas-Castillo, A.; Camprubí-Robles, M.; Costa-Fernández, J. M.; Pereiro, R.; Mallavia, R.; Sanz-Medel, A. *Anal. Chem.*, **2011,** *83*, 2712.

(109) Dong, S.; Ou, D.; Qin, J.; Li, Z. *J. Polym. Sci., Part A: Polym. Chem.*, **2011,** *49*, 3314.

(110) Zhou, X. H.; Yan, J. C.; Pei, J. *Macromolecules* ***2004***, *37*, 7078.

(111) Li, Z.; Lou, X.; Yu, H.; Li, Z.; Qin, J. *Macromolecules* **2008**, *41*, 7433.

(112) Li, Z.; Lou, X.; Li, Z.; Qin, J. *ACS Appl. Mater. Interfaces*, 2009, *1*, 232.

(113) Saikia, G.; Dwivedi, A. K.; Iyer, P. K. *Anal. Methods*, **2012,** *4*, 3180.

(114) Saikia, G.; Iyer, P. K. *Macromolecules*, **2011,** *44*, 3753.

(115) Haugland, R. P. Handbook of Fluorescent Probes and Research Chemicals, ed. M. T. Z. Spence, Molecular Probes, Eugene, OR, 6th edn, **1996,** pp. 530.

(116) Xu, Z.; Yoon, J.; Spring, D. R. *Chem. Soc. Rev.*, **2010**, *39*, 1996.

(117) Lou, X.; Zhang, Y.; Li, S.; Ou, D.; Wan, Z.; Qina, J.; Li, Z. *Polym. Chem.*, **2012,** *3*, 1446.

(118) Gaylord, B. S.; Heeger, A. J.; Bazan, G. C. *Proc. Natl. Acid. Sci. USA* **2002**, *99*, 10954.

(119) Galord, B. S.; Heeger, A. J.; Bazan, G. C. *J. Am. Chem. Soc.* **2003**, *125*, 896.

(120) Gaylord, B. S.; Massie, M. R.; Feinstein, S. C.; Bazan, G. C. *Proc. Natl. Acid. Sci. USA* **2005**, *102*, 34.

(121) He, F.; Tang, Y.; Wang, S.; Li, Y.; Zhu, D. *J. Am. Chem. Soc.* **2005**, *127*, 12343.

(122) Liu, B.; Bazan, G. C. *J. Am. Chem. Soc.* **2004**, *126*, 1942.

(123) He, F.; Ren. X. S.; Shen, X. Q.; Xu, Q. H. *Macromolecules* **2011**, *44*, 5373.

(124) Wang, H.; Yan, R.; Wang, X.; Zhu, X.; Li, L. *ACS Appl. Mater. Interfaces* **2013**, *5*, 8254.

(125) Laurent, S.; Ejtehadi, M. R.; Rezaei, M.; Kehoe, P. G.; Mahmoudi, M. *RSC Adv.*, **2012,** *2*, 5008.

(126) Faller, P.; Hureau, C.; Berthoumieu, O. *Inorg. Chem.* **2013,** *52*, 12193.

(127) Dobson, C. M. *Nature*, **2003,** *426*, 884.

(128) Alzheimer, A.; Stelzmann, R. A.; Schnitzlein, H. N.; Murtagh, F. R. *Clin. Anat.* **1995**, *8*, 429.

(129) Kidd, M. *Nature* **1963,** *197*, 192.

(130) Kidd, M. *Brain* **1964,** *86*, 309.

(131) Terry, R. *J. Neuropathol. Exp. Neurol.* **1963,** *22*, 629.

(132) Terry, R.; Gonatas, N. K.; Weiss, M. *Am. J. Pathol.* **1964,** *44*, 269.

(133) Glenner, G. G.; Wong, C. W. *Biochem. Biophys. Res. Commun.* **1984,** *120*, 885.

(134) Gorevic, P.; Goni, F.; Pons-Estel, B.; Alvarez, F.; Peress, R.; Frangione, B. *J.Neuropathol. Exp. Neurol.* **1986,** *45*, 647.

(135) Masters, C. L.; Simms, G.; Weinman, N. A.; Multhaup, G.; McDonald, B. L.; and Beyreuther, K. *Proc. Natl. Acad. Sci. USA* **1985,** *82*, 4245.

(136) Selkoe, D. J.; Abraham, C. R.; Podlisny, M. B.; Duffy, L. K. *J. Neurochem.* **1986,** *146*, 1820.

(137) Grundke-Iqbal, I.; Iqbal, K.; Tung, Y. C.; Quinlan, M.; Wisniewski, H. M.; Binder, L. I. *Proc. Natl. Acad. Sci. USA* **1986,** *83*, 4913.

(138) Kosik, K. S.; Joachim, C. L.; Selkoe, D. J. *Proc. Natl. Acad. Sci. USA* **1986,** *83*, 4044.

(139) Nukina, N.; Ihara, Y. *J. Biochem.* **1986,** *99*, 1541.

140) Wood, J. G.; Mirra, S. S.; Pollock, N. L.; Binder, L. I. *Proc. Natl. Acad. Sci. USA* **1986,** *83*, 4040.

(141) Terry, R. D.; Hansen, L. A.; DeTeresa, R.; Davies, P.; Tobias, H.; Katzman, R. *J. Neuropath. Exp. Neurol.* **1987,** *46*, 262.

(142) Selkoe, D. J. *Physiol.Rev.* **2001,** *81*, 741.

(143) Plassman, B. L.; Langa, K. M.; Fisher, G. G.; Heeringa, S. G.; Weir, D. R.; Ofstedal, M. B.; Burke, J. R.; Hurd, M. D.; Potter, G. G.; Rodgers, W. L.; Steffens, D. C.; Willis, R. J.; Wallace, R.B. *Neuroepidemiology*, **2007,** *29*, 125.

(144) Hebert, L. E.; Scherr, P. A.; Bienias, J. L.; Bennett, D. A.; Evans, D. A. *Arch. Neurol.*, **2003,** *60*, 1119.

(145) Heron, M.; Hoyert, D. L.; Murphy, S. L.; Xu, J.; Kochanek, K. D.; Tejada-Vera, B. Deaths: final data for 2006., *National Vital Statistics Report*, **2009,** *57*, 1.

(146) Ferri, C. P.; Prince, M.; Brayne, C.; Brodaty, H.; Fratiglioni, L.; Ganguli, M.; Hall, K.; Hasegawa, K.; Hendrie, H.; Huang, Y.; Jorm, A.; Mathers, C.; Menezes, P. R.; Rimmer, E.; Scazufca, M. *Lancet*, **2005,** *366*, 2112.

(147) Tanzi, R. E. In Scientific American Molecular Neurology; Martin, J. B., Ed.; Scientific American: New York, **1998**.

(148) Hamley, I. W. *Chem. Rev.* **2012,** *112*, 5147.

(149) Sisodia S. S. *Proc. Natl. Acad. Sci. U. S. A.*, **1992,** *89*, 6075.

(150) Abbott, A. *Nature* **2011,** 475, S2.

(151) Mount, C.; Downton, C. *Nat. Med.* **2006,** *12*, 780.

(152) Jakob-Roetne, R.; Jacobsen, H. *Angew. Chem., Int. Ed.* **2009,** *48*, 3030.

(153) Rodríguez-Rodríguez, C.; Telpoukhovskaia, M.; Orvig, C. *Coord. Chem. Rev.* **2012,** *256*, 2308.

(154) Savelieff, M. G.; Lee, S.; Liu, Y.; Lim, M. H. *ACS Chem. Biol.* **2013,** *8*, 856.

(155) Savelieff, M. G.; DeToma, A. S.; Derrick, J. S.; Lim, M. H. *Acc. Chem. Res.* **2014,** *47*, 2475.

(156) Kepp, K. P. *Chem. Rev.* **2012,** *112*, 5193.

(157) Rauk, A. *Chem. Soc. Rev.*, **2009,** *38*, 2698.

(158) Holtzman, D. M.; Morris, J. C.; Goate, A. M. *Sci. Transl. Med.* **2011,** *3*, 77sr1.

(Broersen, K.; Benilova, I.; Rozenski, J.; Jonckheere, W.; Debulpaep, M.; Vandersteen, A.; Segers-Nolten, I.; Van Der Werf, K. V. D.; Subramaniam, V.; Braeken, D.; Callewaert, G.; Bartic, C.; D'Hooge, R.; Martins, I. C.; Rousseau, F.; Schymkowitz, J.; De Strooper, B. *EMBO J.* **2010,** *29*, 3408.

(160) Pauwels, K.; Williams, T. L.; Morris, K. L.; Jonckheere, W.; Vandersteen, A.; Kelly, G.; Schymkowitz, J.; Rousseau, F.; Pastore, A.; Serpell, L. C.; Broersen, K. *J. Biol. Chem.* **2012,** *287*, 5650.

(161) Lovell, M. A.; Robertson, J. D.; Teesdale, W. J.; Campbell, J. L.; Markesbery, W. R. *J. Neurol. Sci.* **1998,** *158*, 47.

(162) Miller, L. M.; Wang, Q.; Telivala, T. P.; Smith, R. J.; Lanzirotti, A.; Miklossy, J. *J. Struct. Biol.* **2006,** *155*, 30.

(163) Opazo, C.; Huang, X.; Cherny, R. A.; Moir, R. D.; Roher, A. E.; White, A. R.; Cappai, R.; Masters, C. L.; Tanzi, R. E.; Inestrosa, N. C.; Bush, A. I. *J. Biol. Chem.* **2002,** *277*, 40302.

(164) Reinke, A. A.; Gestwicki, J. E. *Chem. Biol. Drug Des.* **2011,** *77,* 399.

(165) Roychaudhuri, R.; Yang, M.; Hoshi, M. M.; Teplow, D. B. *J. Biol. Chem.* **2009,** *284,* 4749.

(166) Viles, J. H. *Coord. Chem. Rev.* **2012,** *256,* 2271.

(167) You, H.; Tsutsui, S.; Hameed, S.; Kannanayakal, T. J.; Chen, L.; Xia, P.; Engbers, J. D.; Lipton, S. A.; Stys, P. K.; Zamponi, G. W. *Proc. Natl. Acad. Sci. U.S.A.* **2012,** *109,* 1737.

(168) Sparks, D. L.; Schreurs, B. G. *Proc. Natl. Acad. Sci. U.S.A.* **2003,** *100,* 11065.

(169) Sanokawa-Akakura, R.; Cao, W.; Allan, K.; Patel, K.; Ganesh, A.; Heiman, G.; Burke, R.; Kemp, F. W.; Bogden, J. D.; Camakaris, J.; Birge, R. B.; Konsolaki, M. *PLoS One* **2010,** *5,* e8626.

(170) Chassaing, S.; Collin, F.; Dorlet, P.; Gout, J.; Hureau, C.; Faller, P. *Curr. Top. Med. Chem.* **2012,** *12,* 2573.

(171) Smith, D. G.; Cappai, R.; Barnham, K. J. *Biochim. Biophys. Acta* **2007,** *1768,* 1976.

(172) Hawe, A.; Sutter, M.; Jiskoot, W. *Pharm. Res.* **2008,** *25,* 1487.

(173) Buell, A. K.; Dobson, C. M.; Knowles, T. P. J.; Welland, M. E. *Biophys. J.* **2010,** *99,* 3492.

(174) Jameson, L. P.; Smith, N. W.; Dzyuba, S. V. *ACS Chem. Neurosci.* **2012,** *3,* 807.

(175) Nilsson, M. R. *Methods* **2004,** *34,* 151.

(176) Klunk, W. E.; Jacob, R. F.; Mason, R. P. *Anal. Biochem.* **1999,** *266,* 66.

(177) Eisert, R.; Felau, L.; Brown, L. R. *Anal. Biochem.* **2006,** *353,* 144.

(178) Klunk, W. E.; Pettegrew, J. W.; Abraham, D. J. *J. Histochem. Cytochem.* **1989,** *37,* 1273.

(179) Furumoto, S.; Okamura, N.; Iwata, R.; Yanai, K.; Arai, H.; Kudo, Y. *Curr. Top. Med. Chem.* **2007,** *7,* 1773.

(180) Frid, P.; Anisimov, S. V.; Popovic, N. *Brain Res. Rev.* **2007,** *53,* 135.

(181) Howie, A. J.; Brewer, D. B. *Micron* **2009,** *40,* 285.

(182) Biancalana, M.; Koide, S. *Biochim. Biophys. Acta,* **2010,** *1804,* 1405.

(183) Rodriguez-Rodriguez, C.; Rimola, A.; Rodriguez-Santiago, L.; Ugliengo, P.; Alvarez-Larena, A.; Gutierrez-de-Teran, H.; Sodupe, M.; Gonzalez-Duarte, P. *Chem. Commun.*, **2010,** *46,* 1156.

(184) Mao, X.; Cuo, Y.; Wang, C.; Zhang, M.; Ma, X.; Liu, L.; Niu, L.; Zeng, Q.; Yang, Y.; Wang, C. *ACS Chem. Neurosci.* **2011,** *2,* 281.

(185) Middleton, C. T.; Marek, P.; Cao, P.; Chiu, C-C.; Singh, S.; Woys, A. M.; de Pablo, J. J.; Raleigh, D. P.; Zanni, M. T. *Nat. Chem.* **2012,** *4,* 355.

(186) Ding, F.; Borreguero, J. M.; Buldyrey, S. V.; Stanley, H. E.; Dokholyan, N. V. *Proteins* **2003,** *53,* 220.

(187) Wetzel, R. *Acc. Chem. Res.* **2006,** *39,* 671.

(188) Morris, A. M.; Watzky, M. A.; Finke, R. G. *Biochim. Biophys. Acta* **2009,** *1794,* 375.

(189) Butterfield S. M.; Lashuel, H. A. *Angew. Chem., Int. Ed.,* **2010,** *49,* 5628.

(190) DeToma, A. S.; Salamekh, S.; Ramamoorthy, A.; Lim, M. H. *Chem. Soc. Rev.*, **2012,** *41,* 608.

(191) Bieschke, J.; Zhang, Q.; Bosco, D. A.; Lerner, R. A.; Powers, E. T.; Wentworth, P., Jr.; Kelly, J. W. *Acc. Chem. Res.* **2006,** *39,* 611.

(192) Bhak, G.; Choe, Y. J.; Paik, S. R. *BMB Rep.* **2009,** *42,* 541.

(193) LeVine, H. *Protein Sci.* **1993,** *2,* 404.

(194) Li, M.; Howson, S. E.; Dong, K.; Gao, N.; Ren, J.; Scott, P.; Qu, X. *J. Am. Chem. Soc.* **2014,** *136,* 11655.

(195) Song, Y.; Cheng, P–N.; Zhu, L.; Moore, E. G.; Moore, J. S. *J. Am. Chem. Soc.* **2014,** *136,* 5233.

(196) Rajasekhar, K.; Suresh, S. N.; Manjithaya, R.; Govindaraju, T. *Sci. Rep.* **2015,** *5,* 8139.

(197) Zhang, M.; Yu, Y.; Wang, C. X.; Yang, Y. L.; Wang, C. *Adv. Mater.* **2013,** *25,* 3780.

(198) Cabaleiro–Lago, C.; Quinlan–Pluck, F.; Lynch, I.; Dawson, K. A.; Linse, S. *ACS Chem. Neurosci.* **2010,** *1,* 279.

(199) Yoo, S. I.; Yang, M.; Brender, J. R.; Subramanian, V.; Sun, K.; Joo, N. E.; Jeong, S.–H.; Ramamoorthy, A.; Kotov, N. A. *Angew. Chem., Int. Ed.* **2011,** *50,* 5110.

(200) Lee, S.; Zheng, X.; Krishnamoorthy, J.; Savelieff, M. G.; Park, H. M.; Brender, J. R.; Kim, J. H.; Derrick, J. S.; Kochi, A.; Lee, H. J. Kim, C.; Ramamoorthy, A.; Bowers, M. T.; Lim, M.H. *J. Am. Chem. Soc.* **2014,** *136,* 299.

(201) Cherny R. A.; Atwood, C. S.; Xilinas, M. E.; Gray, D. N.; Jones, W.D.; McLean, C. A.; Barnham, K.J.; Volitakis, I.; Fraser, F.W.; Kim, Y.; Huang, X.; Goldstein, L. E.; Moir, R. D.; Lim, J. T.; Beyreuther, K.; Zheng, H.; Tanzi, R.E.; Masters, C. L.; Bush, A. I. *Neuron* **2001,** *30,* 665.

(202) Barnham, K. J.; Masters, C. L.; Bush, A. I. *Nat. Rev. Drug Discovery* **2004,** *3,* 205.

(203) Gaggelli, E.; Kozlowski, H.; Valensin, D.; Valensin, G. *Chem. Rev.* **2006,** *106,* 1995.

(204) Cahoon, L. *Nat. Med.* **2009,** *15,* 356.

(205) Adlard, P.A.; Cherny, R.A.; Finkelstein, D.I.; Gautier, E.; Robb, E.; Cortes, M.; Volitakis, I.; Liu, X.; Smith, J. P.; Perez, K.; Laughton, K.; Li, Q. X.; Charman, S. A.;

Nicolazzo, J. A.; Wilkins, S.; Deleva, K.; Lynch, T.; Kok, G.; Ritchie, C. W.; Tanzi, R. E.; Cappai, R.; Masters, C. L.; Barnham, K. J.; Bush, A. I. *Neuron* **2008,** *59,* 43.

(206) Scott, L. E.; Orvig, C. *Chem. Rev.* **2009,** *109,* 4885.

(207) Sharma, A. K.; Pavlova, S. T.; Kim, J.; Finkelstein, D.; Hawco, N. J.; Rath, N. P.; Kim, J.; Mirica, L. M. *J. Am. Chem. Soc.* **2012,** *134,* 6625.

(208) Hindo, S. S.; Mancino, A. M.; Braymer, J. J.; Liu, Y.; Vivekanandan, S.; Ramamoorthy, A.; Lim, M. H. *J. Am. Chem. Soc.* **2009,** *131,* 16663.

(209) Choi, J-S.; Braymer, J. J.; Park, S. K.; Mustafa, S.; Chae, J.; Lim, M. H. *Metallomics,* **2011,** *3,* 284.

(210) Braymer, J. J.; Choi, J-S.; DeToma, A. S.; Wang, C.; Nam, K.; Kampf, J. W.; Ramamoorthy, A.; Lim, M. H. *Inorg. Chem.* **2011,** *50,* 10724.

(211) He, X.; Park, H. M.; Hyung, S-J.; DeToma, A. S.; Kim, C.; Ruotoloc, B. T.; Lim, M. H. *Dalton Trans.,* **2012,** *41,* 6558.

(212) Pithadia, A. S.; Kochi, A.; Soper, M. T.; Beck, M. W.; Liu, Y.; Lee, S.; DeToma, A. S.; Ruotolo, B. T.; Lim, M. H. *Inorg. Chem.* **2012,** *51,* 12959.

(213) Liu, Y.; Kochi, A.; Pithadia, A. S.; Lee, S.; Nam, Y.; Beck, M. W.; He, X.; Lee, D.; and Lim, M. H. *Inorg. Chem.* **2013,** *52,* 8121.

(214) Jones, M. R.; Service, E. L.; Thompson, J. R.; Wang, M. C. P.; Kimsey, I. J.; DeToma, A. S.; Ramamoorthy, A.; Lim, M. H.; Storr, T. *Metallomics,* **2012,** *4,* 910.

(215) Beck, M. W.; Oh, S. B.; Kerr, R. A.; Lee, H. J.; Kim, S. H.; Kim, S.; Jang, M.; Ruotolo, B. T.; Lee, J-Y.; Lim, M. H. *Chem. Sci.,* **2015,** *6,* 1879.

(216) Sharma, A. K.; Kim, J.; Prior, J. T.; Hawco, N. J.; Rath, N. P.; Kim, J.; Mirica, L. W. *Inorg. Chem.* **2014,** *53,* 11367.

(217) Zhang, Q.; Liu, J.; Hu, X.; Wang, W.; Yuan, Z. *ACS Macro Lett.* **2015,** *4,* 339.

(218) Yang, S.-T.; Guo, W.; Lin, Y.; Deng, X.-Y.; Wang, H.-F.; Sun, H.-F.; Liu, Y.-F.; Wang, X.; Wang, W.; Chen, M.; Huang, Y.-P.; Sun, Y.-P. *J. Phys. Chem. C,* **2007,** *111,* 17761.

(219) Yang, R. S.; Chang, L. W.; Wu, J.-P.; Tsai, M.-H.; Wang, H.-J.; Kuo, Y.-C.; Yeh, T.-K.; Yang, C. S. Lin, P. *Environ. Health Perspect.,* **2007,** *115,* 1339.

(220) Choi, I.; Lee, L. P. *ACS Nano,* **2013,** *7,* 6268.

(221) Cabaleiro-Lago, C.; Quinlan-Pluck, F.; Lynch, I.; Lindman, S.; Minogue, A. M.; Thulin, E.; Walsh, D. M.; Dawson, K. A. Linse, S. *J. Am. Chem. Soc.* **2008,** *130,* 15437.

(222) Yang, L.; Chen, Q.; Liu, Y.; Zhang, J.; Sun, D.; Zhoua, Y.; Liu, J. *J. Mater. Chem. B,* **2014,** *2,* 1977.

(223) Palmal, S.; Jana, N. R.; Jana, N. R. *J. Phys. Chem. C* **2014,** *118,* 21630.

(224) Li, M.; Zhao, C.; Yang, X.; Ren, J.; Xu, C.; Qu, X. *Small* **2013,** *9,* 52.

(225) Du, W-J.; Guo, J-J.; Gao, M-T.; Hu, S-Q.; Dong, X-Y.; Han, Y-F.; Liu, F-F.; Jiang, S.; Sun, Y. *Sci. Rep.* **2015,** *5,* 7992.

(226) Lee, Y. O.; Shin, J-W.; Yi, C.; Lee, Y. H.; Sohn, N-W.; Kang, C.; Kim, J. S. *Chem. Commun.*, **2014,** *50,* 5741.

(227) Zhu, L.; Song, Y.; Cheng, P-N.; Moore, J. S. *J. Am. Chem. Soc.* **2015,** *137,* 8062.

(228) Zhang, X.; Tian, Y.; Li, Z.; Tian, X.; Sun, H.; Liu,H.; Moore, A.; Ran, C. *J. Am. Chem. Soc.* **2013,** *135,* 16397.

(229) Cui, M.; Ono, M.; Watanabe, H.; Kimura, H.; Liu, B.; Saji, H. *J. Am. Chem. Soc.* **2014,** *136,* 3388.

(230) Fu, H.; Cui, M.; Tu, P.; Pan, Z.; Liu, B.; *Chem. Commun.*, **2014,** *50,* 11875.

Chapter: 2a

A Rapid and Sensitive Detection of Ferritin in Nanomolar Level using Fluorescent Conjugated Polymer

Abstract

A neutral conjugated polymer poly-p-phenylene (PPP) derivative, poly(1,4-bis-(8-(8-hydroxyquinoline)-octyloxy)-benzene) (PHQ), was prepared by using a simple and economical method of oxidative polymerization reaction. This newly synthesized polymer PHQ has absorption maximum at 327 nm and emission at 401 nm in aqueous solutions. Moreover, PHQ displays fluorescence "turn-off" characteristic with metal ion and selectively detects Fe^{2+}, Fe^{3+} and non-heme metalloprotein ferritin compare to other metallo and nonmetalloproteins in physiological conditions. The Stern−Volmer constant (K_{SV}) value obtained for the detection of ferritin is 0.84×10^{7} M^{-1}, confirming high sensitivity of this polymer for ferritin among other proteins.

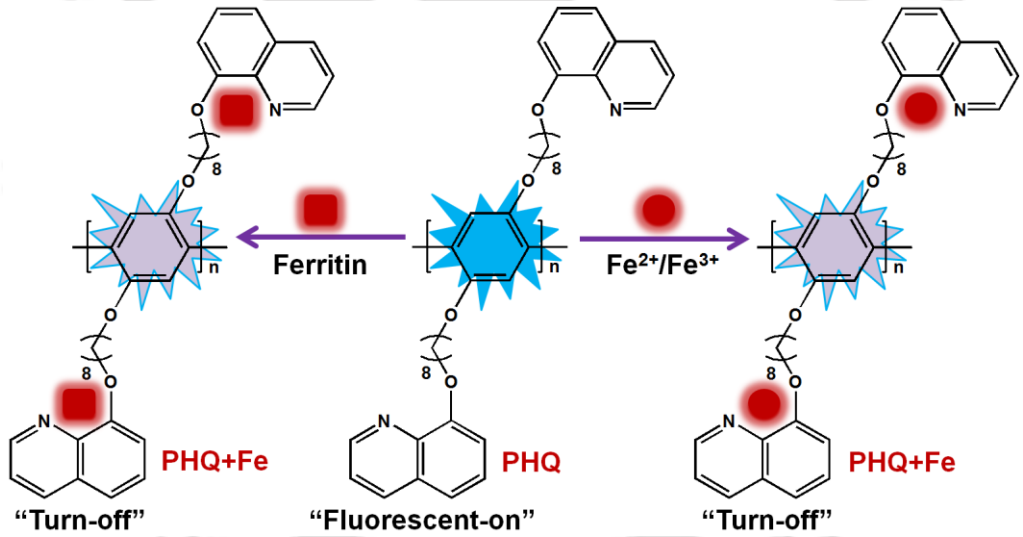

2a.1. Introduction

Development of new fluorescent probes for biosensors are necessary that can easily and quantitatively respond to individual proteins because of their fundamental importance in proteomics, medical diagnostics, and pathogen detection.[1-3] A highly selective and sensitive fluorescent sensors offer a distinct advantage in the early diagnosis of diseases. Conjugated polymers (CPs) have received particular attention for sensing proteins, due to their fluorescence properties.[4-6] More specifically, the possibility of energy or electron transfer from the CPs to the biological analyte, results in fluorescence change and renders CPs useful for sensing metalloproteins. However, it has been shown through a set of careful experiments that such a change in fluorescence behavior could also be achieved through binding of nonmetalloproteins.[7] Several fluorescent reagents that target proteins have been developed for the detection of proteins, these include o-phthaldialdehyde, fluorescamine,[8] cyanine dyes,[9] acridizinium[10] and NanoOrange[8] which can detect proteins in solution. Thayumanavan and co-workers have utilized water-soluble polyelectrolyte to generate fluorescence-based patterns for both metalloprotein and nonmetalloprotein sensing using solution based detection schemes.[11-13] Although, the specially designed amphiphilic sensors exhibited highly selective and sensitive to metalloprotein in solution. Moreover, the hydrophobicity of most fluorescent organic dyes limited their applications such as in fluorescent probes for protein detection in aqueous media. Therefore, a simple approach to create new biosensors for solution based protein detection is still needed.

Iron is the most abundant essential trace element in human body and both the ions, Fe^{2+} and Fe^{3+}, play vital roles in many biological processes.[14-16] In well-nourished people the total iron content is ~4 g (70% in haemoglobin (Hb), 25% in storage). Iron is indispensable in living systems since it is the oxygen carrier in all tissues in the form of hemoglobin and helps to transport electrons as cytochromes. Deficiency of iron in primary stages can cause anemia, which can harm or even kill by depriving organs of oxygen. Therefore, the development of selective and sensitive fluorescent probes for the detection of biologically relevant ions has been the cynosure among the chemists during recent years due to the ease of detection, sensitivity and tenability of fluorescence method over other techniques.[17-22] Interestingly, various sensors have been reported specifically for Fe^{3+} ions.[23-28]

2a.2. Results and discussion

The synthesis of PHQ involves mainly minimum reaction steps without requiring costly metal catalysts/phase-transfer catalysts, while still employing very easy and mild reaction conditions (Scheme 2a.1). The 8-hydroxyquinoline (8-HQ) moieties were introduced onto the pendent group of CP by substituting the terminal bromine atoms of the alkyl chains to obtain the desired PHQ by a post polymerization functionalization method (Scheme 2a.1). Due to the ease in synthesis and structural tunability, nontoxic nature, cell permeability and the wide ranging biological activity of CPs, they were utilized efficiently as biomarkers to study genetic alterations and proteomics.[29-31] The backbone of CPs assists electron delocalization and exciton migration, resulting in amplified signals[32] in the presence of analytes that modify the photophysical characteristics of CP which is utilized to study the interaction with biological molecules or analytes of interest. Herein, we present the CP PHQ that efficiently bind metals like Fe^{2+}, Fe^{3+} and non-heme metalloprotein ferritin in physiological conditions and competitive biological environment.

2a.2.1. Synthesis of monomer

Synthesis of monomer 1,4-bis-(8-bromooctyloxy)-benzene and its polymer PPP-Br was carried out using a previously established procedures.[33-36]

2a.2.2. Synthesis of Poly (1,4-Bis-(8-bromo-octyloxy)-benzene) (PPP-Br)

The synthesis of polymer PPP-Br proceeded as follows. In a 100 mL three-necked round-bottom flask equipped with a nitrogen inlet, anhydrous ferric chloride (1.48 g, 9.18 mmol) was dissolved in 20 mL of nitrobenzene. Further, 1,4-Bis-(8-bromo-octyloxy)-benzene (2.0 g, 4.08 mmol) dissolved in 15 mL nitrobenzene was added to the flask using a syringe. The reaction mixture was stirred at room temperature for 36 h, followed by precipitation from methanol. This was stirred for 1 h, centrifuged and washed repeatedly with methanol. The resulting polymer was dried under reduced pressure to obtain 1.39 g (70%) as light brown powder. ^{1}H NMR (400 MHz, $CDCl_3$): δ ppm, 7.08 (s), 3.92 (m), 3.36 (m) 1.82 (m), 1.68 (m), 1.37 (m), 1.2 (m). ^{13}C NMR (100 MHz, $CDCl_3$): δppm, 150.2, 115.1, 67.8, 40.1, 33.6, 33.1, 28.9, 28.0, 27.8, 27.2, 26.3. $M_W = 3.48 \times 10^4$, PDI = 1.9 (GPC in THF, polystyrene standard).

2a.2.3. Synthesis of Poly (1,4-bis-(8-(8-hydroxyquinoline)-octyloxy)-benzene) (PHQ)

PPP-Br (0.1 g, 0.20 mmol) and 8-hydroxyquinoline (0.118 g, 0.816 mmol) were dissolved in dry DMF (15 mL) in the presence of potassium carbonate (197 mg, 1.43 mmol). After 16 h

reflux the mixture was filtered, followed by precipitation from methanol. Then, the precipitate was centrifuged and washed repeatedly with methanol. The resulting polymer was dried under reduced pressure to obtain yield 78% as light brown powder. ^{1}H NMR (400 MHz, $CDCl_3$): δ ppm, 8.88 (broad), 8.02 (broad), 7.32 (m), 7.08 (s), 6.92 (broad) 4.09 (m), 3.86 (m), 1.91(m), 1.79(m), 1.62 (m), 1.25(m), 0.85 (m).

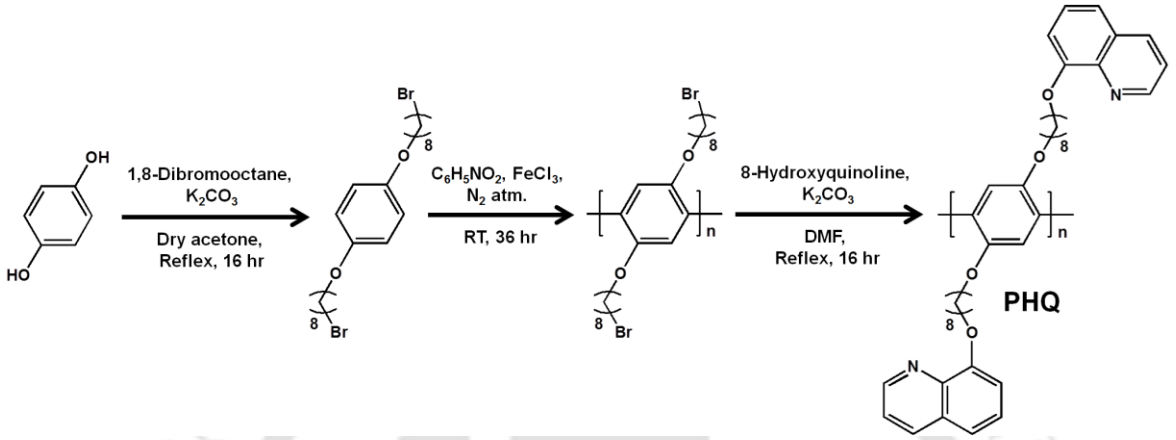

Scheme 2a.1 Synthesis of polymer PHQ by oxidative polymerization and post polymerization functionalization of 8-hydroxyquinoline.

2a.2.4. Selective and sensitive detection of Fe^{2+} and Fe^{3+} ions by PHQ

The decrease in fluorescence intensity was investigated by adding successive aliquots of aqueous stock solutions of Fe^{2+} and Fe^{3+} ions (6.6 µM) to the solution of PHQ (6.6 µM) in 4:1, THF: H_2O (Figure 2a.1a). Upon gradual addition of Fe^{2+} and Fe^{3+} metal ions into PHQ, the results showed very large quenching in the fluorescence of PHQ (Figure 2a.1a) and >99% reduction in fluorescence intensity occurred, implying very strong and selective association of PHQ with both Fe^{2+} and Fe^{3+} (6.6 µM) (Figure 2a.1c and 2a.1d). The interaction of PHQ with metal salts such as Mn^{2+}, Cd^{2+}, Pb^{2+}, Hg^{2+}, Ni^{2+}, Co^{2+}, Cr^{3+}, Zn^{2+}, Cu^{2+}, Fe^{2+} and Fe^{3+} with the concentrations of 6.6×10^{-6} M in 4:1 THF: H_2O was carried out at pH 7 at room temperature and the changes were recorded in the fluorescence peak of PHQ at 401 nm and presented as bar diagram (Figure 2a.1b). As seen from the bar diagram no other metals caused notable fluorescence quenching of PHQ even at higher concentrations indicating that PHQ is not selective for other metals examined here, due to the poor coordination ability of the 8-HQ receptor with other metal ions. The efficiency of quenching was studied by plotting Stern–Volmer plot (K_{SV}) (I_0/I vs. [Q]) where I_0 is the fluorescence intensity of PHQ and I is the fluorescence intensity of PHQ after addition of a given concentration of quencher [Q]

where [Q] = Fe^{2+} and Fe^{3+} ions concentration. The K_{SV} value was calculated from the plot and found to be 0.371× 10^6 M^{-1} and 0.283 × 10^6 M^{-1} for Fe^{2+} and Fe^{3+} ions respectively.

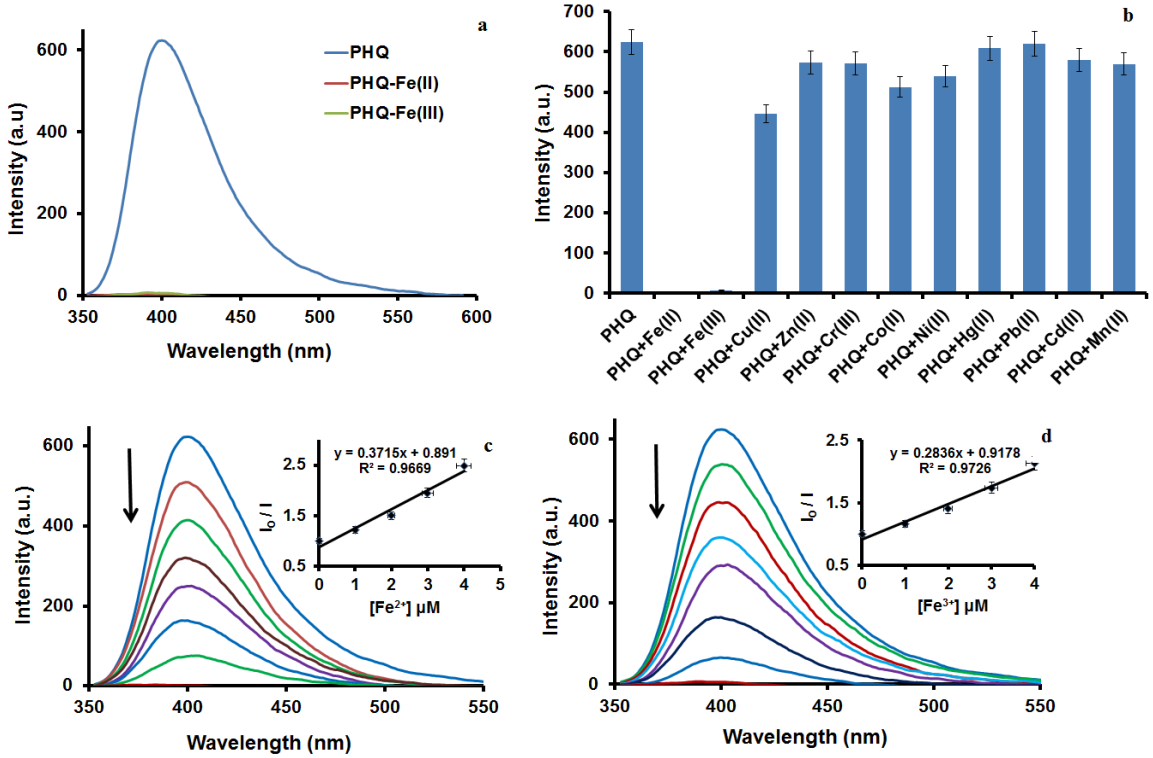

Figure 2a.1 (a) Fluorescence quenching (>99 %) of PHQ (6.6 µM) in presence of Fe^{2+} and Fe^{3+} (6.6 µM) ion in THF: H_2O (4:1). λ_{ex} 332 nm, and λ_{em} 401 nm. (b) Bar diagram of changes observed in the fluorescence peak of PHQ in presence of various metal ions. (c) Fluorescence spectra of PHQ in THF: H_2O (4:1) (6.6 µM) at various concentrations of Fe^{2+} ion. (d) Fluorescence spectra of PHQ in THF: H_2O (4:1) (6.6 µM) at various concentrations of Fe^{3+} ion. Insets (c) and (d) are the respective Stern-Volmer plots for the fluorescence quenching of PHQ by Fe^{2+} and Fe^{3+} ions respectively (error bars = ± 5%).

2a.2.5. Selective and sensitive detection of ferritin by PHQ

Since, PHQ showed such remarkable quenching with both Fe^{2+} and Fe^{3+} ion, we studied its interactions with iron containing metalloproteins like Cyt *c*, MetHb, ferritin and hemin via fluorescence spectroscopic studies (Figure 2a.2). Figure 2a.2a, suggests that nanomolar quantity of ferritin (41 × 10^{-9} M) causes ~25% quenching of PHQ and on further addition of up to 81 × 10^{-8} M ferritin resulted in >98% fluorescence quenching of PHQ with a K_{SV} value of 0.84 × 10^7 M^{-1}. Furthermore, other metalloproteins also studied here, caused 90% quenching at concentrations of ~30 µM (Figure 2a.2b, 2a.2c and 2a.2d). Consequently, the binding affinity of PHQ with non-heme metalloprotein was found to be higher than heme

containing metalloproteins. The heme group consists of porphyrin ring in which an iron ion is bound in the centre of heterocyclic ring consisting four pyrrole molecules. There is a possibility of some competition between PHQ and porphyrin ring to bind iron. The UV-visible plots depicting that PHQ absorption enhancement at 332 nm upon gradual addition of ferritin due to the interaction of PHQ with metalloproteins of ferritin as shown in figure 2a.3.

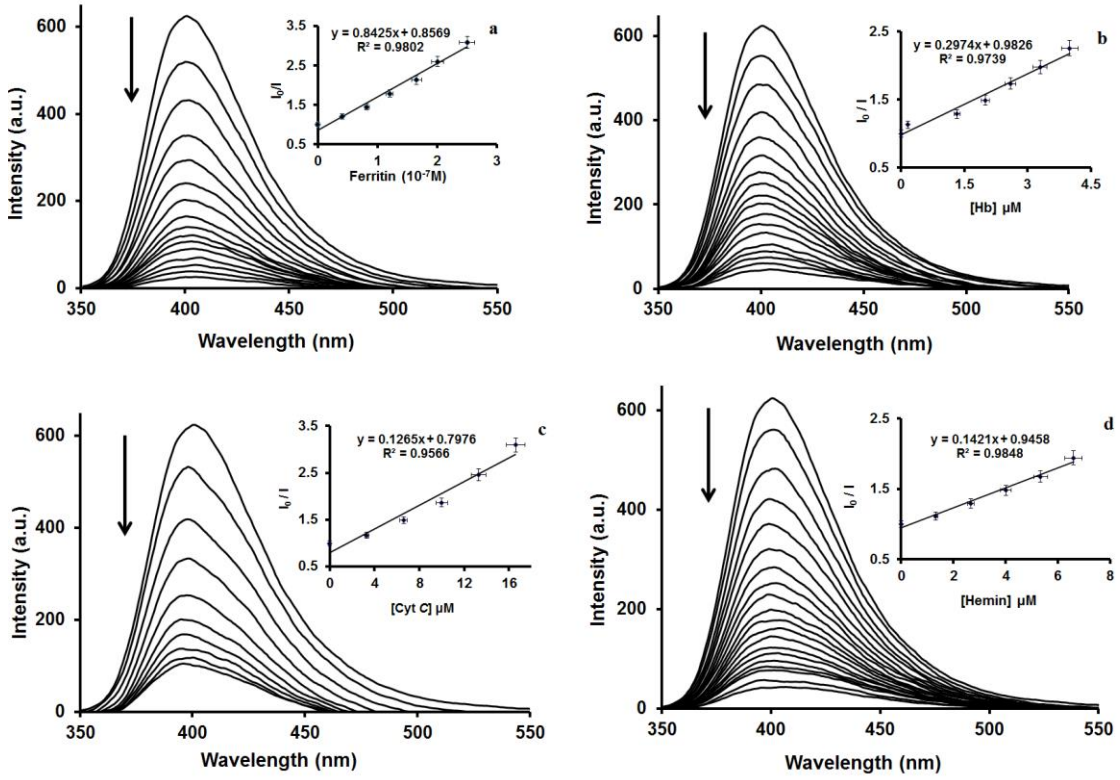

Figure 2a.2 Fluorescence quenching spectra of PHQ in THF:H_2O (4:1) with various concentrations of metalloproteins were recorded at pH 6.5 in room temperature conditions. (a) Ferritin, (b) Methemoglobin, (c) Cyt *c*, and (d) Hemin. Inset: corresponding K_{SV} plot and values of different proteins: (Ferritin = 0.84 × 10^7 M^{-1}), (Methemoglobin = 0.29 × 10^6 M^{-1}), (Cyt *c* = 0.126 × 10^6 M^{-1}), (Hemin = 0.142 × 10^6 M^{-1}). Complete fluorescence quenching of PHQ occurred at the following final concentrations of metalloproteins: ferritin (0.81 μM), methemoglobin (16 μM), Cyt *c* (30 μM) and hemin (29 μM) (error bars ± 5%).

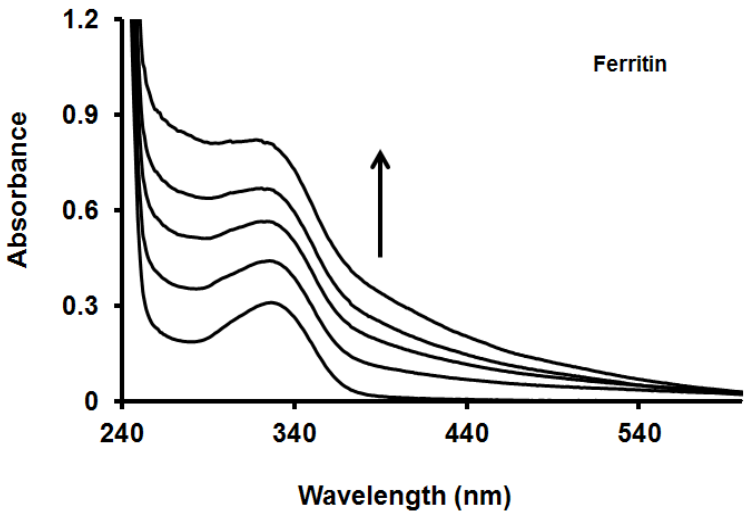

Figure 2a.3 UV-Visible spectra of PHQ observed (16 μM) in 4:1 THF: H_2O with increasing concentration of ferritin from 0-0.16 μM. All the measurements were conducted in pH 6.5 at room temperature.

Furthermore, we studied the interaction of PHQ with non–metalloproteins BSA, lysozyme and ribonuclease A using fluorescence techniques (Figure 2a.4), but non–metalloproteins barely caused any changes to the fluorescence of PHQ even at higher concentrations compared to ferritin.[36]

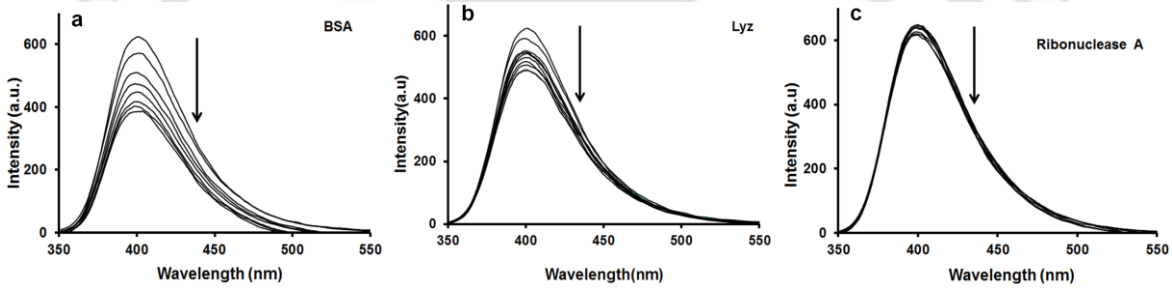

Figure 2a.4 (a-c) Fluorescence quenching of PHQ (6.6 μM) in 4:1 THF: H_2O with increasing concentration of BSA, Lyz and Ribonuclease A from 0-50 μM. The λ_{ex} and λ_{em} was 332 nm and 401 nm respectively. Measurements were conducted in pH 6.5 at room temperature.

2a.3. Conclusion

A neutral conjugated polymer poly-p-phenylene (PPP) derivative, poly(1,4-bis-(8-(8-hydroxyquinoline)-octyloxy)-benzene) (PHQ), was prepared by using a simple and economical method of oxidative polymerization reaction. The highly fluorescent PHQ polymer appeared absorption maximum at 327 nm and emission at 401 nm in aqueous conditions in (4:1 THF: H_2O). Further, PHQ showed selective and sensitive detection to Fe^{2+}, Fe^{3+} and non-heme metalloprotein ferritin by fluorescence "turn-off" method in physiological

conditions. The Stern−Volmer constant (K_{SV}) value obtained for the detection of ferritin is 0.84×10^7 M^{-1}, which confirms the PHQ has highly sensitive toward ferritin among other proteins.

2a.4. Experimental Section

2a.4.1. Materials and methods

All the reagents and chemicals were purchased from Aldrich Chemicals, Merck or Ranbaxy (India) and used as received. Milli-Q water and HPLC grade THF were used in all the experiments. Solvents were degassed using three freeze thaw cycles or flushed with nitrogen for at least 1 h prior to use when necessary.

UV–vis absorption spectra were recorded on a PerkinElmer Lambda–25 spectrometer. Fluorescence spectra were carried out on a Varian Cary Eclipse Spectrometer. A 10 × 10 mm quartz cuvette was used for solution spectra and emission was collected at 90° relative to the excitation beam. Deionized water was obtained from Milli–Q system (Millipore). ^{1}HNMR (400 MHz) and ^{13}CNMR (100 MHz) spectra were obtained with a Varian-AS400NMR spectrometer. GPC was recorded with Waters-2414 instrument (Polystyrene calibration).

2a.4.2. Preparation of PHQ stock solution

The polymer PHQ stock solution was prepared at the concentration of 1.0×10^{-3} M in 10 mL THF. This stock solution was diluted to desired concentration for each titration in a 3 mL cuvette.

2a.4.3. Preparation of metal ion stock solutions

Each inorganic metal salt stock solution was prepared at the concentration of 10.0×10^{-3} M in 5 mL Milli-Q water. The stock solutions were diluted to the desired concentrations with Milli-Q water when needed.

2a.4.4. Fluorescence titration of PHQ with different metal ions

A solution of PHQ (6.6×10^{-6} M) was placed in a 3 mL cuvette (10.0 nm width) with 4:1 (THF: H_2O) solvent ratio and then fluorescence spectrum was recorded. Separately, different metal ion solutions were introduced and the changes of the fluorescence intensity were recorded at room temperature (excitation wavelength: 332).

2a.4.5. Fluorescence intensity changes of PHQ with metalloproteins and non-metalloproteins

The polymer PHQ stock solution was prepared at the concentration of 1.0×10^{-3} M in 10 mL THF. This was diluted to 6.6×10^{-6} M for each titration in a 3 mL cuvette. A solution of PHQ

was placed in a 3 mL cuvette (10.0 nm width) with 4:1 (THF: H_2O) solvent ratio and then fluorescence spectrum was recorded. Separately, from the stock solutions, metalloproteins and non-metalloproteins were introduced into PHQ solution and then fluorescence intensity changes were recorded at pH 6.5 at room temperature (excitation wavelength: 332 nm).

2a.4.6. Absorbance changes of PHQ with metalloprotein ferritin

The stock solution of metalloprotein ferritin (1.24×10^{-4} M) was prepared in MilliQ water. A solution of PHQ was placed in a 3 mL cuvette (10.0 nm width) with 4:1 (THF: H_2O) solvent ratio and then absorbance spectrum was recorded. From the stock solutions, metalloprotein ferritin was introduced in portions and absorbance changes were recorded at pH 6.5 in room temperature.

References

(1) Pinto, M. R.; Schanze, K. S. *Proc. Natl. Acad. Sci. U. S. A.,* **2004,** *101,* 7505.

(2) Wiskur, S. L.; Ait-Haddou, H.; Lavigne, J. J.; Anslyn, E. V. *Acc. Chem. Res.,* **2001,** *34,* 963.

(3) Pu, L. *Chem. Rev.,* **2004,** *104,* 1687.

(4) Fan, C.; Plaxco, K. W.; Heeger, A. J. *J. Am. Chem. Soc.* **2002,** *124,* 5642.

(5) Wilson, J. N.; Wang, Y.; Lavigne, J. J.; Bunz, U. H. F. *Chem. Commun.,* **2003,** 1626.

(6) Chen, L.; McBranch, D. W.; Wang, H.-L.; Helgeson, R.; Wudl, F.; Whitten, D. G. *Proc. Natl. Acad. Sci. U.S.A.* **1999,** *96,* 12287.

(7) Kim, I.-B.; Dunkhorst, A.; Bunz, U. H. F. *Langmuir* **2005,** *21,* 7985.

(8) Jones, L. J.; Haugland, R.; Singer, V. *BioTechniques* **2003,** *34,* 850.

(9) Mishra, A.; Behera, R. K.; Behera, P. K.; Mishra, B. K.; Behera, G. B. *Chem. Rev.,* **2000,** *100,* 1973.

(10) Granzhan, A.; Ihmels, H. *Org. Lett.,* **2005,** *7,* 5119.

(11) Savariar, E. N.; Ghosh, S.; Gonzalez, D. C.; Thayumanavan, S. *J. Am. Chem. Soc.,* **2008,** *130,* 5416.

(12) Sandanaraj, B. S.; Demont, R.; Thayumanavan, S. *J. Am. Chem. Soc.,* **2007,** *129,* 3506.

(13) Sandanaraj, B. S.; Demont, R.; Aathimanikandan, S. V.; Savariar, E. N.; Thayumanavan, S. *J. Am. Chem. Soc.,* **2006,** *128,* 10686.

(14) Beutler, E.; Felitti, V.; Gelbart, T.; Ho, N. *Drug Metab. Dispos.,* **2001,** *29,* 495.

(15) Touati, D. *Arch. Biochem. Biophys.,* **2000,** *373,* 1.

(16) Cairo, G.; Pietrangelo, A. *Biochem. J.,* **2000,** *352,* 241.

(17) Esposito, B. P.; Epsztejn, S.; Breuer, W. Cabantchik, Z. I. *Anal. Biochem.,* **2002,** *304,* 1.

(18) Valeur, B.; Leray, I. *Coord. Chem. Rev.,* **2000,** *205,* 3.

(19) Saha, U. C.; Dhara, K.; Chattopadhyay, B.; Mandal, S. K.; Mondal, S.; Sen, S.; Mukherjee, M.; Smaalen, S.V.; Chattopadhyay, P. *Org. Lett.,* **2011,** *13,* 4510.

(20) Saha, U. C.; Chattopadhyay, B.; Dhara, K.; Mandal, S. K.; Sarkar, S.; Khuda-Bukhsh, A. R.; Mukherjee, M.; Helliwell, M.; Chattopadhyay, P. *Inorg. Chem.,* 2**011,** *50,* 1213.

(21) Sen, S.; Mukherjee, T.; Sarkar, S.; Mukhopadhyay, S. K.; Chattopadhyay, P. *Analyst,* **2011,** *136,* 4839.

(22) Dhara, K.; Saha, U. C.; Dan, A.; Manassero, M.; Sarkar, S.; Chattopadhyay, P. *Chem. Commun.,* **2010,** *46,* 1754.

(23) Zhan, J.; Wen, L.; Miao, F.; Tian, D.; Zhu, X.; Li, H. *New J. Chem.,* **2012,** *36,* 656.

(24) Xiang, Y. Tong, A. *Org. Lett.*, **2006,** *8*, 1549.

(25) Mao, J.; Wang, L. N.; Dou, W.; Tang, X. L.; Yan, Y.; Liu, W. S. *Org. Lett.*, **2007,** *9*, 4567.

(26) Tumambac, G. E.; Rosencrance, C. M.; Wolf, C. *Tetrahedron*, **2004,** *60*, 11293.

(27) Bricks, J. L.; Kovalchuk, A.; Trieflinger, C.; Nofz, M.; Buschel, M.; Tolmachev, A. I.; Daub, J.; Rurack, K. *J. Am. Chem. Soc.*, **2005,** *127*, 13522.

(28) Sen, S.; Sarkar, S.; Chattopadhyay, B.; Moirangthem, A.; Basu, A.; Dharad, K.; Chattopadhyay, P. *Analyst*, **2012,** *137*, 3335.

(29) Zhu, C.; Liu, L.; Yang, Q.; Lv, F.; Wang, S. *Chem. Rev.*, **2012,** *112*, 4687.

(30) McQuade, D. T.; Pullen, A. E. Swager, T. M. *Chem. Rev.*, **2000,** *100*, 2537.

(31) Nilsson, K. P. R.; Inganas, O. *Nat. Mater.*, **2003,** *2*, 419.

(32) Swager, T. M. *Acc. Chem. Res.*, **1998,** *31*, 201.

(33) Saikia, G.; Dwivedi, A. K.; Iyer, P. K. *Anal. Methods*, **2012,** *4*, 3180.

(34) Fukuda, M.; Sawada, K.; Yoshino, K. *Jpn. J. Appl. Phys.*, **1989,** *28*, L1433.

(35) Paul, G. S.; Sarmah, P. J.; Iyer, P. K.; Agarwal, P. *Macromol. Chem. Phys.* **2008,** *209*, 417.

(36) Muthuraj, B.; Hussain, S.; Iyer, P. K. *Polym. Chem.* **2013,** *4*, 5096.

Chapter: 2b

Modulation of Aβ Fibrils using Fluorescent Conjugated Polymer

Abstract

A non–toxic conjugated polymer, poly(1,4–bis–(8–(8–hydroxyquinoline)–octyloxy)–benzene) (PHQ) binds Fe^{2+}/Fe^{3+} ion and non–heme metalloprotein ferritin in nanomolar level with highest known selectivity (K_{SV} value of 0.84×10^7 M^{-1}) (previous chapter 2a). Further, PHQ was utilized to interact with the bound iron containing Aβ fibril aggregates and diminishes their accumulation via metal chelation method. The enhanced levels of toxic metals, especially iron, from the labile iron pool in brain are primarily responsible for the pathogenesis of several neurological disorders, namely, Alzheimer's disease (AD). They are the major source for generating highly toxic reactive oxygen species (ROS), accelerating the Aβ peptide aggregation in the brain of AD patients. The anti–AD activity of PHQ was confirmed via *in vitro* control studies by the mixture of cerebrospinal fluid (CSF Aβ fibrils) and Aβ1–40 fibrils with and without iron by using Thioflavin–T (ThT) binding assay test and electron microscopy analysis. Conceptually, this new strategy to clear the cerebral deposits in CSF and Aβ1–40 fibrils using PHQ was confirmed successfully under physiological conditions.

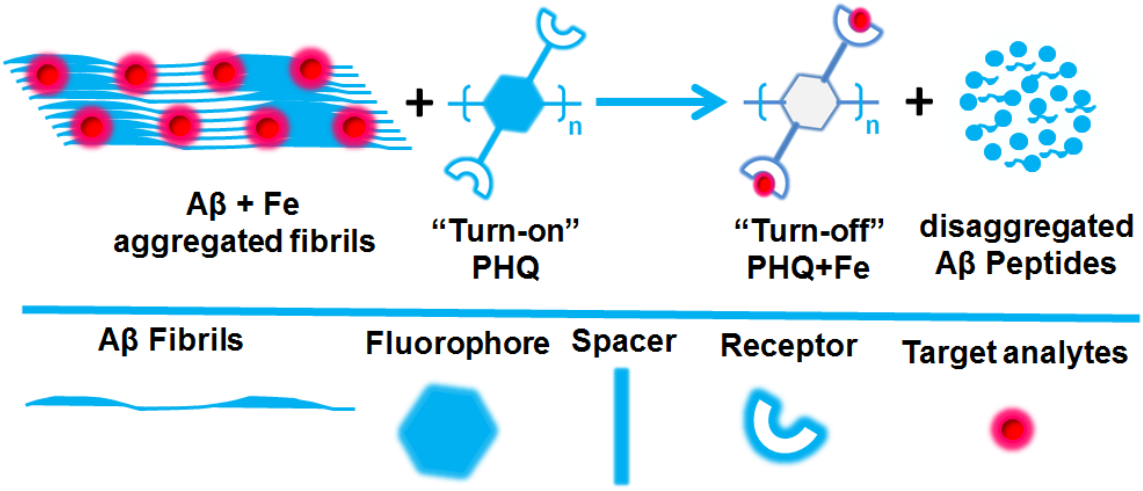

2b.1. Introduction

Numerous heme and non-heme iron proteins along with other transition metals such as copper, zinc etc. are found to be responsible for several neurodegenerative disorders such as Alzheimer's disease (AD), Parkinson's disease (PD), Huntington's disease (HD), amyotrophic lateral sclerosis (ALS) and prion disease.[1] AD is a prevalent neurodegenerative disorder causing senile dementia, known to affect approximately 40 million people across the world.[2] The cognitive and behavioral symptoms associated with AD include gradual loss of brain function, inability to recollect specific events and memory loss, physical disability and ultimately leading to death.[3,4] In AD, the aggregates are formed by Aβ peptide which is a well-known proteolytic fragment of the amyloid precursor protein (APP). While the monomeric Aβ is primarily composed of α-helical and/or unordered structure of misfolded structures are rich in β-sheet conformation. The conformational modification leads to the formation of extended β-sheets promoting homophilic interactions and consequently leading to Aβ oligomer formation. Moreover, kinetic studies are report that misfolding of monomeric Aβ accelerates the formation of oligomers, which serve as seeds for accelerated fibril growth.[5-10] It has been reported[11] that innocuous monomers of Aβ become neurotoxic upon aggregation (oligomers). It was also reported that toxicity of Aβ, involved the self-association of monomers into oligomers and higher aggregated forms.[12,13] This was further supported by *in vitro* and *in vivo* studies illustrating that oligomeric and prefibrillar Aβ assemblies are strong neurotoxins.[14-19] Among various transition metals, iron is the highest in human brain as well as in almost all biological organs and metabolic systems. Iron is essential for life and is involved extensively in several vital biological functions, hence, its dysregulation not only leads to major complications but is also considered as the most potential toxin when it gets accumulated in abnormally high concentrations. The number of ROS that are produced in brain also increases with age due to excess iron homeostasis and can have devastating neurological effects since iron is capable to efficiently catalyze the generation of free radicals.[20,21] Although the mechanism of AD pathogenesis is not completely understood, metal ions and the amyloid cascade are the central targets for the development of anti-AD molecules.[22-24] The accumulation and imbalance of iron and other transition metals in the brain over the life span of an individual are also responsible for the generation of reactive oxygen species (ROS) including highly neurotoxic hydrogen peroxide, oxidative stress and free radical formation play key roles in the development of AD, PD, HD, ALS and prion disease.[25,26] Hence, controlling the neurotoxicity would involve the regulation of redox–

active metals accumulating in the brain which in turn would prevent neurological disorders to aggravate further. Recently few metal chelators have been used to diminish metal-mediated Aβ aggregation,[27-33] however, they are reported to be highly nonspecific in biological medium. Since, iron containing metalloprotein detection and activity study is highly important for the pathological screening and therapeutic development, few sensitive and selective reports have been established recently, which include the detection of heme and non-heme iron and their activity study in physiological conditions using conjugated polymer (CP) fluorescence based assays.[34-41] Moreover, few previously reported literatures[13,22-24,32] highlight the application of metal binding ligands and hydroxyquinoline derivatives for anti-AD therapeutics. This has helped us to design PHQ and develop a strategy to clear the cerebral deposits using this conjugated polymer.

2b.2. Results and discussion

2b.2.1. Synthesis of PHQ

The synthesis of polymer PHQ was mentioned and discussed in previous chapter 2a (Scheme 2a.1),[42] PPP-Br (0.1 g, 0.20 mmol) and 8-hydroxyquinoline (0.118 g, 0.816 mmol) were dissolved in dry DMF (15 mL) in the presence of potassium carbonate (197 mg, 1.43 mmol). After 16 h reflux the mixture was filtered, followed by precipitation from methanol. Then, the precipitate was centrifuged and washed repeatedly with methanol. The resulting polymer was dried under reduced pressure to obtain yield 78% as light brown powder. Notably, CP's of PHQ was monitored over long duration in *in vitro* studies and have confirmed to be non-toxic and be able to easily penetrate cell membrane (Figure A2b.1).[43,44]

2b.2.2. Modulating effect of PHQ on amyloid aggregates monitored by Congo red assay

An approach to convert Aβ aggregates into disaggregated forms is a vital procedure to control AD pathogenesis. Several body fluids such as blood serum, urine, saliva, sweat etc., are used as biomarkers in laboratory and clinical examination to monitor a patient's health. Cerebrospinal fluid (CSF) is one of the main pathological biomarkers to study neurological disorders since it is produced in the brain. It has the highest diagnostic potential for the clinical examination of several neurological diseases due to its continuous proximity to the brain and any disorder events occurring in the brain can generally be recognized in CSF, including the early diagnosis and progression of AD, PD and HD.[45-47] Due to these reasons we examined several CSF samples (Table A1) in our experiments to study the presence of Aβ

fibrils and possible metal deposits and further evaluate the role of PHQ in the homeostasis process. On adding 10 mL aliquots of CSF to a solution of PHQ we observed 12% quenching in the fluorescence peak of PHQ (Figure A2b.2a). Several other CSF samples were also titrated with PHQ in a similar way, however, all other samples either showed no quenching or <5% quenching (Figure A2b.2b) and hence the samples having the highest iron content of Aβ fibrils were considered for our experiments and reported. The changes in the photophysical properties of PHQ in the presence of several CSF samples are an indication that metal (iron) aggregated Aβ fibrils are present in varying quantities in the analyzed CSF samples. Further, this CSF sample was confirmed to have Aβ peptide by recording a UV-visible spectrum in the presence of congo red (CR) dye and the thioflavin T (ThT) fluorescence activity test in HEPES buffer. Figure 2b.1a, indicates a significant red shift of 17 nm in the 498 nm absorption peak of the CR solution due to the formation of a complex between the Aβ fibrils (CSF sample) and CR.[48,49] This test confirms the existence of a complex formed between the CR dye and the Aβ fibrils. On addition of 5.0×10^{-5} M PHQ to this CSF–CR complex the red shifted UV-visible peak was blue shifted back to its original position (Figure 2b.1a) of 498 nm due to the disruption of the CR–Aβ complex that is known to be a highly nonspecific complex.[27-33] In a similar way, we performed control experiments with another CSF sample that did not influence the PHQ fluorescence in the spectroscopic experiments. These samples did not induce any spectral shift of the CR dye indicating that these samples lack Aβ fibrils (Figure 2b.1b).

The existence of Aβ fibrils in CSF is characteristic of AD and the onset or existence of numerous other human neurodegenerative disorders. In addition to the spectroscopic data reported above for the confirmation of iron, as well as Aβ fibrils, we have also utilized microscopic techniques to validate their presence in CSF samples. The formation of the CR–Aβ complex was visualized under a polarizable optical microscope (POM) as a bright birefringence (Figure 2b.1c).[48,49] On adding 5 mL aliquots of PHQ solution (1×10^{-5} M) to the preincubated Aβ containing CSF sample the bright birefringence gradually diminished, as shown in figure 2b.1c (i-vi). However, CSF that lacked Aβ fibrils did not show any birefringence under POM in the presence of CR dye due to the nonexistence of any complex formation [Figure 2b.1 (d-f)]. Subsequently, from the spectroscopic experiments we confirmed that PHQ can bind with iron metals in competitive biological environments, therefore, any iron present in the CSF sample can chelate by PHQ via “turn-off” method. Accordingly, selective binding of the toxic metal and breaking the aggregated Aβ peptides, as

confirmed from the disruption of CR–Aβ complex by a nontoxic compound, such as PHQ used in our experiments would facilitate the controlling of the AD pathogenesis.

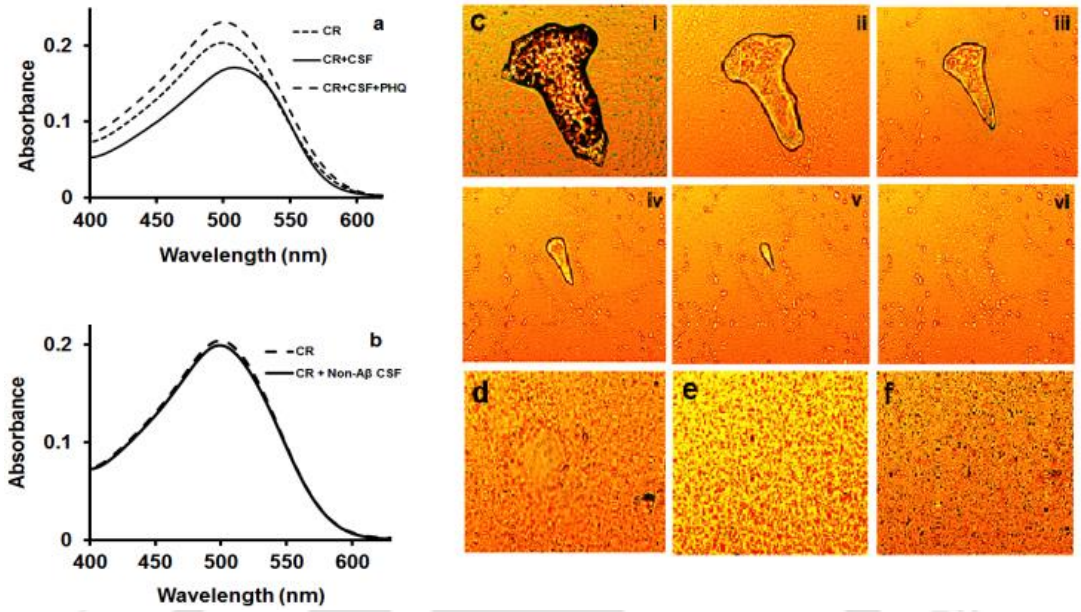

Figure 2b.1 (a) Aβ aggregation was characterised by red shifted in congo red (CR) absorption maximum from 498 nm to 515 nm and blue shifted back to 498 nm on addition of PHQ (10 μM). (b) No shift on adding CSF in CR indicates lack of Aβ fibrils. (c) Birefringence was diminished on addition of PHQ in preincubated Aβ containing CSF from (i-vi). (d-f) No birefringence was observed in CSF that lacked Aβ fibrils.

2b.2.3. Modulating effect of PHQ on amyloid aggregates monitored by ThT assay

The presence of Aβ protofibrils was further confirmed by the addition up to 150 mL of the CSF sample to a 5 μM solution of (thioflavin T) ThT (pH 7.4 in HEPES) to observe a gradual enhancement in the fluorescence intensity of ThT at 488 nm validating strongly the presence of Aβ in the CSF sample (Figure 2b.2a).[50] In figure 2b.2b, the ThT does not show any emission at 488 nm in the absence of Aβ containing peptide sample (dotted line), whereas upon addition of the CSF sample (which present Aβ) into ThT we observe an emission peak at 488 nm (λ_{ex} – 440 nm) (Figure 2b.2a and the solid line of figure 2b.2b) indicating the formation of a complex between the ThT–Aβ. On addition of 10 μM PHQ to this cuvette the 488 nm peak was completely quenched (broken line) indicating that the ThT–Aβ complex is disrupted in the presence of PHQ and the aggregated fibrils are disaggregated in the presence of the polymer PHQ.

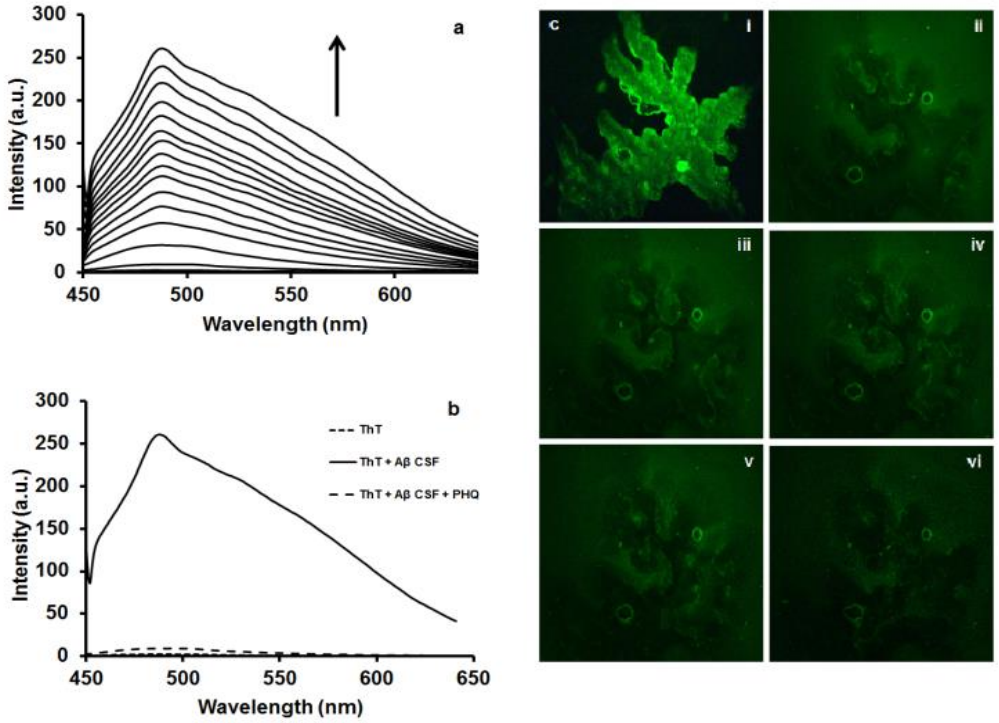

Figure 2b.2 (a) Fluorescence spectra (λ_{ex} 440 nm, λ_{em} 488 nm) of ThT (5 μM) (pH 7.4 in HEPES) with gradual addition of preincubated Aβ containing CSF (150 μL). (b) The ThT dye does not show any emission at 488 nm in the absence of Aβ (dotted line), whereas the ThT-Aβ in CSF complex showed emission peak (solid line) at λ_{em} 488 nm (λ_{ex} 440 nm) and the emission of ThT-Aβ in CSF complex is quenched on adding PHQ (broken line). (c) (i) Bright green fluorescence of preincubated CSF Aβ fibrils with ThT and (ii-vi) Disappearance of bright green fluorescence occur due to the disruption of Aβ fibrils in CSF by PHQ (5 μL).

Further, to confirm the formation of ThT–Aβ complex and its disruption with PHQ were performed by fluorescence microscope as done for the birefringence study. A glass slide containing preincubated Aβ containing CSF sample was observed under a fluorescence microscope after staining it with ThT dye, highly green fluorescence images are appeared (Figure 2b.2c (i)). The observed images depicted that the Aβ fibrils in the CSF and appeared "turn-off" fluorescence upon addition of 5 mL aliquots of PHQ from (1×10^{-5} M) the stock solution to the glass slide (Figure 2b.2c (i-vi)). This disappearance of fluorescence indicates that two events may taken place, first the ThT was displaced from the Aβ fibrils upon addition of PHQ due to the disruption of ThT–Aβ complex and second, due to the possible iron deposits in the CSF sample quenched the PHQ fluorescence by metal chelation, which is corroborated in earlier experiments also, to generate a fluorescence quenching event. This

observation is similar and in agreement to the systematic disappearance of the birefringence observed under the polarizable optical microscope.

2b.2.4. Modulating effect of PHQ on amyloid aggregates monitored by FT-IR spectroscopy

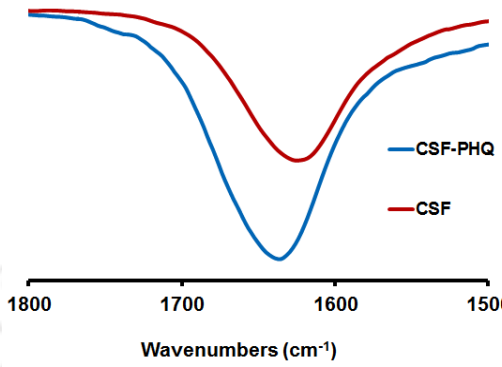

Figure 2b.3 FT-IR spectrum recorded at room temperature for Aβ containing CSF (in absence of polymer PHQ showed a band at 1629 cm^{-1} (red line) and the FT-IR spectrum recorded at room temperature for Aβ containing CSF + PHQ showed an band at 1646 cm^{-1} (blue line) indicating disruption of amyloid β structure.

Fourier-transform infrared (FT-IR) spectroscopy is an extensively used technique to study the Aβ protofibrils structural transformation in biology. These transformations normally happen in the presence of external therapeutic agents or changes in the pH, salt effect, etc. The FT-IR spectrum depicts the presence of a 1629 cm^{-1} band that is assigned to the Aβ protofibrils present in the real CSF sample. Addition of PHQ into the CSF sample resulted in the 17 cm^{-1} shift of this band to approximately 1646 cm^{-1} confirming the structural transformation of the Aβ fibrils into disaggregated form (Figure 2b.3).[51,52]

2b.2.5. Modulating effect of PHQ on Aβ1–40 aggregates monitored by ThT assay

Further, Aβ fibrils disaggregation with polymer PHQ was confirmed by performing a control study using commercially available Aβ1–40 peptides. The abundant fragments of Aβ protofibrils that are considered to be highly neurotoxic and prone to aggregation[53,54] are the Aβ1–40 and Aβ1–42, out of which Aβ1–40 is the most abundant and present in the cerebral cortex of AD patients.[55,56] Aβ1–42 is also associated with the AD development process, but is found to be much less soluble compared to Aβ1–40 and can aggregate into fibril forms faster.[57] Hence, we selected Aβ1–40 for performing the control studies. We utilized various Aβ1–40 and healthy CSF (H-CSF) samples with ThT in the absence and presence of iron and

iron containing metalloproteins that were incubated for 60 h at 37 °C followed by observing the changes in fluorescence (Figure 2b.4 and A2b.3). The fluorescence emission peak at 488 nm of incubated Aβ1–40 with ThT confirms formation of the complex which was found to match with the emission peak observed using Aβ protofibrils containing real CSF samples as a biomarker (Figure A2b.3a and Figure 2b.2b). This important observation proves that Aβ protofibrils were present in the real CSF samples. In addition, we observed that the Aβ1–40 and H-CSF-doped Aβ1–40 samples containing iron or iron containing metalloproteins showed significant fluorescence quenching after adding PHQ (Figure 2b.4c, 2b.4d and A2b.3c, A2b.3d).

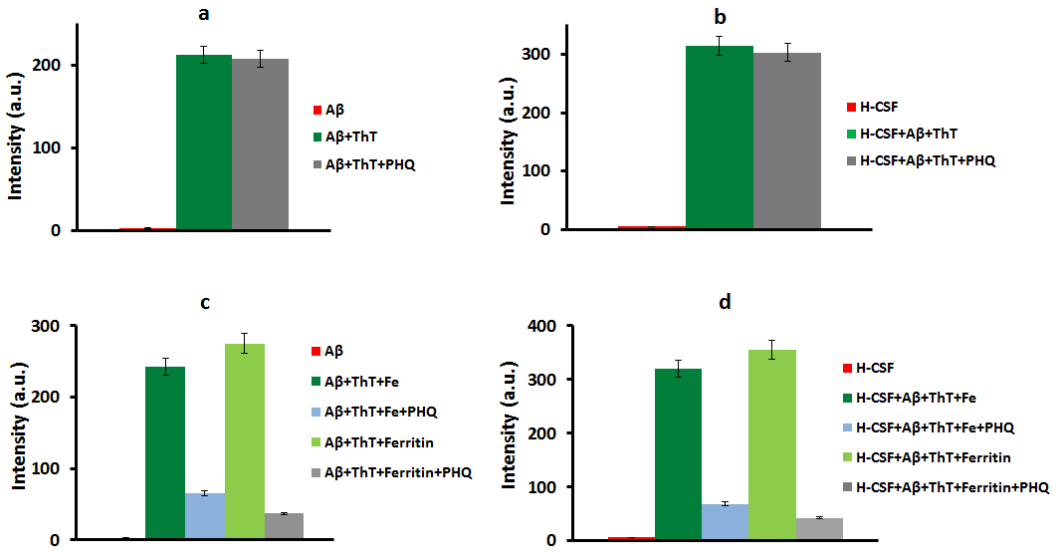

Figure 2b.4 ThT fluorescence changes observed in various incubated samples. (a-d) No enhancement was obtained in Aβ1-40 and H-CSF without ThT. (a) No significant changes was obtained in Aβ1-40 + ThT with PHQ. (b) No significant changes were obtained in H-CSF + ThT with PHQ. (c) Fluorescence changes were obtained in Aβ1-40 + ThT with iron and ferritin, followed by subsequent quenching with PHQ. (d) Fluorescence changes were obtained in H-CSF + Aβ(1-40) + ThT with iron and ferritin, followed by subsequent quenching with PHQ. Excitation and emission values are 440 nm and 488nm (error bars = ± 5%).

This observation further confirms that PHQ can chelate iron by "turn-off" method since the main binding unit of hydroxyquinoline is present in PHQ which are highly selective to iron only. Furthermore, no significant changes were observed after adding PHQ to the non-iron containing samples (Figure 2b.4a and 2b.4b). Further, to confirm that the polymer scaffold is necessary for the efficient disruption of Aβ fibrils, parallel experiments were also performed

using 8-HQ instead of PHQ (Figure A2b.4). The result of ThT fluorescence changes observed by 8-HQ were found to be significantly less, as compared to the presence of polymer PHQ.

2b.2.6. Modulating effect of PHQ on amyloid aggregates monitored by morphology

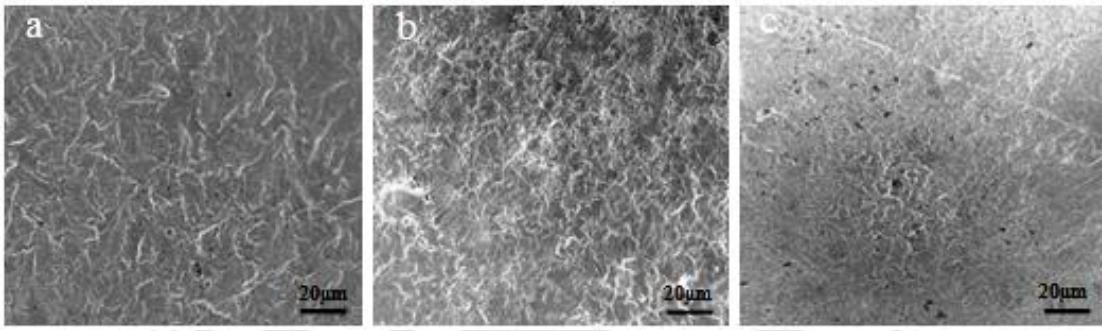

Figure 2b.5 The morphology of Aβ aggregated CSF were analysed by electronic microscopy. (a) CSF (30 µL) sample showed protofibrils after incubation for 12 h at 37 °C. (b) Iron (10 µM) doped CSF (30 µL) sample showed protofibrils after incubation for 12 h at 37 °C. (c) Iron (10 µM) doped CSF (30 µL) sample containing fibrils were disrupted by PHQ (10 µM) after incubation for 12 h at 37 °C.

Disruption of the Aβ protofibrils by PHQ and its morphology changes were analyzed by electron microscopy. The electron microscopic images of figure 2b.5 confirms that Aβ protofibrils were present in the real CSF samples in the absence and presence of iron and that are disrupted by PHQ (Figure 2b.5a, 2b.5b and 2b.5c). Finally, both the samples such as the real CSF sample and *in vitro* iron doped Aβ1–40 fibrils showed a complete structural disruption in the presence of PHQ due to the metal chelation method (Figure 2b.5 and 2b.6). Consequently, the polymer PHQ binds iron existing in ferrous and ferric forms with very high affinity and disrupts the Aβ peptides in the CSF sample, which can significantly reduce the formation of neurotoxic chemicals in the brain and disaggregate the polypeptides. This strategy of removing toxic metals and disaggregating the Aβ aggregates by the PHQ polymer is very important and a conceptually novel strategy for the clearance of the cerebral deposits and control the AD pathogenesis.

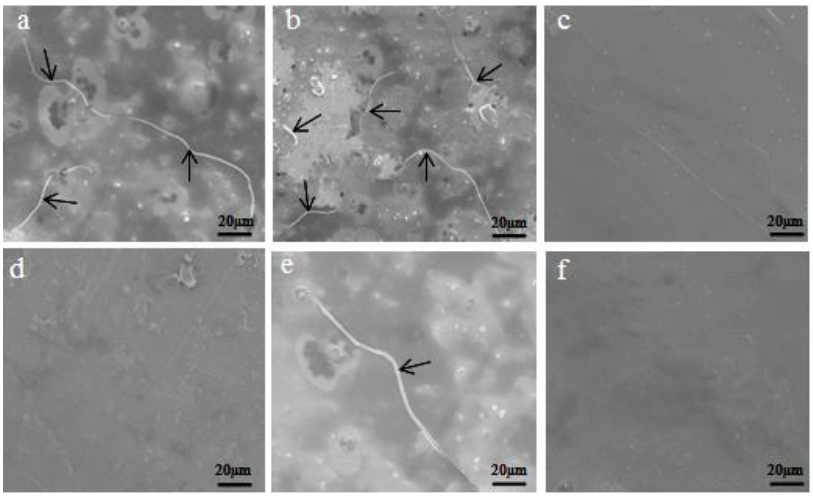

Figure 2b.6 Disruption of Aβ aggregation by PHQ and its morphology changes were analysed by electronic microscopy. (a) Aβ1-40 (30 µM) sample showed mature fibrils after incubation for 12 h at 37 °C. (b) Iron (10 µM) doped Aβ1-40 (30 µM) sample showed mature fibrils after incubation for 12 h at 37 °C. (c) Iron (10 µM) doped Aβ1-40 (30 µM) sample containing fibrils were disrupted by PHQ (10 µM) after incubation for 12 h at 37 °C. (d) No Aβ fibrils were observed in H-CSF (30 µL) sample after incubation for 12 h at 37 °C. (e) Iron (10 µM) doped H-CSF (30 µL) with Aβ1-40 (30 µM) sample showed mature Aβ fibrils after incubation for 12 h at 37 °C. (f) Iron (10 µM) doped H-CSF (30 µL) with Aβ1-40 (30 µM) sample containing fibrils were disrupted in presence of PHQ.

2b.3. Conclusion

In conclusion, conjugated polymer poly(1,4-bis-(8-(8-hydroxyquinoline)-octyloxy)-benzene) (PHQ) has a unique ability to bind inorganic ion Fe^{2+}/Fe^{3+} and ferritin selectively in a competitive biological environment. Hence, PHQ was utilized to interact with the bound iron, in the presence of Aβ peptide aggregates to ultimately disaggregate the accumulated Aβ fibrils. The evaluation of PHQ activity towards toxic metal binding was performed in cerebrospinal fluid since it is a very important biomarker for AD due to its continuous presence and contact with the brain. Hence, therapeutic strategies involving clearance of either the Aβ accumulated in the plaques of brain tissues or removal of metals to reduce neurotoxicity and structurally modifying the aggregates into a disaggregate form. Control studies using a Thioflavin-T binding assay shows that the polymer PHQ can effectively chelate iron from Aβ1–40 and H-CSF-doped Aβ1–40 fibrils due to the presence of hydroxyquinoline as a highly selective metal binding group for iron. Electron microscopy analysis confirms the disruption of Aβ fibrils by PHQ in commercial Aβ1–40, H-CSF-doped

Aβ1–40 and real CSF samples. This conceptually new strategy to clear the cerebral deposits using a conjugated polymer allows us to conclusively proclaim that the aggregated Aβ fibrils present in the CSF could be successfully disrupted and modified into disaggregated forms. This biocompatible nontoxic conjugated polymer system also promises a valuable strategy and novel way for developing AD therapy and may serve as an important macromolecule in improving our understanding of the biology of the aggregated Aβ peptide fibrils and methods to disaggregate the Aβ fibrils.

2b.4. Experimental Section

2b.4.1. Materials and methods

All the reagents and chemicals were purchased from Aldrich Chemicals, Merck or Ranbaxy (India) and used as received. Milli-Q water and HPLC grade solvents were used in all the experiments. Solvents were degassed using three freeze thaw cycles or flushed with nitrogen for at least 1 h prior to use when necessary. β-Amyloid (1-40), human was purchased from GL Biochem Ltd., Shanghai, China. The cerebrospinal fluid (CSF) samples were gifted by Guwahati Neurological Research Center and Hospital, Guwahati, India and were obtained as part of routine care from patients. Nonetheless, information on explaining the purpose of this study was specified at the time of sample collection adhering to the bioethics policy of the hospital.

UV–vis absorption spectra were recorded on a PerkinElmer Lambda–25 spectrometer. Fluorescence spectra were carried out on a Varian Cary Eclipse spectrometer. A 10 × 10 mm quartz cuvette was used for solution spectra and emission was collected at 90° relative to the excitation beam. Leica DM 2500P polarizable optical microscope (POM) was used to image the aggregation and disruption studies. Nikon Eclipse 80i microscope was used to study the fluorescent images. FT–IR spectra were recorded on a PerkinElmer spectrometer with samples prepared as KBr pellets. A fresh glass slide was used for every experiment. Deionized water was obtained from Milli–Q system (Millipore). Images were investigated by scanning electron microscopy (SEM) on a LEO 1430vp instrument operated at 8–10 kV. Field emission scanning electron microscopy (FE-SEM) measurements were made on a Carl Zeiss, SIGMA VP instrument.

2b.4.2. TFA/HFIP treatment of Aβ 1-40 peptides

Aβ 1-40 peptide was disaggregated using trifluoroaceticacid/1,1,1,3,3,3-hexafluor-2-propanol (TFA/HFIP) by established method.[56,58] 0.5 mg of Aβ1-40 was taken in 2.5 mL Eppendorf tube and dissolved in TFA to obtain homogeneous solution free of aggregates. TFA was then

evaporated using argon gas. Any left-over TFA was further removed by adding HFIP followed by evaporation using argon gas flow to obtain a film like material. This process was repeated twice. To the Eppendorf tube, 2.5 mL of HEPES (10 mM, pH 7.4) was added followed by sonication and vortex to obtain a final concentration of 4.6×10^{-4} M. Fibril formation was monitored using ThT binding assay.

2b.4.3. PHQ fluorescence quenching with CSF

PHQ (6.6×10^{-6} M) was mixed with CSF (10 µL) in 3 mL THF: H_2O solution. The emission was recorded at 401 nm, keeping excitation wavelength at 332 nm. Similarly, done for H-CSF (100 µL) with PHQ (6.6×10^{-6} M) in 3 mL THF: H_2O.

2b.4.4. CR binding assay

A 0.2 mM stock solution of CR was prepared in water. The solution was filtered thrice by using 0.2 micron filters before use. The CSF sample (0 to 200 µL) was mixed with CR solution to make the final concentration of 10 µM in a 3 mL solution and then incubated at room temperature for 30 min. The same experiment was repeated in presence of PHQ (5.0×10^{-5} M) and incubated for 30 min. before recording the absorption spectra.

2b.4.5. CR birefringence study

The birefringence images of CSF-CR and CSF-CR with PHQ were observed by Leica DM 2500P microscope.

2b.4.6. ThT binding assay using fluorescence instrument

CSF from 0 to 150 µL was incubated in 10 mM HEPES, pH 7.4 at room temperature with ThT (5 µM) solution for 30 min. The emission was recorded at 488 nm, keeping excitation wavelength at 440 nm.

2b.4.7. ThT fluorescence study using microscope

The incubated CSF-ThT binding assay was examined under Nikon Eclipse 80i microscope and changes were observed after adding PHQ.

2b.4.8. FT-IR spectroscopy

FT-IR spectra were recorded by preparing pellets with KBr. Sample was prepared by spreading 20 µL of CSF solution in the absence and presence of PHQ (1×10^{-5} M) on glass slide and by drying under gentle nitrogen flow.

2b.4.9. Preparation of solutions for control study

Seven different samples of Aβ1-40 (30 µM) were prepared in HEPES buffer solution (10 mM, pH 7.4). HEPES buffer solution was further added to one of the sample to make the

final volume upto 600 µL. ThT (50 µM) was added to the sample II and the final volume was made upto 600 µL in HEPES buffer (10 mM, pH 7.4). Incubation was done by keeping the sample for 60 h at 37 °C in water bath. Other samples III (ThT-50 µM, PHQ-10 µM), IV (ThT-50 µM, Fe-10 µM), V (ThT-50 µM, Fe-10 µM, PHQ-10 µM), VI (ThT-50 µM, Ferritin-5 µM), VII (ThT-50 µM, Ferritin-5 µM, PHQ-10 µM) were also prepared in the same way to make the final volume of 600 µL in HEPES buffer (10 mM, pH 7.4) and kept incubation for 60 h at 37 °C in water bath. These samples were then used to study the changes observed in fluorescence. Similarly, seven different samples of healthy CSF (H-CSF) (30 µL) were prepared using HEPES buffer (10 mM, pH 7.4). HEPES buffer solution was further added to one of the sample to make the final volume upto 600 µL. Aβ1-40 (30 µM) and ThT (50 µM) were added to the II sample, and the final volume was made upto 600 µL in HEPES buffer (10 mM, pH 7.4). Incubation was done by keeping the sample for 60 h at 37 °C in water bath. Other samples III (Aβ1-40 (30 µM), ThT-50 µM, PHQ-10 µM), IV (Aβ1-40 (30 µM), ThT-50 µM, Fe-10 µM), V (Aβ1-40 (30 µM), ThT-50 µM, Fe-10 µM, PHQ-10 µM), VI (Aβ1-40 (30 µM), ThT-50 µM, Ferritin-5 µM), VII (Aβ1-40 (30 µM), ThT-50 µM, Ferritin-5 µM, PHQ-10 µM) were also prepared in the same way to make the final volume of 600 µL in HEPES (10 mM, pH 7.4) and kept incubation for 60 h at 37 °C in water bath. These samples were then studied for the fluorescence changes.

2b.4.10. Cytotoxicity of PHQ measured by MTT assay

Cytotoxicity of PHQ was assessed by the method described previously.[59] In brief, 10^5 MCF-7 cells were treated with different concentration of PHQ (0-10µM) in complete media (RPMI 1640 + 10% serum) for 48 h at 37 °C. Cells were washed with PBS and viability was assessed by MTT assay. Cells treated with DMSO that is considered as control and used to calculate the viability of PHQ treated cells. The toxicity of PHQ toward fast growing breast cancer MCF-7 shows no reduction of cellular viability upto 10 µM in a 48 h exposure period (Figure A2b.3). The solubility of PHQ in aqueous solvent system limits us to test higher concentrations. In conclusion, PHQ has no negative effect on the growth of proliferative MCF-7 cells.

References

(1) Sayre, L. M.; Perry, G.; Smith, M. A. *Curr. Opin. Chem. Biol.*, **1999,** *3*, 220.

(2) Holtzman, D. M.; Morris, J. C.; Goate, A. M. *Sci. Transl. Med.,* **2011,** *3*, 77.

(3) Blennow, K.; Leon, M. J. D.; Zetterberg, H. *Lancet.,* **2006,** *368*, 387.

(4) Mattson, M. P. *Nature.*, **2004,** *430*, 631.

(5) Ni, C. L.; Shi, H. P.; Yu, H. M.; Chang, Y. C.; Chen, Y. R. *FASEB J.*, **2011,** *25*, 1390.

(6) Opazo, C.; Huang, X.; Cherny, R. A.; Moir, R. D.; Roher, A. E.; White, A. R.; Cappai, R.; Masters, C. L.; Tanzi, R. E.; Inestrosa, N. C.; Bush, A. I. *J. Biol. Chem.*, **2002,** *277*, 40302.

(7) Ciccotosto, G. D.; Tew, D.; Curtain, C. C.; Smith, D.; Carrington, D.; Masters, C. L.; Bush, A. I.; Cherny, R. A.; Cappai, R. Barnham, K. J. *J. Biol. Chem.*, **2004,** *279*, 42528.

(8) Boldron, C.; Auwera, I. V.; Deraeve, C.; Gornitzka, H.; Wera, S.; Pitié, M.; Leuven, F. V.; Meunier, B. *ChemBioChem,* **2005,** *6*, 1976.

(9) Cherny, R. A.; Legg, J. T.; McLean, C. A.; Fairlie, D. P.; Huang, X.; Atwood, C. S.; Beyreuther, K.; Tanzi, R. E.; Masters, C. L.; Bush, A. I. *J. Biol. Chem.*, **1999,** *274*, 23223.

(10) Lee, J. Y.; Friedman, J. E.; Angel, I.; Kozak, A.; Koh, J. Y. *Neurobiol. Aging,* **2004,** *25*, 1315.

(11) Pike, C. J.; Walencewicz, A. J.; Glabe, C. G.; Cotman, C. W. *Brain Res.*, **1991,** *563*, 311.

(12) Lorenzo, A. Yankner, B. A. *Proc. Natl. Acad. Sci., U.S.A.*, **1994,** *91*, 12243.

(13) Deraeve, C.; Pitié, M.; Mazarguilb, H.; Meunierz, B. *New J. Chem.,* **2007,** *31*, 193.

(14) Hartley, D. M.; Walsh, D. M.; Ye, C. P.; Diehl, T.; Vasquez, S.; Vassilev, P. M.; Teplow, D. B.; Selkoe, D. J. *J. Neurosci.*, **1999,** *19*, 8876.

(15) Lambert, M. P.; Barlow, A. K.; Chromy, B. A.; Edwards, C.; Freed, R.; Liosatos, M.; Morgan, T. E.; Rozovsky, I.; Trommer, B.; Viola, K. L.; Wals, P.; Zhang, C.; Finch, C. E.; Krafft, G. A.; Klein, W. L. *Proc. Natl. Acad. Sci., U.S.A.*, **1998,** *95*, 6448.

(16) Townsend, M.; Shankar, G. M.; Mehta, T.; Walsh, D. M.; Selkoe, D. J. *J. Physiol.*, **2006,** *572*, 477.

(17) Walsh, D. M.; Selkoe, D. J. *J. Neurochem,* **2007,** *101*, 1172.

(18) Klein, W. L.; Krafft, G. A.; Finch, C. E. *Trends Neurosci.*, **2001,** *24*, 219.

(19) Kumar, S.; Walter, J. *Ageing,* **2011,** *3*, 803.

(20) Yagi, K.; Ishida, N.; Komura, S.; Ohishi, N.; Kusai, M. Kohno, M. *Biochem Biophys. Res. Commun.*, **1992,** *183*, 945.

(21) Kepp, K. P.; *Chem. Rev.*, **2012,** *112*, 5193.

(22) Hureau, C.; Sasaki, I.; Gras, E.; Faller, P. *ChemBioChem* **2010,** *11*, 950.

(23) Rodriguez, C.; Telpoukhovskaia, M.; Orvig, C. *Coord. Chem. Rev.*, **2012,** *256*, 2308.

(24) Scott, L. E.; Orvig, C. *Chem. Rev.*, **2009,** *109*, 4885.

(25) Donnor, J. R. in Metals and oxidative damage in neurological disorders, New York: Plenum Press, **1997**.

(26) Christen, Y. *Am. J. Clin. Nutr.*, **2000,** *71*, 621S.

(27) Cuajungco, M. P.; Fagét, K. Y.; Huang, X.; Tanzi, R. E.; Bush, A. I.; Tanzi, R. E. Bush, A. I. *Ann. N Y Acad. Sci.*, **2000,** *920*, 292.

(28) Bush, A. I. *Trends Neurosci.*, **2003,** *26*, 207.

(29) Rauk, A. *Chem. Soc. Rev.* **2009,** *38*, 2698.

(30) Jakob-Roetne, R.; Jacobsen, H. *Angew. Chem., Int. Ed.* **2009,** *48*, 3030.

(31) Braymer, J. J.; Choi, J.-S.; DeToma, A. S.; Wang, C.; Nam, K.; Kampf, J. W.; Ramamoorthy, A.; Lim, M. H. *Inorg. Chem.*, **2011,** *50*, 10724.

(32) Deraeve, C.; Boldron, C.; Maraval, A.; Mazarguil, H.; Gornitzka, H.; Vendier, L.; Pitie, M.; Meunierz, B. *Chem. Eur. J.*, **2008,** *14*, 682.

(33) Gouras, G. K.; Beal, M. F. *Neuron.*, **2001,** *3*, 641.

(34) Fan, C.; Plaxco, K. W.; Heeger, A. J. *J. Am. Chem. Soc.*, **2002,** *124*, 5642.

(35) Sandanaraj, B. S.; Demont, R.; Aathimanikandan, S. V.; Savariar, E. N.; Thayumanavan, S. *J. Am. Chem. Soc.*, **2006,** *128*, 10686.

(36) Dwivedi, A. K.; Prasad, K. M.; Trivedi, V.; Iyer, P. K. *ACS Appl. Mater. Interfaces.*, **2012,** *4*, 6371.

(37) Zako, T.; Sakono, M.; Kobayashi, T.; Sörgjerd, K.; Nilsson, K. P. R.; Hammarström, P.; Lindgren, M.; Maeda, M. *ChemBioChem* **2012,** *13*, 358.

(38) Bricks, J. L.; Kovalchuk, A.; Trieflinger, C.; Nofz, M.; Büschel, M.; Tolmachev, A. I.; Daub, J.; Rurack, K. *J. Am. Chem. Soc.*, **2005,** *127*, 13522.

(39) Qin, C.; Cheng, Y.; Wang, L.; Jing, X.; Wang, F. *Macromolecules*, **2008,** *41*, 7798.

(40) Dwivedi, A. K.; Saikia, G.; Iyer, P. K. *J. Mater.Chem.*, **2011,** *21*, 2502.

(41) Saikia, G.; Iyer, P. K. *Macromolecules*, **2011,** *44*, 3753.

(42) Muthuraj, B.; Hussain, S.; Iyer, P. K. *Polym. Chem.* **2013,** *4*, 5096.

(43) Rahim, N. A. A.; McDaniel, W.; Bardon, K.; Srinivasan, S.; Vickerman, V.; So, P. T. C.; Moon, J. H. *Adv. Mater.*, **2009,** *21*, 3492.

(44) Zhu, C.; Liu, L.; Yang, Q.; Lv, F.; Wang, S. *Chem. Rev.*, **2012,** *112*, 4687.

(45) Blennow, K.; Hampel, H. *Lancet Neurol.*, **2003,** *2,* 605.

(46) Blennow, K.; Hampel, H.; Weiner, M.; Zetterberg, H. *Nat. Rev. Neurol.*, **2010,** *6,* 131.

(47) Peter, S.; Carmen, V.; Fred, E.; Michael, L.; Harry, D.; Dave, D.; Sukanto, S.; Michael, S.; Justine, W.; Cathy, S.; Robert, M.; Robert, W.; Dennis, S.; Ivan, L.; Schenk, D. *Nature.*, **1992,** *359,* 325.

(48) Klunk, W. E.; Jacob, R. F.; Mason, R. P. *Anal. Biochem.*, **1999,** *266,* 66.

(49) Benditt, E. P.; Eriksen, N.; Berglund, C. *Proc. Natl. Acad. Sci., U.S.A.*, **1970,** *66,* 1044.

(50) Bolder, S. G.; Sagis, L. M.; Venema, P. Linden, E. V. D. *Langmuir.*, 2007, *23,* 4144.

(51) Cordeiro, Y.; Kraineva, J.; Suarez, M. C.; Tempesta, A. G.; Kelly, J. W.; Silva, J. L.; Winter, R.; Foguel, D. *Biophys. J.*, **2006,** *91,* 957.

(52) Zandomeneghi, G.; Krebs, M. R. H.; McCammon, M. G. Fändrich, M. *Protein Science.*, **2004,** *13,* 3314.

(53) Bitan, G.; Kirkitadze, M. D.; Lomakin, A.; Vollers, S. S.; Benedek, G. B. Teplow, D. B. *Proc. Natl. Acad. Sci., U.S.A.*, **2003,** *100,* 330.

(54) Rauk, A. *Chem. Soc. Rev.*, **2009,** *38,* 2698.

(55) Mori, H.; Takio, K.; Ogawara, M.; Selkoe, D. J. *J. Biol Chem.*, **1992,** *24,* 17082.

(56) Hortschansky, P.; Schroeckh, V.; Christopeit, T.; Zandomeneghi, G.; Fändrich, M. *Protein Science*, **2005,** *14,* 1753.

(57) Caughey, B.; Lansbury, P. T. *Annu. Rev. Neurosci.*, 26, 267.

(58) Chen, S.; Wetzel, R. *Protein Science,* **2001,** *10,* 887.

(59) Deshmukh, R. Trivedi, V. *Toxicol. In Vitro* **2013,** *27,* 16.

Appendix

Table A1. Data of analyzed CSF samples of subjects obtained from GNRC, Guwahati, India.

S. No	Sample	Age	Sex
1	Non healthy CSF (Aβ)	45	F
2	Non healthy CSF (Aβ)	40	M
3	Non healthy CSF (Aβ)	42	M
4	Healthy CSF (non-Aβ)	32	M
5	Healthy CSF (non-Aβ)	36	M
6	Healthy CSF (non-Aβ)	52	M
7	Healthy CSF (non-Aβ)	46	F
8	Healthy CSF (non-Aβ)	48	M
9	Healthy CSF (non-Aβ)	44	M
10	Healthy CSF (non-Aβ)	40	F
11	Healthy CSF (non-Aβ)	33	M
12	Healthy CSF (non-Aβ)	42	M
13	Healthy CSF (non-Aβ)	32	M
14	Healthy CSF (non-Aβ)	45	F
15	Healthy CSF (non-Aβ)	51	M
16	Healthy CSF (non-Aβ)	37	M
17	Healthy CSF (non-Aβ)	42	M
18	Healthy CSF (non-Aβ)	46	F
19	Healthy CSF (non-Aβ)	32	M
20	Healthy CSF (non-Aβ)	40	M

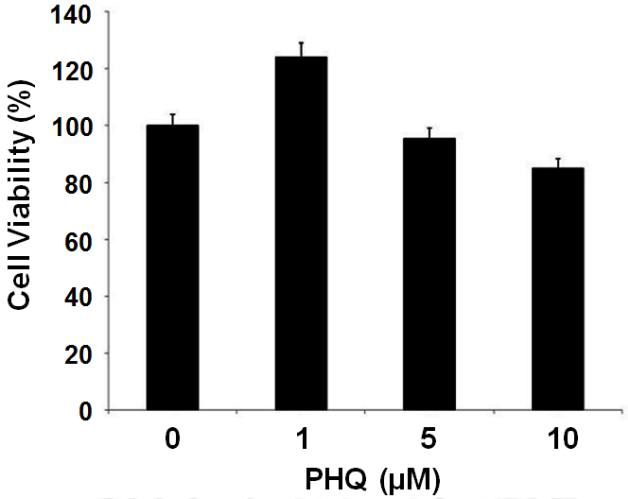

Figure A2b.1 Cell viability of PHQ by MTT assay.

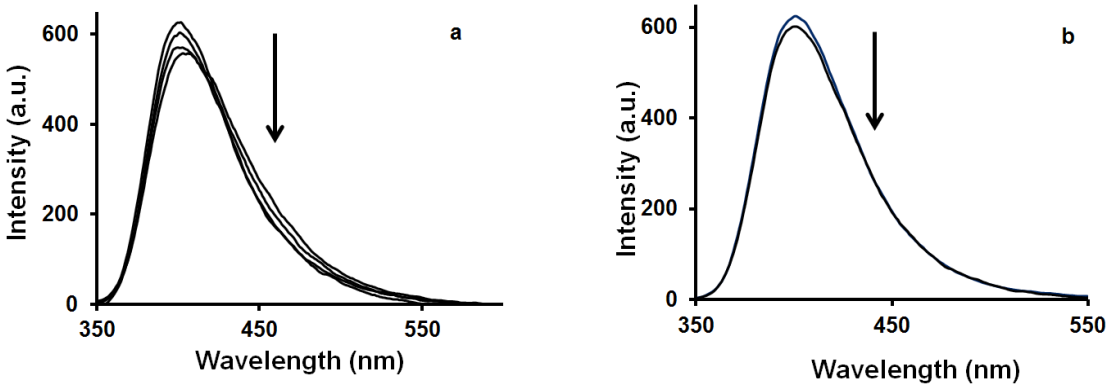

Figure A2b.2 (a) Gradual reduction in fluorescence intensity (12%) of PHQ (6.6 μM) occurred upon addition of upto 10 μL CSF. (b) No quenching of PHQ (6.6 μM) occurred upon addition of CSF upto 100 μL indicating these samples lack iron.

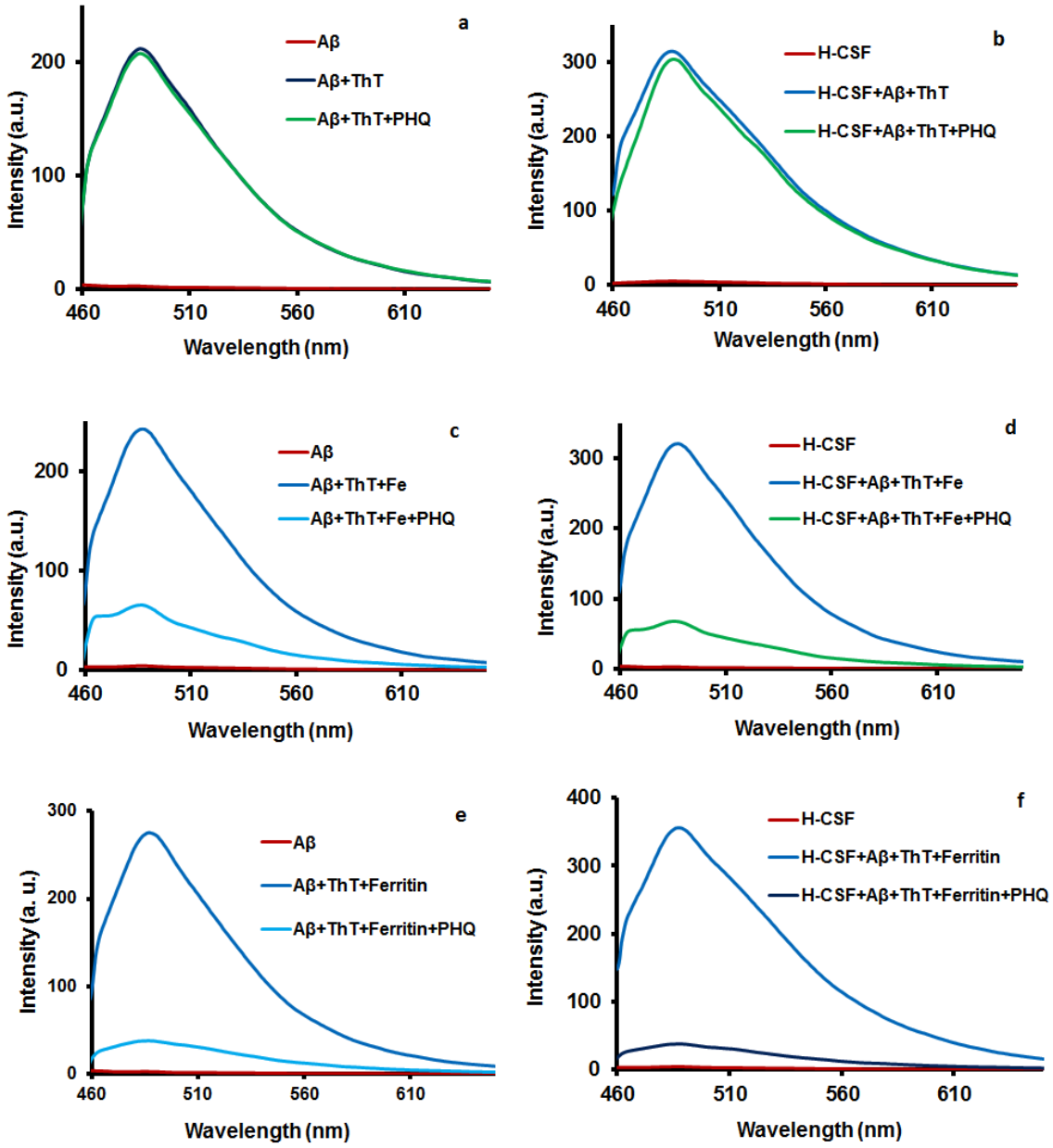

Figure A2b.3 ThT fluorescence changes were observed in various incubated samples. No enhancement was observed in Aβ1-40 and H-CSF without ThT (a) No significant changes was observed in Aβ1-40 + ThT with PHQ. (b) No significant changes was observed in H-CSF + ThT with PHQ. (c, e) Flourescence enhancement was observed in Aβ1-40 + ThT with iron and ferritin, followed by subsequent quenching was observed with PHQ. (d, f) Flourescence enhancement was observed in H-CSF + Aβ1-40 + ThT with iron and ferritin, followed by subsequent quenching was observed with PHQ. Excitation and emission values are 440 nm and 488 nm respectively.

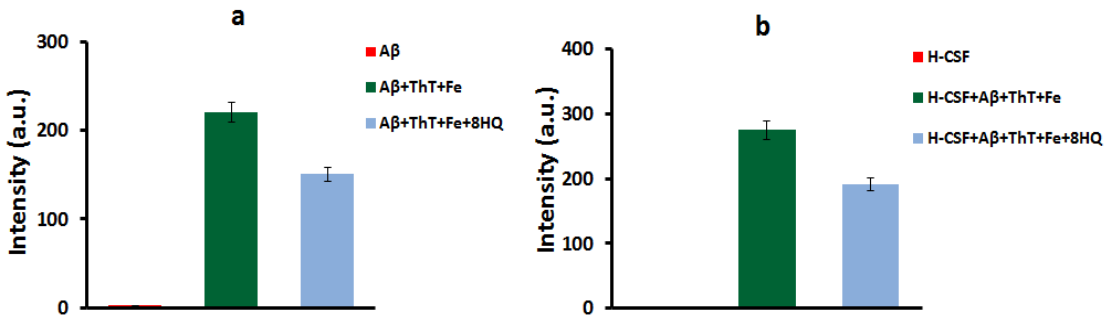

Figure A2b.4 ThT fluorescence changes were observed in various incubated samples. No fluorescence enhancement was obtained in Aβ1-40 and H-CSF without ThT. (a) Fluorescence enhancement was observed in Aβ1-40 + ThT with iron (10 µM), followed by subsequent quenching was observed with 8-HQ (100 µM) (b) Fluorescence enhancement was observed in H-CSF + Aβ1-40 + ThT with Fe (10 µM), followed by subsequent quenching was observed with 8-HQ (100 µM) (error bars = ± 5%).

Chapter: 3a

Amplified Fluorescence from Polyfluorene Nanoparticles with Aggregation Induced Enhanced Emission: Multifunctional Role as Cobalt, Vitamin B_{12} Sensor and Living Cell Imaging

Abstract

A new polyfluorene derivative comprising pendant di(2–picolyl)amine (PF–DPA) was designed and utilized for the detection of Co^{2+} and vitamin B_{12} (VB_{12}), cancer theranostics and cell imaging via aggregation induced enhanced emission (AIEE). Upon coordination with Co^{2+}, the fluorescence of PF–DPA was quenched by ~98% at low concentrations (0.33 μM). Further, the PF–DPA was utilized for the selective detection of vitamin B_{12}, a cobalt containing biological macrocycle. The limit of detection (LOD) calculated for Co^{2+} and VB_{12} from the 3σ/k equation was found as 3.83×10^{-7} M and 4.9×10^{-6} M respectively. PF–DPA showed highly biocompatible up to 1.6 mg/mL in normal cells but shows potent cytotoxicity against cancer cell in higher doses (>80 μg/mL) enhanced its utility for cancer theranostics. PF–DPA, exhibits a large and unique red shifted enhanced emission at 556 nm in higher water ratio of THF: H_2O (1:9) due to the formation of polymer nanoparticles or PDots by intra and intermolecular self–assembly induced aggregation phenomenon. AIEE in PF–DPA homopolymer nanoparticles is fundamentally very unique and attributed to the combined effect of intramolecular planarization and J–type aggregate formation in the nanoparticles (20 ± 5 nm). Therefore, the PF–DPA PDots showed exceptional live cell imaging applications, exhibiting bright green and red fluorescence.

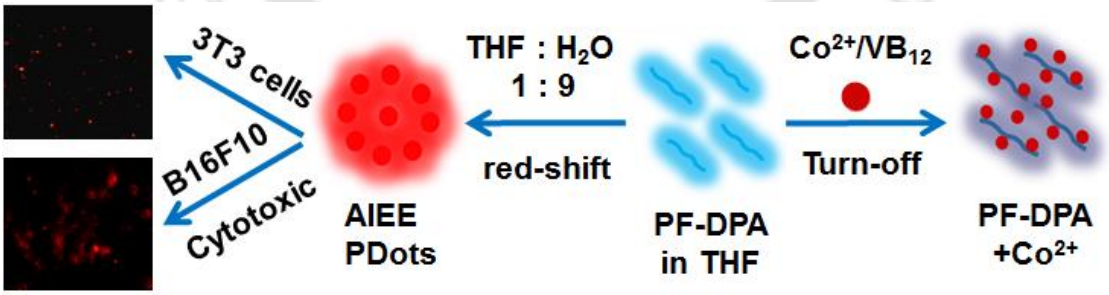

3a.1. Introduction

It is well–known that Co^{2+} is one of the most important transition metal ion have vital roles in the metabolism of iron, synthesis of hemoglobin and also as a main composition of vitamin B_{12} including other biological compounds.[1-3] Vitamin B_{12} is widely responsible for the production of red blood cells (4.35%) and the prevention of pernicious anemia.[4] It appears in almost all multicellular organisms, such as in liver, bones and kidneys.[1,5] The deficiency of cobalt in human body leads to unlikely pathological conditions whereas in excess it can be a significant environmental pollutant.[6] Deficient natural levels of cobalt in feed causes deficiency diseases characterized by pernicious anemia, weight loss or retarded growth and is one of the main risk factors for cardiovascular diseases.[7,8] However, at high concentrations in body, cobalt is toxic and has been reported to produce pulmonary disorders, dermatitis, nausea, vomiting, diarrhea, blood pressure, slowed respiration, giddiness cardiomyopathy, hyperglycemia and so on.[8] The maximum recommended concentration of toxic ions such as cobalt in drinking water for livestock is 1.0 mg L^{-1}.[8]

In recent years, there has been a growing interest in the development of selective Co^{2+} sensors for biological and environmental applications. Therefore, investigation on developing new fluorophores for the sensitive detection of Co^{2+} is highly important yet remains a huge challenge because it occurs in nature along with other metals such as copper, nickel, manganese and arsenic. Hence, designing receptor and sensor systems specific for Co^{2+} has resulted in poor selectivity. The development of fluorescent sensors for Co^{2+}, must involve a specific fluorescence sensing probe consisting of a fluorophore (signaling moiety) linked to a receptor (recognition moiety), called as fluoroionophore or probe.[9-10] The recognition process takes place in receptor part of the probe that is then converted to a change in the fluorophore's signal, brought about by the perturbation of such photoinduced processes as energy transfer, charge transfer, electron transfer, formation or disappearance of excimers and exciplexes.[9-12] In recent years, very few small molecule based fluorescence sensors have been developed and reported for the detection of cobalt metal ions,[11, 13-19] however, to the best of our knowledge, no reports for the detection of cobalt metal ions or vitamin B_{12} by any polymer based platform that are known for their high sensitivity exists.

The development of fluorophores for sensing and imaging applications mainly utilized, based on small molecule dyes, quantum dots and nanoparticles. Many fluorescent dyes[20,21] are widely used for applications in living cell fluorescent bioimaging experiments because of their small size and biocompatibility. Yet, poor photo stability of these probes and leakage of

heavy metals in quantum dots limits their broad applicability in long–term monitoring of live cells. Hence, there is a great need to develop probes for bioimaging that are simple, nontoxic and can provide high sensitivity. Conjugated polymers (CPs) are attractive materials which could fulfil the suitable optical requirements for fluorescence microscopic imaging.[22,23] CPs are known to have high fluorescence quantum yield, large extinction coefficients, efficient optical signal transduction and synthetic versatility of CPs allows a wide selection of functional groups for biological applications.[23] Herein, we introduce a new fluorescent CP that is capable of fluorescence imaging of living cells due to its multicolor imaging ability in aqueous media. Consequently, the multicolor fluorescent imaging occurs in living cells due to the formation of conjugated polymer nanoparticles (CNPs) also known as semiconducting polymer dots (PDots).[24-30] The PDots exhibit strongly enhanced fluorescence emission, which are attributed to the combined effect of planarization and J–aggregation due to the aggregation induced emission enhancement (AIEE) phenomenon.[31]The propeller–shaped molecules and CPNs exhibit the phenomenon of aggregation induced emission (AIE), due to the restriction of the intramolecular rotation (RIR) of the multiple phenyl rotors in the aggregate state.[32] The tetraphenylethylene and silole fluorophores have attracted enormous attention in chemo– and biosensing, imaging and therapy since they emit strong fluorescence in the aggregated state due to which they have been incorporated into polymers and macromolecules either as a pendant or as a copolymerizing unit.[33-37] Therefore, the development of bright multicolor fluorescent PDots with AIEE properties remains interesting for widespread biological applications and cancer research. However, the use of highly specific AIEE fluorogens, expensive multistep synthesis involving expensive catalysts and purification steps, limits their practical utility. To encompass the benefits of AIEE effect at the same time reduce the overall reaction economy, alternate structures overcoming the drawbacks in existing systems are required. We present here a polyfluorene (PF) homopolymer appended with a flexible di(2–picolyl)amine pendant unit on the PF side chains (PF–DPA) that spontaneously displays AIEE phenomenon (in contrast to blue emitting polyfluorene). This PF–DPA has no restricted rotation in organic solvent (THF) whereas, at higher water ratio the RIR behavior likely dominates, resulting in bright and remarkable red shifted enhanced emission.

3a.2. Results and discussion

To construct heterocyclic molecules such as di(2–picolyl)amine (DPA) based chemo– and biosensors, they can be functionalized directly with various fluorophores. The secondary

amine nitrogen atom of DPA serves as an excellent reaction site to be linked with various fluorophores and an effective signal transduction responds to the binding events through PET or ICT mechanisms. Generally, the optimum spacer length between the fluorophore and receptor is less than three–carbon linker, which can guarantee the maximum efficiency for PET. Here, we present that DPA could perform exceptionally selective sensing of Co^{2+} due to the longer spacer unit allowing no interactions between receptor lone pair and the fluorophore. This unique strategy also has advantages of avoiding the use of additional encapsulation of dyes or blending NIR materials with the probe to generate a cascade FRET effect. In addition, the presence of DPA also facilitates in realizing aggregation induced enhanced emission (AIEE) phenomenon which has never been observed in normal PF molecules substituted with linear alkyl chains.[38] The presence of this DPA molecule on the polymer pendant chain restricts the intramolecular rotation (RIR) in higher water/buffer ratio (THF: H_2O, 1:9) that results in bright red shifted emission from the polymer PF–DPA due to the AIEE effect. This bright red emission served as a motivation to utilize this probe in cellular imaging and cancer therapeutics.

3a.2.1. Synthesis of monomer

Synthesis of 9,9-Bis-(6-bromohexyl)-fluorene. Fluorene (4 gm, 24.064 mmol), 50% aq. NaOH and a catalytic amount of tetrabutylammonium iodide (1.7 gm, 3.248 mmol) were added to a flask. The flask was degassed 3 times by applying freeze-thaw cycles. 1, 6 dibromohexane (35.22 gm, 215.13 mmol) was added through a syringe (degassed) and the mixture stirred continuously for 4 h at 70 °C (Scheme 3a.1).[39-42] Further, the reaction mixture was cooled to room temperature and extracted with chloroform. The organic layer was washed with water and dried over anhydrous sodium sulfate. The solvent was removed under vacuum and the crude was purified using column chromatography over a small pad of silica gel using pure hexane as an eluent to give the desired fluorene dialkylated product. Yield = 3.68 g (92 %). ^{1}H NMR (400 MHz, $CDCl_3$): δ (ppm): 7.68 (m, 2H), 7.28 (m, 6H), 3.26 (t, 4H), 1.96 (m, 4H), 1.63 (m, 4H), 1.17 (m, 4H), 1.07 (m, 4H), 0.60 (m, 4H). ^{13}C NMR (150 MHz, $CDCl_3$) δ (ppm): 150.50, 141.32, 127.29, 127.05, 122.95, 119.92, 55.10, 40.42, 34.12, 32.83, 29.23, 27.95, and 23.71.

3a.2.2. Synthesis of PF-Br

In a 100 mL three-necked round-bottom flask equipped with a nitrogen inlet, anhydrous ferric chloride (2.25g, 13.86 mmol) was dissolved in 20 mL of nitrobenzene. 9,9-Bis-(6-bromohexyl)-fluorene (1.0 g, 6.09 mmol) dissolved in 15 mL of nitrobenzene was added to

the flask using a syringe. The reaction mixture was stirred at room temperature for 36 h, followed by precipitation from methanol (Scheme 3a.1).[39-42] Further the precipitates were stirred for 1 h, then centrifuged and washed repeatedly with methanol. The resulting polymer was dried under reduced pressure to obtain 1.39 g (70%) as dark brown powder. ^{1}H NMR (400 MHz, $CDCl_3$), δ (ppm): 7.65-7.79 (ArH, broad), 7.33 (ArH, broad), 3.26 (broad), 2.02 (broad), 1.54 (broad), 1.23 (broad), 0.78 (broad). ^{13}C NMR (150 MHz, $CDCl_3$) δ (ppm): 151.68, 141.30, 127.29, 127.04, 122.94, 119.91, 40.41, 34.15, 32.82, 31.13, 29.25, 27.95, and 23.86. $M_w = 2.04 \times 10^4$, PDI = 1.95 (GPC in THF, polystyrene standard).

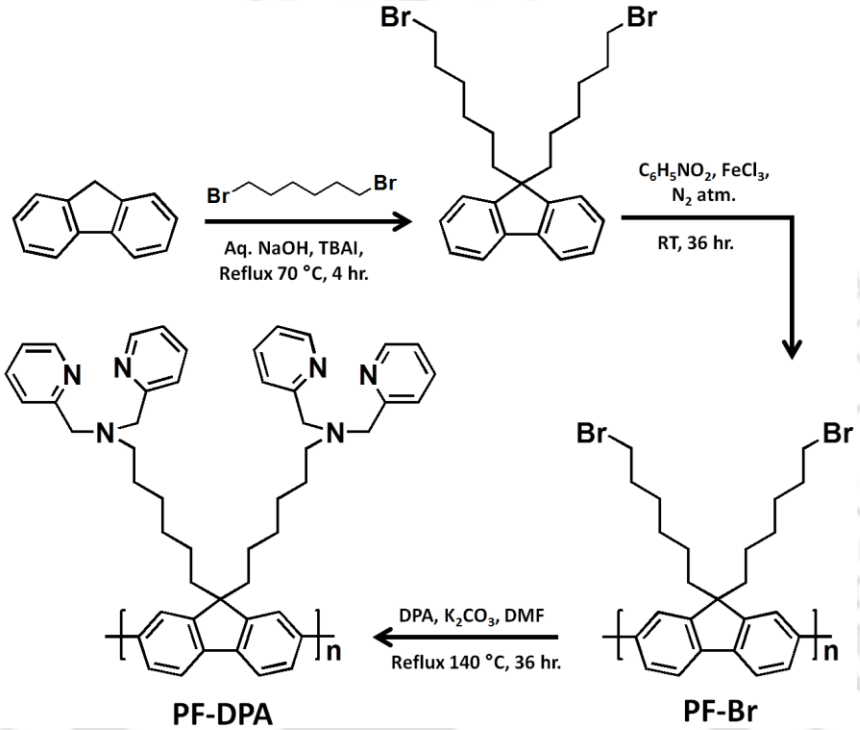

Scheme 3a.1 Synthesis of PF-DPA.

3a.2.3. Synthesis of PF-DPA

Polymer PF-Br (67 mg), di(2-picolyl)amine (DPA) (60 mg, 0.3 mmol), potassium carbonate (70 mg, 0.5 mmol) were mixed and heated at 150 °C for 36 h in dry DMF (Scheme 3a.1).[39-42] The mixture was cooled to room temperature and poured into methanol (100 mL). The brown precipitant was collected and washed with acetone and dried overnight in a vacuum desiccator (68 mg, 86.8%). ^{1}H NMR (600 MHz, $CDCl_3$), δ (ppm) : 8.46 (ArH, broad), 7.80 (ArH, broad), 7.65 (ArH, broad), 7.56 (ArH, broad), 7.43 (ArH, broad), 7.32 (ArH, broad), 7.07 (ArH, broad), 3.70 (–NCH_2–), 2.39 (–CH_2-N–, broad), 2.04 (–CH_2–, broad), 1.35 (–CH_2–, broad), 1.10 (–CH_2–, broad), 1.03 (–CH_2–, broad), 0.74 (–CH_2, broad). ^{13}C NMR (150 MHz, $CDCl_3$) δ (ppm): 160.40, 151.43, 149.02, 139.55, 136.48, 125.76, 122.99, 121.99,

121.46, 120.31, 114.26, 60.60, 54.53, 40.44, 34.01, 32.11, 29.55, 27.20, and 22.88. UV-vis (THF: H_2O (9: 1), 5.0 × 10^{-6} mol L^{-1}): max (nm): 370; Emission (THF: H_2O (9: 1), 0.33 × 10^{-6} mol L^{-1}): 412 nm. M_w = 2.96 × 10^4, PDI = 1.43 (GPC in THF, polystyrene standard).

3a.2.4. Selective detection of cobalt ion

The quantitative evaluation of fluorescence quenching and the PF–DPA–Co^{2+} binding efficiency was measured by the fluorescence intensities of PF–DPA (0.33 × 10^{-6} mL^{-1}) in the presence of different concentrations of Co^{2+} ions. As shown in figure 3a.1a, the fluorescence intensity at 412 nm was quenched rapidly upon the addition of Co^{2+} ions. At 0.33 × 10^{-6} mL^{-1} concentration of Co^{2+}, nearly no significant fluorescence could be observed due to the formation of a complex between the pendant DPA and Co^{2+} ions (Scheme 3a.2). These results indicate that the receptor di(2–picolyl) amine linked to the polymer side chains via carbon spacer, could efficiently transfer the energy from the CP backbone to the Co^{2+} ions, leading to the instant quenching of the strong luminescence of PF–DPA by the general electron transfer (ET) mechanism.[43] The quenching efficiency was nearly fit to the Stern–Volmer equation, $I_0/I = K_{SV}[Q] + 1$, which related the fluorescence intensity, I, at different concentrations of analyte quencher, [Q], where I_0 was the intensity at [Q] = 0, and K_{SV} was the Stern–Volmer constant. According to the fluorescence titration of PF–DPA with Co^{2+}, K_{SV} was determined to be 5.2 × 10^6 M^{-1} at lower concentrations (Figure A3a.1). The K_{SV} which provides a direct measure of the quenching sensitivity for Co^{2+} (Figure A3a.1), clearly indicates the formation of super linear behavior due to a sphere of action mechanism.[44,45] The limit of detection (LOD) was calculated to be 3.83 × 10^{-7} M for Co^{2+} by 3σ/k equation.[46] Further, the interaction of PF–DPA (0.33 μM) with different metal salts such as Co^{2+}, Cr^{3+}, Mn^{2+}, Fe^{2+}, Fe^{3+}, Ni^{2+}, Cu^{2+}, Zn^{2+}, Cd^{2+}, Pb^{2+} and Hg^{2+}, with the concentrations of 0.33 × 10^{-6} mL^{-1} in THF: H_2O (9:1) solution (HEPES buffer, pH 7.4) were carried out at room temperature and the changes were recorded in the fluorescence peak of PF–DPA at 412 nm (Figure 3a.1b). Negligible or no fluorescence intensity changes were observed for PF–DPA in the presence of all other metal ions due to the poor coordination ability of the DPA with these ions confirming its exclusive selectivity for Co^{2+} (Figure 3a.1b).

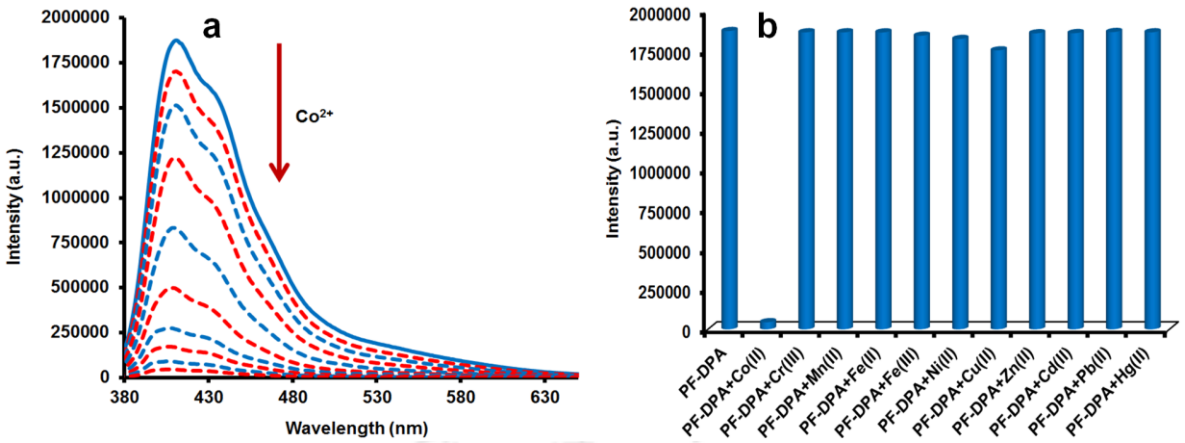

Figure 3a.1 (a) Fluorescence quenching spectra of PF–DPA (0.33 µM) in the presence of different concentrations of Co^{2+} (0–0.33 µM) in THF: H_2O (9:1), (HEPES buffer, pH 7.4), λ_{ex} = 355 nm, λ_{em} = 412 nm. (b) Bar diagram indicates that the fluorescence changes of PF–DPA (0.33 µM) observed at 412 nm in presence of various metal ions (0.33 µM). THF: H_2O (9:1), (HEPES buffer, pH 7.4); λ_{ex}= 355 nm, λ_{em} = 412 nm.

3a.2.5. Morphological changes of PF–DPA and PF–DPA + Co^{2+} complex

Further evidence for the complex formation of PF–DPA with Co^{2+} was obtained from the morphological changes of PF–DPA and PF–DPA+Co^{2+} observed by scanning electron microscopy (SEM) and atomic force microscopy (AFM) (Figure 3a.2). The SEM image of pure PF–DPA showed spherical polymer beads which indicate the self–assembly of PF–DPA polymer (Figure 3a.2A (a)). The changes in the morphology of PF–DPA on binding with Co^{2+} ion was studied by SEM and AFM images (Figure 3a.2) that shows the formation of metal induced aggregates which is different from the free PF–DPA. The AFM topography images of PF–DPA+Co^{2+} was observed to be in the formation of nano aggregates with the diameter size of around 20–60 nm and 1–1.5 nm height (Figure 3a.2B).

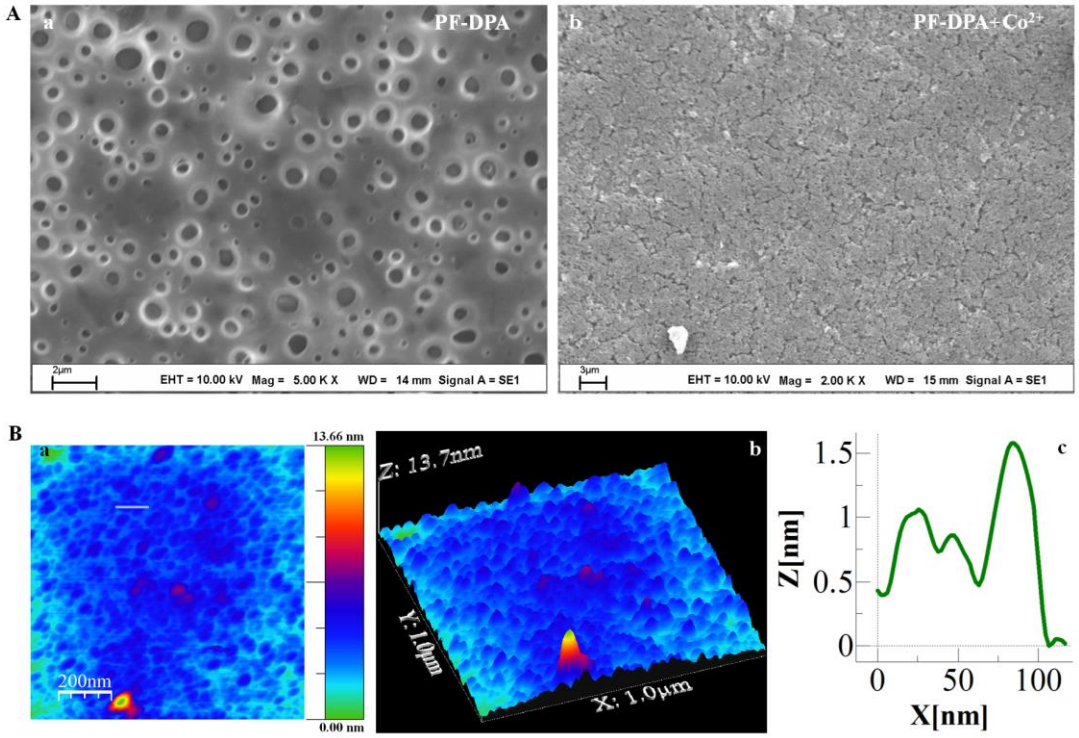

Figure 3a.2 A (a, b) SEM images of PF–DPA and PF–DPA+Co^{2+} complex. B (a, b, c) AFM topography, 3D image and height line profile of PF–DPA+Co^{2+} complex (X = Distance and Z = Height).

3a.2.6. Schematic diagram for the formation of PF–DPA+Co^{2+} complex

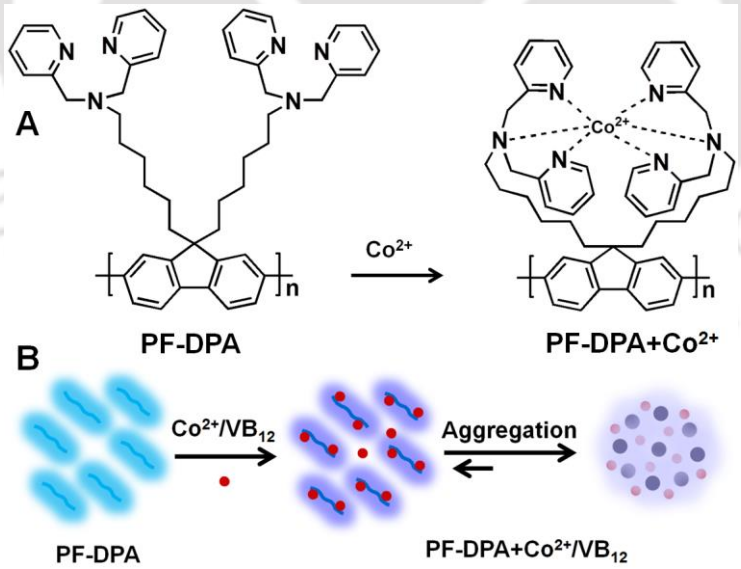

Scheme 3a.2 Schematic diagram for the formation of PF–DPA+Co^{2+} complex.

3a.2.7. Sensitive detection of vitamin B_{12}

Since, the PF–DPA was found to be highly selective for Co^{2+} ion, we utilized it for the detection of vitamin B_{12} (VB_{12}). Figure 3a.3a, depicts the fluorescence responses of the PF–

DPA (0.33 μM) towards VB_{12} (0–5 μM) in HEPES buffer solution (10 mM, pH 7.4). The value of I_0/I (I and I_0 are the fluorescence intensities of the PF–DPA in the presence and absence of VB_{12}) of PF–DPA increased linearly (R^2 = 0.9924) on increasing the concentration of VB_{12} ions over the range 0–2 μM. The fluorescence intensity vs. the VB_{12} plot (Figure 3a.3b) can be curve fitted into $(I_0/I) = K_{SV}[VB_{12}] + 1.0275$, close to the Stern–Volmer equation with a correlation coefficient (R^2) of 0.9924 and K_{SV} of 4.5×10^5 M^{-1}. The VB_{12} LOD was calculated to be 4.9×10^{-6} M by 3σ/k equation.[46]

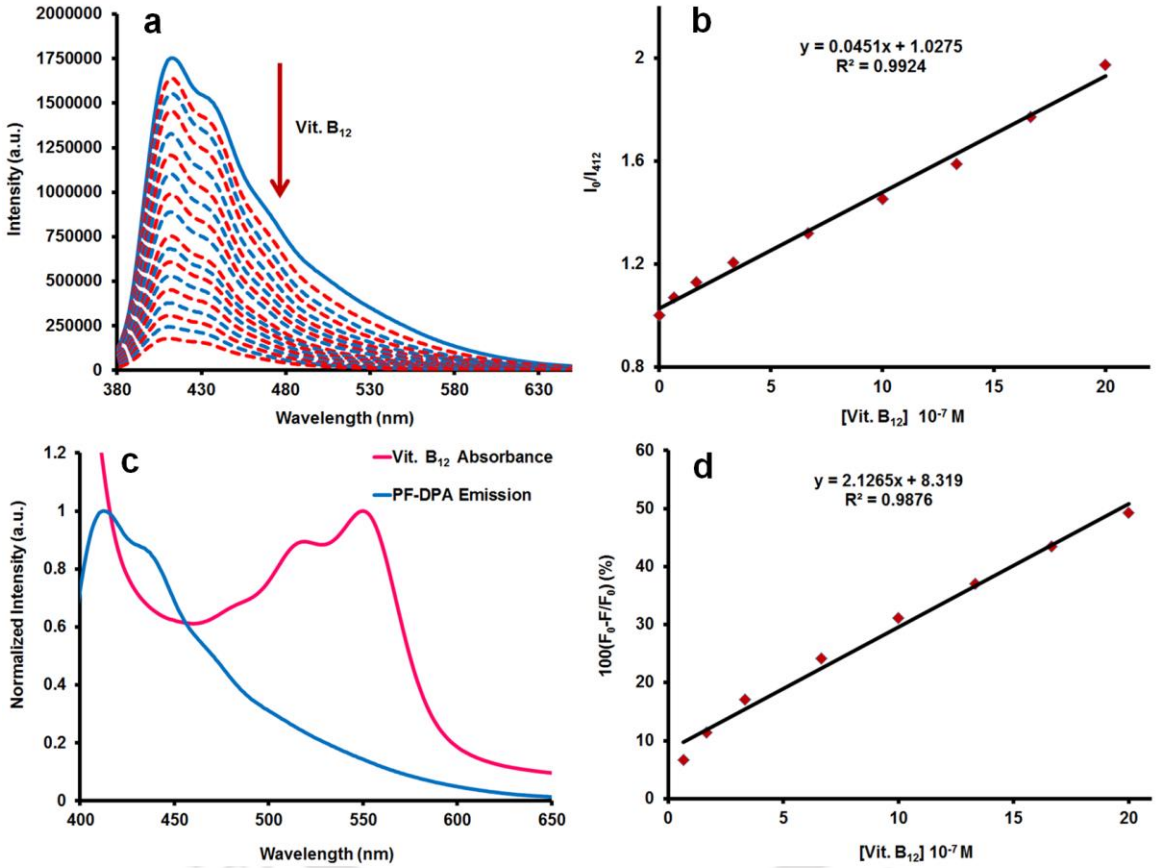

Figure 3a.3 (a) Fluorescent quenching spectra of PF–DPA (0.33 μM) in the presence of different concentrations of VB_{12} (0–5 μM) in THF: H_2O (9:1), (HEPES buffer, pH 7.4), λ_{ex} = 355 nm, λ_{em} = 412 nm. (b) Corresponding Stern–Volmer plot for the fluorescence quenching of PF–DPA by VB_{12} (0–5 μM). (c) The spectral overlap between the fluorescence of the donor PF–DPA (355 nm excitation) and the absorbance spectrum of acceptor VB_{12}. (d) The calibration graph for the efficiency of the FRET process vs. concentration.

The integral overlap spectra of the UV–vis spectrum of VB_{12} and the emission spectra of the PF–DPA exhibited a clear overlap (Figure 3a.3c) indicating the possibility of a fluorescence resonance energy transfer (FRET) process from the PF–DPA to VB_{12}.[47] The emission intensity of the PF–DPA decreased with increasing the concentration of VB_{12}, which

indicated that these systems were efficient FRET pair systems. Under the specified optimal reaction conditions, linear calibration graphs were constructed for the energy transfer efficiency of the PF–DPA at different concentrations of the VB_{12} samples. The efficiency of the FRET process was calculated from the following equation $E = (F_0–F/F_0) \times 100$ (%) where F is the donor fluorescence intensity in the absence (F_0) and presence (F) of the acceptor. For a 0.66 μM addition of VB_{12} to the PF–DPA aqueous solution, only a 6.6% energy transfer occurred, whereas for a 2 μM addition the energy transfer was 49% (Figure 3a.3d). The graph of the PF–DPA (Figure 3a.3d) was linear in the concentration range 0.66–2 μM with correlation coefficient $R^2 = 0.98623$. This efficiency of the energy transfer increases to ~90% with the gradual addition of VB_{12} from 0.66–5 μM which confirmed that the PF–DPA is an excellent donor in the FRET process as also verifying that the PF–DPA had a strong affinity to VB_{12}.

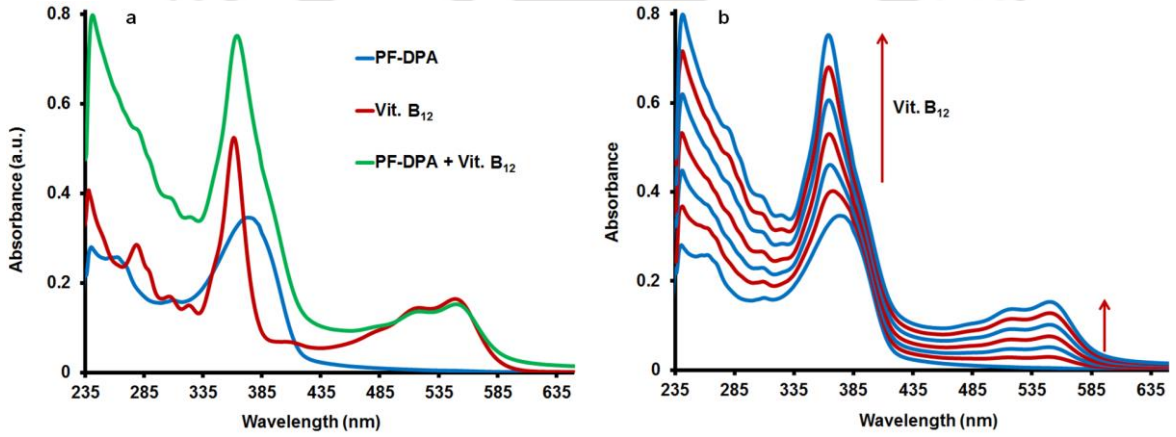

Figure 3a.4 (a) UV–visible absorption spectra of PF–DPA (5 μM), free VB_{12} (20 μM) and PF–DPA (5 μM) + VB_{12} (300 μM) in THF: H_2O (9:1), (HEPES buffer, pH 7.4). (b) UV–visible spectra of PF–DPA (5 μM) with increasing concentrations of VB_{12} (0–300 μM) in THF: H_2O (9:1), (HEPES buffer, pH 7.4).

To confirm the mechanism of the interaction between PF–DPA and VB_{12}, the UV–vis spectra of PF–DPA was recorded in the absence and presence of VB_{12}. As shown in figure 3a.4a, VB_{12} had absorption in the 300–600 nm wavelength range and could be assumed that the fluorescence quenching of PF–DPA was attributed to VB_{12}. When the different concentrations of VB_{12} (0–300 μM) was added into PF–DPA (5 μM), a gradual shift in the absorption spectra of PF–DPA from 370 to 362 nm (Figure 3a.4a and 3a.4b) was observed. Consequently, the changes in absorption spectrum of PF–DPA or blue shift occurs due to the electron or energy transfer from the donor PF–DPA to acceptor VB_{12}.[48]

3a.2.8. Aggregation induced enhanced emission (AIEE) behavior in PF–DPA

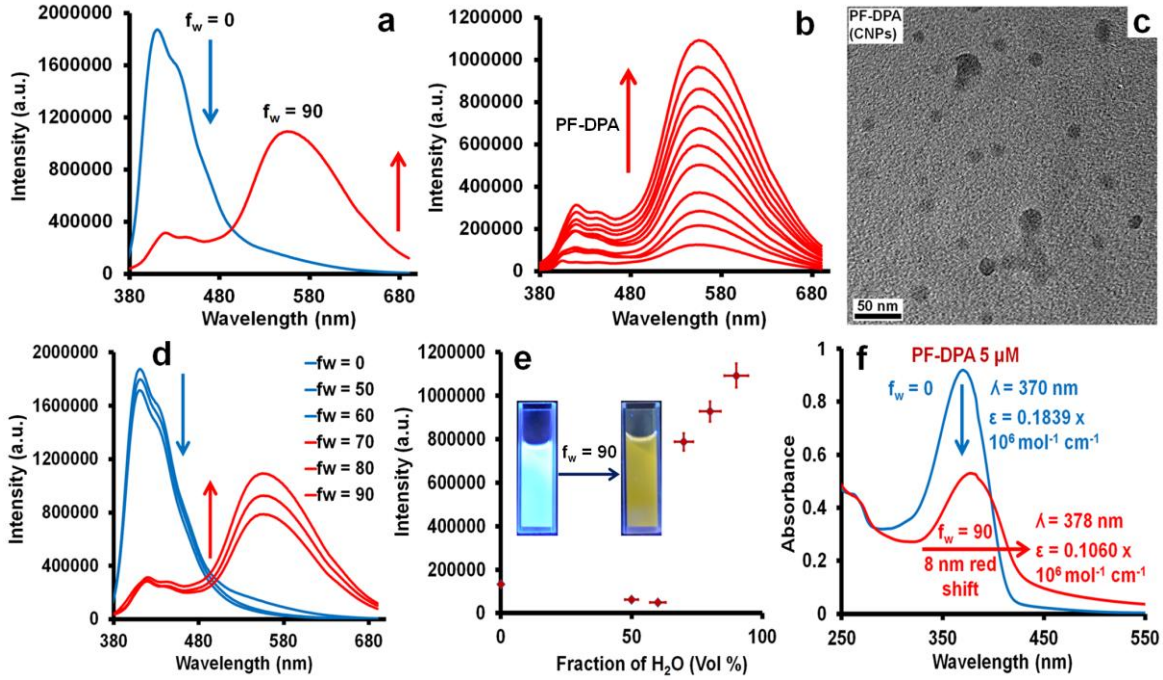

Figure 3a.5 (a) Fluorescence spectra of PF–DPA (0.33 µM) in THF: H_2O (100:0) (blue line) and PF–DPA (50 µM) THF: H_2O (1:9) (HEPES buffer, pH 7.4) (red line). (b) AIEE spectra of PF–DPA (5–50 µM) at 556 nm in THF: H_2O (1:9) (HEPES buffer, pH 7.4). (c) TEM images of PF–DPA NPs (PDots). (d, e) AIEE spectra of PF–DPA (50 µM) at 556 nm in THF: H_2O (100:0) to THF: H_2O (1:9) (HEPES buffer, pH 7.4). (e) The inset photos taken under UV light shows the color change of PF–DPA from blue [THF: H_2O (100:0)] to intense yellow orange [THF: H_2O (1:9), (HEPES buffer, pH 7.4)]. (f) Absorbance spectra of PF–DPA (5 µM) in THF: H_2O (100:0) and THF: H_2O (1:9) (HEPES buffer, pH 7.4)

The PF–DPA exhibited blue emission at 412 nm (355 nm excitation) in THF (Figure 3a.5a). In this state, the PF–DPA may likely exist in an isolated state and no emission at 556 nm was observed.[49,50] In contrast, PF–DPA exhibited strong red shifted emission at 556 nm (Figure 3a.5 (a, b)) in THF: H_2O (1:9) (HEPES buffer, pH 7.4) solution at higher PF–DPA concentration (50 µM) (355 nm excitation). In aqueous medium, PF–DPA spontaneously formed nanoparticles (20±5 nm) (PDots) which was confirmed by TEM images (Figure 3a.5c) and by measuring the size distribution of PF-DPA Pdots in solution state (average size distribution range = 24 d. nm) by dynamic light scattering (DLS) (Figure A3a.2).[51-53] At low concentration (0.33 µM) the fluorescence intensity of PF–DPA at 412 nm showed no significant changes till the ratio of water in THF: H_2O was 4:6 (HEPES buffer, pH 7.4),

however, when the ratio of water increased from 3:7 to 1:9 (THF: H_2O) (HEPES buffer, pH 7.4) the fluorescence intensity of PF–DPA was completely quenched (Figure A3a.3) due to the formation of intermolecular self–assembly induced aggregation in the polymer. Furthermore, at higher concentration of PF–DPA (50 μM), the fluorescence intensity of PF–DPA at 412 nm was similar as above with no significant changes till the THF: H_2O ratio was 4:6 (HEPES buffer, pH 7.4), however, when the ratio of water was increased from 3:7 to 1:9 (THF: H_2O) (HEPES buffer, pH 7.4) the fluorescence intensity of PF–DPA showed a remarkable red shift from 412 nm and a new intense emission appeared at 556 nm (Figure 3a.5d and 3a.5e)) due to the formation of intermolecular polymer self–assembly induced aggregation and is in agreement to the earlier observation (Figure 3a.5b).

This decrease in emission at 412 nm could be either due to H or J–aggregation (Scheme 3a.3). When the water fraction was lower than 70%, the molecules are more emissive at 412 nm compared to 556 nm.[54,55] However, in a system with higher water, THF: H_2O (1:9), the PF–DPA agglomerated spontaneously in a random way to form PDots that were less emissive in the blue region (at 412 nm) but highly fluorescent in the red region (at 556 nm). The inset photos taken under UV light illumination depict the color change from blue to intense yellow orange (Figure A3a.3b and 3a.5e) assigned to the PF–DPA PDots formation (20±5 nm) spontaneously in aqueous solution that display strong fluorescence due to the AIEE behavior (Figure 3a.5c). This unique and yet unexplored observation of the AIEE phenomenon in an inherent blue emitting fluorene homopolymer derivative has never been examined previously and presents immense application potential in cell imaging, cancer therapy, sensors and optical devices. The AIEE effect could be explained in terms of intra and intermolecular effects on PF–DPA polymer in aqueous and solid state. In the THF solution of PF–DPA, the alkyl chain restricts the aggregate formation due to parallel–type intermolecular interactions of polymer chains thereby exhibiting blue–shifted emission bands compared to the isolated state (H–aggregate formation).[49,50,56] However, PF–DPA at 1:9, THF: H_2O ratio shows remarkable red shifted emission band at 556 nm indicating that the prevention of H–aggregate formation compelled the formation of J–aggregation by likely end–to–end arrangements which induces a huge bathochromic shift (~150 nm) and enhancement in the emission maximum at 556 nm (Scheme 3a.3).[56-59] This emission maximum shift at 556 nm, is assigned to the combined effects of aggregation induced planarization and J–aggregate formation in the PF–DPA polymer.

3a.2.9. Confirmation of J-aggregate formation in PF-DPA

Figure 3a.5f, displays the UV−vis absorption spectra of PF-DPA (5 µM) in THF: H_2O (100:0) and THF: H_2O (1:9) ratio. In THF: H_2O (100:0), 5 µM PF-DPA shows a band at 370 nm which indicates it to be in isolated state and the extinction coefficient (ε) was calculated to be 0.183 × 10^6 mol^{-1} cm^{-1} [Figure 3a.5f and A3a.4]. Similarly, in THF: H_2O (1:9), the isolated PF-DPA (5 µM) band at 370 nm is 8 nm red shifted to 378 nm and the absorption decreases, indicating that PF-DPA is aggregated and the extinction coefficient (ε) was calculated to be 0.106 × 10^6 mol^{-1} cm^{-1} [Figure 3a.5f and A3a.5]. This red-shifted absorption confirms the J-aggregate formation by π–π stacking between intermolecular PF-DPA polymers through end-to-end type assembly.[60,61]

3a.2.10. Schematic diagram for the formation of PF–DPA PDots showing AIEE behavior

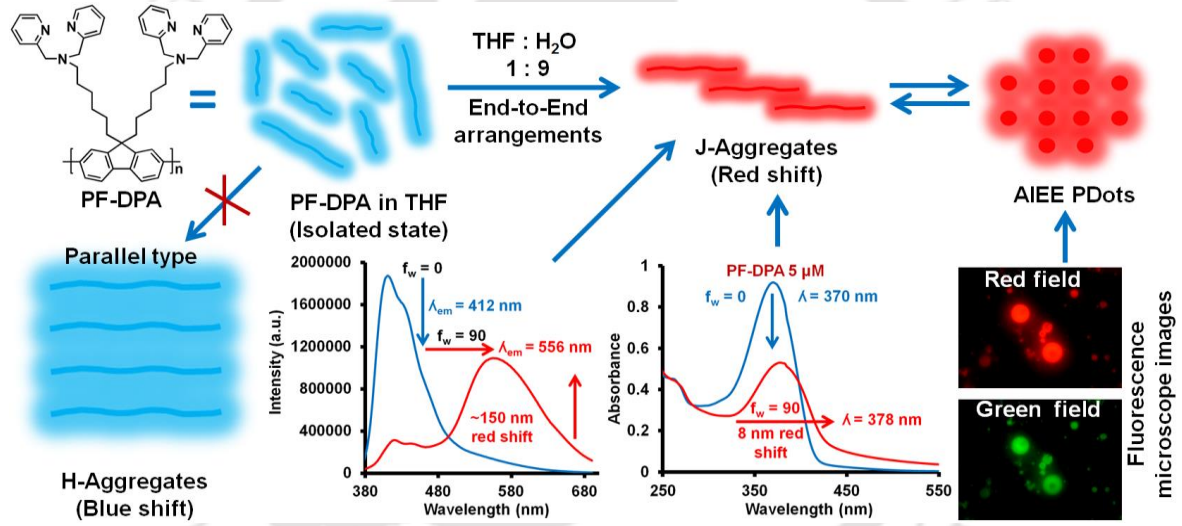

Scheme 3a.3 Schematic diagram for the formation of PF–DPA PDots showing AIEE behavior.

3a.2.11. Cell viability assay of PF-DPA by MTT assay

For the successful applications of PF–DPA in therapeutics it is necessary to confirm its cellular toxicity. Various normal (3T3 & CHO) and cancer cells (SKOV3 & B16F10) were incubated with PF–DPA in dose dependent manner for 24 h to evaluate the *in vitro* cytotoxicity (Figure 3a.6).[62,63] The results establish that PF–DPA was biocompatible upto ~1.6 mg/mL and 500 µg/mL in 3T3 and CHO cells, respectively. However, the PF-DPA PDots exhibited significant inhibition of proliferation even at ~200 µg/mL or below dose levels in cancer cells (SKOV3 and B16F10) (24 h incubation). Doxorubicin (2.5 µM) was used as a standard chemotherapeutic drug to compare the cytotoxicity with PF-DPA. Yet, in

all the cases, 40 µg/mL of PF–DPA was nontoxic and hence was safe for cell imaging studies. Moreover, the effect of solvent system (THF: H_2O) was also studied in B16F10 cells as a dose dependent manner and no significant toxicity effect (Figure A3a.6) was observed.

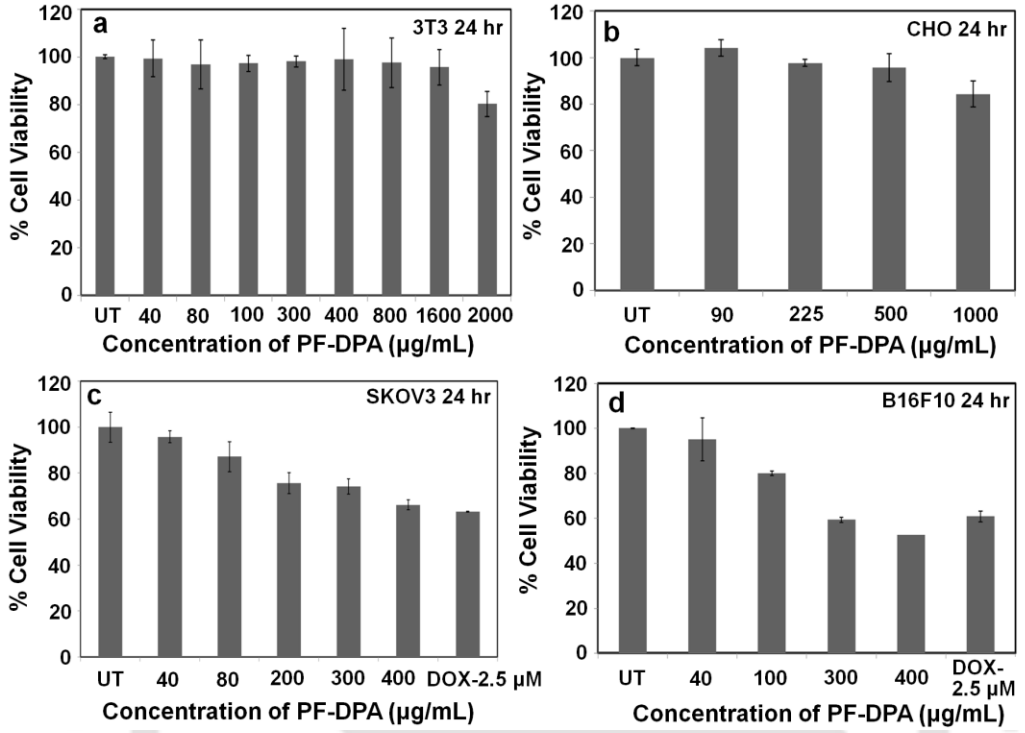

Figure 3a.6 Cell viability assay of PF-DPA with different cell lines (a) 3T3: mouse fibroblast normal cell, (b) CHO: Chinese hamster ovarian cell, (c) SKOV3: ovarian cancer cells, and (d) B16F10: melanoma cancer cells. Doxorubicin (DOX) was used as positive control experiment.

Figure 3a.5 (a, b, c & f) confirmed that PF-DPA exists as PDots due to the π−π stacking that leads to J-aggregates formation thereby exhibiting multicolor imaging ability as confirmed by fluorescence microscopy (Figure A3a.7). Since, PF–DPA spontaneously forms PDots (20±5 nm) in aqueous solution, strong AIEE effect is realized (Figure 3a.5), it presenting huge application potential in cell labeling. PF–DPA showed intense red (605 nm) and green (525 nm) fluorescence inside live cells under a fluorescence microscope (at λ_{ex} = 510–560 nm and λ_{ex} = 420–495 nm) due to the AIEE effect which was exceptional and motivated us to further check its fluorescence ability in few other live cells. This tunable red and green fluorescence of a probe inside the live cells are critical requirements to examine even small fold changes in a cell which are difficult to observe in fluorophores emitting in the UV–vis range. To demonstrate the ability of PF–DPA PDots for cellular imaging, cancer cells such as SKOV3, B16F10 and normal cells (3T3) were incubated with 40 µg/mL and 80 µg/mL of PF–DPA,

respectively (Figure 3a.7 and A3a.8). Figure 3a.7 shows the bright field (BF) and fluorescence (red and green) images of SKOV3, B16F10 and 3T3 cells incubated with PF–DPA. The obtained images confirmed a bright green and red fluorescence in SKOV3 and B16F10 cells but lower fluorescence intensity was observed in normal 3T3 cells. There was no auto fluorescence in control untreated cells (Figure A3a.9). The intense red and green fluorescence in cancer cells compared to normal cells, suggests that the uptake of PF–DPA PDots was more specific towards cancer cells than normal cells. These results also corroborate with the *in vitro* cytotoxicity data where PF–DPA PDots showed potent cytotoxicity to cancer cells compared to the normal cells under the same concentration. The AIEE phenomenon exhibiting PF–DPA PDots represent highly prospective materials for cancer cell imaging as well as cell labeling agents for *in vitro* applications due to their unique chemical constitution, water dispensability as well as their superior photophysical properties. This phenomenon could also be useful for *in vivo* applications. Hence, the PF–DPA PDots are demonstrated as unique cell imaging probes that could clearly distinguish cancer cells from normal cells and have enormous potential for selective delivery of bioactive molecules or anticancer drugs in cells.

3a.2.12. Cell imaging and cytotoxicity against cancer cell studies

According to the cell viability results (Figure 3a.6), it is established that PF–DPA is more cytotoxic to cancer cells (SKOV3 and B16F10) compared to normal cells (NIH3T3 and CHO) that further suggests the selective cytotoxic nature of PF-DPA toward cancer cells. Further, the dissimilarity in fluorescence among the normal and cancer cells (Figure 3a.7) confirms that the uptake of PF–DPA is more in cancer cells than in normal cells. There might be several probable reasons for the cancer cell specificity of PF–DPA over normal cells. Firstly, specific receptors present in the cancer cells help in more uptake of PF–DPA than the normal cells. For example, some receptors (e.g. EGFR, IGF–1R, HER–2, and folate receptor etc.) are over expressed in cancer cells whereas they are less/not expressed in normal cells.[64,65] The difference in receptors expression in cancer cells as well as normal cells discriminates the uptake of PF–DPA. The PF–DPA likely targets some specific over–expressed cancer cell receptors, which enhances their uptake, thereby resulting in increased toxicity. Secondly, the uptake may depend on the membrane integrity also which can be lost on interaction with PF–DPA that may further help to uptake more PF-DPA PDots inside the cells.[66] Therefore, PF–DPA behaves differently in cancer cells compared to normal cells. Curcumin is a well-known anticancer agent that is widely studied. Interestingly, low dose of

curcumin stimulates proliferation, migration and phagocytic activity of olfactory ensheathing cells, important for neural repair therapies.[67] Thus, more uptake of PF–DPA in cancer cells than normal cells may lead to increased cytotoxicity which can be effectively utilized as potential anti–cancer agent. The specificity of PF–DPA towards cancer cells over normal cells indicates the high potential of this polymer for cancer theranostics. Thirdly, it has also been demonstrated recently that cancer cells have different rates of metabolism compared to normal cells, which may differ the particle toxicity in normal cells than cancer cells.[68] Matching cellular metabolic output with cellular function is crucial for tissue integrity under stress and homeostatic conditions, which can manipulate the toxic behavior of any particle in different cellular conditions. Thus, it can be hypothesized that the cell specific toxicity of any materials towards normal or cancer cells is a complex phenomenon and needs to be investigate rigorously. Thus, the specificity of PF–DPA towards cancer cells over normal cells indicates the high potential of this polymer for cancer theranostics and needs careful and extensive investigation.

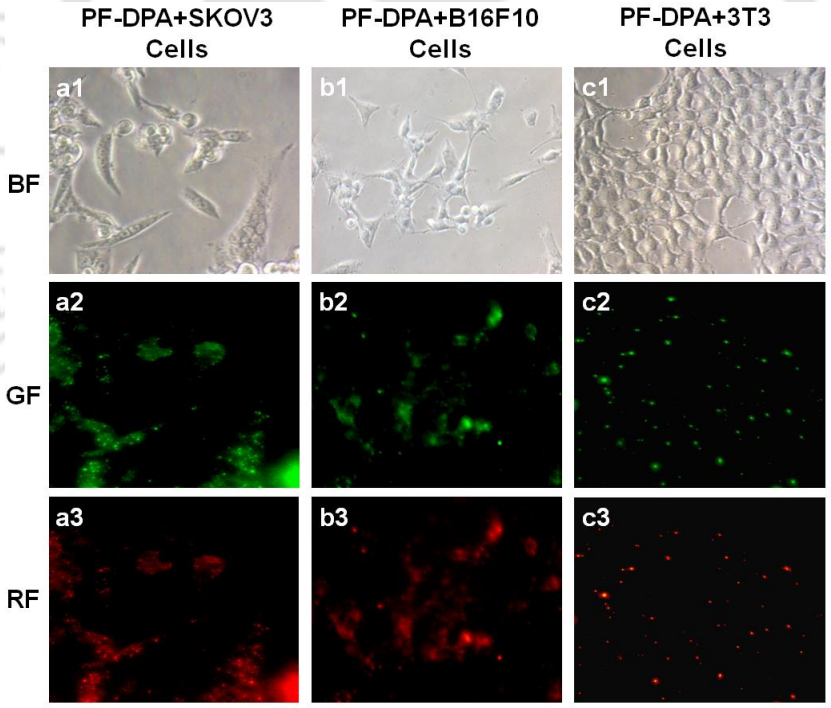

Figure 3a.7 Cell imaging of PF–DPA (40 µg/mL) with different cell lines at 20X optical zoom. (a1, a2, a3) Fluorescence images of PF–DPA in SKOV3–ovarian cancer cells. (b1, b2, b3) Fluorescence images of PF–DPA in B16F10–melanoma cancer cells. (c1, c2, c3) Fluorescence images of PF–DPA in 3T3–mouse fibroblast normal cells using fluorescence microscope.

Moreover, both green and red fluorescence provides the flexibility to choose either green or red fluorescence during cancer diagnosis, imaging and therapeutic applications. However, to have an improved understanding of the mechanisms involved to predict the precise mechanism of cancer cell death by PF-DPA Pdots a more detailed analysis of the complex diversity of cell death will be required. These PF-DPA PDots provide an unusual and efficient working platform for AIEE molecules in addition to overcoming the aggregation caused quenching (ACQ) effect usually observed in PF derivatives. Furthermore, PF-DPA provides a simpler structure for the rapid multicolor imaging of cancer cells and presents immense opportunities for the development of newer probes with multiple applications in imaging, cancer theranostics as well as for optoelectronics.

3a.3 Conclusion

In summary, a new fluorophore based on poly (9,9–Bis–(6–bromohexyl)–fluorene) homopolymer was designed, synthesized and its AIEE properties were utilized as a multicolor probe for cancer cell imaging and therapy. PF–DPA showed excellent selectivity for Co^{2+} over competing metal ions even at low concentrations. This chemosensor could be used in both quantitative detection and qualitative monitoring of Co^{2+} ion. Very importantly PF–DPA can efficiently detect biological important vitamin B_{12} via FRET mechanism. The remarkable performance of the sensor PF–DPA helped to extend the design and application in biosensors. The limit of detection was calculated to be 3.83×10^{-7} M and 4.9×10^{-6} M for Co^{2+} and VB_{12} respectively. Interestingly, PF–DPA PDots exhibited red and green emission in cellular environment and was highly biocompatible in normal cells but kills cancer cells selectively thereby extending its utility as drug delivery vehicles. Further PF–DPA PDots were used as cell imaging and diagnostic agents due to their excellent green and red fluorescence owing to the unique aggregation induced enhanced emission (AIEE) properties, which is fundamentally very significant for a polyfluorene homopolymer. We believe that the biocompatible nature of PF–DPA and its high selectivity for cancer cells extended its use for cancer theranostics. Notably, the highly selective killing of cancer cells by PF–DPA over normal cells provides extra benefits in cancer therapeutics. Together, these results demonstrated that appropriate functionalization of polyfluorene derivatives such as PF–DPA could be utilized to generate AIEE with potential applications in biosensors, cell imaging, delivery of bioactive molecules or anticancer drugs in cells as well as theranostic agents and in optoelectronic devices.

3a.4. Experimental Section

3a.4.1. Materials and methods

All reagents and solvents were purchased from commercial sources and solvents used were of spectroscopic grade. UV-vis absorption spectra were recorded on a PerkinElmer Lambda-25 spectrometer. Fluorescence spectra were carried out on a FluoroMax-4 Spectrofluorometer-Horiba Scientific. A 10 × 10 mm quartz cuvette was used for solution spectra and emission was collected at 90° relative to the excitation beam. Deionized water was obtained from Milli-Q system (Millipore). ^{1}H NMR (400 and 600 MHz) and ^{13}C NMR (150 MHz) spectra were obtained with a Varian-AS400NMR and Bruker spectrometer. FT-IR was recorded in a PerkinElmer spectrometer with samples prepared as KBr pellets. Morphological images were investigated by scanning electron microscopy (SEM) on a LEO 1430vp instrument. Atomic force microscopy images (AFM) were taken by Agilent 5500-STM instrument. The PF-DPA NPs were examined using an ultrahigh resolution transmission electron microscope (TEM; JEM 2100; Jeol, Peabody, MA, USA). DLS were measured by Zetasizer Nano series Nano-ZS90 instrument.

3a.4.2. Preparation of stock solutions

The polymer PF-DPA stock solution was prepared at the concentration of 1.0×10^{-3} mL^{-1} in 10 mL THF. This stock solution was diluted to desired concentration for each titration in a 3 mL cuvette.

3a.4.3. Preparation of cation stock solutions

Each inorganic metal salt stock solution was prepared at the concentration of 10.0×10^{-3} mL^{-1} in 5 mL Milli-Q water. The stock solutions were diluted to the desired concentrations with Milli-Q water when needed.

3a.4.4. Fluorescence titration of PF-DPA with Co^{2+} ion

A solution of PF-DPA (0.33×10^{-6} mL^{-1}) in THF: H_2O (9:1) (HEPES buffer, pH 7.4) was placed in a 3 mL cuvette (10.0 mm width) and then a fluorescence spectrum was recorded. Different concentration of cobalt ion solutions were added and the changes of the fluorescence intensity were recorded at room temperature each time (excitation wavelength: 355 nm) in THF: H_2O (9:1) (HEPES buffer, pH 7.4).

3a.4.5. Fluorescence spectra titration of PF-DPA with different metals

A solution of PF-DPA (0.33×10^{-6} mL^{-1}) in THF: H_2O (9:1) (HEPES buffer, pH 7.4) was placed in a 3 mL cuvette (10.0 mm width) and then a fluorescence spectrum was recorded.

Different concentration of different metal ion solutions were added and the changes of the fluorescence intensity were recorded at room temperature each time (excitation wavelength: 355 nm) in THF: H_2O (9:1) (HEPES buffer, pH 7.4).

3a.4.6. Fluorescence spectra titration of PF-DPA with vitamin B_{12}

A solution of PF-DPA (0.33×10^{-6} mL^{-1}) in THF: H_2O (9:1) (HEPES buffer, pH 7.4) was placed in a 3 mL cuvette (10.0 mm width) and then a fluorescence spectrum was recorded. Different concentration of VB_{12} solutions were added and the changes of the fluorescence intensity were recorded at room temperature each time (excitation wavelength: 355 nm) in THF: H_2O (9:1) (HEPES buffer, pH 7.4).

3a.4.7. Preparation of PF-DPA nano particles or PDots

PF-DPA (10 μM) polymer was regularly injected into THF: H_2O (1: 9) with vigorous stirring at room temperature, using a syringe. After the injection of PF-DPA, the solution was filtered by membrane filter with 0.2 μm pore size. Then the collected PF-DPA nano particles or PDots were used for other studies.

3a.4.8. Concentration dependent UV−Visible spectra of PF-DPA in THF (100%)

Figure A3a.4 displays the UV−vis spectra of PF-DPA in THF (100%) with different concentrations of PF-DPA (from 1 to 5 μM). This isolated PF-DPA polymer shows maximum absorption band at 370 nm without any shift, upon increasing the concentration from 1 to 5 μM. The absorbance of PF–DPA enhanced linearly (R^2 = 0.9997) on increasing the concentration of PF-DPA over the range 1–5 μM.

3a.4.9. Concentration dependent UV−Visible spectra of PF-DPA in THF: H_2O (1:9) ratio

Figure A3a.5 displays the UV−vis spectra of PF-DPA in THF: H_2O (1:9) ratio with different concentrations (1 to 10 μM). The isolated PF-DPA polymer absorption band at 370 nm is red shifted by 8 nm to 378 nm and is enhanced with the increase in concentration from 1 to 10 μM. This red-shifted phenomenon can be interpreted as a result of J-aggregation by non-covalent interactions between intermolecular polymers. The absorbance of PF–DPA increased linearly (R^2 = 0.999) on increasing the concentration of PF-DPA over the range 1–10 μM.

3a.4.10. Fluorescence images study of PF-DPA in THF: H_2O (1:9) ratio

100 µL of PF-DPA (1.65 mg in THF (100 µL) + H_2O (900 µL)) were taken in 96 well plate and the images were captured using fluorescence microscopy in red, green and blue filter respectively (Figure A3a.7). Subsequently, the observed multicolor fluorescence images greatly support the formation J- aggregate PF-DPA nanoparticles via AIEE behavior.

3a.4.11. Cell culture experiments

All cancer and normal cell lines were cultured in DMEM (Dulbecco's Modified Eagle Medium) media supplemented with 5% L-glutamine, 1% antibiotics (penicillin-streptomycin) and 10% fetal bovine serum (FBS), in a humidified 5% CO_2 incubator at 37 °C for *in vitro* experiments. All samples were kept under UV irradiation for 10 minutes before giving *in vitro* treatment.

3a.4.12. Cell viability of PF-DPA by using MTT assay

Cell viability of 3T3, Chinese hamster ovarian cell, SKOV3 and B16F10 cells treated with different doses of PF-DPA for 24 h that was carried out using MTT reagents according to standard protocol. Results were expressed as percent cell viability = {[A570 $_{\text{(treated cells) - background}}$] / [A570 $_{\text{(untreated cells) - background}}$]} ×100.

3a.4.13. Cell imaging study using fluorescence microscopy

3T3, CHO, SKOV3 and B16F10 cells were incubated with 40 µg/mL of PF-DPA for 24 h. All the treated cells were washed extensively by PBS (phosphate buffer saline) for 4-5 times and kept in HBSS buffer (Hank's Balanced Salt Solution, pH = 7.4). Finally, the fluorescence images were taken in a fluorescence microscope (Nikon Eclipse TE2000-E). The red fluorescence emission (λ_{em} = 605 nm) was collected with a 20X microscope objective after excitation at λ_{ex} = 510-560 nm. Accordingly the green fluorescence emission (λ_{em} = 525 nm) was collected with a 20X microscope objective after excitation at λ_{ex} = 420-495 nm.

References

(1) Santander, P. J.; Kajiwara, Y.; Williams, H. J.; Scott, A. I. *Bioorg. Med. Chem.* **2006,** *14,* 724.

(2) Frank, A.; McPartlin, J.; Danielsson, R. *Sci. Total Environ.* **2004,** *318,* 89.

(3) Al–Habsi, K.; Johnson, E. H.; Kadim, I. T.; Srikandakumar, A.; Annamalai, K.; Al–Busaidy R.; Mahgoub, O. *Vet. J.* **2007,** *173,* 133.

(4) C. D. Klaassen, Casarett, Doull's Toxicology the Basic Science of Poisoning. 6th ed.; McGraw–Hill: Medical Publishing Division, New York, **1986**; p. 839.

(5) Knauer, G. A.; Martin, J. H.; Gordon, R. M. *Nature* **1982,** *297,* 49.

(6) Reimann, C.; Koller, F.; Kashulina, G.; Niskavaara, H.; Englmaier, P. *Environ. Pollut.* **2001,** *115,* 239.

(7) Zhang, Z. Y. *Stud. Trace Elem. Health* **1996,** *21,* 3.

(8) Venugopal, B.; Luckey, T. D. A Metal Toxicity in Mammals, vol.2, Plenum Press, New York, **1979**.

(9) Shamsipur, M.; Alizadeh, K; Hosseini, M.; Caltagiroe, C.; Lippolis, V. *Sens. Actuators B* **2006,** *113,* 892.

(10) Aragoni, M. C.; Arca, M.; Bencini, A.; Blake, A. J.; Caltagirone, C.; Filippo, G. D.; Devillanova, F. A.; Garau, A.; Gelbrich, T.; Hurssthouse, M. B.; Isaia, F.; Lippolis, V.; Mameli, M.; Mariani, P.; Valtancoli, B.; Wilson, C. *Inorg. Chem.* **2007,** *46,* 4548.

(11) Shamsipur, M.; Sadeghi, M.; Alizadeh, K.; Sharghi, H.; Khalifeh, R. *Anal. Chim. Acta* **2008,** *630,* 57.

(12) Valeur, B.; Leray, I. *Coord. Chem. Rev.* **2003,** *205,* 3.

(13) Mori, I.; Takasaki, K.; Fujita, Y.; Matsuo, T. *Talanta* **1998,** *47,* 631.

(14) Luo, H. Y.; Zhang, X. B.; He, C. L.; Shen, G. L.; Yu, R. Q. *Spectrochim. Acta, Part A* **2008,** *70,* 337.

(15) Wang, X.; Zheng, W.; Lin, H.; Liu, G.; Chen, Y.; Fang, J. *Tetrahedron Lett.* **2009,** *50,* 1536.

(16) Montalti, M.; Prodi, L.; Zaccheroni, N. *J. Mater. Chem.* **2005,** *15,* 2810.

(17) Maity, D.; Govindaraju, T. *Inorg. Chem.* **2011,** *50,* 11282.

(18) Tan, Y.; Yu, J.; Cui, Y.; Yang, Y.; Wang, Z.; Hao, X.; Qian, G. *Analyst,* **2011,** *136,* 5283.

(19) Zhou, J.–R.; Liu, D.–P.; He, Y.; Kong, X.–J.; Zhang, Z.–M.; Ren, Y.–P.; Long, L.–S.; Huang, R.–B.; Zheng, L.–S. *Dalton Trans.,* **2014,** *43,* 11579.

(20) Chan, J.; Dodani, S. C.; Chang, C. J. *Nat. Chem.* **2012,** *4,* 973.

(21) Yang, Y.; Zhao, Q.; Feng, W.; Li, F. *Chem. Rev.* **2013,** *113,* 192.

(22) McQuade, D. T.; Pullen, A. E.; Swager, T. M. *Chem. Rev.* **2000,** *100,* 2537.

(23) Moon, J. H.; McDaniel, W.; MacLean, P.; Hancock, L. E. *Angew. Chem., Int. Ed.* **2007,** *46,* 8223.

(24) Kim, S.; Lim, C. K.; Na, J.; Lee, Y. D.; Kim, K.; Choi, K.; Leary, J. F.; Kwon, I. C. *Chem. Commun.*, **2010,** *46,* 1617.

(25) Tuncel, D.; Demir, H. V. *Nanoscale*, **2010,** *2,* 484.

(26) Lee, K.; Lee, J.; Jeong, E. J.; Kronk, A.; Elenitoba–Johnson , K. S. J.; Lim, M. S.; Kim, J. *Adv. Mater.* **2012,** *24,* 2479.

(27) Wu, P. J.; Kuo, S. Y.; Huang, Y. C.; Chen, C. P.; Chan, Y. H. *Anal. Chem.* **2014,** *86,* 4831.

(28) Zhu, C.; Liu, L.; Yang, Q.; Lv, F.; Wang, S. *Chem. Rev.* **2012,** *112,* 4687.

(29) Wu, I.; Yu, J.; Ye, F.; Rong, Y.; Gallina, M. E.; Fujimoto, B. S.; Zhang, Y.; Chan, Y. H.; Sun, W.; Zhou, X. H.; Wu, C.; Chiu, D. T. *J. Am. Chem. Soc.* **2015,** *137,* 173.

(30) Rong, Y.; Yu, J.; Zhang, X.; Sun, W.; Ye, F.; Wu, I.; Zhang, Y.; Hayden, S.; Zhang, Y.; Wu, C.; Chiu, D. T. *ACS Macro Lett.* **2014,** *3,* 1051.

(31) An, B.–K.; Kwon, S.–K.; Jung, S.–D.; Park, S. Y. *J. Am. Chem. Soc.*, **2002,** *124,* 14410.

(32) Luo, J.; Xie, Z.; Lam, J. W. Y.; Cheng, L.; Chen, H.; Qiu, C.; Kwok, H. S.; Zhan, X.; Liu, Y.; Zhu, D.; Tang, B. Z. *Chem. Commun.*, **2001,** 1740.

(33) Hong, Y.; Lam, J. W. Y.; Tang, B. Z. *Chem. Soc. Rev.*, **2011,** *40,* 5361.

(34) Ding, D.; Li, K.; Qin, W.; Zhan, R.; Hu, Y.; Liu, J.; Tang, B. Z.; Liu, B. *Adv. Healthc. Mater.* **2013,** *2,* 500.

(35) Hu, R.; Leung, N. L. C.; Tang, B. Z. *Chem. Soc. Rev.*, **2014,** *43,* 4494.

(36) Lia, K.; Liu, B. *Chem. Soc. Rev.*, **2014,** *43,* 6570.

(37) Yuan, Y.; Zhang, C–J.; Gao, M.; Zhang, R.; Tang, B. Z.; Liu, B. *Angew. Chem., Int. Ed.* **2015,** *54,* 1780.

(38) Wu, W.; Ye, S.; Tang, R.; Huang, L.; Li, Q.; Yu, G.; Liu, Y.; Qin, J.; Li, S. *Polymer* **2012,** *53,* 3163.

(39) Saikia, G.; Iyer, P. K. *J. Org. Chem.* **2010,** *75,* 2714.

(40) Fukuda, M.; Sawada, K.; Yoshino, K. *Jpn. J. Appl. Phys.*, **1989,** *28,* L1433.

(41) Paul, G. S.; Sarmah, P. J.; Iyer, P. K.; Agarwal, P. *Macromol. Chem. Phys.* **2008,** *209,* 417.

(42) Muthuraj, B.; Hussain, S.; Iyer, P. K. *Polym. Chem.* **2013,** *4,* 5096.

(43) Lou, X.; Zhang, Y.; Li, S.; Ou, D.; Wan, Z.; Qin, J.; Li, Z. *Polym. Chem.,* **2012,** *3,* 1446.

(44) Wang, J.; Wang, D.; Miller, E. K.; Moses, D.; Bazan, G. C.; Heeger, A. J. *Macromolecules* **2000,** *33,* 5153.

(45) Wang, D.; Wang, J.; Moses, D.; Bazan, G. C.; Heeger, A. J. *Langmuir*, **2001,** *17,* 1262.

(46) Cao, C.; Kim, J. P.; Kim, B. W.; Chae, H.; Yoon, H. C.; Yang, S. S.; Sim, S. J. *Biosens. Bioelectron.* **2006,** *21,* 2106.

(47) Wang, J.; Wei, J.; Su, S.; Qiu, J. *New J. Chem.,* **2015,** *39,* 501.

(48) Gore, A. H.; Kale, M. B.; Anbhule, P. V.; Patil, S. R.; Kolekar, G. B. *RSC Adv.* **2014,** *4,* 683.

(49) Oelkrug, D.; Tompert, A.; Gierschner, J.; Egelhaaf, H.; Hanack, M.; Hohloch, M.; Steinhuber, E. *J. Phys. Chem. B,* **1998,** *102,* 1902.

(50) An, B. K.; Gierschner, J.; Park, S. Y. *Acc. Chem. Res.,* **2012,** *45,* 544.

(51) Jin, Y.; Ye, F.; Zeigler, M.; Wu, C.; Chiu, D. T. *ACS Nano,* **2011,** *5,* 1468.

(52) Rong, Y.; Wu, C.; Yu, J.; Zhang, X.; Ye, F.; Zeigler, M.; Gallina, M. E.; Wu, I.-C.; Zhang, Y.; Chan, Y.-H.; Sun, W.; Uvdal, K.; Chiu, D. T. *ACS Nano,* **2013,** *7,* 376.

(53) Wu, I.-C.; Yu, J.; Ye, F.; Rong, Y.; Gallina, M. E.; Fujimoto, B. S.; Zhang, Y.; Chan, Y.-H.; Sun, W.; Zhou, X.-H.; Wu, C.; Chiu, D. T. *J. Am. Chem. Soc.* **2015,** *137,* 173.

(54) Tong, H.; Dong, Y.; Haussler, M.; Lam, J. W. Y.; Sung, H. H. Y.; Williams, I. D.; Sun, J.; Tang, B. Z. *Chem. Commun.,* **2006,** 1133.

(55) Tong, H.; Dong, Y.; Hong, Y.; Haussler, M.; Lam, J. W. Y.; Sung, H. H. Y.; Sun, X.; Yu, J.; Williams, I. D.; Kwok, H. S.; Tang, B. Z. *J. Phys. Chem. C,* **2007,** *111,* 2287.

(56) Deng, Y.; Yuan, W.; Jia, Z.; Liu, G. *J. Phys. Chem. B,* **2014,** *118,* 14536.

(57) Gadde, S.; Batchelor, E. K.; Kaifer, A. E. *Chem. -Eur. J.* **2009,** *15,* 6025.

(58) Kumar, V.; Baker, G. A.; Pandey, S. *Chem. Commun.,* **2011,** *47,* 4730.

(59) Berlepsch, H. V.; Ludwig, K.; Boöttcher, C. *Phys. Chem. Chem. Phys.,* **2014,** *16,* 10659.

(60) Ogi, S.; Sugiyasu, K.; Manna, S.; Samitsu, S.; Takeuchi, M. *Nat. Chem.* **2014,** *6,* 188.

(61) Laban, B.; Vodnik, V.; Dramićanin, M.; Novaković, M.; Bibić, N.; Sovilj, S. P.; Vasić V. M. *J. Phys. Chem. C* **2014,** *118,* 23393.

(62) Mukherjee, S.; Rao, B. R.; Sreedhar, B.; Paik, P.; Patra, C. R. *Chem. Commun.,* **2015,** *51,* 7325.

(63) Mukherjee, S.; Chowdhury, D.; Kotcherlakota, R.; Patra, S.; Vinothkumar, B.; Bhadra, M. P.; Sreedhar, B.; Patra, C. R. *Theranostics* **2014,** *4,* 316.

(64) Patra, C. R.; Bhattacharya, R.; Wang, E.; Katarya, A.; Lau, J. S.; Dutta, S.; Muders, M.; Wang, S.; Buhrow, S. A.; Safgren, S. L.; Yaszemski, M. J.; Reid, J. M.; Ames, M. M.; Mukherjee, P.; Mukhopadhyay, D. *Cancer Res.*, **2008,** *68*, 1970.

(65) Hu, D.; Sheng, Z.; Fang, S.; Wang, Y.; Gao, D.; Zhang, P.; Gong, P.; Ma, Y.; Cai. L. *Theranostics*, **2014,** *4*, 142.

(66) Kobayashi, H.; Watanabe, R.; Choyke, P. L. *Theranostics*, **2014,** *4*, 81.

(67) Velasquez, J. T.; Watts, M. E.; Todorovic, M.; Nazareth, L.; Pastrana, E.; Diaz–Nido, J.; Lim, F.; Ekberg, J. A. K.; Quinn, R. J.; St. John, J. A. *PLoS ONE*. **2014,** *9*, e111787.

(68) Wang, Y. H.; Israelsen, W. J.; Lee, D.; Yu, V. W.; Jeanson, N. T.; Clish, C. B.; Cantley, L. C.; Vander Heiden, M. G.; Scadden, D. T. *Cell*, **2014,** *158*,1309.

Appendix

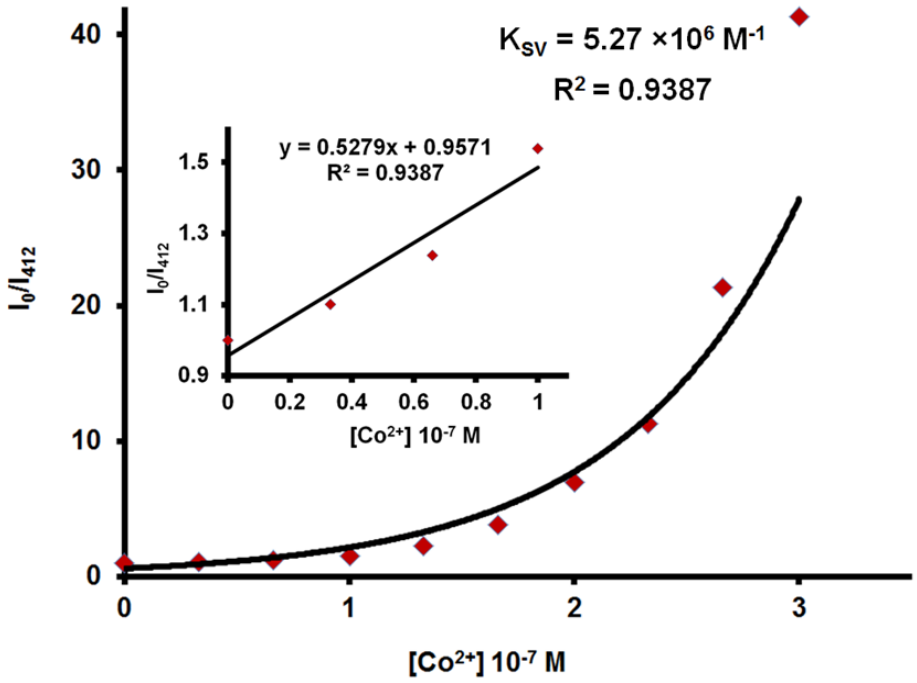

Figure A3a.1 Stern–Volmer plot for the fluorescence quenching of PF–DPA by Co^{2+} (0.33 µM) in THF: H_2O (9:1), (10 mM HEPES buffer, pH 7.4).

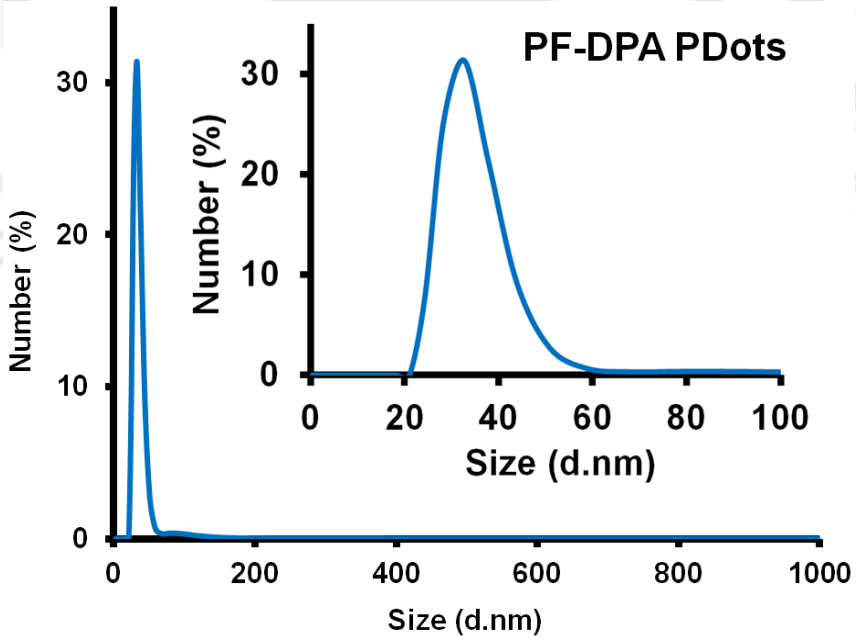

Figure A3a.2 The size distribution of PF-DPA Pdots in solution state (average size distribution range = 24 d. nm) measured by DLS.

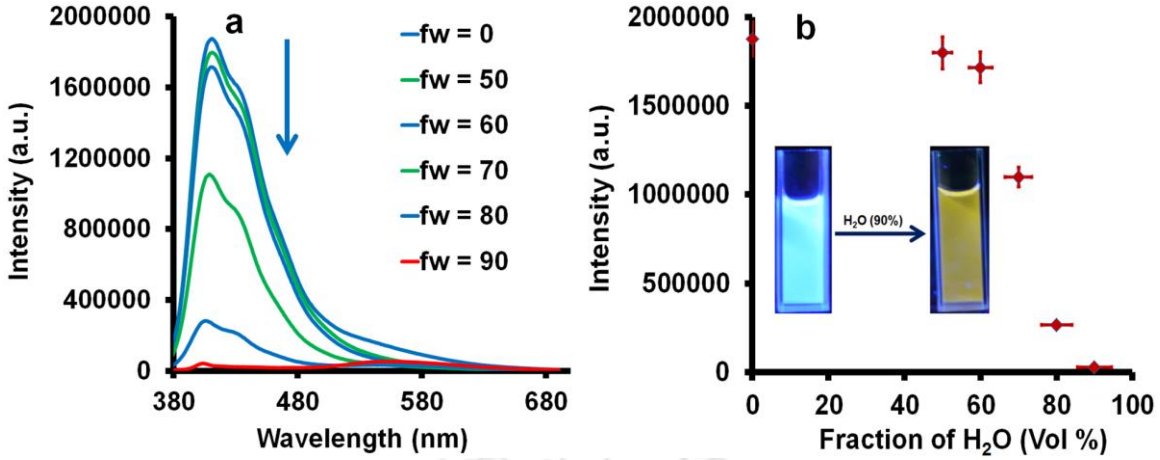

Figure A3a.3 (a, b) Fluorescence quenching spectra of PF–DPA (0.33 μM) at 412 nm in THF: H_2O (100:0) to THF: H_2O (1:9), (HEPES buffer, pH 7.4). The inset photos taken under UV light illumination shows the PF–DPA color change from blue [THF: H_2O (100:0)] to intense yellow orange [THF: H_2O (1:9), (HEPES buffer, pH 7.4)].

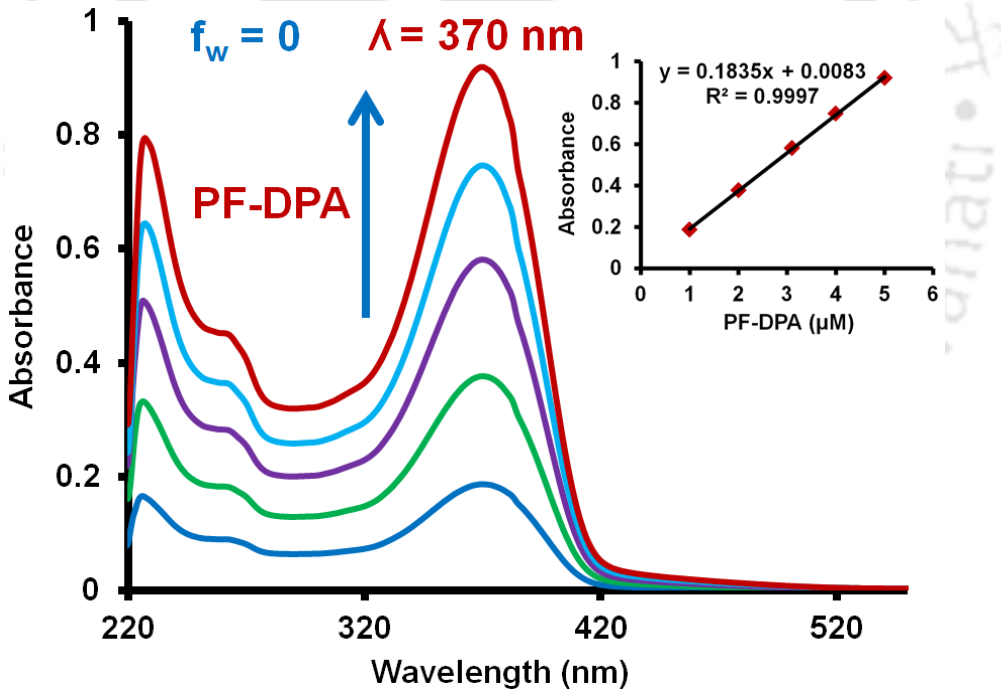

Figure A3a.4 Absorbance spectra of PF–DPA (1 to 5 μM) in THF: H_2O (100:0) (HEPES buffer, pH 7.4). The maxima absorption band observed for PF–DPA at 370 nm.

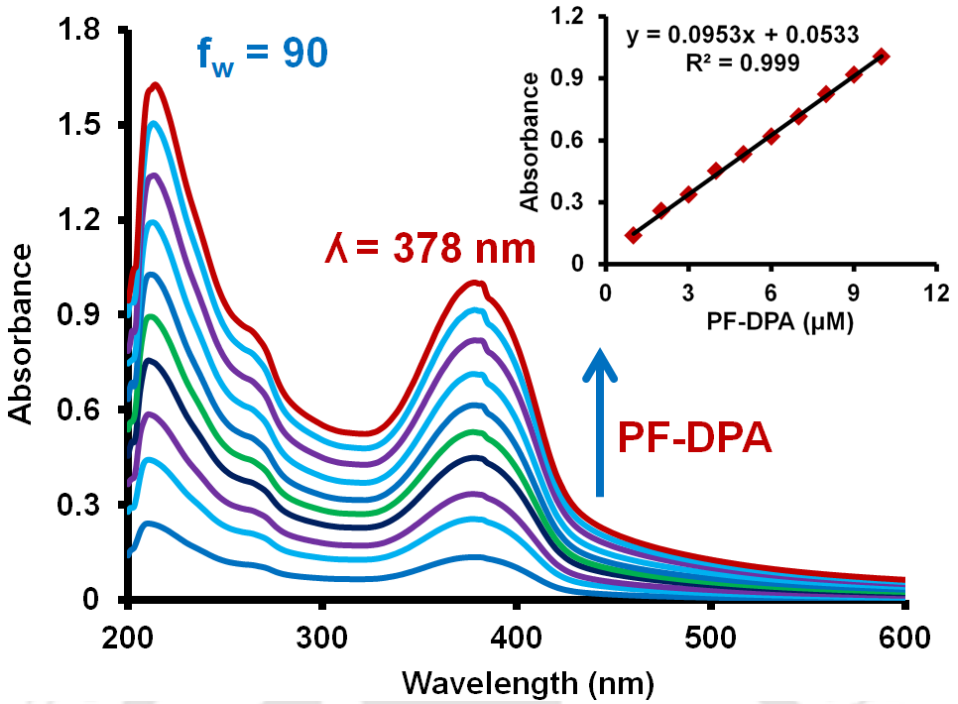

Figure A3a.5 Absorbance spectra of PF–DPA (1 to 10 μM) in THF: H_2O (1:9) (HEPES buffer, pH 7.4). The maxima absorption band observed for PF–DPA at 378 nm.

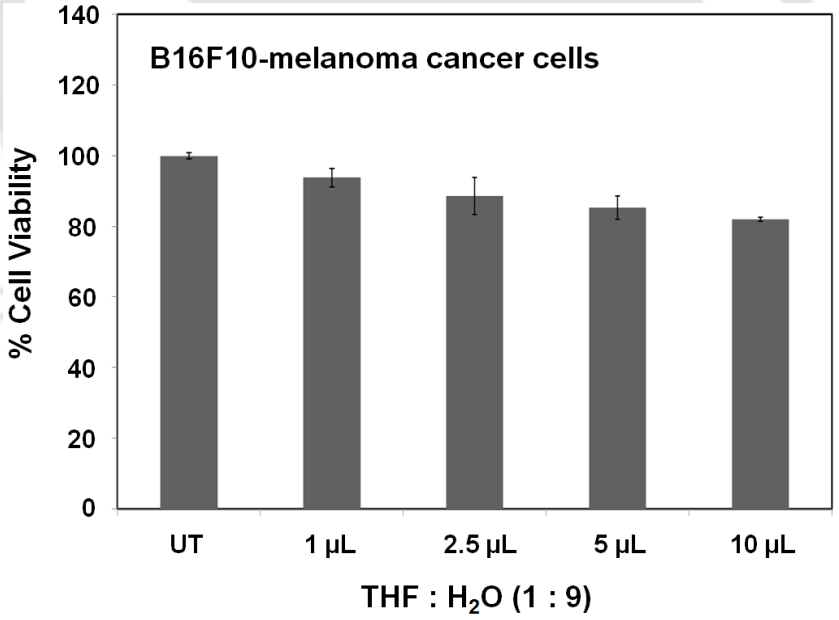

Figure A3a.6 Cell viability study for the solvent system of THF: H_2O (1:9) on B16F10 cells in different doses of THF: H_2O (1:9) solvents.

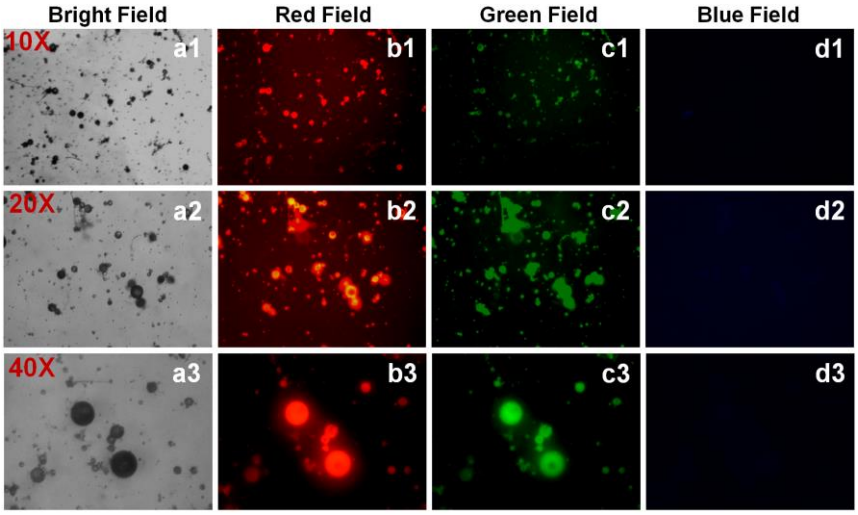

Figure A3a.7 Bright field and fluorescence images of PF-DPA in solvent ratio of THF: H_2O (9:1) captured by fluorescence microscopy. 100 µL of PF-DPA (1.65 mg in THF (100 µL) + H_2O (900 µL)) were taken in 96 well plate and the images were captured using fluorescence microscopy in red, green and blue filter respectively.

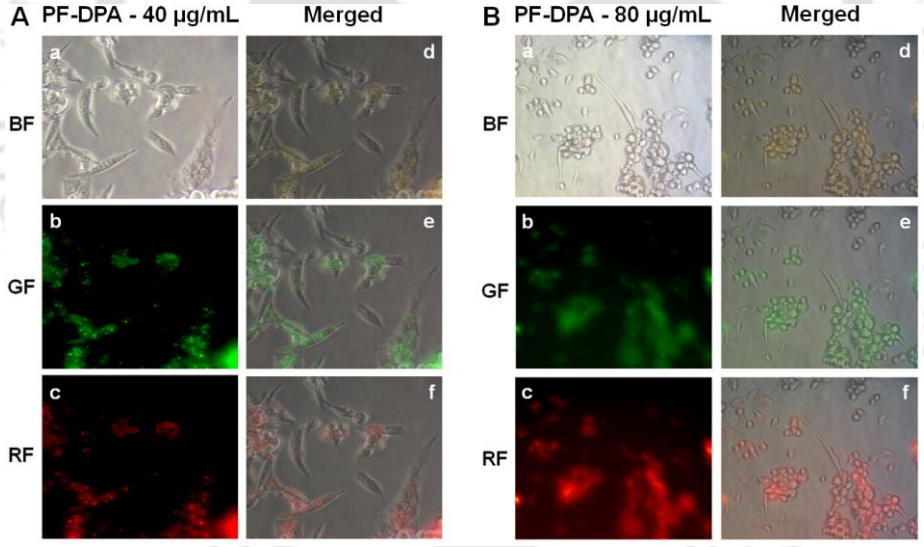

Figure A3a.8 A (a, b, c) Bright, green and red field images of SKOV3-ovarian cancer cells treated with PF-DPA (40 µg/mL) incubated for 24 h. (d, e, f) Merged images of bright, green and red field images of SKOV3-ovarian cancer cells treated with PF-DPA (40 µg/mL). B (a, b, c) Bright, green and red field images of SKOV3-ovarian cancer cells treated with PF-DPA (80 µg/mL) incubated for 24 h. (d, e, f). Merged images of bright, green and red field images of SKOV3-ovarian cancer cells treated with PF-DPA (80 µg/mL).

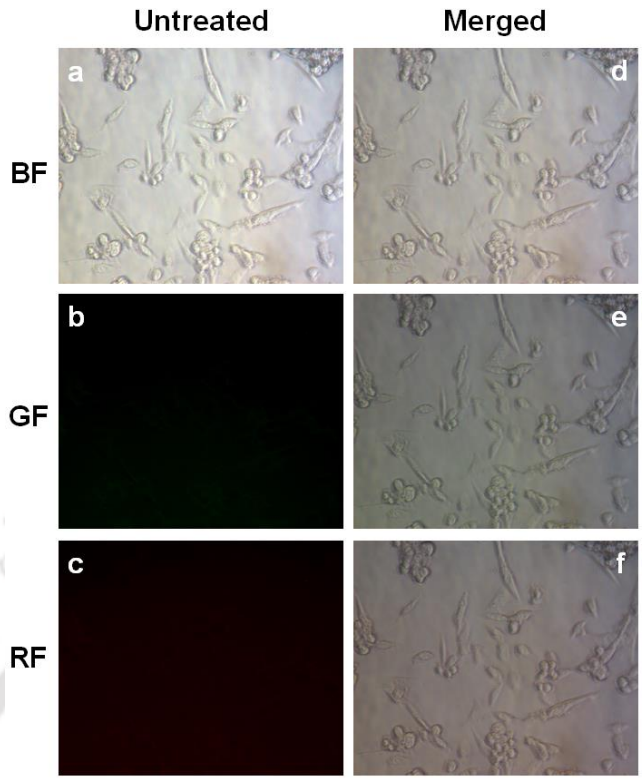

Figure A3a.9 A (a, b, c) Bright, green and red field images of SKOV3-ovarian cancer cells untreated with PF-DPA incubated for 24 h. (d, e, f). Merged images of bright, green and red field images of SKOV3-ovarian cancer cells untreated with PF-DPA.

Chapter: 3b

Inhibition of Aβ Fibrillation and Modulation Effect on Preformed Aβ Oligomers and Fibrils by an Influence of Aggregation Induced Enhanced Emission luminogen of PF–DPA PDots

Abstract

The design and synthesis of a conjugated polyfluorene derivative (PF-DPA) which displays aggregation induced enhanced emission (AIEE) phenomenon in the nanoparticle / polymer dots (PDots) form and its inhibition and modulation effect on Aβ1-40 aggregation is reported. It is established that PF-DPA PDots (5 μM) inhibited Aβ1-40 fibrillization to form spherical oligomers into Aβ1-40 aggregates. Furthermore, in the presence of PF-DPA PDots (5 μM) preformed Aβ1-40 oligomers, Aβ1-40 fibrils and CSF Aβ aggregates, showed an exceptional modulation effect due to the formation of co-assembly between the PF-DPA PDots and Aβ aggregates. Consequently, the formation of co-assembly between PF-DPA PDots and Aβ aggregates is due to the formation of face-to-face arrangements by hydrophobic interactions resulting in modulation of the aggregated peptides which may likely lead to the prevention or treatment for AD.

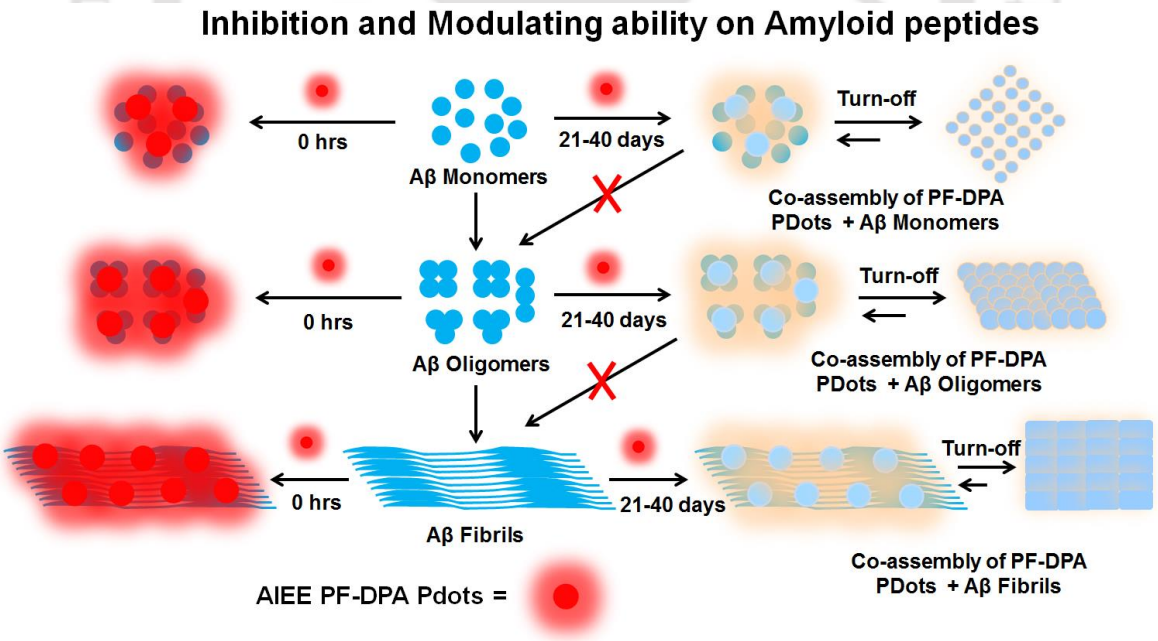

3b.1. Introduction

Aβ fibrils are well-defined cross-β-sheet structures formed by misfolded native proteins, to generate neurodegenerative disorders such as Alzheimer's disease (AD).[1-3] Amyloid peptides (Aβ1–40, Aβ1–42) are mainly derived from amyloid precursor protein (APP) through β- and γ-secretase-based proteolysis which is mainly responsible for amyloidal fibril formation.[4] These well-ordered protein aggregates (soluble oligomers and mature fibrils) are neurotoxic and cause neuronal cell death which affects millions of people in worldwide.[5-11] To overcome this problem, the inhibition of Aβ self-assembly aggregation and the modulation of preformed Aβ fibrils have been considered as the primary therapeutic strategy for the neurodegenerative diseases.

Several approaches have been attempted to prevent Aβ oligomer formation into fibrils *in vitro*.[12-33] Among them, nanoparticle-based inhibition is the most efficient, and has received more attention in the therapeutics of AD due to their unique structural superiority, such as size, high stability, ease of surface functionalization and tunable physical/chemical properties of nanoparticles. For example, a variety of nanoparticles,[34,35] anionic nanoparticles[36,37] and specific proteins or peptides (α-synuclein, Aβ1−40) functionalized nanoparticles are reported to promote amyloid fibrillation.[38,39] In contrast, hydrophobic nanoparticles or nanoparticles functionalized with hydrophobic molecules such as KLVFF[40] and VVIA peptide,[41] phenylalanine-phenylalanine dipeptide,[30] PEGylated NPs,[42] polymeric NPs,[27,34,43] Fe_3O_4 NPs,[44] gold NPs,[32,45-47] fullerene NPs,[48] and thioglycolic acid-capped CdTe QDs[29] have been identified for their inhibitory ability to prevent amyloid fibrillation. In addition, nanoparticles functionalized with specific affinity molecules to inhibit fibrillation processes such as curcumin,[49] dextran,[50] and sialic acid.[51] These reports indicate that further studies are required for understanding the effects of modular surface chemistry on amyloid fibrillation.

3b.2. Results and discussion

3b.2.1. Synthesis of PF-DPA

Polymer PF-Br (67 mg), di(2-picolyl)amine (DPA) (60 mg, 0.3 mmol), potassium carbonate (70 mg, 0.5 mmol) were mixed and heated at 150 °C for 36 h in dry DMF (Scheme 3a.1).[52-55] Further, the mixture was cooled to room temperature and poured into methanol (100 mL). The brown precipitant was collected and washed with acetone and dried overnight in a vacuum desiccator (68 mg, 86.8%). Notably, CP's of PF-DPA were monitored over long

duration in *in vitro* studies and have confirmed to be nontoxic to normal cells and be able to easily penetrate cell membrane as mentioned in earlier chapter (Figure 3a.6).

Herein, we have demonstrated a conjugated polyfluorene (PF-DPA) derivative based AIEE fluorescent nanoparticles or Pdots that are blue emissive in organic solvents but highly luminescent in red region with red shifted emission when they are supramolecularly aggregated in aqueous medium or solid state (Figure 3b.1a). The PDots exhibit strongly enhanced fluorescence emission due to the synergetic effect of planarization and J-aggregation by the restriction of the intramolecular rotation (RIR) of the multiple phenyl rotors and picolyl groups in the aggregate state.[56,57] AIEE based fluorescent probes including fluorophores containing polymeric nanoparticles have been widely used due to their superior fluorescence brightness, excellent photostability, minimal cytotoxicity and easy surface functionalization for specific targeting in various applications *in vitro* and *in vivo*.[58] However, to the best of our knowledge, there are no reports for the inhibition or modulation of Aβ self-assembly aggregation by PDots based AIEE luminogen.

In figure 3b.1b, PF-DPA (5 μM) exhibits strong blue emission at 412 nm in 100% THF solution at 355 nm excitation since it may likely exist in an isolated state due to the nonradiative decay processes brought about by the molecular torsions and rotations. In contrast, PF-DPA (5 μM) exhibited strong red shifted emission at 556 nm in the ratio of THF: H_2O (1:9) solution at 355 nm excitation (Figure 3b.1b) due to the formation of intermolecular polymers self-assembly induced aggregation or aggregation induced planarization and J-aggregate formation.[59,60] In situ formed highly fluorescent organic PF-DPA PDots (20 ± 5) (Inset figure 3b.1b) were used for effective inhibition of Aβ1-40 aggregation and modulators for preformed Aβ1-40 oligomers and fibrils. However, the PF-DPA PDots were designed to perform multiple functions such as to prevent Aβ1-40 aggregation and modulate the preformed Aβ1-40 oligomers and fibrils by introducing the PF-DPA PDots into Aβ1-40 oligomers, Aβ1-40 aggregates and the real sample CSF Aβ aggregates. Thioflavin T (ThT) binding assay was used to monitor Aβ1-40 fibril formation, followed by monitoring the effect of inhibition and the modulating ability of PF-DPA PDots by fluorescence spectroscopy. Moreover, the modulating effects of PF-DPA PDots on Aβ aggregates were validated using other techniques such as optical spectroscopy, Fourier transform infrared spectroscopy (FT-IR), atomic force microscopy (AFM) and dynamic light scattering (DLS). Thus, we report on the efficient inhibitory activities of PF-DPA PDots

towards preventing the formation of Aβ 1-40 aggregates and its modulating effect on preformed Aβ1-40 and CSF aggregates.

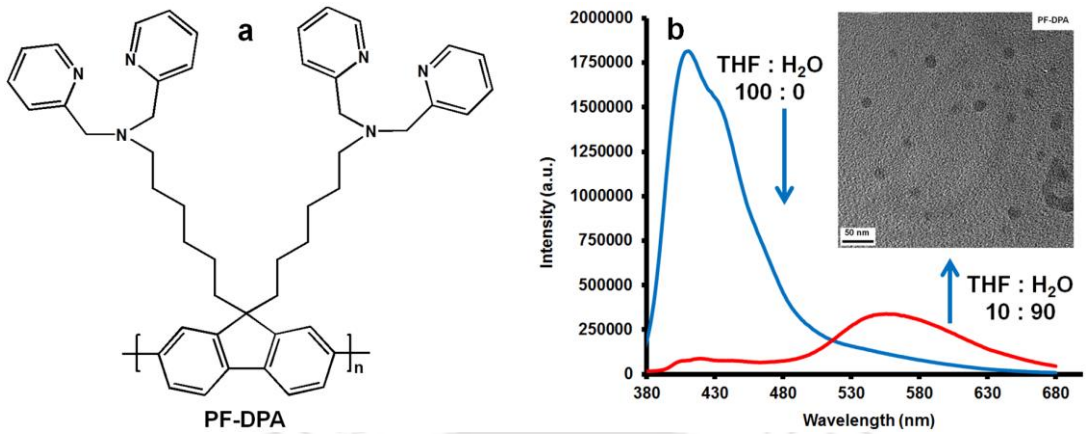

Figure 3b.1 (a) A polymer PF-DPA used as an inhibitor and modulator. (b) Fluorescence spectra of PF-DPA (5 μM) in THF: H_2O (100: 0) and aggregation induced enhanced emission (AIEE) spectra of PF-DPA (5 μM) at 556 nm in THF: H_2O (1: 99). Inset figure 1b: The formation of PF-DPA NPs was observed by TEM.

3b.2.2. ThT assay for the confirmation of Aβ1-40 fibrils and CSF aggregates

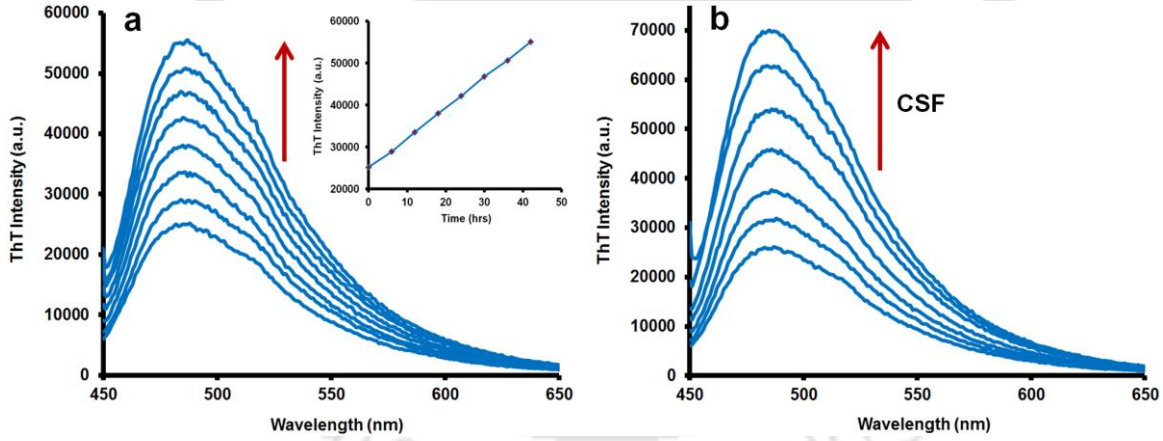

Figure 3b.2 (a) Fluorescence spectra (λ_{ex}= 440 nm, λ_{em} = 488 nm) of ThT (20 μM) (pH 7.4 in HEPES) with Aβ1-40 (5 μM) was measured every 6 h interval incubation time from 0-42 h. (b) Fluorescence spectra (λ_{ex}= 440 nm, λ_{em}= 488 nm) of ThT (20 μM) (pH 7.4 in HEPES) with addition of CSF (100 mL).

The Aβ fibrils were prepared by incubating Aβ1-40 monomers in presence of ThT (20 μM) at 37 °C (pH 7.4 in HEPES buffer) for 0-42 h. Thioflavin T (ThT) is the specific dye to identify Aβ fibrils.[61,62] A gradual enhancement of emission peak at 488 nm (Figure 3b.2a) was observed over an incubation time of 0-42 h (λ_{ex} – 440 nm), which confirms the formation of

Aβ fibrils. Further, the presence of Aβ fibrils in CSF was also confirmed by the addition of up to 100 μL of the CSF sample to ThT (20 μM solution, pH 7.4 in HEPES), while observing a rapid enhancement in the fluorescence intensity of ThT at 488 nm validating strongly the presence of Aβ fibrils in the CSF sample (Figure 3b.2b).[63]

3b.2.3. Modulating effect on Aβ 1-40 fibrils and CSF aggregates by PF-DPA PDots

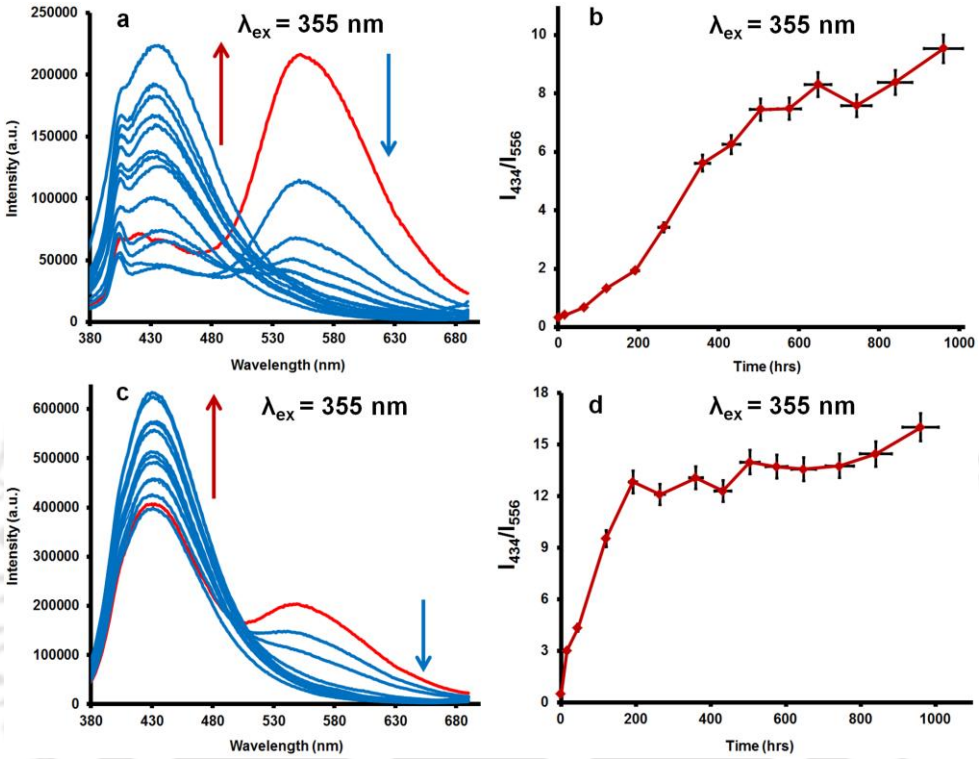

Figure 3b.3 (a, c) A gradual fluorescent blue shift of PF-DPA Pdots (5 μM) by the addition of Aβ1–40 (5 μM) fibrils and CSF (100 μL) aggregates in 1:99, THF: HEPES buffer solution (10 mM, pH 7.4) at 355 nm excitation (0-40 days). (b, d) The enhancements in emission intensity ratios I_{434}/I_{556} for PF-DPA Pdots+Aβ1–40 fibrils and PF-DPA Pdots+CSF aggregate at 355 nm excitation (0-40 days).

The modulating effect on Aβ fibrils is a general therapeutic strategy in AD. Therefore, the ability of modulating mature Aβ fibrils is an essential feature of a potential drug for AD. Hence, the effect of PF-DPA PDots on preformed Aβ1-40 and CSF aggregates were investigated. PF-DPA (5 μM) shows strong red shifted emission band at 556 nm in 1:99, THF: HEPES buffer solution (10 mM, pH 7.4) at 355 and 365 nm excitation (Figure A3b.1). Upon separate addition of Aβ1–40 (5 μM) and CSF (100 μL) aggregates into the PF-DPA Pdots solution, significant fluorescence changes were observed for PF-DPA Pdots + Aβ1–40 fibrils and PF-DPA Pdots + CSF aggregates at 355 and 365 nm excitation respectively

(Figure 3b.3, A3b.2 and A3b.3). After the incubation (0-40 days) of these mixtures at 37 ^{o}C we observed a gradual blue shift in the fluorescence intensities of both PF-DPA Pdots–Aβ1–40 fibrils as well as PF-DPA Pdots–CSF solutions respectively (Figure 3b.3, A3b.2 and A3b.3). The appearance of blue shifted emission band at 434 nm indicated that Aβ1-40 fibrils and CSF aggregates co-assembled into well-ordered supramolecular structures with PF-DPA Pdots via noncovalent interactions such as π-π stacking and hydrogen bonding. These coassembled structures appeared due to the formation of aggregation in parallel face-to-face intermolecular interactions that exhibit (hypsochromic shift) blue-shifted emission bands (H-aggregate formation).[59,60]

In figure 3(b, d), the enhancements in emission intensity ratios (I_{434}/I_{556}) were observed for PF-DPA Pdots+Aβ1-40 fibrils and PF-DPA Pdots+CSF aggregates respectively, from 0 to 960 h (40 days) incubation time. In case of PF-DPA Pdots+Aβ1-40 fibrils, the emission intensity ratios (I_{434}/I_{556}) began to enhance after 20-60 h incubation which is evidenced for the modulation of Aβ1-40 aggregates. Figure 3b.3b depicts elevated emission intensity ratios (I_{434}/I_{556}) with increasing time of incubation until a plateau is reached at 504-960 h, suggesting that completion of reaction between PF-DPA Pdots and Aβ1-40 fibrils occurs at the incubation time of ~504 h (21 days). Similarly, in case of PF-DPA Pdots+CSF aggregates, the emission intensity ratios (I_{434}/I_{556}) began to enhance after 16 h incubation and the plateau is reached at 200-960 h, suggesting that completion of reaction between PF-DPA Pdots and CSF aggregates occurs at the incubation time of ~504 h (21 days) which confirms the modulating effect on CSF aggregates. Subsequently, these results indicate that PF-DPA Pdots can modulate the Aβ1-40 and CSF aggregates in *in vitro* conditions by the formation of coassembled structures via H-aggregation in parallel face-to-face intermolecular interactions.

3b.2.4. Inhibition and modulating effect on Aβ aggregates monitored by ThT assay using PF-DPA PDots

ThT assay has been predominantly used to monitor the transformation of Aβ1-40 monomers to fibrillar aggregates. Herein, we used ThT assay to evaluate the ability of PF-DPA PDots to either control the fibril formation (inhibition) or to modulate the preformed fibrils of Aβ1-40. In case of inhibition assay, PF-DPA PDots (5 μM) and Aβ1-40 monomer (5 μM) was added together with ThT (20 μM) in 1:99, THF: HEPES buffer solution (10 mM, pH 7.4) and monitored the changes from 0-40 days incubation at 37 °C. In case of modulating study, the PF-DPA PDots (5 μM) were separately added into preformed Aβ1-40 oligomers (5 μM), Aβ1-40 fibrils (5 μM) and CSF Aβ aggregates (100 μL) in 1:99, THF: HEPES buffer solution

(10 mM, pH 7.4) and the changes were monitored from 0-40 days incubation at 37 °C (Figure 3b.4). These three mixtures were analyzed using ThT assay by measuring the fluorescence changes at 488 nm (440 nm excitation). Inhibition experiments demonstrated that PF-DPA PDots were able to prevent Aβ1-40 aggregation from Aβ1-40 monomers as indicated by a significant reduction in the fluorescence intensity of ThT from 1-40 days of incubation at 37 °C (Figure 3b.4a). Similarly, we observed that the modulation effect in the mixtures of PF-DPA PDots with Aβ1-40 oligomers, PF-DPA PDots + Aβ1-40 fibrils and PF-DPA PDots + CSF aggregates (Figure 3b.4a). Thus, PF-DPA PDots were found to have prominent effect on inhibition of Aβ1-40 fibrillation and modulation effect on Aβ1-40 oligomers, Aβ1-40 fibrils and CSF aggregates.

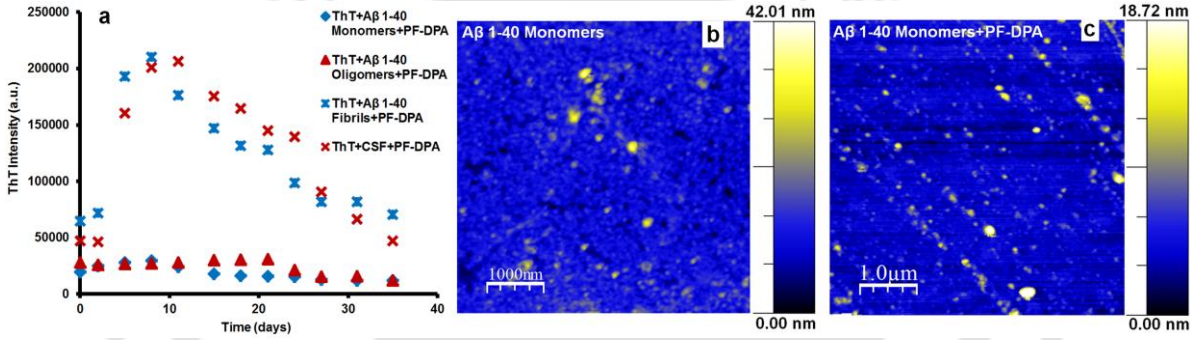

Figure 3b.4 (a) Inhibition and modulating effect of PF-DPA PDots: PF-DPA PDots (5 μM) and Aβ1-40 monomers (5 μM) were added together with ThT (20 μM) in the mixture of solvent fraction of THF: H_2O (1:99) in 10 mM HEPES buffer solution (pH 7.4) from 0-40 days incubation at 37 °C. Modulating effect was observed separately in the mixtures of PF-DPA PDots with preformed Aβ1-40 oligomers, PF-DPA PDots + Aβ1-40 fibrils and PF-DPA PDots + CSF aggregates with ThT (20 μM). (b) AFM images of Aβ1-40 monomers. (c) AFM images of inhibition of Aβ1-40 fibril formation from Aβ1-40 monomers in presence of PF-DPA PDots.

Concurrently, while exciting (at 355 and 365 nm) the mixture of solutions separately, we observed significant fluorescence changes on PF-DPA PDots + Aβ1-40 oligomers, PF-DPA PDots + Aβ1-40 fibrils and PF-DPA PDots + CSF aggregates in presence of ThT (Figure 3b.5a-3b.5c and A3b.4-A3b.6). Subsequently, we observed fluorescence changes after incubation (0-40 days) of these mixture of solutions at 37 ^{o}C with a gradual blue shift (hypsochromic shift) in ThT+PF-DPA Pdots–Aβ1–40 oligomers, ThT+PF-DPA Pdots–Aβ1–40 fibrils and ThT+PF-DPA Pdots–CSF aggregates respectively (Figure 3b.5a-3b.5c and A3b.4-A3b.6). The blue shifted emission at 434 nm occurs due to Aβ1–40 oligomers, Aβ1-40 fibrils and CSF aggregates which forms a well-ordered supramolecular co-assembly structure

with PF-DPA Pdots via noncovalent interactions. This noncovalent interactions may likely form as a result of hydrophobic interaction between hydrophobic region of Aβ1–40 and PF-DPA Pdots hydrophobic functionalities which induces the π-π stacking and leads to the formation of parallel face-to-face intermolecular aggregation.[18,64] The hydrophobic region in Aβ1-40 from 17 to 21 is very crucial for their assembly into fibrils formation,[25] due to this reason, it is presumed that PF-DPA Pdots have modulating ability towards Aβ peptides. These results indicate that the hydrophobic backbone of PF-DPA polymer can recognize and modulate Aβ aggregates and could also be used as inhibitor for Aβ fibrillization.

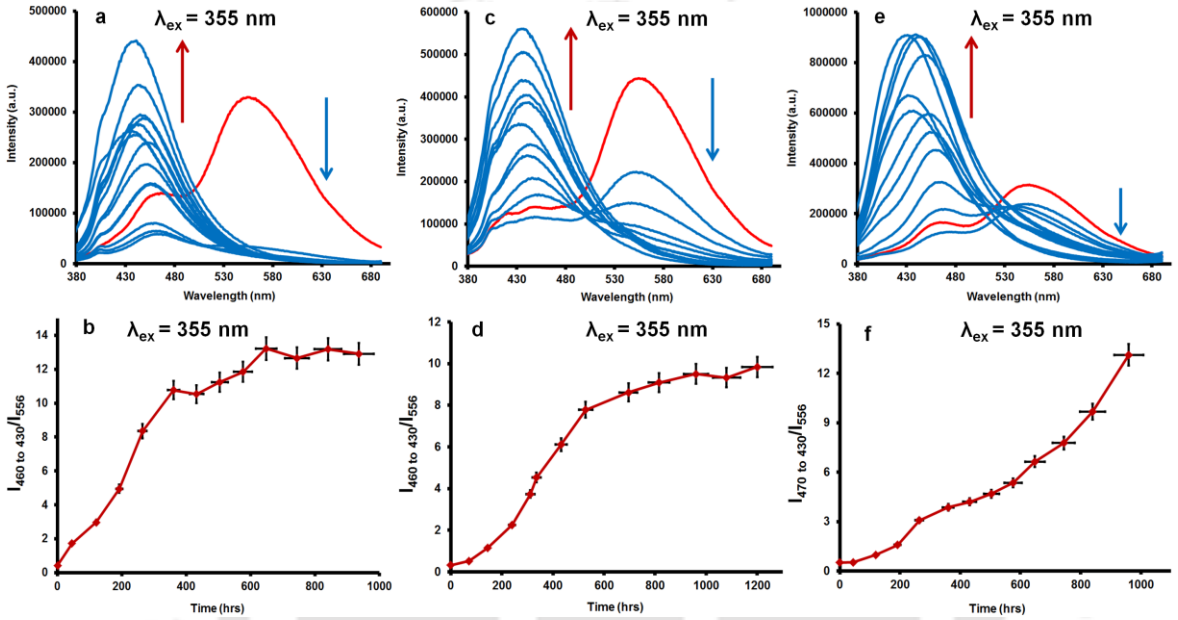

Figure 3b.5 (a, c and e) A gradual fluorescent blue shift of PF-DPA Pdots (5 μM) by the addition of Aβ1–40 (5 μM) oligomers, Aβ1–40 (5 μM) fibrils and CSF (100 μL) aggregates with ThT (20 μM) in the mixture of solvent fraction of THF: H_2O (1:99) in 10 mM HEPES buffer solution (pH 7.4) at 355 nm excitation (0-40 days). (b, d and e) The enhancement in emission intensity ratios I_{434}/I_{556} for PF-DPA Pdots+Aβ1–40 oligomers, PF-DPA Pdots+Aβ1–40 fibrils and PF-DPA Pdots+CSF aggregates at 355 nm excitation (0-40 days).

Since, ThT is a known dye to recognize Aβ1-40 fibrils (but not Aβ oligomers), we examined PF-DPA Pdots modulating effect in presence of ThT mixed solutions such as ThT+Aβ1-40 oligomers, ThT+Aβ1-40 fibrils and ThT+CSF aggregates. Moreover, its competing nature with ThT was also examined to ascertain how PF-DPA Pdots modulates Aβ1-40 oligomers, Aβ1-40 fibrils and CSF aggregates by forming co-assembly structures. The competing study and modulating effect are examined by the investigation of enhancements in emission intensity ratios ($I_{470\text{-}434}/I_{556}$). In figure 3b.5b, 3b.5d and 3b.5f, the enhancements in emission

intensity ratios ($I_{470-434}/I_{556}$) were observed for PF-DPA Pdots+Aβ1-40 oligomers, PF-DPA Pdots+Aβ1-40 fibrils and PF-DPA Pdots+CSF aggregates in presence of ThT, from 0 to 960 h (40 days) incubation time. In case of PF-DPA Pdots+Aβ1-40 oligomers, the emission intensity ratios ($I_{460-434}/I_{556}$) began to enhance after 16-45 h incubation which confirmed the modulation of Aβ1-40 oligomers. Figure 3b.5b depicts elevated emission intensity ratios ($I_{460-434}/I_{556}$) with increasing time of incubation until a plateau is reached at 648-936 h, suggesting that formation of coassembly structure or completion of reaction between PF-DPA Pdots and Aβ1-40 oligomers occurs after the incubation time of around 360-648 h (15-27 days).

In case of PF-DPA Pdots+Aβ1-40 fibrils, the emission intensity ratios ($I_{460-434}/I_{556}$) began enhancing after 75-144 h incubation which also confirms the modulation of Aβ1-40 aggregates. Figure 3b.5d depicts elevated emission intensity ratios ($I_{460-434}/I_{556}$) with increasing time of incubation until a plateau is reached at 816-1200 h, suggesting the completion of reaction between PF-DPA Pdots and Aβ1-40 fibril that occurs after the incubation time of around 816-960 h (40 days). Similarly, in case of PF-DPA Pdots+CSF aggregates (Figure 3b.5f), the emission intensity ratios ($I_{470-434}/I_{556}$) began enhancing after 120-168 h incubation time and the formation of coassembly structure or completion of reaction between PF-DPA Pdots and CSF aggregates occurred at ~960 h (40 days) incubation time which confirms complete modulating effect on CSF aggregates. Consequently, the plateau is reached for Aβ1-40 oligomers at 360-648 h but for Aβ1-40 and CSF aggregates it reached at 936 and 960 h respectively which indicates that Aβ1-40 oligomers were trapped or modulated by PF-DPA Pdots with less time as compared to Aβ1-40 and CSF aggregates in presence of ThT. In conclusion, these results indicate that PF-DPA Pdots are able to co-assemble and modulate the Aβ1-40 oligomers, Aβ1-40 fibrils and CSF aggregates in presence of ThT and *in vitro* conditions by the formation of H-aggregation in parallel face-to-face intermolecular interactions.

3b.2.5. Inhibition and modulating effect on Aβ aggregates confirmed by AFM images using PF-DPA PDots

To further confirm the results obtained from the fluorescence study (Figure 3b.3) and ThT assay, we recorded AFM images to analyse the effect of PF-DPA PDots on the process of inhibition of fibrillization and modulation effect on preformed Aβ1-40 oligomers, Aβ1-40 and CSF aggregates (Figure 3b.4 and 3b.6). When, Aβ1-40 monomers were incubated in HEPES buffer solutions (10 mM, pH 7.4) at 37 °C for 0-4 days, the formation of long

fibrillary aggregates were confirmed (Figure 3b.6a). Surprisingly, in presence of PF-DPA PDots, Aβ1-40 monomers showed no fibrils in the inhibition experiment (21 days incubation), which confirms the prevention of fibrillar formation from Aβ1-40 monomers (Figure 3b.4b and 3b.4c). In case of modulation experiment (21 days incubation), no fibrils were observed in the presence of PF-DPA PDots with Aβ1-40 oligomers, Aβ1-40 fibrils and CSF aggregates (Figure 3b.6A and 3b.6B). Consequently, PF-DPA PDots effectively inhibited Aβ1-40 fibril formation and modulated the preformed Aβ1-40 oligomers, Aβ1-40 fibrils and CSF aggregates which strongly support the ThT assay results.

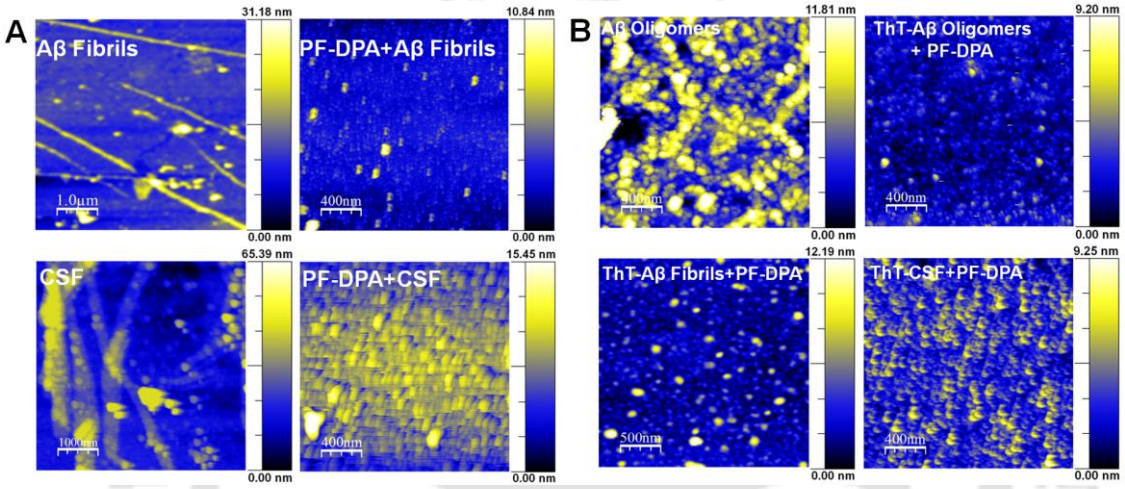

Figure 3B.6 (A) Disaggregation or modulation effect on Aβ1-40 fibrils and CSF aggregates by PF-DPA PDots (21 days incubation time). (B) Disaggregation or modulation effect on Aβ1-40 oligomers, Aβ1-40 fibrils and CSF aggregates by PF-DPA PDots in presence of ThT (21 days incubation time).

3b.2.6. Modulating effect on Aβ aggregates confirmed by FT-IR and UV-visible spectra using PF-DPA PDots

The formation of β-sheet-rich structure is an early crucial step in amyloidogenesis towards major Aβ aggregates.[65-67] In order to find the modulating effect on Aβ1-40 fibrils and CSF aggregates, we performed FT-IR spectra in the absence and presence of PF-DPA PDots (Figure 3b.7a and 3b.7b). The initial secondary structure of Aβ1-40 fibrils and CSF aggregates appeared as a major peak at 1632 ±2 cm^{-1} which is a confirmation peak for β-sheet structure (Figure 3b.7a and 3b.7b). Further, PF-DPA PDots (5 μM) was mixed into preformed Aβ1-40 and CSF aggregates in 1:99, THF: HEPES buffer solution (10 mM, pH 7.4) and the spectra were monitored after 21 days incubation at 37 °C for investigating the modulation effect on Aβ1-40 fibrils (5 μM) and CSF aggregates (100 μL). The major peak at 1632 ± 2 cm^{-1} diminishes and a new peak appeared at 1644 ± 2 cm^{-1} indicating that Aβ1-40

fibrils and CSF aggregates converted from its initial β-sheet structure into a random coil structure (Figure 3b.7a and 3b.7b).

Further, the modulating effect on Aβ1-40 fibrils and CSF aggregates was investigated by UV-vis spectra in the absence and presence of PF-DPA PDots (Figure 3b.7c). The PF-DPA PDots (5 μM) absorption band appears at 377 nm which is a characteristic peak for PF-DPA PDots aggregation. Later, PF-DPA PDots absorption band at 377 nm disappeared in the presence of Aβ1-40 fibrils (5 μM) and CSF aggregates (100 μL) (21 days incubation time) and a new enhanced absorption band was observed at ~264 nm which is 9 nm blue-shifted from the 272 nm of Aβ aggregates. These absorbance changes were observed due to the formation of face-to-face coassembly structure between PF-DPA PDots and Aβ aggregates by H-aggregation (Figure 3b.7c).[68,69]

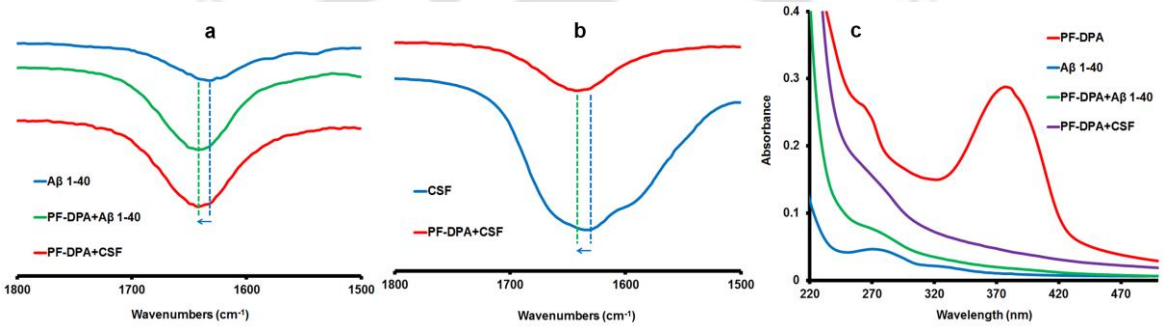

Figure 3b.7 (a, b) FT-IR spectra of Aβ1–40 fibrils (5 μM), PF-DPA PDots + Aβ1–40 fibrils, CSF and PF-DPA PDots + CSF aggregates (100 μL) in the mixture of solvent fraction of THF: H_2O (1:99) in 10 mM HEPES buffer solution (pH 7.4). (c) UV-vis spectra of PF-DPA PDots (5 μM) (blue curve), Aβ1–40 fibrils (5 μM), PF-DPA PDots + Aβ1–40 fibrils, and PF-DPA PDots + CSF aggregates (100 μL) in the mixture of solvent fraction of THF: H_2O (1:99) in 10 mM HEPES buffer solution (pH 7.4).

3b.2.7. Modulating effect on Aβ aggregates confirmed by DLS using PF-DPA PDots

DLS measurements were carried out to determine the size of the PF-DPA PDots, Aβ aggregates (Aβ1–40, CSF) and modulating effect on Aβ aggregates (Aβ 1–40, CSF) with PF-DPA PDots in 10 mM HEPES buffer solution (pH 7.4). It is established that the PF-DPA PDots (~164 ± 60) could accelerate the disaggregation of Aβ fibril aggregates (Aβ1–40, CSF) in aqueous solution (Figure 3b.8a and 3b.8b). These results confirmed that the hydrodynamic particle diameter of Aβ1–40 fibrils (396–615 nm) and CSF aggregates (530–1106 nm) are bigger in size as compared to the co-assembly structure of PF-DPA PDots + Aβ1–40 (190 ±

65 nm) and PF-DPA PDots + CSF (164–190 nm) respectively. Thus, this result supports the results of ThT assay study and proves that PF-DPA PDots efficiently modulate the Aβ1–40 fibrils and CSF aggregates by the formation of co-assembly structure between PF-DPA PDots and Aβ aggregates by noncovalent interactions.

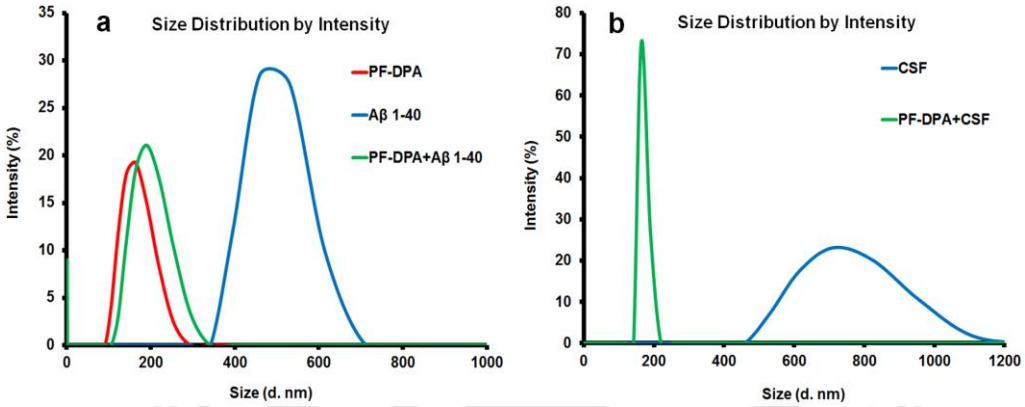

Figure 3b.8 (a, b) Hydrodynamic particle diameter of PF-DPA PDots (5 μM), Aβ1–40 fibrils (5 μM), PF-DPA PDots + Aβ1–40 fibrils, and PF-DPA PDots + CSF aggregates (100 μL) were measured by dynamic light scattering method (21 days incubation).

3b.2.8. Mechanism for Aβ aggregation and modulating effect on Aβ fibrils

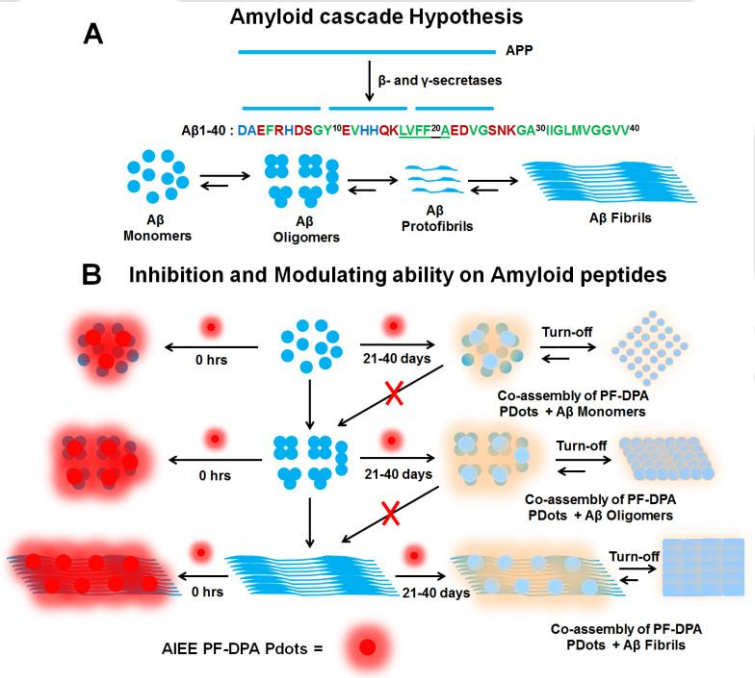

Scheme 3b.1 (A) Schematic representation of the amyloid cascade hypothesis. The amino acid sequences of Aβ1-40 are shown: metal binding residues (blue); hydrophilic (brown), hydrophobic residues (green) and self-recognition sequence (underlined). (B) Schematic representation for inhibition of Aβ fibrillation and modulating effect on Aβ oligomers and fibrils.

Initially, Aβ peptides are derived from the cleavage of trans-membrane amyloid precursor protein (APP) by β- and γ-secretases. Then, the Aβ aggregates are formed by a highly complex process that involves sequential formations of various Aβ aggregation species, like oligomers, protofibrils and fibrils. There are two phases involved in Aβ aggregate formation, namely, one is the lag phase (nucleation) and second one is the growth phase (elongation). During lag phase, Aβ monomers self-assemble into β-sheet-rich oligomers and then form stabilized nuclei. Then, the stabilized nuclei grow and elongate in growth phase via monomer or oligomer addition to form protofibrils and fibrils (Scheme 3b.1A).[3b.18]

Moreover, based on the obtained experimental results, herein, we proposed a schematic representation to interpret the working mechanism of PF-DPA PDots on Aβ monomers, Aβ oligomers and Aβ aggregates (Scheme 3b.1B). In presence of PF-DPA PDots, Aβ1-40 monomers are inhibited to form Aβ1-40 fibrillation which we examined and discussed in above figure 4a (0-40 days incubation) because PF-DPA PDots and Aβ1-40 monomers form co-assembly structure via noncovalent interactions such as hydrophobic interactions or hydrogen bonding (Scheme 3b.1B). Further, PF-DPA PDots can also modulate the Aβ oligomers and Aβ fibrils into different forms of co-assembly structure via noncovalent interactions like hydrophobic interactions or hydrogen bonding (Scheme 3b.1B). In case of Aβ oligomers, PF-DPA PDots block the step of elongation to form Aβ oligomers into the protofibrils and fibrils (Scheme 3b.1B). This significant modulating effect on Aβ oligomers is an important step in the treatment of AD because oligomers are highly toxic in nature which are mainly formed through the nucleation or lag phase. As a result, the multifunctional PF-DPA PDots have great utility in AD treatments due to its ability of inhibition on Aβ fibrillation and modulating effect on Aβ oligomers and fibrils by the formation of H-aggregation in parallel face-to-face intermolecular interactions.

3b.3. Conclusion

In summary, herein we designed and developed an aggregation induced enhanced emission (AIEE) PF-DPA PDots polymer and examined its inhibition ability on Aβ fibrillation and modulating effect on Aβ oligomers and fibrils. Various techniques such as ThT assay, FT-IR and UV-vis spectra, DLS and atomic force microscopy (AFM) were utilized to confirm this modulating effect. According to the obtained experimental results, we found that PF-DPA PDots has the ability to inhibit Aβ fibrillation and prevent the formation of Aβ spherical oligomers into aggregated fibrils. In addition, PF-DPA PDots showed an exceptional modulating effect on preformed Aβ1-40 oligomers and fibrils or CSF aggregates by the

formation of coassembly structure between PF-DPA PDots and Aβ aggregates. Therefore, the multifunctional PF-DPA PDots have great utility in AD treatments due to its ability of inhibition on Aβ fibrillation and modulating effect on Aβ oligomers and fibrils by the formation of H-aggregation in parallel face-to-face intermolecular interactions.

3b.4. Experimental Section

3b.4.1. Materials and methods

All the reagents and chemicals were purchased from Aldrich Chemicals, Merck or Ranbaxy (India) and used as received. Milli-Q water and HPLC grade solvents were used in all the experiments. Solvents were degassed using three freeze thaw cycles or flushed with nitrogen for at least 1 h prior to use when necessary. β-Amyloid (1-40), human was purchased from GL Biochem Ltd., Shanghai, China. The cerebrospinal fluid (CSF) samples were gifted by Guwahati Neurological Research Center and Hospital, Guwahati, India and were obtained as part of routine care from patients. Nonetheless, information on explaining the purpose of this study was specified at the time of sample collection adhering to the bioethics policy of the hospital.

UV–vis absorption spectra were recorded on a PerkinElmer Lambda–25 spectrometer. Fluorescence spectra were carried out on a FluoroMax-4 Spectrofluorometer-Horiba Scientific. A 10 × 10 mm quartz cuvette was used for solution spectra and emission was collected at 90° relative to the excitation beam. FT–IR spectra were recorded on a PerkinElmer spectrometer with samples prepared as KBr pellets. A fresh glass slide was used for every experiment. Deionized water was obtained from Milli–Q system (Millipore). Atomic force microscopy (AFM) was recorded on Agilent instrument, model 5500 series with noncontact mode. The PF-DPA NPs were examined using an ultrahigh resolution transmission electron microscope (TEM; JEM 2100; Jeol, Peabody, MA, USA). DLS were measured by Zetasizer Nano series Nano-ZS90 instrument.

3b.4.2. Preparation of PF-DPA stock solution

PF-DPA stock solution was prepared at the concentration of 1.0×10^{-3} mL^{-1} in 10 mL THF. This stock solution was diluted to desire concentration for each titration in 3 mL cuvette.

3b.4.3. Preparation of HEPES buffer solutions

All the experiments like UV-Visible, FT-IR and fluorescence titrations were performed in 10 mM HEPES buffer and pH maintained at 7.4 by using 4M NaOH or 5M HCl solution.

3b.4.4. TFA/HFIP treatment of Aβ1–40 peptides

Aβ1–40 was disaggregated using trifluoroacetic acid/1,1,1,3,3,3-hexafluuor-2-propanol (TFA/HFIP) by an established method. 0.5 mg of Aβ1–40 was added to a 2.5 mL Eppendorf tube and dissolved in TFA to obtain a homogeneous solution free of aggregates. TFA was then evaporated using argon gas. Any leftover TFA was further removed by adding HFIP followed by evaporation using an argon gas flow to obtain a film like material. This process was repeated twice. To the Eppendorf tube, 2.5 mL of HEPES (10 mM, pH 7.4) was added followed by sonication and vortexing to obtain a final concentration of 4.6×10^{-4} M. Fibril formation was monitored using a ThT binding assay.

3b.4.5. Preparation of Aβ1–40 aggregates and ThT Binding Assay

For the preparation of amyloid peptide aggregates, after the TFA/HFIP treatment for amyloid peptide the Aβ1–40 (5 μM) was initially incubated with ThT (20 μM) at 37 °C for 0-42 h (pH 7.4 in HEPES) with steady agitation. Further, Aβ1–40 aggregated amyloid fibrils were monitored with different time incubations by monitoring ThT (20 μM) fluorescent enhancement peak at λ_{em} 488 nm (λ_{ex} 440 nm).

3b.4.6. ThT binding assay for CSF using fluorescence spectroscopy

The presence of Aβ fibrils in CSF was confirmed by the gradual addition of CSF sample up to 100 μL solution (each addition 10 μL) into ThT (20 μM) solution (pH 7.4 in HEPES). Further, we observed a gradual enhancement in the fluorescence intensity of ThT at 488 nm validating strongly the existence of aggregated Aβ fibrils in the CSF sample.

3b.4.7. Preparation of PF-DPA nanoparticles or PDots

PF-DPA (10 μM) polymer was regularly injected into THF: H_2O (1:9) with vigorous stirring at room temperature, using a syringe. After the injection of PF-DPA, the solution was filtered by membrane filter with 0.2 μm pore size. Then the collected PF-DPA nano particles or PDots were used for other studies.

3b.4.8. Modulating effect on Aβ1–40 fibrils and CSF aggregates by PF-DPA PDots

The blue shifted emission spectra at 534 from 556nm for PF-DPA PDots (5 μM) with Aβ1-40 fibrils (5 μM) and CSF aggregates (100 μL) were observed while exciting at 355 and 365 nm. Aβ1-40 fibrils (5 μM) and CSF aggregates (100 μL) were mixed with PF-DPA PDots (5 μM) in 3 mL of 10 mM HEPES buffer solution (pH 7.4). Then, fluorescence spectra were

monitored for all the samples in different interval of incubation time from 0-40 days at 37 °C in water bath.

3b.4.9. Inhibition of Aβ1–40 fibrils formation monitored by ThT assay using PF-DPA PDots

ThT emission changes at 488 nm were measured for inhibition of Aβ1–40 fibrils formation for the mixture of PF-DPA PDots with Aβ1-40 monomer in presence of ThT while exciting at 440 nm. Aβ1-40 monomer (5 μM) was mixed with PF-DPA PDots (5 μM) in 3 mL of 10 mM HEPES buffer solution (pH 7.4). Then, fluorescence spectra were monitored in different interval of incubation time from 0-40 days at 37 °C in water bath.

3b.4.10. Modulating effect on Aβ1–40 oligomers, Aβ1–40 fibrils and CSF aggregates monitored by ThT assay using PF-DPA PDots

The blue shifted emission spectra at 534 from 556nm for PF-DPA PDots with Aβ1–40 oligomers, Aβ1-40 fibrils and CSF aggregates were measured in presence of ThT while exciting at 355 and 365 nm. Aβ1-40 oligomers (5 μM), Aβ1-40 fibrils (5 μM) and CSF aggregates (100 μL) were mixed with PF-DPA PDots (5 μM) separately in presence of ThT (20 μM) in 3 mL of 10 mM HEPES buffer solution (pH 7.4). Then, fluorescence spectra were monitored for all the samples in different interval of incubation time from 0-40 days at 37 °C in water bath.

3b.4.11. Sample preparation for AFM images

As prepared solutions of PF-DPA PDots (5 μM) + Aβ1-40 monomers (5 μM), PF-DPA PDots (5 μM) + Aβ1-40 fibrils (5 μM), PF-DPA PDots (5 μM) + CSF aggregates (100 μL), PF-DPA PDots (5 μM) + Aβ1-40 oligomers (5 μM) + ThT (20 μM), PF-DPA PDots (5 μM) + Aβ1-40 fibrils (5 μM) + ThT (20 μM), and PF-DPA PDots (5 μM) + CSF aggregates (100 μL) + ThT (20 μM) were kept in 3 mL of 10 mM HEPES buffer solution (pH 7.4) for 0−40 days incubation at 37 °C in water bath. These solutions were further utilized to monitor the AFM morphology. All the solutions were separately diluted by 10 times and then from the diluted solutions 5 μL of all the samples were dropped onto freshly cleaned glass slide separately and dried at room temperature overnight and recorded by atomic force microscopy (AFM) on an Agilent instrument, model 5500 series with noncontact mode. Moreover, similarly we monitor the AFM morphology of PF-DPA PDots (5 μM), Aβ1-40 fibrils (5 μM) and CSF aggregates (30 μL).

3b.4.12. Sample preparation for FT-IR spectra

As prepared solutions of PF-DPA PDots (5 μM) + Aβ1-40 fibrils (5 μM) and PF-DPA PDots (5 μM) + CSF aggregates (100 μL) were kept in 3 mL of 10 mM HEPES buffer solution (pH 7.4) for 0−40 days incubation at 37 °C in water bath. These solutions were further utilized to monitor the FT-IR spectra. 30−50 μL of all the samples were dropped onto the freshly cleaned glass slide separately and dried at room temperature overnight and FT−IR spectra recorded on a PerkinElmer spectrometer with samples prepared as KBr pellets. Moreover, similarly we recorded FT-IR spectra of Aβ1-40 fibrils (5 μM) and CSF aggregates (30-50 μL).

3b.4.13. Dynamic light scattering study

As prepared solutions of PF-DPA PDots (5 μM) + Aβ1-40 fibrils (5 μM) and PF-DPA PDots (5 μM) + CSF aggregates (100 μL) were kept in 3 mL of 10 mM HEPES buffer solution (pH 7.4) for 0−40 days incubation at 37 °C in water bath. These solutions were further utilized to monitor the hydrodynamic particle diameter by DLS. All the solutions were separately diluted by 10 times, and then, from the diluted solution, 500 μL of all the samples were used to record DLS measurements by Zetasizer Nano series Nano-ZS90 instrument. Moreover, similarly we recorded hydrodynamic particle diameter of PF-DPA PDots (5 μM), Aβ1-40 fibrils (5 μM) and CSF aggregates (30 μL in 500 HEPES Buffer).

References

(1) Selkoe, D. J. *Nature* **2003,** *426*, 900.

(2) Fink, A. L. *Acc. Chem. Res.* **2006,** *39*, 628.

(3) Li, M.; Howson, S. E.; Dong, K.; Gao, N.; Ren, J.; Scott, P.; Qu, X. *J. Am. Chem. Soc.* **2014,** *136*, 11655.

(4) Selkoe, D. J. *Nature* **1999,** *399*, A23.

(5) Hardy, J.; Selkoe, D. J. *Science* **2002,** *297*, 353.

(6) Cleary, J. P.; Walsh, D. M.; Hofmeister, J. J.; Shankar, G. M.; Kuskowski, M. A.; Selkoe, D. J.; Ashe, K. H. *Nat. Neurosci.* **2004,** *8*, 79.

(7) Petkova, A. T.; Leapman, R. D.; Guo, Z.; Yau, W.-M.; Mattson, M. P.; Tycko, R. *Science* **2005,** *307*, 262.

(8) Glabe, C. G. *Neurobiol. Aging* **2006,** *27*, 570.

(9) Lansbury, P. T.; Lashuel, H. A. *Nature* **2006,** *443*, 774.

(10) Haass, C.; Selkoe, D. J. *Nat. Rev. Mol. Cell Biol.* **2007,** *8*, 101.

(11) Eisenberg, D.; Nelson, R.; Sawaya, M. R.; Balbirnie, M.; Sambashivan, S.; Ivanova, M. I.; Madsen, A. O.; Rieke, C. *Acc. Chem. Res.* **2006,** *39*, 568.

(12) Li, M.; Howson, S. E.; Dong, K.; Gao, N.; Ren, J.; Scott, P.; Qu, X. *J. Am. Chem. Soc.* **2014,** *136*, 11655.

(13) Hawkes, C. A.; Ng, V.; Mclaurin, J. *Drug Dev. Res.* **2009,** *70*, 111.

(14) Mangialasche, F.; Solomon, A.; Winblad, B.; Mecocci, P.; Kivipelto, M. *Lancet Neurol.* **2010,** *9*, 702.

(15) Man, B. Y. W.; Chan, H. M.; Leung, C. H.; Chan, D. S. H.; Bai, L. P.; Jiang, Z. H.; Li, H. W.; Ma, D. L. *Chem. Sci.* **2011,** *2*, 917.

(16) Scott, L. E.; Telpoukhovskaia, M.; Rodriguez-Rodriguez, C.; Merkel, M.; Bowen, M. L.; Page, B. D. G.; Green, D. E.; Storr, T.; Thomas, F.; Allen, D. D.; Lockman, P. R.; Patrick, B. O.; Adam, M. J.; Orvig, C. *Chem. Sci.* **2011,** *2*, 642.

(17) Wang, Q.; Yu, X.; Patal, K.; Hu, R.; Chuang, S.; Zhang, G.; Zheng, J. *ACS Chem. Neurosci.* **2013,** *4*, 1004.

(18) Du, W. J.; Guo, J. J.; Gao, M. T.; Hu, S. Q.; Dong, X. Y.; Han, Y. F.; Liu, F. F.; Jiang, S. Y.; Sun, Y. *Sci. Rep.* **2015,** *5*, 7992.

(19) Savelieff, M. G.; DeToma, A. S.; Derrick, J. S.; Lim, M. H. *Acc. Chem. Res.* **2014,** *47*, 2475.

(20) Song, Y.; Cheng, P-N.; Zhu, L.; Moore, E. G.; Moore, J. S. *J. Am. Chem. Soc.* **2014,** *136,* 5233.

(21) Palmal, S.; Jana, N. R.; Jana, N. R. *J. Phys. Chem. C* **2014,** *118,* 21630.

(22) Miura, Y.; You, C.; Ohnishi, R. *Adv. Mater.* **2008,** *9,* 024407.

(23) Wada, M.; Miyazawa, Y.; Miura, Y. *Polym. Chem.* **2011,** *2,* 1822.

(24) Funke, S. A.; Willbold, D. *Curr. Pharm. Des.* **2012,** *18,* 755.

(25) Rajasekhar, K.; Suresh, S. N.; Manjithaya, R.; Govindaraju, T. *Sci. Rep,* **2015,** *5,* 8139.

(26) Zhang, M.; Yu, Y.; Wang, C. X.; Yang, Y. L.; Wang, C. *Adv. Mater.* **2013,** *25,* 3780.

(27) Cabaleiro-Lago, C.; Quinlan-Pluck, F.; Lynch, I.; Lindman, S.; Minogue, A. M.; Thulin, E.; Walsh, D. M.; Dawson, K. A.; Linse, S. *J. Am. Chem. Soc.* **2008,** *130,* 15437.

(28) Cabaleiro-Lago, C.; Quinlan-Pluck, F.; Lynch, I.; Dawson, K. A.; Linse, S. *ACS Chem. Neurosci.* **2010,** *1,* 279.

(29) Yoo, S. I.; Yang, M.; Brender, J. R.; Subramanian, V.; Sun, K.; Joo, N. E.; Jeong, S.-H.; Ramamoorthy, A.; Kotov, N. A. *Angew. Chem., Int. Ed.* **2011,** *50,* 5110.

(30) Skaat, H.; Chen, R.; Grinberg, I.; Margel, S. *Biomacromolecules* **2012,** *13,* 2662.

(31) Mahmoudi, M.; Akhavan, O.; Ghavami, M.; Rezaee, F.; Ghiasi, S. M. A. *Nanoscale* **2012,** *4,* 7322.

(32) Liao, Y.-H.; Chang, Y.-J.; Yoshiike, Y.; Chang, Y.-C.; Chen, Y.-R. *Small* **2012,** *8,* 3631.

(33) Wang, C.; Yang, A.; Li, X.; Li, D.; Zhang, M.; Du, H.; Li, C.; Guo, Y.; Mao, X.; Dong, M.; Besenbacher, F.; Yang, Y. *Nanoscale* **2012,** *4,* 1895.

(34) Linse, S.; Cabaleiro-Lago, C.; Xue, W.-F.; Lynch, I.; Lindman, S.; Thulin, E.; Radford, S. E.; Dawson, K. A. *Proc. Natl. Acad. Sci. U.S.A.* **2007,** *104,* 8691.

(35) Wu, W.-H.; Sun, X.; Yu, Y.-P.; Hu, J.; Zhao, L.; Liu, Q.; Zhao, Y.-F.; Li, Y.-M. *Res. Commun.* **2008,** *373,* 315.

(36) Zhang, D.; Neumann, O.; Wang, H.; Yuwono, V. M.; Barhoumi, A.; Perham, M.; Hartgerink, J. D.; Wittung-Stafshede, P.; Halas, N. J. *Nano Lett.* **2009,** *9,* 666.

(37) Wagner, S. C.; Roskamp, M.; Pallerla, M.; Araghi, R. R.; Schlecht, S.; Koksch, B. *Small* **2010,** *6,* 1321.

(38) Roberti, M. J.; Morgan, M.; Menéndez, G.; Pietrasanta, L. I.; Jovin, T. M.; Jares-Erijman, E. A. *J. Am. Chem. Soc.* **2009,** *131,* 8102.

(39) Vannoy, C. H.; Leblanc, R. M. *J. Phys. Chem. B* **2010,** *114,* 10881.

(40) Tjernberg, L. O.; Naslund, J.; Lindqvist, F.; Johansson, J.; Karlstrom, A. R.; Thyberg, J.; Terenius, L.; Nordstedt, C. *J. Biol. Chem.* **1996,** *271,* 8545.

(41) Gessel, M. M.; Wu, C.; Li, H.; Bitan, G.; Shea, J. E.; Bowers, M. T. *Biochemistry* **2012,** *51,* 108.

(42) Brambilla, D.; Verpillot, R.; Droumaguet, B. L.; Nicolas, J.; Taverna, M.; Kona, J.; Lettiero, B.; Hashemi, S. H.; Kimpe, L. D.; Canovi, M.; Gobbi, M.; Nicolas, V.; Scheper, W.; Moghimi, S. M.; Tvaroska, I.; Couvreur, P.; Andrieux, K. *ACS Nano* **2012,** *6,* 5897.

(43) Cabaleiro-Lago, C.; Szczepankiewicz, O.; Linse, S. *Langmuir* **2012,** *28,* 1852.

(44) Li, M.; Liu, Z.; Ren, J. S.; Qu, X. G. *Chem. Sci.* **2012,** *3,* 868.

(45) Ma, Q.; Wei, G.; Yang, X. *Nanoscale* **2013,** *5,* 10397.

(46) Olmedo, I.; Araya, E.; Sanz, F.; Medina, E.; Arbiol, J.; Toledo, P.; Alvarez-Lueje, A.; Giralt, E.; Kogan, M. J. *Bioconjugate Chem.* **2008,** *19,* 1154.

(47) Adura, C.; Guerrero, S.; Salas, E.; Medel, L.; Riveros, A.; Mena, J.; Arbiol, J.; Albericio, F.; Giralt, E.; Kogan, M. J. *ACS Appl. Mater. Interfaces* **2013,** *5,* 4076.

(48) Lu, T. Y.; Kao, P. F.; Lee, C. M.; Huang, S. T.; Lin, C. M. *J. Food Drug Anal.* **2011,** *19,* 151.

(49) Palmal, S.; Maity, A. R.; Singh, B. K.; Basu, S.; Jana, N. R.; Jana, N. R. *Chem. Eur. J.* **2014,** *20,* 6184.

(50) Mahmoudi, M.; Quinlan-Pluck, F.; Monopoli, M. P.; Sheibani, S.; Vali, H.; Dawson, K. A.; Lynch, I. *ACS Chem. Neurosci.* **2013,** *4,* 475.

(51) Kouyoumdjian, H.; Zhu, D. C.; El-Dakdouki, M. H.; Lorenz, K.; Chen, J.; Li, W.; Huang, X. *ACS Chem. Neur. Sci.* **2013,** *4,* 575.

(52) Saikia, G.; Iyer, P. K. *J. Org. Chem.* **2010,** *75,* 2714.

(53) Fukuda, M.; Sawada, K.; Yoshino, K. *Jpn. J. Appl. Phys.,* **1989,** *28,* L1433.

(54) Paul, G. S.; Sarmah, P. J.; Iyer, P. K.; Agarwal, P. *Macromol. Chem. Phys.* **2008,** *209,* 417.

(55) Muthuraj, B.; Hussain, S.; Iyer, P. K. *Polym. Chem.* **2013,** *4,* 5096.

(56) An, B.-K.; Kwon, S.-K.; Jung, S.-D.; Park, S. Y. *J. Am. Chem. Soc.* **2002,** *124,* 14410.

(57) Luo, J.; Xie, Z.; Lam, J. W. Y.; Cheng, L.; Chen, H.; Qiu, C.; Kwok, H. S.; Zhan, X.; Liu, Y.; Zhu, D.; Tang, B. Z. *Chem. Commun.*, **2001,** 1740.

(58) Chen, C-P.; Huang, Y-C.; Liou, S-Y.; Wu, P-J.; Kuo, S-Y.; Chan, Y-H. *ACS Appl. Mater. Interfaces* **2014,** *6,* 21585.

(59) Oelkrug, D.; Tompert, A.; Gierschner, J.; Egelhaaf, H.; Hanack, M.; Hohloch, M.; Steinhuber, E. *J. Phys. Chem. B,* **1998,** *102,* 1902.

(60) An, B. K.; Gierschner, J.; Park, S. Y. *Acc. Chem. Res.,* **2012,** *45,* 544.

(61) Ma, Q.; Wei, G.; Yang, X. *Nanoscale*, **2013,** *5*, 10397.

(62) Ban, T.; Hamada, D.; Hasegawa, K.; Naiki, H.; Goto, Y. *J. Biol. Chem.*, **2003,** *278*, 16462.

(63) Muthuraj, B.; Hussain, S.; Iyer, P. K. *Polym. Chem.* **2013,** *4*, 5096.

(64) Ow, S-Y.; Bekard, I.; Blencowe, A.; Qiaoa, G. G.; Dunstan, D. E. *J. Mater. Chem. B,* **2015,** *3*, 1350.

(65) Ridgley, D. M.; Ebanks, K. C.; Barone, J. R. *Biomacromolecules* **2011,** *12*, 3770.

(66) Dehn, S.; Castelletto, V.; Hamley, I. W.; Perrier, S. *Biomacromolecules* **2012,** *13*, 2739.

(67) Nilsson, M. R.; Dobson, C. M. *Biochemistry* **2003,** *42*, 375.

(68) Ogi, S.; Sugiyasu, K.; Manna, S.; Samitsu, S.; Takeuchi, M. *Nat. Chem.* **2014,** *6*, 188.

(69) Laban, B.; Vodnik, V.; Dramićanin, M.; Novaković, M.; Bibić, N.; Sovilj, S. P.; Vasić V. M. *J. Phys. Chem. C* **2014,** *118*, 23393.

Appendix

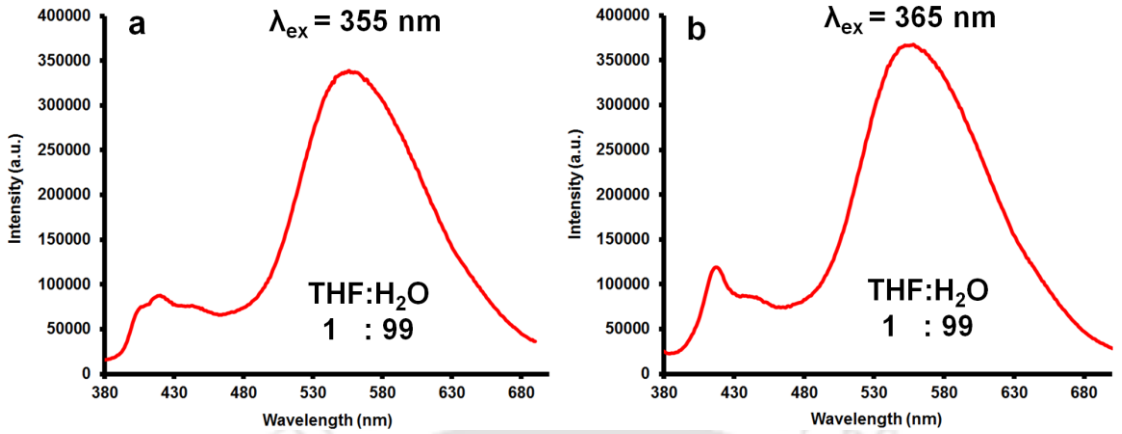

Figure A3b.1 (a, b) Aggregation induced enhanced emission (AIEE) of PF-DPA (5 μM) at 556 nm in THF: H_2O (1:99). Excitation at 355 and 365 nm.

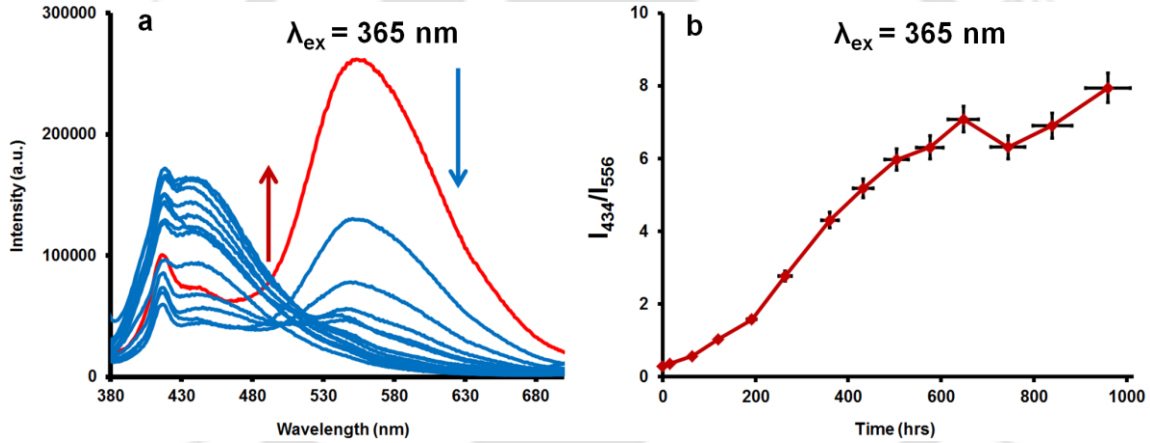

Figure A3b.2 (a) A gradual fluorescent blue shift of PF-DPA Pdots (5 μM) by the addition of Aβ1–40 (5 μM) fibrils in the mixture of solvent fraction of THF: H_2O (1:99) in 10 mM HEPES buffer solution (pH 7.4) at 365 nm excitation (0-40 days). (b) I_{434}/I_{556} fluorescence spectra of PF-DPA Pdots+Aβ1–40 fibrils at 365 nm excitation (0-40 days).

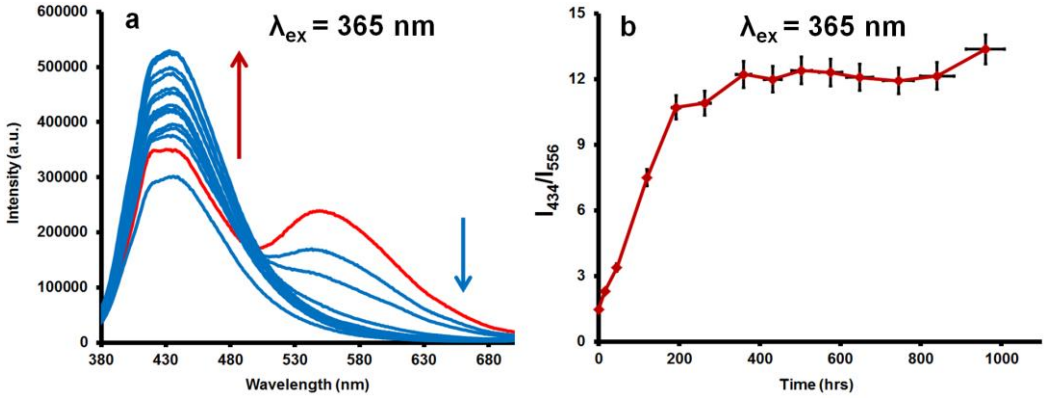

Figure A3b.3 (a) A gradual fluorescent blue shift of PF-DPA Pdots (5 μM) by the addition of CSF (100 μL) aggregates in the mixture of solvent fraction of THF: H_2O (1:99) in 10 mM HEPES buffer solution (pH 7.4) at 365 nm excitation (0-40 days). (b) I_{434}/I_{556} fluorescence spectra of PF-DPA Pdots+CSF aggregates at 365 nm excitation (0-40 days).

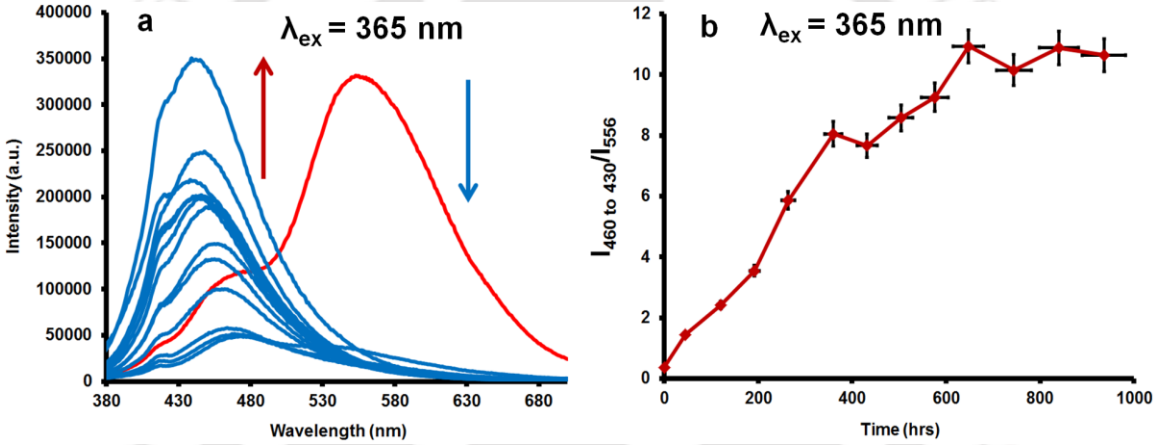

Figure A3b.4 (a) A gradual fluorescent blue shift of PF-DPA Pdots (5 μM) by the addition of Aβ1–40 (5 μM) oligomers with ThT (20 μM) in the mixture of solvent fraction of THF: H_2O (1:99) in 10 mM HEPES buffer solution (pH 7.4) at 365 nm excitation (0-40 days). (b) I_{434}/I_{556} fluorescence spectra of PF-DPA Pdots+Aβ1–40 oligomers at 365 nm excitation (0-40 days).

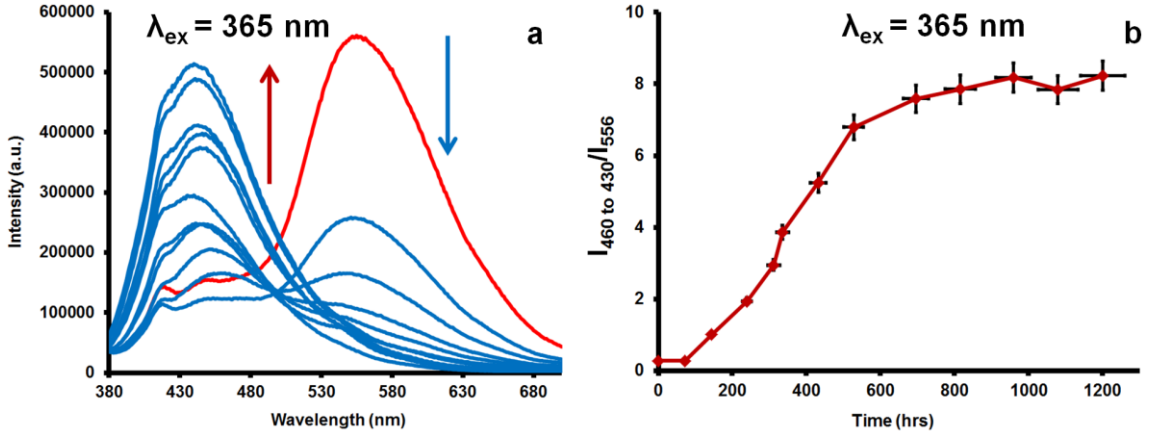

Figure A3b.5 (a) A gradual fluorescent blue shift of PF-DPA Pdots (5 μM) by the addition of Aβ1–40 (5 μM) fibrils with ThT (20 μM) in the mixture of solvent fraction of THF: H_2O (1:99) in 10 mM HEPES buffer solution (pH 7.4) at 365 nm excitation (0-40 days). (b) I_{434}/I_{556} fluorescence spectra of PF-DPA Pdots+Aβ1–40 fibrils at 365 nm excitation (0-40 days).

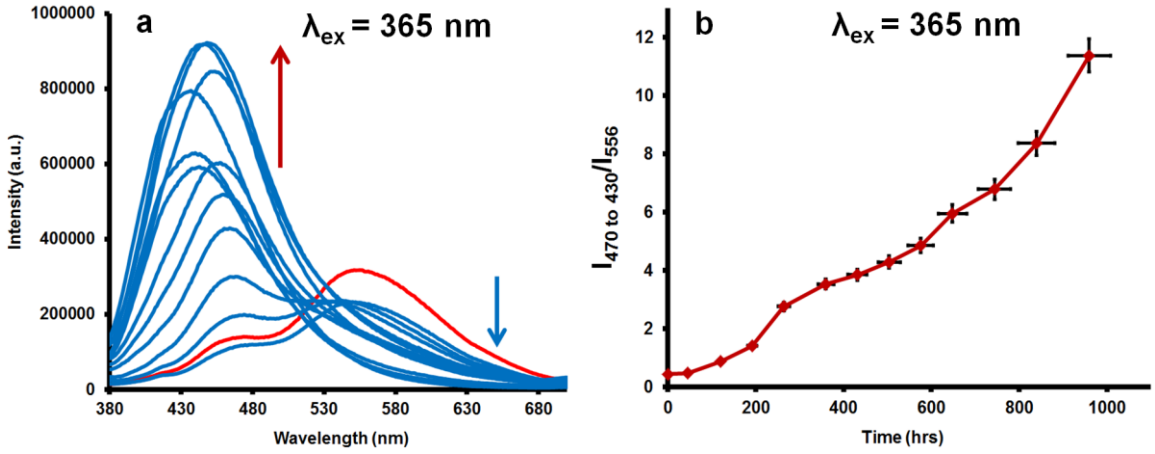

Figure A3b.6 (a) A gradual fluorescent blue shift of PF-DPA Pdots (5 μM) by the addition of CSF (100 μL) aggregates with ThT (20 μM) in the mixture of solvent fraction of THF: H_2O (1:99) in 10 mM HEPES buffer solution (pH 7.4) at 365 nm excitation (0-40 days). (b) I_{434}/I_{556} fluorescence spectra of PF-DPA Pdots+CSF aggregates at 365 nm excitation (0-40 days).

Chapter: 4a

Highly Selective Probe Detects Cu^{2+} and Endogenous NO Gas in Living Cells

Abstract

The rapid, highly selective and sensitive detection of extremely short-lived nitric oxide (NO) gas by a fluorescein derivative was developed. This assay system comprises of indole-3-carboxaldehyde functionalized fluorescein hydrazone (FI) assay which displays a typically high absorption at 492 and 620 nm in the presence of Cu^{2+} and also shows FRET induced fluorescence "turn-on" exclusively with Cu^{2+}. FI selectively detects Cu^{2+} ion *in vitro* by the "turn-on" mechanism followed by fluorescence "turn-off" with NO gas generated by the lipopolysaccharide (LPS) action. The experiment performed in the cellular system indicates that FI loaded RAW264.7 cells showed bright fluorescence in the presence of Cu^{2+}, while other metals did not influence the FI fluorescence. In addition, the fluorescence of FI−Cu^{2+} was efficiently quenched by NO generated in macrophages through LPS stimulation. FI demonstrates characteristic "turn-on" behavior in the presence of Cu^{2+} via spirolactom ring-opening, while other metals such as Na^{+}, K^{+}, Ca^{2+}, Cr^{3+}, Mn^{2+}, Fe^{3+}, Fe^{2+}, Co^{2+}, Ni^{2+}, Zn^{2+}, Cd^{2+}, Hg^{2+} and Ag+ did not influence FI fluorescence even at very high concentration. Further, the FI−Cu^{2+} complex fluorescence was not quenched with any anions or amino acids but totally quenched by NO and the paramagnetic nature of Cu^{2+} ion converted into the diamagnetic nature when reduced to Cu^{1+}. Moreover, FI and the FI−Cu^{2+} complex are nontoxic to the cellular system and have high potential for biomedical applications.

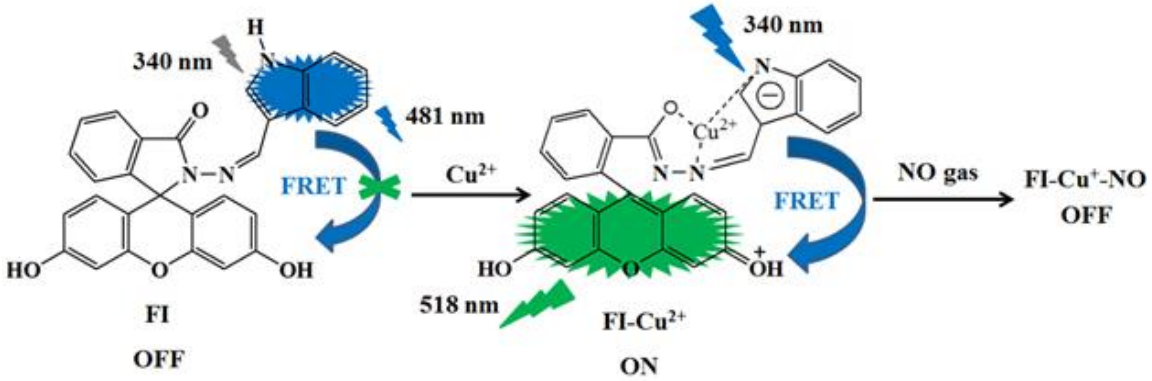

4a.1. Introduction

Copper, one of the foremost metals known to human and the third most plentiful transition metal[1] in the human physiology, is indispensable for carrying out several necessary processes in the human body as well as in the environmental cycle. Copper combines with proteins to produce enzymes that are associated with oxygen processing and also acts as a catalyst in body functions. At low concentration, it is an essential trace nutrient for all organisms, but at high concentration it is poisonous. Accumulation of a large excess of copper in the brain and the liver is highly toxic and causes Alzheimer, Parkinson, Prion, Menkes, and Wilson's disease.[2] Therefore, detection of copper at very low concentrations in the biological environment is very important. Similarly, nitric oxide (NO) gas, produced by nitric oxide synthases enzyme, is now recognized as a vital biological signaling molecule present in the human body and plays significant roles in several biological processes.[3,4] Although NO was identified as an environmental pollutant, it is also recognized now as a biologically relevant signaling molecule in cardiac functions, neurotransmission, vasodilation, etc. since this highly reactive free radical can diffuse through the cells easily.[5,6] The lifetime of NO is usually extremely short-lived and is dependent on the environmental conditions,[7,8] and nitrosated species such as S-nitrosothiols and N-nitrosamines are proposed to act as vehicles for NO storage and transport in biology.[9,10] In addition, NO can also reductively nitrosylate metals, thereby inducing one-electron reduction of the metal and nitros(yl)ation of a nucleophile by the resulting NO^+ to form an E-NO species, where E can be either O or N or S.[11] There are few core requirements to design biologically useful fluorescent NO probes, such as water solubility, low toxicity, cell membrane permeability, easy synthesis, and *in vivo* monitoring. Most importantly, the fluorescent probe must have the capability to detect NO specifically in a competitive environment due to the extremely short-lived nature of this species.[12] Fluorescein, a biologically friendly fluorophore, has high water solubility, high fluorescence quantum yield, and high molar extinction coefficient value.[13] It is used as a core moiety for several common fluorescent probes especially in eye care, tumor surgery,[14-17] etc. and more recently to detect metals, reactive oxygen, and nitrogen species.[6,12,18-21] Nontoxic fluorescein and its derivatives, such as aminofluorescein[22] and some high electron donor containing fluorescein moieties, are nonfluorescent, due to the high HOMO level of its electron donating group. Hence, it can detect NO with very high fluorescence enhancement. Various other NO "turn-on" sensors, including o-diaminofluorescein, o-diaminonaphthalene, o-diaminocyanine, luminescent lanthanide complexes, and 5-amino- 1-naphthonitrile, have

been reported to detect NO.[23-27] A few other recently developed copper-based fluorescent probes provide direct and selective detection of NO both *in vitro* and *in vivo*.[28-34] Although rhodamine based "turn-on" copper sensors are reported to induce spirolactam ring-opening via Cu^{2+} coordination,[1,35-45] there are very few reports on "turn-on" copper sensors that can be utilized for imaging in living cells.[40, 46-50] Hence, the development of efficient fluorescent sensors with potential applications in bioimaging and environmental research remains not only challenging but in most cases are also very difficult to develop.[51,52] In continuation to the efforts in developing new chemical and biological sensors in our laboratory,[53-58] we present here the synthesis of a fluorescein-indole probe (FI) which is completely soluble in aqueous alkaline medium and can be used for the highly selective detection of copper and NO gas in living cells.

4a.2. Results and discussion

4a.2.1. Synthesis of FH

Fluorescein (1g, 2.887 mmole) was dissolved in 20 mL methanol and to it was added excess amount of hydrazine hydrate (0.49 mL, 10.106 mmole) and the reaction mixture was refluxed for 4 h (Scheme 4a.1).[59] After that, the reaction mixture was cooled to room temperature, poured into distilled water and extracted with ethyl acetate (6 × 25 ml). The combined extract was washed with brine, dried with anhydrous sodium sulphate, filtered and concentrated under reduced pressure to yield (69%) FH. ^{1}H NMR (400 MHz, DMSO-d_6), δ (ppm): 4.37 (s, 2H), 6.43 (m, 4H), 6.59 (s, 2H), 6.99 (m, 1H), 7.49 (m, 2H), 7.77 (m, 1H), 9.82 (s, 2H). ^{13}C NMR (150 MHz, DMSO-d_6), δ (ppm): 64.66, 102.39, 112.63, 122.38, 123.42, 127.95, 128.43, 129.32, 132.63, 151.53, 152.42, 158.20, 159.48, 165.52. ESI-MS. 347.1030 $[M+H]^+$.

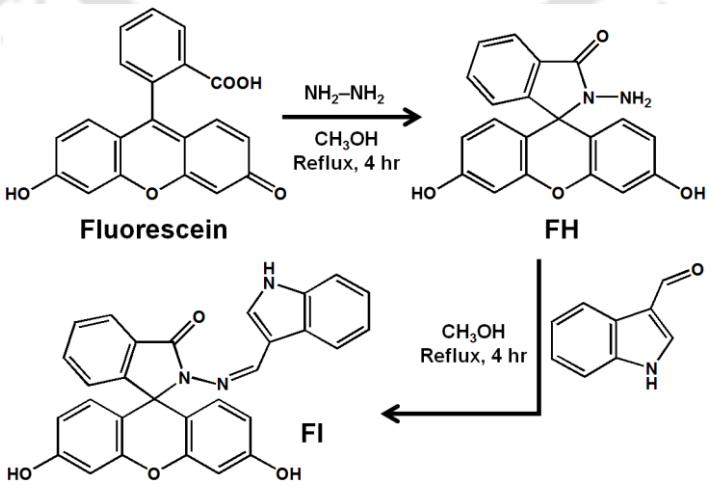

Scheme 4a.1 Synthesis of probe FI.

4a.2.2. Synthesis of probe FI

Indole-3-carboxaldehyde fluorescein hydrazone (FI) was synthesized by a one-step reaction between FH and indole-3-carboxaldehyde in methanol (Scheme 4a.1).[59] The mixture of fluorescein hydrazone (0.1g, 0.287 mmoles) and indole-3-carboxaldehyde (0.046g, 0.317 mmoles) were added into 25 mL of methanol solution and the reaction mixture was refluxed for 3 h followed by cooling to room temperature. Precipitates were formed when the reaction mixture was poured onto crushed ice. Then, the precipitate was separated by filtration and washed with 3 × 10 mL water. The crude product was recrystallized in CH_3OH and obtained indole-3-carboxaldehyde fluorescein hydrazone (FI) as a brown powder in 70% yield. Brown colour single crystals were obtained in CH_3OH solution after few days (Figure A4a.1). ^{1}H NMR (400 MHz, DMSO-d_6), δ (ppm): 6.47 (m, 3H), 6.54 (s, 1H), 6.65 (d, 2H), 6.97 (t, 1H), 7.10 (m, 2H), 7.34 (d, 1H), 7.63 (m, 3H), 7.71 (s, 1H), 7.89 (d, 1H), 9.41 (s, 1H) 9.88 (s, 2H), 11.51 (s, 1H). ^{13}C NMR (100 MHz, DMSO-d_6), δ (ppm): 65.76, 102.305, 110.854, 111.746, 112.150, 120.410, 122.134, 122.614, 122.820, 123.872, 124.002, 128.326, 129.074, 130.790, 131. 232, 133.314, 137.044, 149.193, 149.803, 152.686, 162.829. ESI-MS. 474.1486 $[M+H]^+$.

The fluorescein-indole probe (FI) presented here (Figure 4a.1a) offers advantages such as the ease in synthesis and highly efficient homogeneous assay system with very low detection limit for copper and NO gas both *in vitro* and *in vivo* generated endogenously. This probe also presents a convenient mix-and-detect strategy with rapid output, representing a simple and continuous assay to monitor the extremely small and short-lived NO gas evolved inside the cell. We observe a coordination induced Förster resonance energy transfer (FRET) which "turn-on" the FI in the presence of Cu^{2+} (Figure 4a.1b) from a nonfluorescent state. This probe possesses a donor (indole-3-carboxaldehyde) and an acceptor fluorophore (xanthene) (Figure 4a.1), and the Cu^{2+} induces FRET between these pairs intramolecularly.

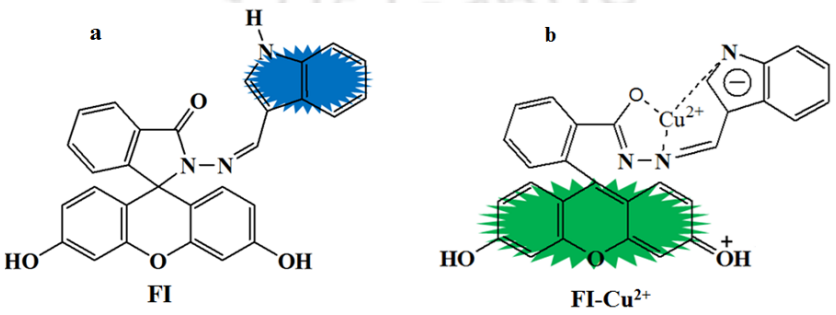

Figure 4a.1 (a) Nonfluorescent probe FI and (b) Highly fluorescent FI+Cu^{2+} complex.

4a.2.3. Selective detection of Cu^{2+} ion sensor by UV-visible spectroscopy

A solution of FI (50 μM) in 10 mM HEPES (pH 7.4) buffer showed an absorbance maxima at 340 nm (Figure 4a.2a blue line), corresponding to the indole moiety. On titrating Cu^{2+} with FI, new absorbance peaks at 492 and 620 nm (weak) were observed (green lines) which represents the open spirolactam ring form of the xanthene moiety. Such a huge 152 nm Cu^{2+}-induced absorption shift could be attributed to the high conjugation and planarity of the indole moiety of FI with the binding sites which favors maximum negative charge distribution of the deprotonated receptor in the presence of Cu^{2+}.[60] FI in the presence of other cations did not show any spectral changes (Figure 4a.2b).

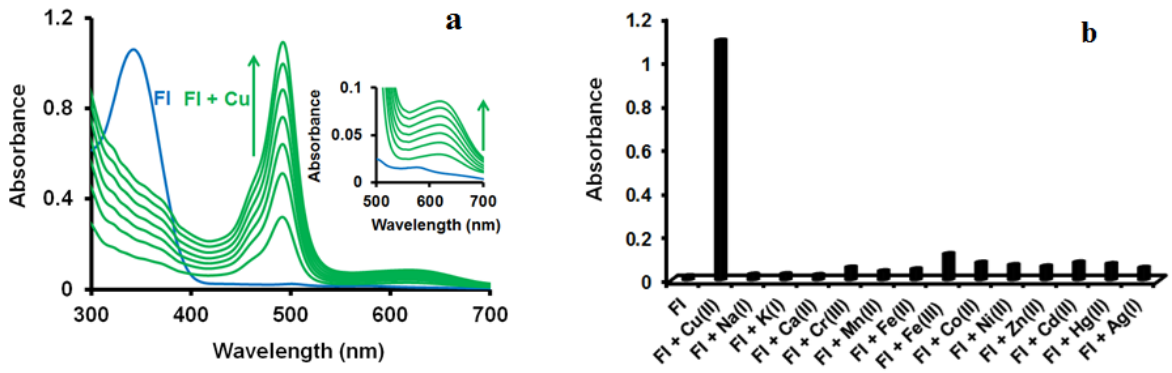

Figure 4a.2 (a) UV−vis spectra of FI (blue line), FI with Cu^{2+} (1:1) (5−35 μM) shows absorbance at 492 and 620 nm (weak) at pH 7.4 (10 mM HEPES buffer). (b) Bar diagram of UV−vis changes observed in the peak of FI (30 μM) in the presence of various metal ions like Na^{+}, K^{+}, Ca^{2+}, Cr^{3+}, Mn^{2+}, Fe^{2+}, Fe^{3+}, Co^{2+}, Ni^{2+}, Cu^{2+}, Zn^{2+}, Cd^{2+}, Hg^{2+}, Ag^{+} (150 μM).

4a.2.4. Selective detection of Cu^{2+} ion sensor by fluorescence spectroscopy

The selective binding of FI (3 μM) with Cu^{2+} ion was studied using fluorescence spectroscopy in aqueous HEPES buffer (10 mM, pH 7.4) (Figure 4a.3a). FI contains two fluorophore units, and we have studied the binding event of FI at two different excitation wavelengths corresponding to the excitation wavelength of the xanthene unit (465 nm) and the indole unit (340 nm), respectively. When excited at 465 nm, FI did not show any emission in the range of 500 to 600 nm (Figure 4a.3a, red line) indicating that in the absence of metal ions, FI remains in the spirolactam form (Figure 4a.1a). Addition of Cu^{2+} to the FI induces a significant "turn-on" fluorescence response at 518 nm, with a highly green fluorescence (Figure 4a.3a and 4a.4a). The apparent binding constant for the formation of the respective complexes were evaluated using the Benesi−Hildebrand (B−H) plot and was estimated to be 1.19×10^{4} M^{-1} by the UV−vis spectral changes at 492 nm (Figure A4a.2). It

was also observed (Figure 4a.3a) that the metal−ligand binding induced ring-opening of FI and the generation of xanthene moiety was highly selective toward Cu^{2+} ion only, whereas no spectral changes occur in the presence of other metal ions like Na^{+}, K^{+}, Ca^{2+}, Cr^{3+}, Mn^{2+}, Fe^{3+}, Fe^{2+}, Co^{2+}, Ni^{2+}, Zn^{2+}, Cd^{2+}, Hg^{2+}, and Ag^{+} (Figure 4a.3b).

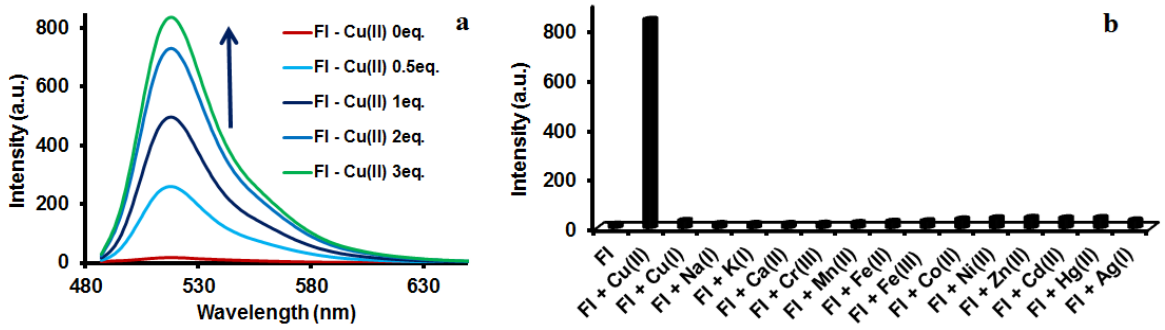

Figure 4a.3 (a) Fluorescent titration spectra of FI (3 μM) in the presence of different concentrations of Cu^{2+} (9 μM) in HEPES buffer solution at pH 7.4. λ_{ex} = 465 nm, λ_{em} = 518. (b) Bar diagram of fluorescence changes observed in the fluorescence peak of FI in the presence of various metal ions like Na^{+}, K^{+}, Ca^{2+}, Cr^{3+}, Mn^{2+}, Fe^{2+}, Fe^{3+}, Co^{2+}, Ni^{2+}, Cu^{2+}, Zn^{2+}, Cd^{2+}, Hg^{2+} and Ag^{+} (30 μM).

Moreover, the fluorescence intensity of FI enhanced with the addition of Cu^{2+} ions when excited at 340 nm, which further confirmed that the probe FI exhibited a high sensitivity only toward Cu^{2+} (Figure 4a.4a). Upon sequential addition of Cu^{2+}, the indole emission signal intensity at 481 nm decreased, and a strong emission signal corresponding to ring-opened fluorescein appeared at 518 nm. This indicates that a highly efficient coordination induced FRET process in the presence of Cu^{2+} produces an intense fluorescein-based green emission (Inset: Figure 4a.4a); i.e., intramolecular energy transfer from the indole donor to the xanthene acceptor is due to the ring opening resulting in an increase of overlap integral between indole and xanthene moiety.[61] This overlap between emission of indole and absorption of ring-opened fluorescein unit strongly supports the high energy transfer efficiency and the proof of FRET mechanism in aqueous buffer medium (10 mM HEPES/CH_3CN, 6:4, v/v; pH 7.4). Furthermore, it was confirmed that the Cu^{2+} sensing behavior of FI remains largely unaffected in the pH range of 6−14 extending the application potential of FI in biology (Figure A4a.3). The detection limit (3σ/k) of Cu^{2+} by FI was determined to be 22.2 nM (Figure A4a.4),[62] much lower than the permissible Cu^{2+} level in drinking water (31 μM) prescribed by the World Health Organization (WHO).[63]

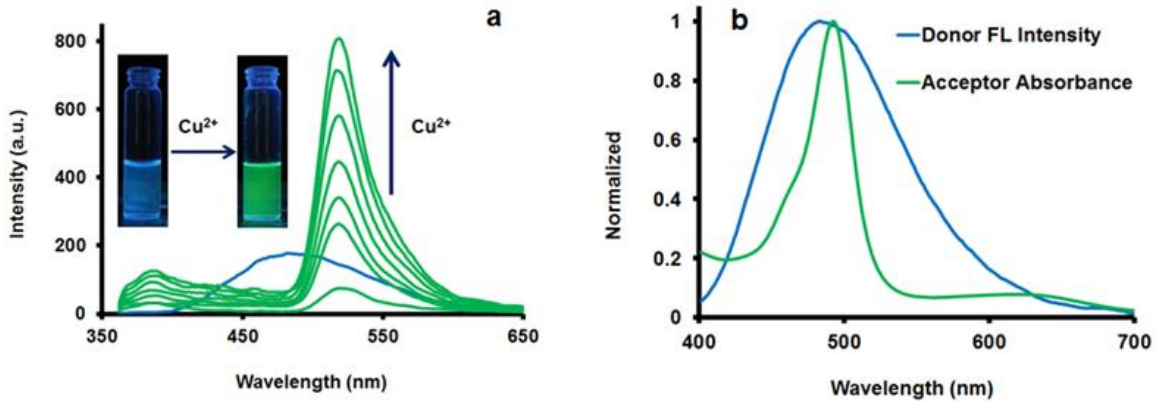

Figure 4a.4 (a) Fluorescence spectra of FI (10 μM) with Cu^{2+} (0−70 μM) in 10 mM HEPES:CH_3CN, 6:4, v/v; pH 7.4, λ_{ex} = 340 nm, Inset: FI in the absence (blue) and the presence (green) of Cu^{2+} upon irradiation using a UV-lamp at 365 nm. (b) Spectral overlap (FRET) between emission of indole (blue) and absorbance of xanthene (green).

4a.2.5. Selective detection of NO sensor by fluorescence spectroscopy

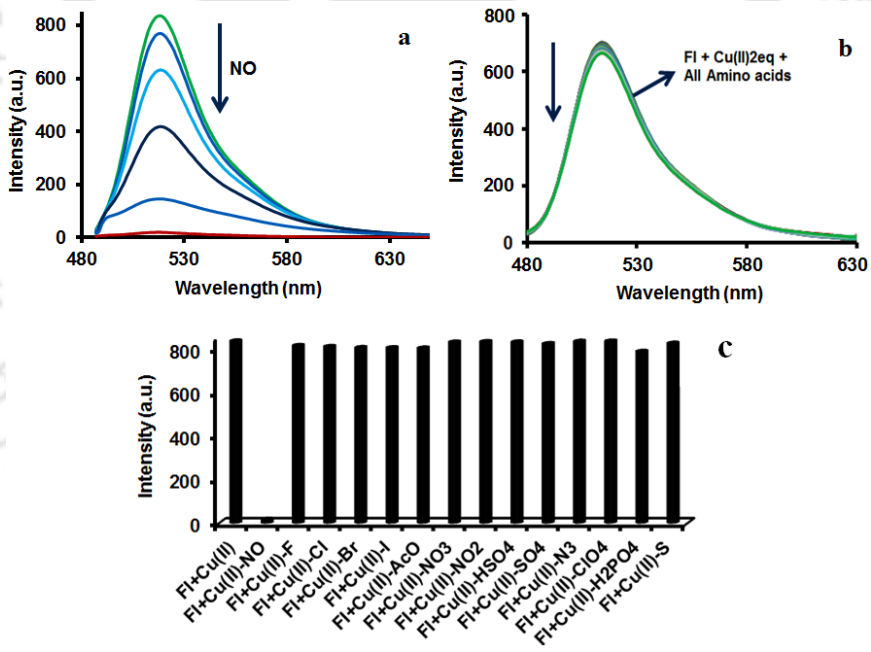

Figure 4a.5 (a) Fluorescent titration spectra of FI (3 μM) + Cu^{2+} (9 μM) in the presence of different concentrations of NO (5 × 20 μL) in HEPES buffer solution at pH 7.4. λ_{ex} = 465 nm, λ_{em} = 518. (b) Fluorescent titration spectra of FI (3 μM) + Cu^{2+} (9 μM) in the presence of different amino acids (100 μM) in HEPES buffered solution at pH 7.4. (c) Fluorescence spectra of FI+Cu^{2+} in HEPES buffer (pH 7.4) solution in the presence of other anions (F^-, Cl^-, Br^-, I^-, CH_3COO^-, NO_3^-, NO_2^-, HSO_4^-, SO_4^{2-}, N_3^-, ClO_4^-, $H_2PO_4^-$, and S^{2-}) (180 μM).

It was further observed that this highly fluorescent FI+Cu^{2+} complex was completely quenched upon gradual addition of NO (Figure 4a.5a) (0−100 μL from the saturated NO stock solution in CH_3CN) which may either be due to nitrosation by NO or fluorophore displacement mechanism by NO resulting in the fluorescence quenching event (Figure A4a.5).[18-21,28-34] The detection limit (3σ/k) of NO for FI+Cu^{2+} was determined to be 13.8 μL (Figure A4a.6).[62] The fluorescence response of FI+Cu^{2+} remained unaffected in the presence of amino acids or other anions like F^-, Cl^-, Br^-, I^-, CH_3COO^-, NO_3^-, NO_2^-, HSO_4^-, SO_4^{2-}, N_3^-, ClO_4^-, $H_2PO_4^-$, and S^{2-} (Figure 4a.5b and 4a.5c).[64] The paramagnetic nature of Cu^{2+} ion in the FI+Cu^{2+} is converted to diamagnetic in the presence of NO when reduced to Cu^{1+} and confirmed by EPR spectra (Figure A4a.7).[28,65-68]

4a.2.6. Colorimetric sensing ability of FI toward Cu^{2+} ion

The colorimetric sensing ability of FI was investigated by adding various cations (Na^+, K^+, Ca^{2+}, Cr^{3+}, Mn^{2+}, Fe^{3+}, Fe^{2+}, Co^{2+}, Ni^{2+}, Cu^{2+}, Zn^{2+}, Cd^{2+}, Hg^{2+} and Ag^+) to an aqueous solution (HEPES buffer at pH 7.4) of sensor FI. When 5 equiv of Cu^{2+} was added to the solution of FI (30 μM), the sensor responded with a dramatic color change from light blue to bright green (Figure 4a.6). In the corresponding UV−vis spectrum, the absorption appeared at 492 and 620 nm at pH 7.4 (Figure 4a.2). In contrast when cations like Na^+, K^+, Ca^{2+}, Cr^{3+}, Mn^{2+}, Fe^{3+}, Fe^{2+}, Co^{2+}, Ni^{2+}, Zn^{2+}, Cd^{2+}, Hg^{2+} and Ag^+ were added to solutions of the sensor FI, no significant color or spectral changes were observed.

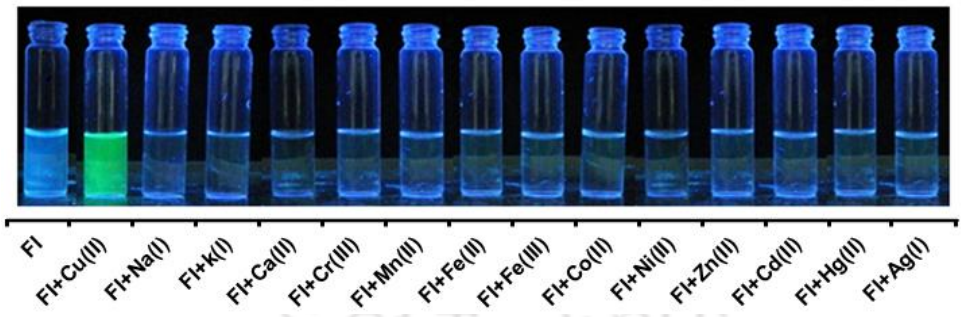

Figure 4a.6 (a) Color and fluorescent changes of FI (30 μM) upon the addition of various metal ions (5eq.) (Na^+, K^+, Ca^{2+}, Cr^{3+}, Mn^{2+}, Fe^{3+}, Fe^{2+}, Co^{2+}, Ni^{2+}, Cu^{2+}, Zn^{2+}, Cd^{2+}, Hg^{2+}, Ag^+) in HEPES buffer solution (10 mM, pH 7.4).

4a.2.7. Colorimetric sensing ability of FI−Cu^{2+} complex toward NO gas

The colorimetric sensing ability of the FI−Cu^{2+} complex was investigated by adding various anions such as NO, F^-, Cl^-, Br^-, I^-, CH_3COO^-, NO_3^-, NO_2^-, HSO_4^-, SO_4^{2-}, N_3^-, ClO_4^-, $H_2PO_4^-$, and S^{2-} to aqueous solution (10 mM HEPES buffer at pH 7.4) of sensor FI−Cu^{2+}.

When a 100 µL saturated solution of NO was added into the solution of FI−Cu^{2+} (30 µM), the sensor responded with a dramatic color change from green to colorless (Figure 4a.7) rapidly. In contrast when anions F^-, Cl^-, Br^-, I^-, CH_3COO^-, NO_3^-, NO_2^-, HSO_4^-, SO_4^{2-}, N_3^-, ClO_4^-, $H_2PO_4^-$, and S^{2-} were added to the solution of FI−Cu^{2+}, no significant color changes were observed.

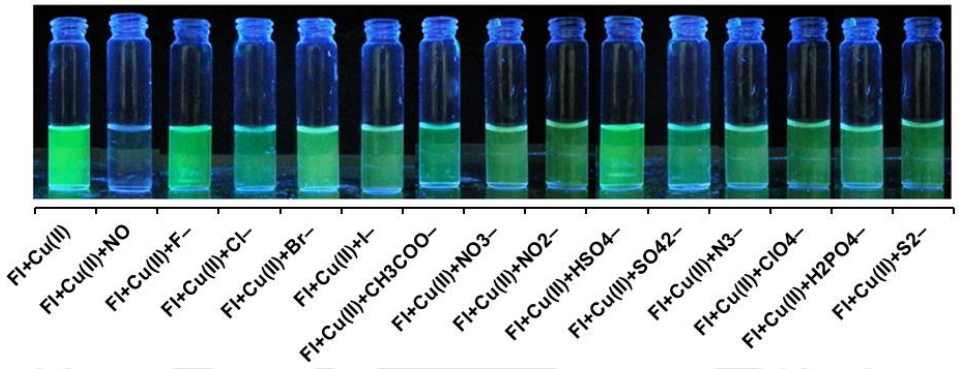

Figure 4a.7 Color and fluorescent changes of FI+Cu^{2+} (30 µM) upon the addition of various anions (6 eq.) (F^-, Cl^-, Br^-, I^-, CH_3COO^-, NO_3^-, NO_2^-, HSO_4^-, SO_4^{2-}, N_3^-, ClO_4^-, $H_2PO_4^-$, S^{2-} and 100 µL NO) in HEPES buffer solution (10 mM, pH 7.4).

4a.2.8. Cell viability of FI by MTT assay

The cellular toxicity of FI was evaluated in J774A.1 cells using MTT assay.[69] Cells exposed to different concentrations of FI for 48 h exhibit no significant change in viability up to the concentration of 500 µM (~15% at 500 µM), but above this concentration it gives dose-dependent toxicity toward macrophage J774A.1 cells (Figure 4a.8).

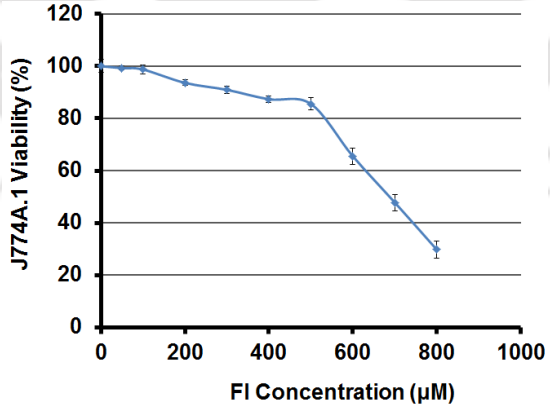

Figure 4a.8 Cellular toxicity of FI in J774A.1 cells using MTT assay. Cells were exposed to different concentration of FI (0-800 µM) for 48 h exhibits no significant change in viability up to the concentration 500 µM (~15% at 500 µM) but afterwards it gives dose-dependent toxicity towards macrophage J774A.1 cells.

4a.2.9. Detection of Cu^{2+} ion by FI in living cells

After performing the cytotoxicity studies, the imaging ability of FI and intracellular Cu^{2+} ion detection was confirmed in an experiment performed with RAW 264.7 cells. FI was observed to respond to the Cu^{2+} ion specifically present in the cell environment. During Cu^{2+} ion toxicity studies in aquatic fauna, the transition metals accumulate within the intracellular storage system of the cell.[70] In our experiments, the cells were loaded with FI overnight and treated with Cu^{2+} (50 μM) for 1 h to explore the suitability of FI in detecting Cu^{2+} present inside the cell. FI loaded cells are healthy and nonfluorescent, and treatment with Cu^{2+} causes a time dependent change in intracellular fluorescence with a maximum fluorescence at 1 h (Figure 4a.9). No significant level of oxidative stress or change in cellular morphology was observed in cells treated with Cu^{2+}, indicating no role of such factors in modulating the fluorescence signal of FI inside the cell. Besides Cu^{2+}, other metals (Co^{2+} and Cd^{2+} presented) did not show a significant change in fluorescence inside the cell (Figure 4a.9). Hence, imaging inside the live cells supports the *in vitro* fluorescence spectroscopy data and confirms suitability of FI to selectively detect intracellular Cu^{2+} ion (Figure 4a.9).

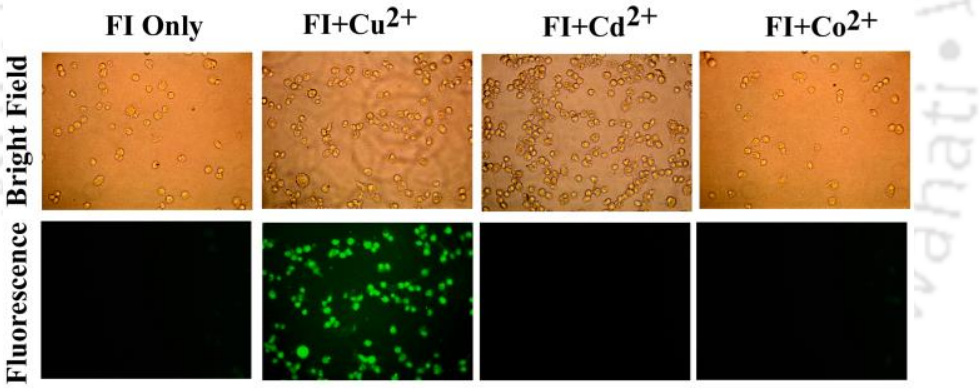

Figure 4a.9 Fluorescence imaging of FI in RAW 264.7 cells in the presence and absence of Cu^{2+} ion. RAW 264.7 loaded with FI and treated with different metals (Cu^{2+}, Cd^{2+}, and Co^{2+}) for 1 h at 37 °C.

4a.2.10. Fluorescence imaging of FI−Cu^{2+} complex in macrophage to detect NO generated through LPS stimulation

Further, the FI−Cu^{2+} complex can specifically detect NO gas generated endogenously, and as a result quenching of the FI−Cu^{2+} fluorescence occurs *in vivo*. Macrophage exposed to heat killed bacteria (lipopolysaccharide (LPS)) causes production of intracellular NO through activation of iNOS.[71] Employing such as *in vivo* tool, we tested the suitability of the FI−Cu^{2+} complex as a NO sensor inside the cell. Macrophages RAW264.7 were loaded with FI and

then treated with Cu^{2+} (50 μM) for 1 h to form the FI−Cu^{2+} complex as evidenced by an increase in fluorescence. Subsequently, the cells were treated with LPS to stimulate the production of endogenous NO gas. Production of endogenous NO quenches the fluorescence of the FI−Cu^{2+} complex in specific time and causes complete reduction of fluorescence intensity (Figure 4a.10). FI loaded cells treated with individual metals or LPS alone did not cause any change in fluorescence. Hence, FI demonstrates the potential for detecting and imaging intracellular Cu^{2+}, and the resulting FI−Cu^{2+} complex can be applied to detect and monitor endogenous NO gas which is extremely short-lived and generally produced in incredibly low concentrations. FI or FI−Cu^{2+} complexes are nontoxic and have immense potential for future biomedical applications to measure Cu^{2+} accumulation or release of NO in biological systems.

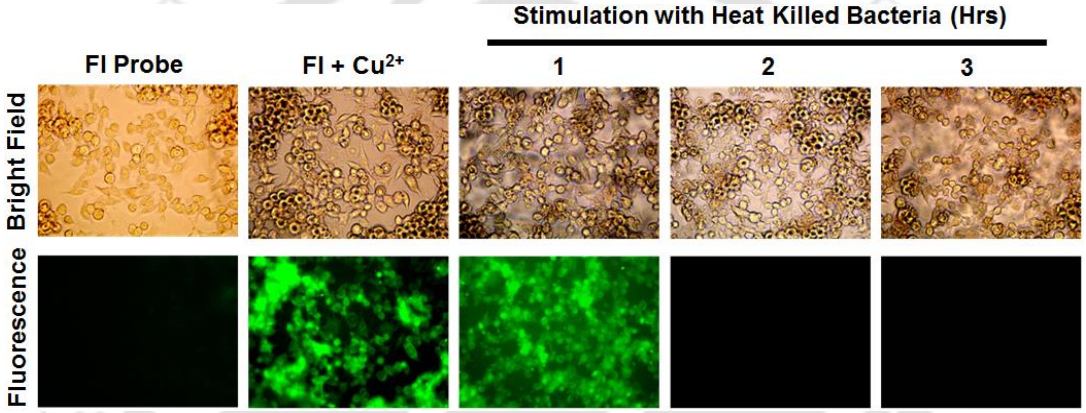

Figure 4a.10 Fluorescence imaging of the FI−Cu^{2+} complex in RAW 264.7 cells in the presence and absence of *in vivo* NO gas using heat killed E. coli (LPS) (1:25) to generate intracellular NO gas. Incubated at 37 °C, the fluorescence signal of the FI−Cu^{2+} complex with heat killed E. coli (LPS) was monitored for different time periods (1−3 h). Complete quenching of FI−Cu^{2+} was observed after 2 h incubation due to NO gas liberated from heat killed E. coli (LPS).

4a.3. Conclusion

In summary, we have developed a highly sensitive and biocompatible probe FI which selectively binds with Cu^{2+} ions and "turn-on" the response in optical and fluorescence spectra *in vitro* and *in vivo*. The new fluorescent Cu^{2+} sensor probe induces FRET based coordination between its two fluorophores donor indole and the acceptor Cu^{2+} bound xanthene moiety of FI and also facilitates imaging within the cells. Successive ring-opening of the spirolactam moiety in the presence of Cu^{2+} ion makes possible naked eye detection by drastic color change and emission enhancement. The detection limit for Cu^{2+} was found to be

22.2 nM, which is much lower than the permissible Cu^{2+} concentration in drinking water as per the World Health Organization (WHO). FI selectively detects Cu^{2+} *in vivo* and *in vitro* by the "turn-on" mechanism followed by fluorescence "turn-off" in the presence of NO gas generated by the lipopolysaccharide (LPS) action. The *in vivo* experiment performed in the cellular system indicates that FI loaded RAW264.7 cells showed bright fluorescence in the presence of Cu^{2+}, while other metals did not influence the FI fluorescence. The complex formed between FI and Cu^{2+} is dissociated only in the presence of NO and remains unaffected in the presence of other anions and amino acids, which makes the FI−Cu complex a highly selective and sensitive sensor for NO *in vitro* and *in vivo* studies.

4a.4. Experimental Section

4a.4.1. Materials and methods

All reagents and solvents were purchased from commercial sources, and the solvents used were of spectroscopic grade. UV−vis absorption spectra were recorded on a PerkinElmer Lambda-25 spectrometer. Fluorescence spectra were carried out on a Varian Cary Eclipse Spectrometer. A 10 × 10 mm quartz cuvette was used for solution spectra, and emission was collected at 90° relative to the excitation beam. Deionized water was obtained from the Milli-Q system (Millipore). ^{1}H NMR (400 MHz) and ^{13}C NMR (100 and 150 MHz) spectra were obtained with a Varian-AS400NMR spectrometer. Crystal data were collected with Bruker Smart Apex-II CCD diffractometer using graphite monochromated Mo−Kα radiation (λ = 0.71073 Å) at 298 K. Mass spectra were recorded on a Agilent Accurate-Mass Q-TOF LC/MS 6520, and peaks are given in m/z (% of basis peak). The X-Band Electron Paramagnetic Resonance (EPR) spectra were recorded on a JES-FA 200 EPR spectrometer, at room temperature. The cells were mounted on the glass slide in CC mount (Sigma) and observed under the 40X objective of fluorescence microscope eclipse 80Ti (Nikon), and images were captured using high resolution camera.

4a.4.2. Preparation of stock solutions

The FI stock solution was prepared at the concentration of 1.0×10^{-3} mL^{-1} in 10 mL of CH_3CN. This stock solution was diluted to a desired concentration for each titration in a 3 mL cuvette with HEPES buffer.

4a.4.3. Preparation of cation and anion stock solutions

Each inorganic metal salt and anions stock solutions were prepared at the concentration of 10.0×10^{-3} mL^{-1} in 5 mL of Milli-Q water. The stock solutions were diluted to the desired concentrations with Milli-Q water when needed.

4a.4.4. Preparation of HEPES buffer solution

All the UV−visible and fluorescence titrations were performed in 10 mM HEPES buffer at pH 7.4 by using 4 M NaOH or 5 M HCl solution.

4a.4.5. UV−Visible spectra titration of FI with Cu^{2+} ion

FI and a series of FI−Cu^{2+} in HEPES buffer solutions with different concentrations of FI and Cu^{2+} in 1:1 ratios were stored for 0−12 h at room temperature. Absorption peak was observed at 340 nm for free FI solution. Interestingly, an absorption peak was observed at 492 nm for all these solutions, and their absorption intensities increased rapidly as the concentration of FI−Cu^{2+} increased from (0 to 35 μM) in HEPES buffered solution. This result indicates that FI can detect Cu^{2+} at very low micromolar levels and produce a fluorescence signal after the complex has been stored for some time.

4a.4.6. Fluorescence titration of FI with Cu^{2+} ion

A series of FI−Cu^{2+} solutions in HEPES buffer solutions (pH 7.4) with different concentrations of FI and Cu^{2+} ratios were stored for 0−12 h at room temperature. Interestingly, an emission peak was observed at 518 nm (λ_{ex} = 465 nm) for all these solutions, and their fluorescence intensities increased rapidly as the concentration of FI (3 μM) with Cu^{2+} (0 to 9 μM) in HEPES buffered solution. This result indicates that FI can detect Cu^{2+} at very low nanomolar levels and produce a fluorescence signal after the mixture was stored for prolonged time.

4a.4.7. Fluorescence titration of FI with Cu^{2+} ion

A series of FI (10 μM) solutions in HEPES: CH_3CN, 6:4, v/v; pH 7.4, solutions with different amounts of copper (0−70 μM) were stored for 0−12 h at room temperature. Interestingly, an emission peak was observed at 518 nm (λ_{ex} = 340 nm) for all these solutions, and their fluorescence intensities increased rapidly as the formation of FI−Cu^{2+} in HEPES: CH_3CN, 6:4, v/v; pH 7.4 buffer solutions.

4a.4.8. Fluorescence titration of FI−Cu^{2+} complex with NO solution

Fluorescence quenching titration of FI+Cu^{2+} was done in the presence of different concentrations of NO (0−100 µL from saturated solution of NO in CH_3CN) in HEPES buffer solution at pH 7.4. The gradual addition of NO by syringe to the FI+Cu^{2+} complex in a 3 mL closed cuvette shows that the fluorescence peak at 518 nm was completely quenched at a final volume of 100 µL of NO solution. The same fluorescent quenching titration of FI+Cu^{2+} with anions like F^-, Cl^-, Br^-, I^-, N_3^-, NO_2^-, NO_3^-, CH_3COO^-, ClO_4^-, $H_2PO_4^-$, SO_4^{2-}, HSO_4^-, and S_2^- was performed in HEPES buffer solution at pH 7.4.

4a.4.9. Detection limit for Cu^{2+} ion

The detection limit was calculated on the basis of the fluorescence titration. The fluorescence emission spectrum of FI was measured 10 times, and the standard deviation of blank measurement was achieved. To get the slope, the ratio of the emission intensity at 518 nm was plotted as a concentration of Cu^{2+}. The detection limit was calculated using the following equation

$$\text{Detection limit} = 3\sigma/k \quad (1)$$

Where σ is the standard deviation of blank measurement, and k is the slope between the ratios of emission intensity versus [Cu^{2+}]. Similarly, the detection limit for NO was calculated on the basis of the fluorescence titration.

4a.4.10. EPR study

On NO purging into the degassed solution of FI-Cu^{2+} complex, the solutions became EPR silent. This can be attributed to the formation of [Cu^{2+}-NO] intermediates in FI-Cu^{2+} complexes. The appearance of EPR silent signals in this case might be because of the complete reduction of Cu^{2+} to Cu^{1+} by nitric oxide.

4a.4.11.Cell viability of FI by MTT assay

MTT assay is used to test the cytotoxicity of FI as described with slight modifications. Ten thousand J774A.1 cells were seeded overnight in a 96 well plate in 0.2 mL of serum containing media (complete media). Cells were treated with different concentration of FI (0−800 µM) in serum free media for 48 h at 37 °C with 5% CO_2. Post-treatment, cells were washed twice with PBS and incubated with 100 µL of MTT (0.5 mg/mL) for 4 h at 37 °C with 5% CO_2. Then, MTT solution was removed, and formazan crystals were dissolved in 100 µL of cell culture grade DMSO. The optical density was determined using a

spectrophotometer at 570 and 660 nm. Cells treated with serum free media were considered as 100% viable, and the result of treatment is expressed as the percent survival in comparison to the control.

4a.4.12. Fluorescence imaging of FI with Cu^{2+} ion and NO in living Cells

The mouse macrophage cell line RAW 264.7 was grown in Dulbecco's Modified Eagle's Medium (DMEM) (Sigma, St. Louis, MO, USA), containing 10% fetal bovine serum (FBS) and 1% penicillin-streptomycin antibiotic (100 units/mL penicillin and 100 μg/mL streptomycin sulfates) at 37 °C in a humidified incubator containing 5% CO_2. A day before the experiment, 10^5 cells were plated on sterilized square coverslips (12 mm) in a total volume of 1.5 mL in 35 mm cell culture dishes. Cells were allowed to adhere to the coverslip. Thereafter, cells were incubated with fluorescent FI probe (100 μM) overnight in complete media. Cells were washed 2 times with sterile cell culture grade PBS and treated with Cu^{2+} (50 μM) for 1 h at 37 °C at 5% CO_2 in 1.5 mL of serum free media. To detect intracellular nitric oxide, cells were treated with heat killed bacteria (LPS) in 1:25 ratio in serum free media for different times (0−4 h) at 37 °C at 5% CO_2. After the particular time point, cells were washed with sterile PBS and fixed with 2% paraformaldehyde in PBS. The cells were mounted on the glass slide in CC mount (Sigma) and observed under the 40X objective of fluorescence microscope eclipse 80Ti (Nikon), and images were captured using high resolution camera. Files were opened in Adobe Photoshop 7.0, and gray levels were adjusted by using the auto level command with a black and white clip set to 0%. Images were cropped again and scaled for final display.

4a.4.13. Fluorescence imaging of FI with Cu^{2+} ion in Living Cells

RAW 264.7 was loaded with FI and treated with different metals (Cu^{2+}, Co^{2+} and Cd^{2+}) for 1 h at 37 °C. Post-treatment, cells were fixed and mounted in a CC mount (Sigma) and observed under the 40X objective of fluorescence microscope eclipse 80Ti (Nikon), and images were captured using high resolution camera.

4a.4.14. Fluorescence imaging of FI+Cu^{2+} complex with endogenous generated NO gas

Fluorescence imaging of FI−Cu^{2+} in the presence of RAW 264.7 cells was performed both in the presence and absence of *in vivo* generated NO gas. RAW 264.7 is loaded with FI (100 μM) overnight in complete media and then incubated with Cu^{2+} for 1 h at 37 °C to form an intracellular FI−Cu^{2+} complex. Then, cells were treated with heat killed E. coli (1:25) to

generate intracellular NO and fluorescence signal of the FI−Cu^{2+} complex and was monitored for different time periods (1−3 h). Generation of NO causes fluorescence quenching of FI−Cu^{2+} in a time-dependent manner with a complete quenching within 2 h.

References

(1) Yang, Y.; Zhao, Q.; Feng, W.; Li, F. *Chem. Rev.* **2013,** *113,* 192.

(2) Gaggelli, E.; Kozłowski, H.; Valensin, D.; Valensin, G. *Chem. Rev.* **2006,** *106,* 1995.

(3) Calabrese, V.; Mancuso, C.; Calvani, M.; Rizzarelli, E.; Butterfield, D. A.; Giuffrida Stella, A. M. *Nat. Rev. Neurosci.* **2007,** *8,* 766.

(4) Shiue, T. W.; Chen, Y. H.; Wu, C. M.; Singh, G.; Chen, H. Y.; Hung, C. H.; Liaw, W. F.; Wang, Y. M. *Inorg. Chem.* **2012,** *51,* 5400.

(5) McQuade, L. E.; Pluth, M. D.; Lippard, S. J. *Inorg. Chem.* **2010,** *49,* 8025.

(6) Ford, P. C.; Lorkovic, I. M. *Chem. Rev.* **2002,** *102,* 993.

(7) Liu, X.; Miller, M. J. S.; Joshi, M. S.; Thomas, D. D.; Lancaster, J. R., Jr. *Proc. Natl. Acad. Sci. U.S.A.* **1998,** *95,* 2175.

(8) Thomas, D. D.; Liu, X.; Kantrow, S. P.; Lancaster, J. R., Jr. *Proc. Natl. Acad. Sci. U.S.A.* **2001,** *98,* 355.

(9) Gladwin, M. T.; Schechter, A. N. *Circ. Res.* **2004,** *94,* 851.

(10) Vanin, A. F. *Biochemistry* **1998,** *63,* 782.

(11) Ford, P. C.; Fernandez, B. O.; Lim, M. D. *Chem. Rev.* **2005,** *105,* 2439.

(12) Lim, M. H.; Wong, B. A.; Pitcock, W. H., Jr.; Mokshagundam, D.; Baik, M. H.; Lippard, S. J. *J. Am. Chem. Soc.* **2006,** *128,* 14364.

(13) Egawa, T.; Koide, Y.; Hanaoka, K.; Komatsu, T.; Teraia, T.; Nagano, T. *Chem. Commun.* **2011,** *47,* 4162.

(14) Okuda, T.; Kataoka, K.; Yabuuchi, T.; Yugami, H.; Kato, A. *J. Clin. Neurosci.* **2010,** *17,* 118.

(15) Okuda, T.; Yoshioka, H.; Kato, A. *J. Clin. Neurosci.* **2012,** *19,* 1719.

(16) Schebesch, K. M.; Proescholdt, M.; Höhne, J.; Hohenberger, C.; Hansen, E.; Riemenschneider, M. J.; Ullrich, W.; Doenitz, C.; Schlaier, J.; Lange, M.; Brawanski, A. *Acta Neurochir.* **2013,** *155,* 693.

(17) Acerbi, F.; Broggi, M.; Eoli, M.; Anghileri, E.; Cuppini, L.; Pollo, B.; Schiariti, M.; Visintini, S.; Orsi, C.; Franzini, A.; Broggi, G.; Ferroli, P. *Acta Neurochir.* **2013,** *155,* 1277.

(18) Pluth, M. D.; McQuade, L. E.; Lippard, S. J. *Org. Lett.* **2010,** *12,* 2318.

(19) McQuade, L. E.; Lippard, S. J. *Inorg. Chem.* **2010,** *49,* 7464.

(20) Pluth, M. D.; Chan, M. R.; McQuade, L. E.; Lippard, S. J. *Inorg. Chem.* **2011,** *50,* 9385.

(21) Tonzetich, Z. J.; McQuade, L. E.; Lippard, S. J. *Inorg. Chem.* **2010,** *49,* 6338.

(22) Hirano, T.; Kikuchi, K.; Urano, Y.; Higuchi, T.; Nagano, T. *J. Am. Chem. Soc.* **2000,** *122*, 12399.

(23) Miles, A. M.; Wink, D. A.; Cook, J. C.; Grisham, M. B. *Methods Enzymol.* **1996,** *268*, 105.

(24) Nagano, T.; Yoshimura, T. *Chem. Rev.* **2002,** *102*, 1235.

(25) Sasaki, E.; Kojima, H.; Nishimatsu, H.; Urano, Y.; Kikuchi, K.; Hirata, Y.; Nagano, T. *J. Am. Chem. Soc.* **2005,** *127*, 3684.

(26) Terai, T.; Urano, Y.; Izumi, S.; Kojima, H.; Nagano, T. *Chem. Commun.* **2012,** *48*, 2840.

(27) Yang, Y.; Seidlits, S. K.; Adams, M. M.; Lynch, V. M.; Schmidt, C. E.; Anslyn, E. V.; Shear, J. B. *J. Am. Chem. Soc.* **2010,** *132*, 13114.

(28) Lim, M. H.; Xu, D.; Lippard, S. J. *Nat. Chem. Biol.* **2006,** *2*, 375.

(29) Rosenthal, J.; Lippard, S. J. *J. Am. Chem. Soc.* **2010,** *132*, 5536.

(30) Royzen, M.; Wilson, J. J.; Lippard, S. J. J. *Inorg. Biochem.* **2013,** *118*, 162.

(31) Tsuge, K.; DeRosa, F.; Lim, M. D.; Ford, P. C. *J. Am. Chem. Soc.* **2004,** *126*, 6564.

(32) Khin, C.; Lim, M. D.; Tsuge, K.; Iretskii, A.; Wu, G.; Ford, P. C. *Inorg. Chem.* **2007,** *46*, 9323.

(33) Wasser, I. M.; Vries, S. D.; Loccoz, P. M.; Schröder, I.; Karlin, K. D. *Chem. Rev.* **2002,** *102*, 1201.

(34) Yuan, L.; Lin, W.; Xie, Y.; Chen, B.; Song, J. *Chem. Commun.* **2011,** *47*, 9372.

(35) Zhang, X.; Shiraishi, Y.; Hirai, T. *Org. Lett.* **2007,** *9*, 5039.

(36) Zhang, X.; Sumiya, S.; Shiraishi, Y.; Hirai, T. *J. Photochem. Photobiol., A:* **2009,** *205*, 215.

(37) Xiang, Y.; Li, Z. F.; Chen, X. T.; Tong, A. J. *Talanta* **2008,** *74*, 1148.

(38) Zhao, Y.; Zhang, X. B.; Han, Z. X.; Qiao, L.; Li, C. Y.; Jian, L. X.; Shen, G. L.; Yu, R. Q. *Anal. Chem.* **2009,** *81*, 7022.

(39) Zhao, M. L.; Yang, X. F.; He, S. H.; Wang, L. P. *Sens. Actuators, B* **2009,** *135*, 625.

(40) Swamy, K.; Ko, S. K.; Kwon, S. K.; Lee, H. N.; Mao, C.; Kim, J. M.; Lee, K. H.; Kim, J. H.; Shin, I.; Yoon, J. Y. *Chem. Commun.* **2008,** *44*, 5915.

(41) Zhou, Y.; Wang, F.; Kim, Y. M.; Kim, S. J.; Yoon, J. Y. *Org. Lett.* **2009,** *11*, 4442.

(42) Tang, R. R.; Lei, K.; Chen, K.; Zhao, H.; Chen, J. W. *J. Fluoresc.* **2011,** *21*, 141.

(43) Yu, C. W.; Zhang, J.; Wang, R.; Chen, L. X. *Org. Biomol. Chem.* **2010,** *8*, 5277.

(44) Xu, Z. H.; Zhang, L. K.; Guo, R.; Xiang, T. C.; Wu, C. Z.; Zheng, Z.; Yang, F. L. A *Sens. Actuators, B* **2011,** *156*, 546.

(45) Zhang, J. F.; Zhou, Y.; Yoon, J.; Kim, Y.; Kim, S. J.; Kim, J. S. *Org. Lett.* **2010,** *12,* 3852.

(46) Xi, P. X.; Dou, J. Y.; Huang, L.; Xu, M.; Chen, F. J.; Wu, Y. J.; Bai, D. C.; Li, W. G.; Zeng, Z. Z. *Sens. Actuators, B* **2010,** *148,* 337.

(47) Huang, L.; Chen, F. J.; Xi, P. X.; Xie, G. Q.; Li, Z. P.; Shi, Y. J.; Xu, M.; Liu, H. Y.; Ma, Z. R.; Bai, D. C.; Zeng, Z. Z. *Dyes Pigm.* **2011,** *90,* 265.

(48) Chereddy, N. R.; Thennarasu, S. *Dyes Pigm.* **2011,** *91,* 378.

(49) Liu, W. Y.; Li, H. Y.; Zhao, B. X.; Miao, J. Y. *Org. Biomol. Chem.* **2011,** *9,* 4802.

(50) Yu, C. W.; Chen, L. X.; Zhang, J.; Li, J. H.; Liu, P.; Wang, W. H.; Yan, B. *Talanta* **2011,** *85,* 1627.

(51) Xu, Z.; Han, S. J.; Lee, C.; Yoon, J.; Spring, D. R. *Chem. Commun.* **2010,** *46,* 1679.

(52) Kim, H. N.; Guo, Z.; Zhu, W.; Yoon, J.; Tian, H. *Chem. Soc. Rev.* **2011,** *40,* 79.

(53) Saikia, G.; Iyer, P. K. *Macromolecules* **2011,** *44,* 3753.

(54) Dwivedi, A. K.; Saikia, G.; Iyer, P. K. *J. Mater. Chem.* **2011,** *21,* 2502.

(55) Saikia, G.; Dwivedi, A. K.; Iyer, P. K. *Anal. Methods* **2012,** *4,* 3180.

(56) Dwivedi, A. K.; Prasad, K. M. N.; Trivedi, V.; Iyer, P. K. *ACS Appl. Mater. Interfaces* **2012,** *4,* 6371.

(57) Dwivedi, A. K.; Iyer, P. K. *J. Mater. Chem. B* **2013,** *1,* 4005.

(58) Muthuraj, B.; Hussain, S.; Iyer, P. K. *Polym. Chem.* **2013,** *4,* 5096.

(59) Muthuraj, B.; Deshmukh, R.; Trivedi, V.; Iyer, P. K. *ACS Appl. Mater. Interfaces* **2014,** *6,* 6562.

(60) Bose, P.; Ghosh, P. *Chem. Commun.* **2010,** *46,* 2962.

(61) Takakusa, H.; Kikuchi, K.; Urano, Y.; Kojima, H.; Nagano, T. *Chem. Eur. J.* **2003,** *9,* 1479.

(62) Cao, C.; Kim, J. P.; Kim, B. W.; Chae, H.; Yoon, H. C.; Yang, S. S.; Sim, S. J. *Biosens. Bioelectron.* **2006,** *21,* 2106.

(63) World Health Organization, Guidelines for Drinking-water Quality, 4th ed.; WHO Press: Geneva, **2011**; p 340.

(64) Huo, F. J.; Yin, C. X.; Yang, Y. T.; Su, J.; Chao, J. B.; Liu, D. S. *Anal. Chem.* **2012,** *84,* 2219.

(65) Sarma, M.; Kalita, A.; Kumar, P.; Singh, A.; Mondal, B. *J. Am. Chem. Soc.* **2010,** *132,* 7846.

(66) Mondal, B.; Kumar, P.; Ghosh, P.; Kalita, A. *Chem. Commun.*, **2011,** *47,* 2964.

(67) Wright, A. M.; Wu, G.; Hayton, T. W. *J. Am. Chem. Soc.* **2010,** *132,* 14336.

(68) Sarma, M.; Mondal, B. *Inorg. Chem.* **2011,** *50,* 3206.

(69) Deshmukh, R.; Trivedi, V. *Toxicol in Vitro* **2013,** *27,* 16.

(70) Gaetke, L. M.; Chow, C. K. *Toxicology* **2003,** *189,* 147.

(71) Bonnefous, C.; Payne, J. E.; Roppe, J.; Zhuang, H.; Chen, X.; Symons, K. T.; Nguyen, P. M.; Sablad, M.; Rozenkrants, N.; Zhang, Y.; Wang, L.; Severance, D.; Walsh, J. P.; Yazdani, N.; Shiau, A. K.; Noble, S. A.; Rix, P.; Rao, T. S.; Hassig, C. A.; Nicholas, D.; Smith, N. D. *J. Med. Chem.* **2009,** *52,* 3047.

Appendix

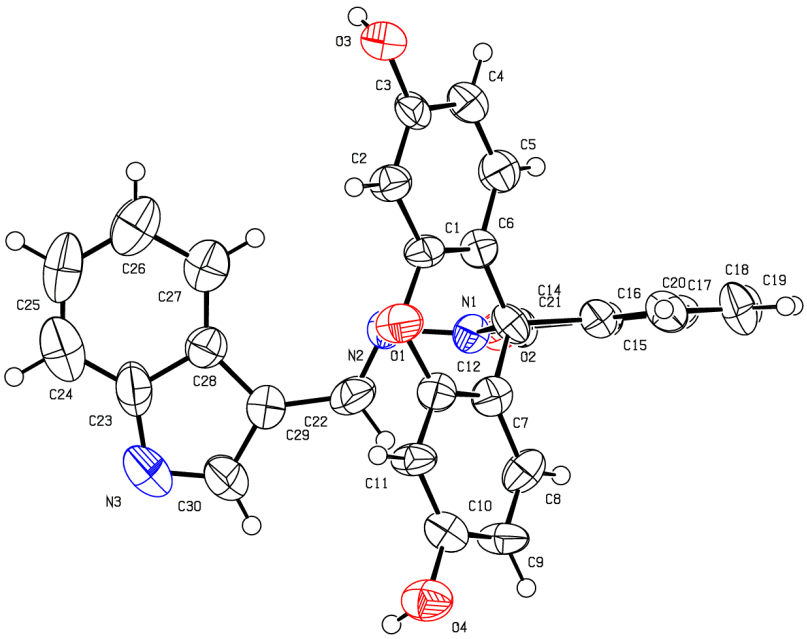

Figure A4a.1 Crystal data for $C_{29}H_{19}N_3O_4$: Bond precision: C-C = 0.0191 Å, Wavelength = 0.71073, monoclinic, space group P21/c. a = 12.099 (2), b = 9.9402 (17), c = 22.170 (3) Å, β = 108.585° (10), V = 2527.3 (7) $Å^3$, Z = 4, T = 293 K, θ_{max} = 25.250°, F_{000} = 980.0, 17591 reflections measured, 4216 unique (R_{int} = 0.1613). Final residual for 315 parameters and 4216 reflections with I>2σ(I): R1 = 0.1501(1353), *w*R2 = 0.4454 (4216), N_{ref} = 4584, N_{par} = 315 and GOF (S) = 0.829. CCDC number for FI is 952791.

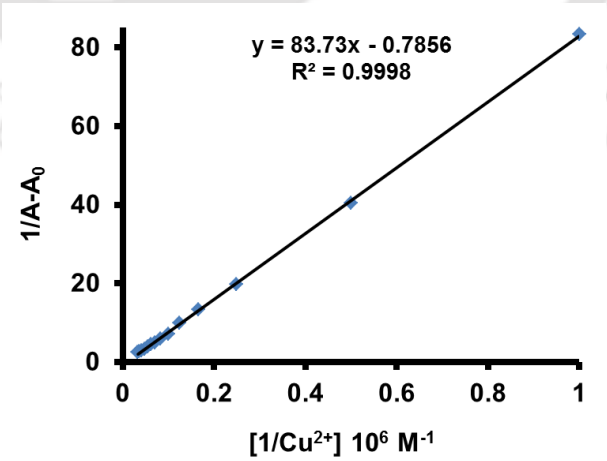

Figure A4a.2 Benesi-Hildebrand plot obtained from the UV-vis absorption (absorbance calculated from 492 nm) studies.

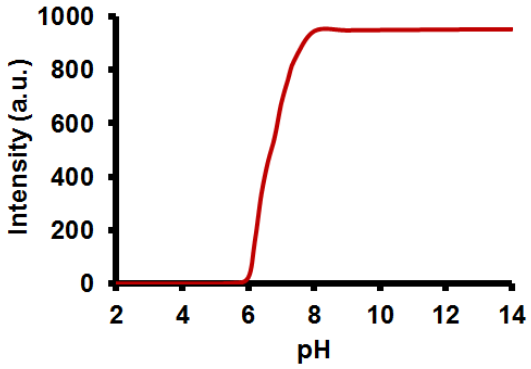

Figure A4a.3 Fluorescence titration of FI+Cu^{2+} at different pH in 10 mM HEPES buffer solution. λ_{em}= 518 nm.

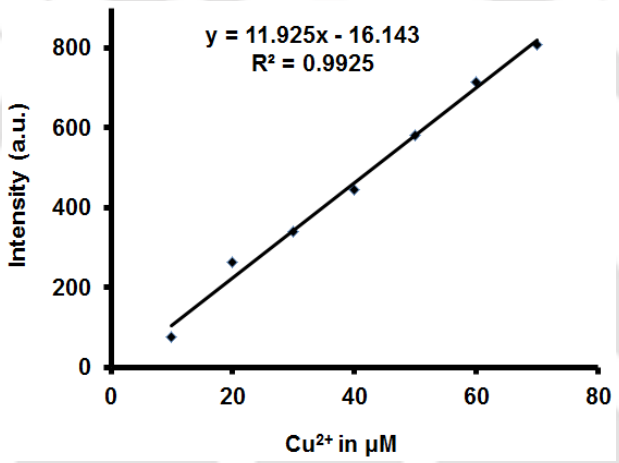

Figure A4a.4 The detection limit calculated for Cu^{2+} by using FI probe.

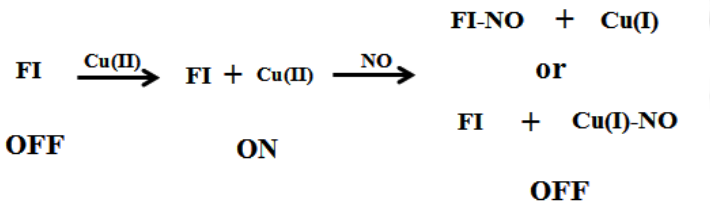

Figure A4a.5 Proposed mechanism for the fluorescent changes of FI upon the addition of Cu^{2+} metal ion and reduction of complex by NO.

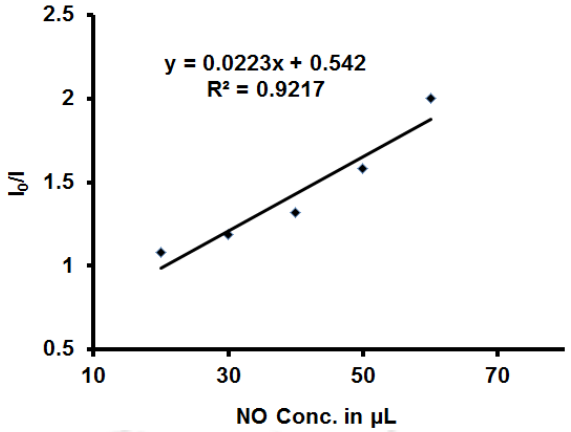

Figure A4a.6 The detection limit calculated for NO by using FI+Cu^{2+} complex.

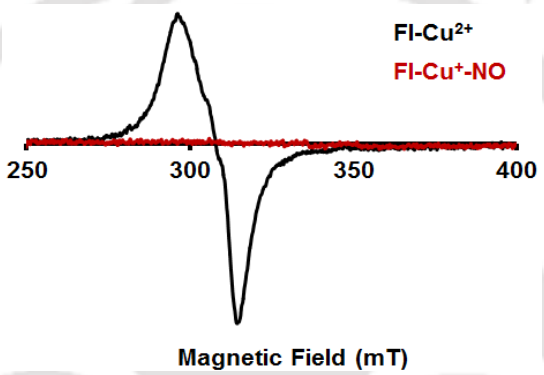

Figure A4a.7 X-band EPR spectra of the complex FI-Cu^{2+} with and without nitric oxide in an acetonitrile solvent at room temperature. Black traces correspond to the respective complexes, and red traces represent the spectra of [Cu-NO] intermediates.

Chapter: 4b

Multiple Function Fluorescein Probe Performs Metal Chelation, Disaggregation and Modulation of Aggregated Aβ fibrils and Aβ-Cu Complex

Abstract

An exceptional probe comprising indole-3-carboxaldehyde fluorescein hydrazone (FI) performs multiple tasks, namely, disaggregating amyloid β (Aβ) aggregates in different biomarker environments such as cerebrospinal fluid (CSF Aβ fibrils), Aβ1-40 fibrils, β-amyloid lysozyme aggregates (LA) and U87 MG Human astrocytes cells. Additionally, the probe FI binds with Cu^{2+} ions selectively, disrupts the Aβ aggregates into disaggregated forms and prevents their reaggregation, thereby performing disaggregation and modulation of amyloid-β in the presence as well as absence of Cu^{2+} ion. The excellent selectivity of probe FI for Cu^{2+} was effectively utilized to modulate the assembly of metal-induced Aβ aggregates by metal chelation with the "turn-on" fluorescence via spirolactam ring opening of FI as well as the metal-free Aβ fibrils by noncovalent interactions. These results confirm that FI has exceptional ability to perform multifaceted tasks such as metal chelation in intracellular conditions using Aβ lysozyme aggregates in cellular environments by the disruption of β-sheet rich Aβ fibrils into disaggregated forms. Subsequently, it was confirmed that FI had the ability to cross the blood brain barrier and it also modulated the metal induced Aβ fibrils in cellular environments by "turn-on" fluorescence, which are the most vital properties of a probe or a therapeutic agent. Furthermore, the morphology changes were examined by atomic force microscopy (AFM), polarizable optical microscopy (POM), fluorescence microscopy and dynamic light scattering (DLS) studies. These results provide very valuable clues on the Aβ (CSF Aβ fibrils, Aβ1-40 fibrils, β-amyloid lysozyme aggregates) disaggregation behavior via *in vitro* studies, which constitute the first insights into intracellular disaggregation of Aβ by "turn-on" method thereby influencing amyloidogenesis.

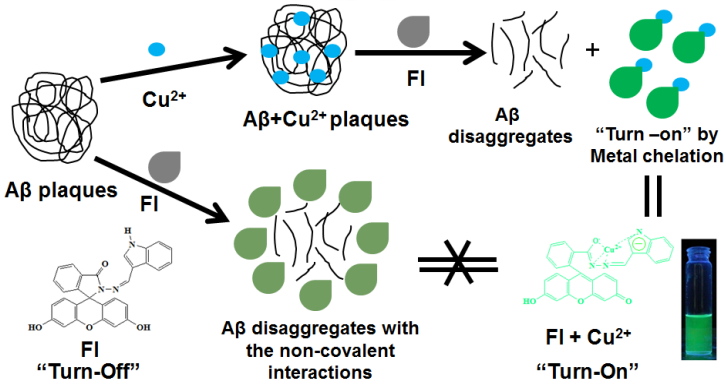

4b.1. Introduction

Alzheimer's disease (AD), the most prevalent cause of dementia among elderly population, affects >40 million people worldwide.[1,2] Early symptoms such as difficulty to remember newly acquired information and other severe symptoms such as mood and behavior changes, perplexity, severe memory loss, and judgment alteration coupled with difficulties in speaking, writing and walking predominantly begin to appear with aging. As per the AD hypothesis, the aggregation of amyloid-β (Aβ) peptide is linked to the etiology of the disease, since soluble monomeric forms are found in the healthy brain while Aβ plaques are detected in an AD patient's brain.[3,4] These Aβ aggregates provides an important pharmacological target in the ability of drugs to (a) disrupt the already formed Aβ aggregates, (b) prevent the Aβ aggregation, or (c) be capable of arresting and inverting the progression of AD.[5,6] Aβ1-40 and Aβ1-42 peptides are the primary species in the structure of the senile plaques found in the brain tissues of AD patients.[6-8] Metal ions, such as iron, copper and zinc are known to interact with Aβ peptides and promote their aggregation as well as generation of neurotoxicity.[9-18] They also have the ability to modulate the aggregation of Aβ peptides as observed by *in vitro* experiments.[9,19-22] Despite being an important pharmacological target for AD pathogenesis, separation of toxic metals from Aβ peptide fibrils along with their disruption and modulation remains unresolved.

The accumulation of metals such as iron, copper and zinc within the senile plaques can reach levels of up to 400, 950 and 1100 mm, respectively, which is 3-5 times higher in concentration as compared to healthy brain.[23-27] To reduce the harmful effects of excess metal deposition, newer therapies that focus on metal ion chelation for AD are being developed.[28-30] Metal chelators are potential therapeutic prospects due to the metal ion hypothesis and the possible contribution of metal−Aβ to AD. For therapeutic strategy, a new type of compound based on inhibiting or modulating metal-Aβ interactions, known as metal-protein attenuating compounds (MPACs), are being designed and developed. Compared with traditional chelators such as DFO and TETA, there are two metal chelators which have accomplished phase II clinical trials like clioquinol (CQ) and its derivative (PBT2) that have been tested in murine AD models and AD patients.[31,32] The hydroxyquinoline derivatives of clioquinol (CQ) decreased Aβ aggregates and showed improved cognition in phase II clinical trials for AD due to its ability to inhibit binding of Cu(II) to Aβ via chelation.[31,33,34] In addition, derivatives of 8-hydroxyquinoline ionophore PBT2 also resulted in improved cognition

ability (learning and memory) by redistributing Cu(II) and Zn(II) and by lowering CSF levels of Aβ in phase II clinical trials.[35,36] Both, CQ and PBT2 have the ability to alter the metal levels as well as the Aβ clearance. Hence, newer and appropriate efforts are necessary for developing efficient molecules for targeting metal–Aβ species and overcome this challenge posed by both metals as well as self-assembled peptides.[37-41] To study this relation between metal−Aβ complexes with AD pathology it is necessary to design and synthesize molecules with multifunctional ability.[42-45] The potential development of metal chelating molecules and AD therapy could help in understanding the importance of fundamental mechanisms involving Cu(II) binding with Aβ peptide and the successful implementation of this strategy could guide the aspect of metal−Aβ-induced aggregation and disaggregation.

The Aβ1-40 peptide contains several binding sites with the hydrophilic N-terminal amine, three His moieties at 6, 13, and 14 as well as four carboxylic acid moieties at 1, 3, 7 and 11.[46] The hydrophilic N-terminal part of Aβ1-40 is responsible for binding the metal ions, namely, copper, zinc and iron, which are accountable for the modulation of Aβ aggregation and neurotoxicity.[5] The redox active metal ions and cofactors (heme) bind Aβ peptides and can produce harmful and partially reduced oxygen species (PROS) under physiological conditions.[47-49] They also lead to the formation of soluble cross linked dimeric species of Tyr10 repeatedly by oxidization of the Aβ peptide side chains.[50,51] This process further leads to the formation of Aβ aggregates responsible for progressive neurodegeneration in AD. Tyrosine (Tyr) is a crucial amino acid for both conformation as well as probing the biological activity of Aβ due to its emission in the visible region.[52-55] Thus, to conform the binding of copper in Aβ peptide, the fluorescence of Tyr was carefully followed, since its fluorescence is quenched on binding Cu^{2+}, whereas, the fluorescence is retained on withdrawal of Cu^{2+} from Aβ peptides.[56]

4b.2. Results and discussion

The indole-3-carboxaldehyde fluorescein hydrazone probe (FI) was synthesized and its selectivity toward copper ion (Figure 4b.1) was discussed in chapter 4a (Scheme 4a.1).[57] Further we selected it as a modulator or anti AD molecule since it possesses several exceptional properties such as easy synthesis, very high aqueous solubility, easy cell penetrability, high fluorescence quantum yield, high molar extinction coefficient value and most importantly a biofriendly nontoxic fluorophore for the highly selective “turn-on” detection of Cu^{2+} ion. Hence, the modulation or disaggregation of Aβ peptides such as, Aβ

fibrils (with and without Cu^{2+}), Aβ aggregates in real CSF and Aβ lysozyme aggregates (LA) (with and without Cu^{2+}) were studied in the presence of multifunctional FI to control the AD progression as well as to develop a method that could lead to the design and development of better therapeutic alternatives for efficient control and prevention of AD.

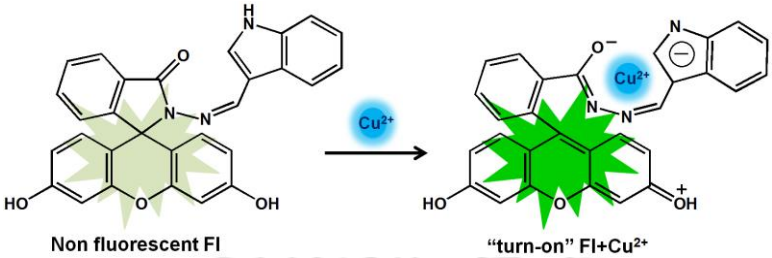

Figure 4b.1 Nonfluorescent FI (3 μM) selectively detects Cu^{2+} ion (3 eq.) in HEPES buffer solution (pH 7.4, 10 mM).

4b.2.1.Tyrosine intrinsic fluorescence assay

Since Tyr10 is located in the close proximity to the three histidine residues (6, 13, and 14) it is expected to be involved in metal coordination, thereby resulting in metal-induced chemical changes.[58] Tyr10 is the main fluorophore for the intrinsic fluorescence of Aβ1-40 and has been utilized to investigate the formation of a complex between Aβ1-40 and Cu^{2+} ions.[59-62] The tyrosine intrinsic fluorescence of Aβ1-40 is quenched when Cu^{2+} ion binds to the Aβ1-40 peptide, whereas, the fluorescence is regained on adding Cu^{2+} ion chelators (FI).[60-64] This transformation in the tyrosine intrinsic fluorescence assay was utilized to exploit the capability of FI for chelating Cu^{2+} ions from Aβ1-40+Cu^{2+}aggregates.

The modifications in the fluorescence of Tyr10 (in Aβ1-40 sequence) were monitored (Figure 4b.2) by adding 10 and 20 μM Cu^{2+} to a 20 μM Aβ1-40 in 10 mM HEPES buffer (pH 7.4). On adding 10 μM concentration of Cu^{2+} ions into the Aβ1-40 solution the fluorescence quenching of Tyr10 at 305 nm (Figure 4b.2a, blue line) occurs rapidly due to the formation of Aβ1-40+Cu^{2+} complex with the three His moieties at 6, 13, and 14 as well as four carboxylic acid moieties at 1, 3, 7 and 11. Further addition of up to 20 μM Cu^{2+} to Aβ1-40 solution resulted in nearly complete quenching of Tyr10 fluorescence (Figure 4b.2a, green, and red lines).[65] The fluorescence quenching of Tyr10 occurred due to the significant increase in the electron density at the Cu^{2+} centre which further results in the charge transfer to other groups in close proximity such as Tyr10 residue. This interaction was expected to reduce the fluorescence intensity upon Cu^{2+} binding by facilitating nonradiative energy transfer from the excited state of Tyr10.[58]

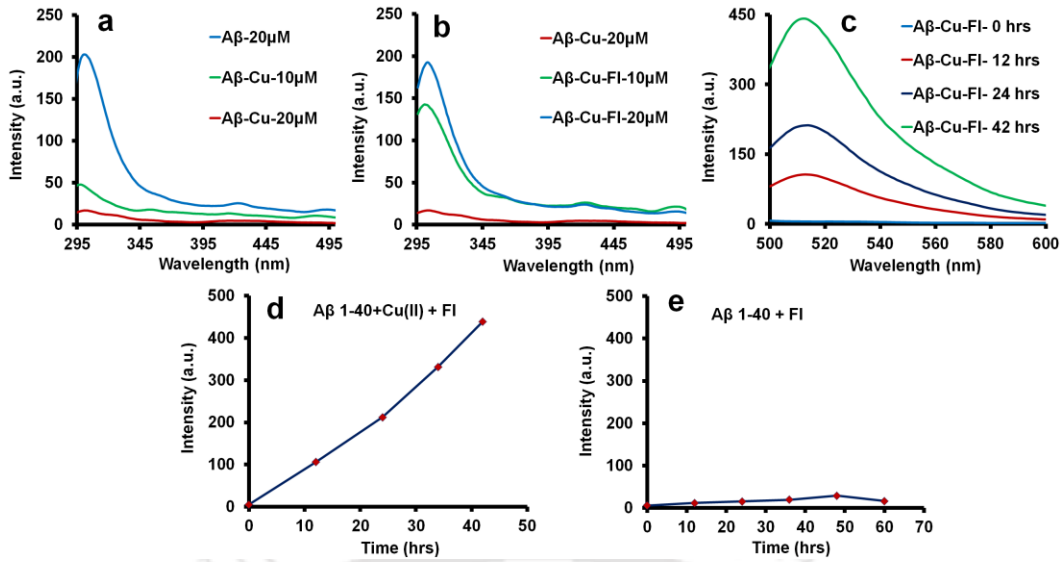

Figure 4b.2 (a) Tyr fluorescence quenching in Aβ1-40 (20 μM), 10 mM HEPES buffer (pH 7.4) upon the addition of 10 and 20 μM Cu^{2+}. (b) Tyr fluorescence dequenching upon the addition of 10 and 20 μM FI into Aβ1-40-Cu^{2+} (1:1) in 10 mM HEPES buffer (10 mM, pH 7.4). (c) At excitation of 465 nm, the emission peak is obtained at 518 nm for FI -Cu^{2+} (0-42 h). (d) Modulation or disaggregation of Aβ1–40+Cu^{2+} aggregates by FI: Fluorescence changes of Aβ1–40+Cu^{2+} (20 μM) aggregates with FI (20 μM) were monitored with different time incubations at 465 nm excitation, the "turn-on" fluorescence enhancement peak is obtained at 518 nm for FI+Cu^{2+} complex. (e) Modulation or disaggregation of Aβ1–40 aggregates by FI: Fluorescence changes of Aβ1–40 (20 μM) aggregates with FI (20 μM) were monitored with different time incubations at 465 nm excitation; no significant "turn-on" fluorescence enhancement peak is obtained at 518 nm.

4b.2.2. Metal chelation from Aβ1-40+Cu^{2+} aggregates using FI chelator

After 24 h incubation of the Aβ1-40+Cu^{2+} complex, the probe FI was utilized to monitor the chelation of Cu^{2+} from the complex of Aβ1-40+Cu^{2+} aggregates. The quenched intrinsic fluorescence of Tyr regained rapidly upon addition of FI (20 μM). The resulting enhanced fluorescence intensity was compared with the fluorescence intensity of Aβ+Cu^{2+} alone to determine whether FI (as chelator) could extract copper and/or modulate Aβ1-40+Cu^{2+} aggregates (Figure 4b.2b). In a typical experiment, the addition of upto 20 μM FI to Aβ1-40+Cu^{2+} aggregates resulted in the Tyr fluorescence being regained completely (without incubation) since the interactions between Cu^{2+} and Tyr OH were disrupted (Figure 4b.2b). To further validate the role of Cu^{2+} ions in Aβ1-40, the Aβ-Cu-FI complex was excited at 465 nm (0-42 h time incubation) resulting in a new and prominent emission peak at 518 nm (Figure 4b.2c and 4b.2d) corresponding to the formation of FI-Cu^{2+} complex (Figure 4b.1).

When excited at 465 nm, Aβ-Cu-FI did not show any emission in the range of 500-600 nm at 0 h (Figure 4b.2c, light blue line) indicating that FI remains in spirolactam ring form but disrupts the Tyr OH interactions with Cu^{2+} ions. After incubation (0-42 h), when the Aβ-Cu-FI complex was excited at 465 nm, Cu^{2+} ion induced the spirolactam ring opening of FI with a significant "turn-on" fluorescence response at 518 nm and a highly bright green fluorescence (Figure 4b.2c and 4b.2d; 0-42 h) was observed. The apparent binding constant for the formation of the respective complexes were evaluated using the Benesi−Hildebrand (B−H) plot and was estimated to be 6.33×10^4 M^{-1} by the emission spectral changes at 518 nm (Figure A4b.1). However, in the present study, the probe FI had a major influence on the Tyr fluorescence of Aβ1-40+Cu^{2+} aggregates (Figure 4b.2b). These results indicate that FI was able to chelate metal ions from metal-bound Aβ species to different extents. When similar experiments were performed with FI (20 μM) and Aβ self-aggregates (without Cu^{2+}), no significant "turn-on" fluorescence response at 518 nm (Figure 4b.2e, 0-60 h) occurred. Moreover, we also performed control experiments to chelate metal ion from Aβ1-40 (20 μM) + Cu^{2+} (20 μM) aggregates by nonfluorescent metal chelator (EDTA 2 equiv), while monitoring Tyr fluorescence at 305 nm. No significant dequenching was observed by EDTA (Figure A4b.2) as compared to the probe FI which confirms that FI has a stronger affinity for Cu^{2+} as compared to Aβ1-40. Thus, the probe FI could retrieve Cu^{2+} from Aβ1-40 and modulate the Aβ aggregates. Finally, these studies confirm the superior performance of FI as compared to the previously reported metal chelators.[66-70]

4b.2.3. Thioflavin T (ThT) assay

ThT is one of the most widely used fluorescent dye to identify Aβ fibrils.[71,72] A gradual enhancement of emission peak at 487 nm (Figure A4b.3a) occurred (0-40 h incubation time, λ_{ex}–440 nm) on addition of monomer Aβ1-40 to ThT (20 μM), signifying the formation of Aβ fibrils. The fluorescence intensity of ThT increased on binding Aβ fibrils due to the changes in the rotational freedom of the C-C bonds between the benzothiazole and aniline rings.[73] On monitoring the ThT assay in the presence of Cu^{2+} ions the emission peak enhancement (487 nm) saturated after 12 h, which confirmed the formation of metal induced Aβ aggregates (Figure A4b.3b). The formation of Aβ1-40 aggregates in the absence of Cu^{2+} was lesser (Figure A4b.3a) compared to that in the presence of Cu^{2+}.[73-75] The presence of Aβ fibrils in CSF was also confirmed by ThT fluorescence enhancement at 487 nm (Figure A4b.3c).[76]

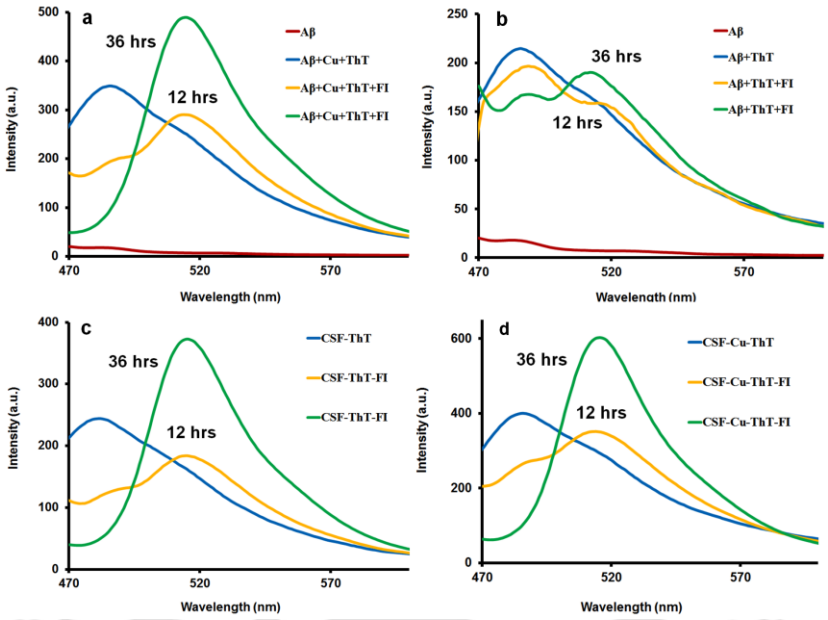

Figure 4b.3 (a) Aggregation of Aβ1-40 with Cu^{2+} in the presence of ThT and disaggregation of Aβ1-40+Cu^{2+} in the presence of FI. (b) Aggregation of Aβ1-40-ThT emission peak at 487 nm shows insignificant change on adding FI. (c, d) CSF aggregates in the absence and presence of Cu^{2+} ion with ThT (pH 7.4 in 10 mM HEPES) showed emission peak at 487 nm (λ_{ex} 440 nm) and disaggregation of CSF Aβ aggregates observed in the presence of FI (λ_{ex} 440 nm, 31 nm shifted to 518 nm with FI).

The Aβ peptide monomers are known to be less toxic.[9-18] When Cu^{2+} ions interact with Aβ peptides, they promote their aggregation into neurotoxic Aβ fibrils.[9-18] Hence, the modulation and disruption of metal-Aβ interaction can significantly influence the AD progression. To establish this metal chelation behavior and disaggregation of Aβ fibrils by FI, we performed *in vitro* experiments using ThT assay (Figure 4b.3). Probe FI containing Cu-Aβ1-40 complex was 31 nm red shifted from the 487 nm emission peak of Aβ-ThT to 518 nm (which is the emission peak of FI-Cu^{2+} complex) after 12 and 36 h incubation at 37 °C (Figure 4b.3a, orange and green lines). This 31 nm red shifted emission once again confirms that probe FI has the ability to chelate Cu^{2+} ions from the complex of Cu-Aβ1-40 aggregated fibrils. This result also strongly supports the metal chelation hypothesis which confirms that trapping Cu^{2+} ion from aggregated Aβ1-40-Cu^{2+} complex using FI, frees the ion binding sites of Aβ1-40 peptides and modulates the Cu^{2+} induced Aβ1-40 aggregation. Further, the probe FI with Aβ1-40 self-aggregates also showed a new emission peak at 518 nm with the emission of Aβ-ThT at 487 nm after 12 and 36 h incubation at 37 °C (Figure 4b.3b, orange and green lines) which was less prominent as compared to that occurring in the presence of Cu^{2+} due to the

noncovalent interactions between FI and Aβ fibrils, namely, H-bonding or weak aromatic interactions.[77-79] Furthermore, we performed additional control experiments to disaggregate Aβ1-40+Cu^{2+} aggregates by nonfluorescent metal chelator (EDTA 20 μM), while monitoring the ThT fluorescence at 487 nm, which showed ~20% quenching by EDTA (Figure A4b.4) that was insignificant as compared to the probe FI since FI showed "turn-on" red shifted emission at 518 nm on metal chelation.

CSF is one of the main pathological biomarker produced in the brain and analyzed routinely for neurological disorders.[80-83] Hence, CSF samples were evaluated to ascertain the presence of Aβ and metal deposits in it and further examine the practical role of FI in the homeostasis process. This experiment was designed to find a superior approach to disaggregate the β-sheets rich Aβ aggregates and also to prevent their reaggregation. Since these experiments were performed using real CSF samples, we tested the Aβ peptide aggregation and the presence of fibrils in it by ThT fluorescence enhancement study in the absence and presence of Cu^{2+} ion (Figure 4b.3c and 4b.3d blue lines). The CSF samples were confirmed to have aggregated fibrils (Figure 4b.3c blue line and A4b.3c).[76] On addition of external Cu^{2+} (20 μM) (incubation for 12 h), the emission peak at 487 nm enhanced significantly (Figure 4b.3d, blue line) due to the formation of excess Aβ aggregation in the presence of Cu^{2+}. When FI was added into CSF-Cu^{2+} complex in the presence of ThT, the emission peak at 487 nm was red shifted by 31 nm to 518 nm which is the emission peak of FI-Cu^{2+} complex (Figure 4b.3d orange and green lines correspond to 12 and 36 h). These results validate the multiple ability of probe FI to strongly chelate the Cu^{2+} ion present within the CSF-Cu complex as well as disaggregate the Aβ fibrils (Figure 4b.3d). The FI mixed real CSF (without external Cu) sample also showed the emission peak at 487 nm corresponding to Aβ-ThT. This 487 nm peak was also 31 nm red shifted to 518 nm as mentioned above, which is the emission peak of FI+Cu complex due to the likely presence of Cu^{2+} ions in the real CSF sample and their chelation by FI (Figure 4b.3c orange and green lines correspond to 12 and 36 h). Thus multiple tasks such as modulation of Aβ peptides, disaggregation or disruption of Aβ fibrils by abstracting Cu^{2+} ion from CSF and preventing them to reaggregate was demonstrated with FI and which has not been perceived till date with any other class of probes or materials.

Further, this small molecule probe FI along with ThT was also screened to identify newer lead compounds that could modify the Aβ-Cu aggregates or Aβ self-aggregates. In order to determine the influence of FI binding with Aβ-Cu aggregates and Aβ self-aggregates, the

fluorescence changes of ThT in the presence of Aβ-Cu aggregates and Aβ self-aggregates with FI (Figure 4b.3) were monitored. Notably, the ThT fluorescence intensity with FI in the presence of Aβ-Cu aggregates is much lower than that without FI and/or Aβ self-aggregates with FI (Figure 4b.3). After 36 h incubation of FI with Aβ-Cu aggregates and ThT, followed by excitation at 440 nm, the ThT emission maximum at 487 nm disappeared since there was a strong FI emission at 518 nm (Figure 4b.3) due to the metal chelation as well as by the consistent energy transfer from donor ThT to acceptor FI (FRET).[84] The spectral overlap was confirmed from the emission spectra of ThT dye in the presence of Aβ-Cu aggregates and the excitation spectra of FI (Figure A4b.5). Finally, the observed spectral overlap results confirm that the "turn-on" fluorescence or red shifted emission band appeared at 518 nm due to the formation of FI-Cu^{2+} complex (Figure A4b.5).[84] Similarly, the experiment was also repeated with Aβ self-aggregates by following ThT fluorescence with FI. When the Aβ self-aggregate was incubated with FI in the presence of ThT and excited at 440 nm, the ThT emission maximum at 487 nm does not disappear as in the case of Aβ-Cu aggregates, but the energy transfer from donor of ThT to acceptor FI (Figure 4b.3b) was as expected.

4b.2.4. UV-Visible spectroscopy study for the modulation of Aβ aggregates and metal chelation confirmation

The retrieval of Cu^{2+} from Aβ1-40+Cu^{2+} aggregates was confirmed by UV-vis spectroscopy (Figure 4b.4 (a-c)) via formation of FI+Cu^{2+} complex.[85] The enhanced absorbance of Aβ (20 μM) + Cu^{2+} (20 μM) aggregates (1:1) was obtained at ~264 nm which is 8 nm blue-shifted from the 272 nm of Aβ peptides due to the charge transfer mechanism (Figure 4b.4 (a)). The absorbance behavior of FI (10 and 20 μM) in the presence of Aβ+Cu^{2+} aggregates (1:1) was subsequently investigated after 24 h incubation. The wavelength of absorption of the closed-ring form of FI at 342 nm clearly vanished and a new absorption band appeared at 492 nm due to the formation of spirolactam ring opening of the xanthene moiety because of the formation of FI-Cu^{2+} complex by metal chelation. Further, a similar experiment performed with Aβ self-aggregates (without Cu^{2+}) in the presence of FI (20 μM), showed no response at 492 nm (Figure 4b.4 (b)). For the control studies, we performed an experiment between FI and free Cu^{2+} and the absorbance behavior of FI was investigated before and after the addition of Cu^{2+} (Figure 4b.4 (c)). The maximum absorption band at 342 nm was obtained for FI in its closed-ring form. Upon addition of Cu^{2+} (20 μM) into FI (20 μM) (1:1), a new absorption band appeared at 492 nm, accompanied by a change in the color from colorless to green which represents the open spirolactam ring form of the xanthene moiety. Such a huge

~150 nm Cu^{2+}-induced absorption shift could be attributed to the high conjugation and planarity of the indole moiety of FI with the binding sites which favors maximum negative charge distribution of the deprotonated receptor in the presence of Cu^{2+} ion.[57]

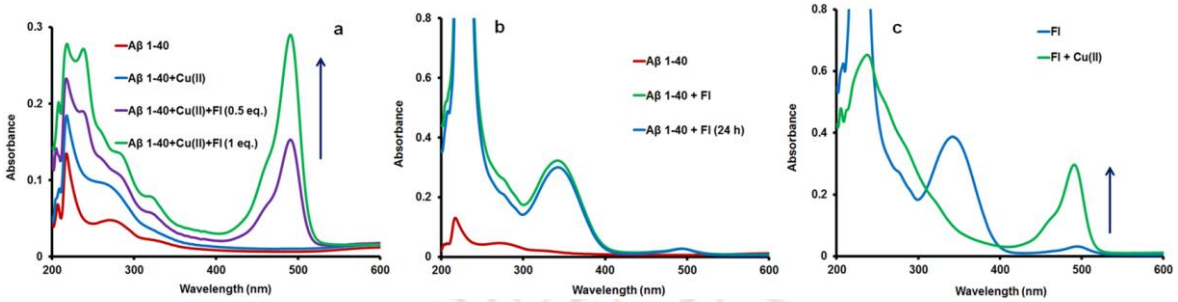

Figure 4b.4 Modulation or disaggregation of Aβ1–40+Cu^{2+} aggregates by FI: (a) UV-vis spectra of Aβ1–40 (20 μM) (red curve) and the formation of Aβ1–40+Cu^{2+} aggregates in the presence of Cu^{2+} (20 μM) (blue curve). Disaggregation of Aβ1–40+Cu^{2+} aggregates with FI (0.5 and 1 equiv) were monitored using UV-vis spectra after 24 h incubations time, with the appearance of new "turn-on" enhancement peak obtained at 492 nm. (b) UV-vis spectra of Aβ1–40 (20 μM) (red curve) and the changes of Aβ1–40 aggregates with FI (1 1 equiv) were monitored by using UV-vis spectra after 0 (green curve) and 24 h (blue curve) incubation time and no significant changes were obtained at 492 nm. (c) UV-vis spectra of FI (20 μM) (blue curve) and the formation of FI+Cu^{2+} complex in the presence of Cu^{2+} (20 μM) (green curve) showed the appearance of a new "turn-on" enhancement peak obtained at 492 nm after 24 h incubation time.

4b.2.5. DLS study to determine the size of aggregated and disaggregated or modulated form of Aβ aggregates

To determine the size of FI with aggregated Aβ peptides (Aβ1–40, CSF) and disaggregation or disruption of Aβ peptides (Aβ1–40, CSF) in the absence and presence of Cu^{2+} in aqueous solution, DLS measurements were performed on these samples. These experiments provided vital clues to arrive at a conclusion that FI could accelerate the disaggregation or disruption of Aβ peptides (Aβ 1–40, CSF) in aqueous solution as shown in figure 4b.5 (a-c). The control experiments confirmed that the hydrodynamic particle diameter of Aβ1–40 (530 ± 70 nm), Aβ1–40+Cu^{2+} (615 ± 100 nm) and Aβ peptides in CSF (712 ± 100 nm) were bigger in size as compared to the complex of FI+Aβ 1–40 (295 ± 50 nm), FI+Aβ 1–40+Cu^{2+} (295 to 340 nm), FI+CSF (295 ± 50 nm) and FI+CSF+Cu^{2+} (255 − 295 nm). Therefore, these results further validated that rapid and efficient disruption or disaggregation of Aβ peptide aggregates

(Aβ1–40, CSF) could be achieved efficiently by the introduction of FI in the presence as well as the absence of Cu^{2+} ion (Figure 4b.5 (a-c)).

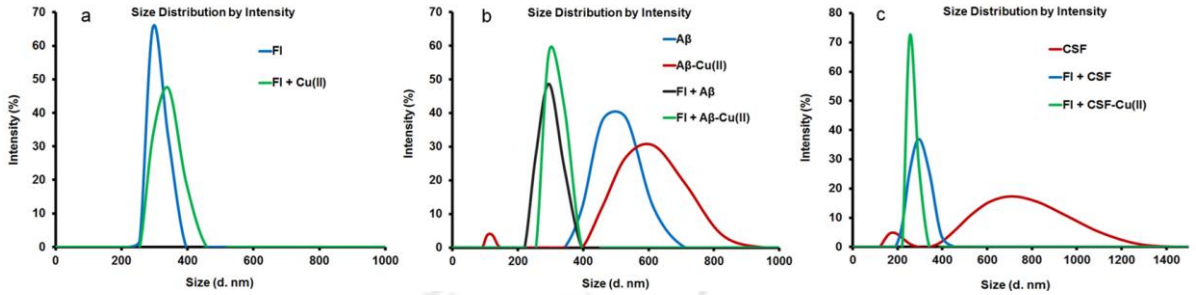

Figure 4b.5 Modulation or disaggregation of Aβ1–40+Cu^{2+} aggregates by FI: (a) Hydrodynamic particle size (d. nm) of the molecular species of FI and FI+Cu^{2+} complex was determined by dynamic light scattering. (b, c) Hydrodynamic particle size (d. nm) of the aggregated Aβ peptides (Aβ 1–40, CSF) and disruption or disaggregation of Aβ peptides (Aβ 1–40, CSF) in the absence and presence of Cu^{2+} with and without FI in aqueous solution measured by dynamic light scattering.

4b.2.6. Preparation and modulation of Lysozyme Aβ aggregates

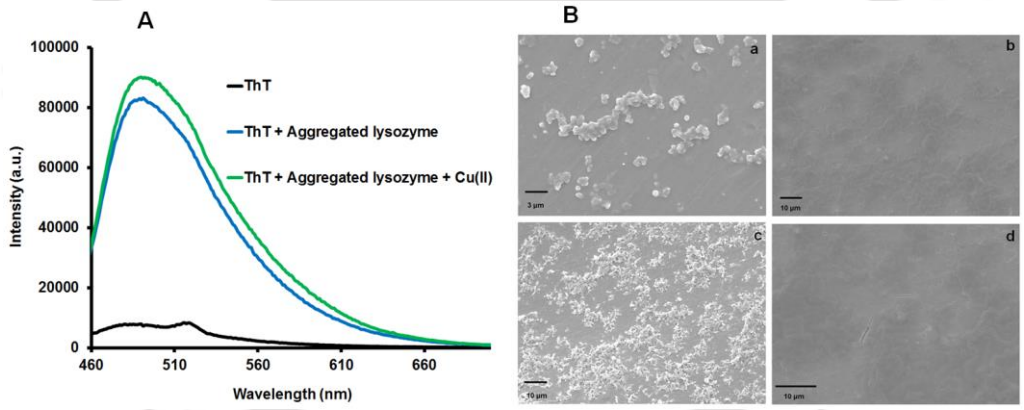

Figure 4b.6 (A) Lysozyme aggregated amyloid fibrils and plaques in the absence and presence of Cu^{2+} with ThT (pH 7.4 in PBS) showed emission peak (blue line) at λ_{em} 487 nm (λ_{ex} 440 nm). (B) (a, c) SEM images of the morphologies of lysozyme aggregated fibrils (absence of Cu^{2+} ion) and aggregated amyloid plaques in the presence of copper ions (20 μM). (b, d) Lysozyme aggregated fibrils and aggregated amyloid plaques are disaggregated in the presence of modulator FI (20 μM).

Large aggregated Aβ fibrils were obtained by heating lysozyme solution for 5 days (10 mg in 1 mL) at pH 2, 65 ^{o}C. The process of lysozyme fibrillation was confirmed by ThT binding assay where ThT is commonly used to detect Aβ since it is reported to bind specifically to the

characteristic β-sheet structure of Aβ fibrils (Figure 4b.6). Morphologies of the formation of LA fibrils without Cu^{2+} and aggregated Aβ plaques with Cu^{2+} were detected by electronic microscopy images (SEM). For the modulation of LA fibrils and aggregated Aβ plaques, 20 μM of lysozyme aggregated fibrils (10 mM PBS, pH 7.4) were incubated without and with Cu^{2+} (20 μM) in the presence of FI (20 μM) at 37 ^{o}C for 2 days. These results demonstrated that FI treated lysozyme aggregated plaques and the Aβ fibrils were disaggregated or modulated completely due to the metal chelation and noncovalent interactions by FI.

4b.2.7. Confirmation studies of aggregation and disaggregation or modulation of Aβ aggregates

Morphological evidence for the disaggregation and modulation of Aβ1-40 fibrils and Cu^{2+}-Aβ1-40 aggregation in the presence of FI (Figure 4b.7A) was obtained by AFM images. As demonstrated, Aβ1-40 aggregates showed well-defined micron sized Aβ fibrils after 36 h incubation at 37 °C. The existence of matured aggregated Aβ fibrils in CSF was also confirmed by AFM images (Figure 4b.7A). Further, in the presence of FI, the Cu^{2+} induced Aβ1-40 aggregates were disaggregated completely due to the metal chelation by FI from the Aβ-Cu^{2+} complex.[86-89] The same experiment when performed using CSF Aβ fibrils in the presence of FI confirmed that the CSF aggregated fibrils also disaggregated due to the metal chelation (Figure 4b.7A). The AFM images obtained after the modulation experiments display completely different morphology unlike the Aβ fibrils (Aβ1-40 and CSF). Surprisingly, the probe FI disaggregated and modulated the Aβ self-aggregated fibrils even in the absence of Cu^{2+} ions, due to the noncovalent interactions between FI and Aβ fibrils.[90-92]

The polarized optical microscopy (POM) images (Figure 4b.7B) demonstrated that aggregated Aβ1-40 and CSF showed presence of spherical Aβ aggregates. These spherical aggregates of Aβ1-40, when incubated with FI for 36 h, in the absence as well as in the presence of Cu^{2+} and CSF mixed FI sample (Figure 4b.7B) gets disaggregated completely, confirming the ability of FI to convert Aβ aggregates into disaggregated forms.

The transformation of Aβ1–40 secondary structure was also examined by FT-IR spectroscopy (Figure 4b.7C). The presence of a major band at 1629 ± 2 cm^{-1} indicates the parallel β-sheet conformation of Aβ1–40 aggregates (Figure 4b.7C, black line).[93-97] The FT-IR spectra of FI mixed with β-sheet rich Aβ1–40 fibrils and with Aβ1–40+Cu^{2+} are shown as pink and green lines respectively (Figure 4b.7C). The parallel β-sheet conformation of Aβ1–40 was transformed into the random coil conformation due to the structure modulation and metal chelation of Aβ1–40+Cu^{2+} with FI, as illustrated by a major band at 1644 ± 2 cm^{-1}.

Similarly, CSF on incubation with FI for 36 h shows a major band at 1644 cm^{-1} confirming that FI converts β-sheet rich Aβ-aggregates in CSF into modulated random coil conformations (Figure 4b.7C, blue line).

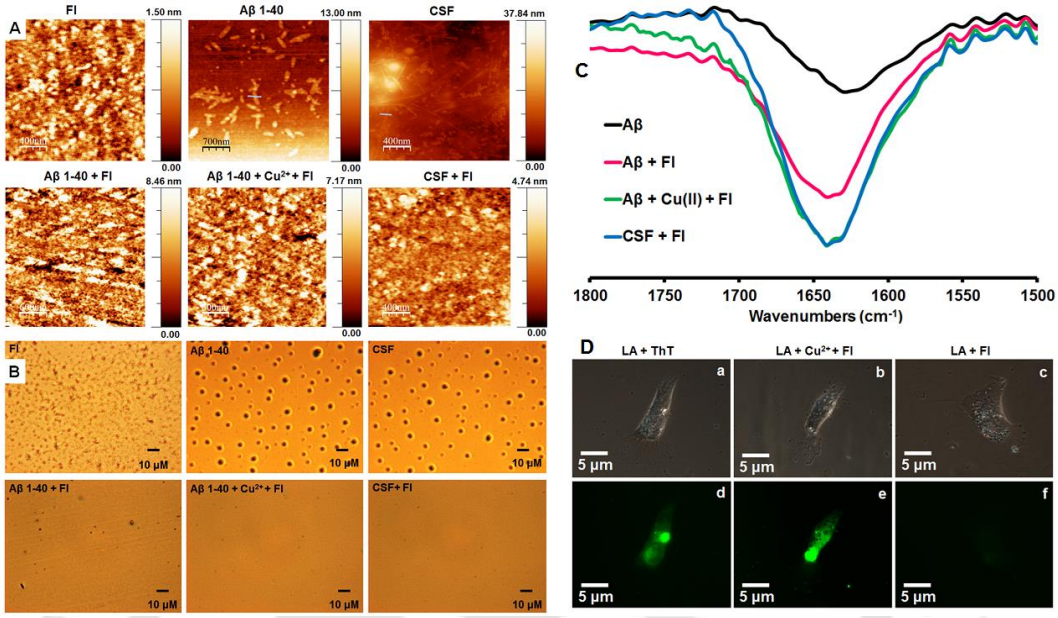

Figure 4b.7 (A) AFM images of the morphologies of FI, Aβ1-40 and CSF fibrils (top left to right). Modulation or disaggregation effect of Aβ aggregates were observed by FI mixed Aβ1-40 in the absence and presence of Cu^{2+} ion and the modulation of CSF aggregates also observed in the presence of FI (bottom left to right) (samples incubated for ~36 h). (B) Optical microscopy images of FI, β-sheet rich spherical images of Aβ1–40 and CSF Aβ aggregates (top left to right). Modulation or disaggregation effects of Aβ aggregates were detected by FI mixed Aβ1-40 in the absence and presence of Cu^{2+} and FI mixed CSF. (bottom left to right) (samples incubated for ~36 h). (C) FT-IR spectra of β-sheet rich Aβ1–40 fibrils (black); pink, green and blue lines indicate random coil structures of Aβ1–40+FI, Aβ1–40+Cu^{2+}+FI and CSF+FI. (D) Disaggregation of β-amyloid LA was detected by fluorescence microscopy: (a, b, c) Bright field images of LA+ThT, LA+Cu^{2+}+FI and LA+FI after 2 h incubation with U87 MG Human astrocytes cells. (d) Cells treated with β-sheet rich LA with ThT show fluorescence after 2 h incubation. (e) Fluorescence detected for the cells treated amyloid-β LA in the presence of Cu^{2+} with FI after incubation for 2 h. (f) No fluorescence was observed for amyloid-β LA with FI in the presence of Cu^{2+} ion after 2 h incubation (excitation at 460 nm).

To establish whether FI can disaggregate and modulate the intracellular Aβ aggregates, we monitored the intracellular Aβ accumulation in U87 MG human astrocytes that had been

loaded with Aβ LA overnight followed by treatment with Cu^{2+}/FI mixture. The cells treated with Aβ LA and stained with ThT shows bright green fluorescence in cell imaging experiments (Figure 4b.7D and A4b.6). As a control, the Aβ LA spread throughout the cells,[98,99] when treated without and with Cu^{2+} ions showed no green fluorescence of Aβ LA in the absence of ThT (Figure A4b.7). The FI treated cells also did not show green fluorescence in intracellular Aβ LA without Cu^{2+} ions but in the presence of Cu^{2+} the Aβ LA showed green "turn-on" fluorescence due to the spirolactam ring opening of FI, proving that Cu^{2+} was chelated by FI and is in agreement with the *in vitro* experiments and the ThT assay results (Figure 4b.7D, A4b.6 and A4b.7). This result also proves that disaggregation or disruption of Aβ fibrils was possible by abstracting Cu^{2+} ion from Aβ LA using FI probe in intracellular condition which is a major advancement for AD. Thus, FI has the exceptional ability to perform multiple tasks of metal chelation in aggregated Aβ LA in cellular environment and most importantly the disruption of β-sheet rich Aβ aggregates into disaggregated forms. Furthermore, FI also prevented their reaggregation into toxic forms which is one of the most crucial properties of a probe or a therapeutic agent to stop recurring of AD.

4b.2.8. Cell viability assay

Endothelial cells were harvested from culture plate and 25,000 cells were seeded per well in 96 well plates. Twelve hours later, cells were treated with different concentration of FI (0 – 200 µM) for 12 h (Figure A4b.8). The dose dependent toxicity of FI was observed at various time points by the standard MTT assay. After 12 h exposure of FI (100 µM) to cells, less than 5 % inhibition of cell growth was observed. However, at 200 µM concentration, the cells experienced ~15 % toxicity. This observation led to utilization of 100 µM of FI for the endothelial monolayer permeability assay.

4b.2.9. Endothelial monolayer permeability assay

FI mediated disaggregation of Aβ fibrils were also studied in a cellular environment. These fibrils are formed and accumulated within brain neuronal cells during AD and the brain cells remain protected by the blood brain barrier (BBB). To act against the Aβ fibrils, this FI had to cross the BBB. Therefore, to examine the BBB crossing ability of FI, a monolayer of human endothelial cells, EA.hy926, was used as an *in vitro* BBB model.[100,101] Prior to the BBB permeability assay, cytotoxicity of FI to endothelial cells was assessed (Figure A4b.8) and a noncytotoxic concentration of 100 µM of FI was used to check *in vitro* BBB crossing ability as described in the experimental section. The post experimental analysis revealed that

during the first hour, the obtained level of FI in the lower chamber was ~65% ±1. Later, the level of FI increased with time and reached maximum ~94% ± 2 at 4 and 6 h (Figure 4b.8). During this period, the cellular morphology remained unchanged and no visible cellular damage or death was observed (inset, Figure 4b.8). Thus, the observation of *in vitro* endothelial monolayer permeability model directly indicated that FI can across BBB.

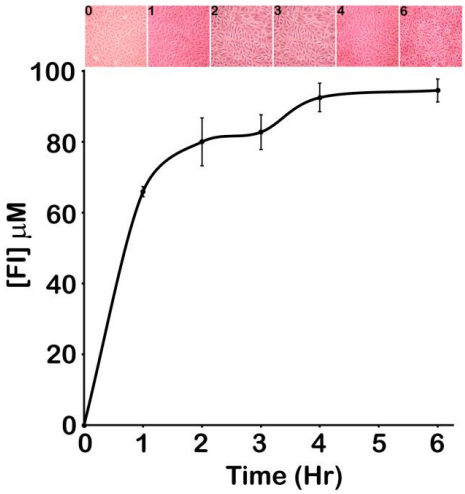

Figure 4b.8 FI can cross endothelial monolayer barrier: Endothelial cells were plated on 3 µM polycarbonate transwell membrane in DMEM supplemented with 10 % FBS and allowed to grow to confluence. FI (100 µM) solution prepared in complete media was added in the upper chamber and after every 1 h, media (~1 mL) was collected from the lower chamber and level of FI was quantified by fluorescence spectroscopy (excitation at 342 nm). The morphology of the endothelial monolayer during the experiment was observed with an inverted microscope TS100 attached to high resolution camera and given in the inset.

4b.3. Conclusion

In summary, the disruption, modulation and elimination of Aβ fibrillar plaques along with metal ions such as Cu(II), Fe(II, III) and Zn(II) are very vital for the prevention of several neurological disorders. Development of metal chelating probes that can selectively bind metals lying deep within the Aβ plaques, CSF or larger systems such as Aβ LA and competitive cellular environment have never been attempted previously. This multiple approach would have immense impact on the etiology of AD and help in developing newer AD therapeutic strategies. The simple indole-3-carboxaldehyde fluorescein hydrazone (FI) probe was nontoxic up to a concentration of 100 µM and was observed to have endothelial monolayer permeability, confirming its ability to cross the blood brain barrier. FI performs multiple tasks of disaggregating and modulating the Aβ aggregates in the absence and

presence of Cu^{2+} in Aβ fibrils, CSF and Aβ LA in U87 MG Human astrocytes cells and prevents them to aggregate again. Most importantly, FI effectively modulated the assembly of metal-free Aβ aggregates also by noncovalent interactions over and above its exceptional ability to bind Cu^{2+} and disrupt the metal-induced Aβ aggregates. This metal chelation resulted in the "turn-on" fluorescence of FI probe via spirolactam ring opening. Although intracellular disaggregation of Aβ fibrils in presence as well as absence of cupric ions is demonstrated in multiple environments by FI, more research is required to improve our understanding on the role of copper and other metals in the pathogenesis of AD and neurologic disorders which would help to envision and design better therapeutic molecules to influence the amyloidogenesis.

4b.4. Experimental Section

4b.4.1. Materials and methods

All the reagents and chemicals were purchased from Aldrich Chemicals, Merck or Ranbaxy (India) and were used as received. Milli-Q water and HPLC grade solvents were used in all the experiments. Solvents were degassed using three freeze thaw cycles or flushed with nitrogen for at least 1 h prior to use when necessary. β-Amyloid (1-40), human was purchased from GL Biochem Ltd., Shanghai, China. The cerebrospinal fluid (CSF) samples were gifted by Guwahati Neurological Research Center and Hospital, Guwahati, India and were obtained as part of routine care from patients. Nonetheless, information on explaining the purpose of this study was specified at the time of sample collection adhering to the bioethics policy of the hospital.

UV–Vis absorption spectra were recorded on a PerkinElmer Lambda–25 spectrometer. Fluorescence spectra were carried out on a Varian Cary Eclipse spectrometer. A 10 × 10 mm quartz cuvette was used for solution spectra and emission was collected at 90° relative to the excitation beam. Leica polarizable optical microscope was used to image the aggregation and disruption studies. Nikon Eclipse 80i microscope was used to study the fluorescent images. FT–IR spectra were recorded on a PerkinElmer spectrometer with samples prepared as KBr pellets. A fresh glass slide was used for every experiment. Deionized water was obtained from Milli–Q system (Millipore). Images were investigated by scanning electron microscopy (SEM) on a LEO 1430vp instrument operated at 8–10 kV. Atomic force microscopy (AFM) was recorded on an Agilent instrument, model 5500 series with noncontact mode. DLS were measured using a Zetasizer Nano series Nano-ZS90 instrument. The POM images were obtained on a Leica DM 2500P microscope.

4b.4.2. Preparation of FI stock solution

The ligand FI stock solution was prepared at the concentration of 1.0×10^{-3} mL^{-1} in 10 mL DMSO. This stock solution was diluted to desired concentration for each titration in 3 mL cuvette.

4b.4.3. Preparation of HEPES buffer solutions

All the UV-Visible and fluorescence titrations were performed in 10 mM HEPES buffer and pH maintained at 7.4 by using 4 M NaOH or 5 M HCl solution.

4b.4.4. TFA/HFIP treatment of Aβ1–40 peptides

Aβ (1–40) was disaggregated using trifluoroacetic acid/1,1,1,3,3,3-hexafluuor-2-propanol (TFA/HFIP) by an established method.[102,103] The amount of 0.5 mg of Aβ (1–40) was added to a 2.5 mL eppendorf tube and dissolved in TFA to obtain a homogeneous solution free of aggregates. TFA was then evaporated using argon gas. Any leftover TFA was further removed by adding HFIP followed by evaporation using an argon gas flow to obtain a film like material. This process was repeated twice. To the eppendorf tube, 2.5 mL of HEPES (10 mM, pH 7.4) was added followed by sonication and vortexing to obtain a final concentration of 4.6×10^{-4} M. Fibril formation was monitored using a ThT binding assay.

4b.4.5. ThT Binding Assay

ThT fluorescence was measured with fluorescence excitation at 440 nm and emission detection at 487 nm. The 20 μM concentration of Aβ1-40 and ThT (20 μM) was used in all the experiments. The concentration of 20 μM Cu^{2+} and FI solution were used where needed for the experiments. The sample was prepared in a final volume of 600 μL in HEPES (10 mM, pH 7.4) and kept for incubation at 37 °C in water bath.

4b.4.6. Benesi-Hildebrand plot

The binding affinity of FI-Cu^{2+} complexes were calculated from the emission spectra of FI-Cu^{2+} complex which is obtained by the chelation of Copper from Aβ1–40+Cu^{2+} aggregates (Figure A4b.1).

The apparent binding constant for the formation of the respective complexes were evaluated using the Benesi−Hildebrand (B−H) plot (equation 1).

$$1/(I - I_0) = 1/\{K\,(I_{max} - I_0)\,C\} + 1/(I_{max} - I_0) \qquad (1)$$

I_0 is the emission intensity of Aβ1–40+Cu^{2+} aggregates at λ = 518 nm, I is the observed emission intensity at that particular wavelength in the presence of a certain concentration of

the FI (C), I_{max} is the maximum emission intensity value that was obtained at λ = 518 nm during titration with varying FI concentration, K is the apparent binding constant (M^{-1}) and was determined from the slope of the linear plot, and C is the concentration of the FI added during titration. Then, the apparent binding constant was estimated to be 6.33×10^4 M^{-1} by the fluorescence spectra changes at 518 nm using Benesi−Hildebrand (B−H) plot (Figure A4b.1).

4b.4.7. Preparation of Aβ1–40 aggregates

For the preparation of Aβ peptide aggregates,[38-40,86,104-106] after the TFA/HFIP treatment for Aβ peptide the Aβ1–40 (20 μM) was initially incubated with ThT (20 μM) at 37 °C for 0-40 h (pH 7.4 in 10 mM HEPES buffer) with steady agitation. Further, Aβ1–40 aggregated Aβ fibrils were monitored (Figure A4b.3a) with different time incubations by monitoring ThT fluorescent enhancement peak at λ_{em} 487 nm (λ_{ex} 440 nm).

4b.4.8. Preparation of Aβ1–40+Cu^{2+} aggregates

For the preparation of Aβ peptide metal aggregates,[38-40,86,104-106] after the TFA/HFIP treatment for amyloid peptide the Aβ1–40 (20 μM) was initially incubated in presence of Cu^{2+} (20 μM) with ThT (20 μM) at 37 °C for 0-24 h (pH 7.4 in 10 mM HEPES buffer) with steady agitation. Further, Aβ1–40+Cu^{2+} amyloid aggregates were monitored (Figure A4b.3b) with different time incubations by monitoring ThT fluorescent enhancement peak at λ_{em} 487 nm (λ_{ex} 440 nm).

4b.4.9. Confirmation of CSF Aβ aggregates using ThT Binding Assay

The existence of Aβ fibrils in CSF was confirmed by the addition of CSF sample up to 100 μL solution (20, 50 and 100 μL) into ThT (20 μM) solution (pH 7.4 in 10 mM HEPES buffer) to observe a enhancement in the fluorescence intensity of ThT at 487 nm validating strongly the existence of aggregated Aβ fibrils in the CSF sample (Figure A4b.3c).

4b.4.10. Tyrosine fluorescence spectroscopy

The 20 μM concentration of Aβ1-40 and 10 or 20 μM Cu^{2+} and FI solution were used where needed for the experiments. The sample was prepared in the final volume of 600 μL in HEPES (10 mM, pH 7.4) and dequenching sample kept at incubation for 48 h at 37 °C in water bath. Fluorescence measurements were performed in a 1 mL quartz fluorescence cuvette with excitation at 274 nm (slit 10 nm) and emission detection at 305 nm (slit 10 nm) in 10 mM HEPES buffer (pH 7.4). Tyrosine emission was used to monitor the binding of

Cu^{2+} to Aβ1-40. It is well established that Cu^{2+} binds to Aβ1-40 and quenches the tyrosine fluorescence.

4b.4.11. Metal chelation or disaggregation of Aβ1–40 + Cu^{2+} aggregates

For the metal chelation or disaggregation experiment, after the TFA/HFIP treatment for Aβ peptide, the Aβ1–40 (20 μM) was initially incubated in the presence of Cu^{2+} (20 μM) with ThT (20 μM) at 37 °C for 0-24 h (pH 7.4 in HEPES) with steady agitation. Further, Aβ1–40+Cu^{2+} Aβ aggregates were monitored with different time incubations by monitoring ThT fluorescent enhancement peak at λ_{em} 487 nm (λ_{ex} 440 nm). After the formation of Aβ1–40+Cu^{2+} aggregates the solution was incubated in the presence of FI (20 μM) with ThT (20 μM) at 37 °C for 0-42 h (pH 7.4 in 10 mM HEPES buffer) with steady agitation. Further, the Aβ-Cu-FI complex was excited at 440 nm and the Cu^{2+} induced the spirolactam ring opening of FI and significant "turn-on" fluorescence response at 515 to 518 nm, with a highly bright green fluorescence.

4b.4.12. Sample preparation for atomic force microscopy (AFM) images

Morphologies of Aβ1–40 and CSF aggregates were studied by AFM. Aβ1–40 peptides (20 μM) in buffer solution (10 mM HEPES, pH 7.4) were incubated with and without Cu^{2+} (20 μM) as well as in the presence and absence of FI (20 μM) at 37 ^{o}C for 2 days. Further, all the solutions were separately diluted by 10 times and then from the diluted solutions 5 μL of the sample was dropped onto the freshly cleaned glass slide for 12 h incubation, gently rinsed with deionized water, and dried at room temperature overnight and then AFM was recorded on an Agilent instrument, model 5500 series with noncontact mode.

4b.4.13. FTIR sample preparation

Aβ1–40 peptides (20 μM) in buffer solution (10 mM HEPES, pH 7.4) were incubated with or without Cu^{2+} (20 μM) and in presence or absence of FI (20 μM) at 37 ^{o}C for 2 days. A volume of 10 μL of the sample was dropped onto the freshly cleaned glass slide for 12 h incubation, gently rinsed with deionized water, and dried at room temperature overnight and then FT–IR spectra recorded on a PerkinElmer spectrometer with samples prepared as KBr pellets.

4b.4.14. Polarized optical microscopy study

Images of Aβ1–40 and CSF aggregates were detected by optical microscopy. Aβ1–40 peptides (20 μM) in buffer solution (10 mM HEPES, pH 7.4) were incubated with and without Cu^{2+} (20 μM) as well as in the presence and absence of FI (20 μM) at 37 ^{o}C for 2

days. Samples were prepared by spreading 30 µL of each solution on a glass slide and then incubated at room temperature for 48 h. Then images were observed for all the incubating samples under Leica DM 2500P microscope.

4b.4.15. Preparation of Lysozyme fibrils

The amyloid fibrils were obtained by heating lysozyme solution (10 mg in 1 mL) in pH 2 at 65 ^{o}C for 5 days. The process of lysozyme fibrillation was confirmed by ThT binding assay, where ThT is commonly used as an amyloid detector as it is reported to bind specifically to the characteristic β-sheet structure of amyloid fibrils.

4b.4.16. SEM images of Lysozyme aggregated (LA) fibrils and Aβ plaques

Morphologies of the formation of LA fibrils without Cu^{2+} and aggregated amyloid plaques with Cu^{2+} were detected by SEM. For the modulation of LA fibrils and aggregated amyloid plaques, 20 µM lysozyme aggregated fibrils (10 mM PBS, pH 7.4) was incubated without and with Cu^{2+} (20 µM) in presence of FI (20 µM) at 37 ^{o}C for 2 days. Result show that FI treated lysozyme aggregated plaques and fibrils were disaggregated or disturbed due to the metal chelation and noncovalent interactions by FI.

4b.4.17. Cell culture and treatment

U87-MG cell line has been procured from NCCS, Pune. Cells were cultured in Dulbecco's modified Eagle's media (DMEM) (Sigma, St. Louis, MO), supplemented with 10% fetal bovine serum (FBS) and 1% penicillin-streptomycin antibiotic (100 units/mL penicillin and 100 µg/mL streptomycin sulfate) and grown at 37 °C in a humidified 5% CO_2 incubator. On the day of the experiment, cells were washed with PBS and loaded with β-amyloid lysozyme aggregate (LA) (1 mg in 1 mL). All wells were washed with PBS at least two times and treated with Cu^{2+} (50 µM) for 1 h. Cells were washed again with PBS three times and treated with FI (100 µM and 400 µM) for 1 to 2 h. To detect LA inside the cells, all samples were treated with ThT (100 µg/ml) for 1 h. Cells loaded with lysozyme solution (1 mg in 1 mL) serves as a negative control.

4b.4.18. Fluorescence microscopic detection and disaggregation of Lysozyme aggregated (LA) fibrils and Aβ plaques

Each coverslip containing cells was fixed in 4% paraformaldehyde at 37 °C for 30 min, mounted and observed under fluorescence microscopy. Cells loaded with Aβ LA gave intense fluorescence signal at 350 and 485 nm when cells were treated with FI/Cu^{2+} mixture

from 1 to 2 h. The fluorescence intensity increased significantly over time of exposure of the probe to copper ions inside the cells containing lysozyme fibrils.

4b.4.19. Cell viability assays

DMEM-high glucose (D5648-sigma), FBS (RM10432-Himedia), Thiazolyl Blue Tetrazolium Bromide (M2128-Sigma), DMSO (61857105001730-Merck), and Whatman filter paper 42 (1442-125, GE Healthcare). Human endothelial cells (EA.hy926) were purchased from ATCC and cultured in DMEM high glucose media containing 10 % FBS.

Endothelial cells were harvested from culture plate and 25,000 cells were seeded per well in 96 well plates. Twelve hours later, cells were treated with different concentration of FI (0 to 200 µM) for 12 h. Cell viability was assessed by following the standard MTT assay protocol. The formed formazone crystals were measured at 570 nm by using the Spectromax M2e microtiter plate reader.

4b.4.20. Endothelial Monolayer Permeability Assays

The immortalized endothelial cells (EA.hy926) were plated on 3 µm polycarbonate trans well membranes in DMEM supplemented with 10% FBS. After reaching confluence, the media in the upper chamber was removed and the complete media containing FI (100 µM) was added to the upper well. The media was collected at different time point intervals (1-6 h) to quantify the FI compound level by using a fluorescence spectroscopy and simultaneously images were collected (1-6 h) by using Nikon TS100 microscope.

References

(1) Holtzman, D. M.; Morris, J. C.; Goate, A. M. *Sci. Transl. Med.* **2011,** *3*, 77.

(2) Thies, W.; Bleiler, L. *Alzheimer's Dementia* **2013,** *9*, 208.

(3) Viles, J. H. *Coord. Chem. Rev.* **2012,** *256*, 2271.

(4) Valensin, D.; Gabbiani, C.; Messori, L. *Coord. Chem. Rev.* **2012,** *256*, 2357.

(5) Wang, Y.-J.; Zhou, H.-D.; Zhou, X.-F. *Drug Discovery Today* **2006,** *11***,** 931.

(6) Jakob-Roetne, R.; Jacobsen, H. *Angew. Chem. Int. Ed.* **2009,** *48*, 3030.

(7) Buxbaum, J. N.; Linke, R. P. *J. Mol. Biol.* **2012,** *421***,** 142.

(8) Rauk, A. *Chem. Soc. Rev.* **2009,** *38*, 2698.

(9) Pithadia, A. S.; Lim, M. H. *Curr. Opin. Chem. Biol.* **2012,** *16*, 67.

(10) Faller, P.; Hureau, C. *Dalton Trans.* **2009,** 1080.

(11) Drew, S. C.; Barnham, K. J. *Acc. Chem. Res.* **2011,** *44*, 1146.

(12) Scott, L. E.; Orvig, C. *Chem. Rev.* **2009,** *109*, 4885.

(13) Savelieff, M. G.; Lee, S.; Liu, Y.; Lim, M. H. *ACS Chem. Biol.* **2013,** *8*, 856.

(14) Hureau, C. *Coord. Chem. Rev.* **2012,** *256*, 2164.

(15) Hureau, C.; Dorlet, P. *Coord. Chem. Rev.* **2012,** *256*, 2175.

(16) Smith, D. G.; Cappai, R.; Barnham, K. J. *Biochim. Biophys. Acta, Biomembr.* **2007,** *1768*, 1976.

(17) Roychaudhuri, R.; Yang, M.; Hoshi, M. M.; Teplow, D. B. *J. Biol. Chem.* **2009,** *284*, 4749.

(18) Zhu, X.; Su, B.; Wang, X.; Smith, M. A.; Perry, G. *Cell. Mol. Life Sci.* **2007,** *64*, 2202.

(19) Kozlowski, H.; Luczkowski, M.; Remelli, M.; Valensin, D. *Coord. Chem. Rev.* **2012,** *256*, 2129.

(20) Duce, J. A.; Bush, A. I. *Prog. Neurobiol.* **2010,** *92*, 1.

(21) Alies, B.; Pradines, V.; Llorens-Alliot, I.; Sayen, S.; Guillon, E.; Hureau, C.; Faller, P. *JBIC, J. Biol. Inorg. Chem.* **2011,** *16*, 333.

(22) Maret, W. *J. Inorg. Biochem.* **2012,** *111*, 110.

(23) Savelieff, M. G.; DeToma, A. S.; Derrick, S. S.; Lim, M. H. *Acc. Chem. Res.* **2014,** *47*, 2475.

(24) Nguyen, M.; Robert, A.; Sournia-Saquet, A.; Vendier, L.; Meunier, B. *Chem. -Eur. J.* **2014,** *20*, 6771.

(25) Savelieff, M. G.; Lee, S.; Liu, Y.; Lim, M. H. *ACS Chem. Biol.* **2013,** *8*, 856.

(26) Pithadia, A. S.; Lim, M. H. *Curr. Opin. Chem. Biol.* **2012,** *16*, 67.

(27) Khan, A.; Ashcroft, A. E.; Korchazhkina, O. V.; Exley, C. *J Inorg Biochem.* **2004,** *98,* 2006.

(28) McLachlan, D. R. C.; Dalton, A. J.; Kruck, T. P.; Bell, M. Y.; Smith, W. L. Kalow, W.; Andrews. D. F. *Lancet,* **1991,** *337,* 1304.

(29) Cherny, R. A.; Legg, J. T.; McLean, C. A.; Fairlie, D. P.; Huang, X.; Atwood, C. S.; Beyreuther, K.; Tanzi, R. E.; Masters, C. L.; Bush, A. I. *J. Biol. Chem.,* **1999,** *274,* 23223.

(30) Franz, K. J. *Curr Opin Chem Biol.* **2013,** *17,* 143.

(31) Ritchie, C. W.; Bush, A. I.; Mackinnon, A.; Macfarlane, S.; Mastwyk, M.; MacGregor, L.; Kiers, L.; Cherny, R., Li, Q. X.; Tammer, A.; Carrington, D.; Mavros, C.; Volitakis, I.; Xilinas, M.; Ames, D.; Davis, S.; Beyreuther, K.; Tanzi, R. E.; Masters, C. L. *Arch. Neurol.* **2003,** *60,* 1685.

(32) Lannfelt, L.; Blennow, K.; Zetterberg, H.; Batsman, S.; Ames, D.; Harrison, J.; Masters, C. L.; Targum, S.; Bush, A. I.; Murdoch, R.; Wilson, J.; Ritchie, C. W. *Lancet Neurol.* **2008,** *7,* 779.

(33) Cherny, R. A.; Atwood, C. S.; Xilinas, M. E.; Gray, D. N.; Jones, W. D.; McLean, C. A.; Barnham, K. J.; Volitakis, I.; Fraser, F. W.; Kim, Y.-S.; Huang, X.; Goldstein, L. E.; Moir, R. D.; Lim, J. T.; Beyreuther, K.; Zheng, H.; Tanzi, R. E.; Masters, C. L.; Bush, A. I. *Neuron,* **2001,** *30,* 665.

(34) Crouch, P. J.; Tew, D. J.; Du, T.; Nguyen, D. N.; Caragounis, A.; Filiz, G.; Blake, R. E.; Trounce, I. A.; Soon, C. P. W.; Laughton, K.; Perez, K. A.; Li, Q.-X.; Cherny, R. A.; Masters, C. L.; Barnham, K. J.; White, A. R. *J. Neurochem.,* **2009,** *108,* 1198.

(35) Faux, N. G.; Ritchie, C. W.; Gunn, A.; Rembach, A.; Tsatsanis, A.; Bedo, J.; Harrison, J.; Lannfelt, L.; Blennow, K.; Zetterberg, H.; Ingelsson, M.; Masters, C. L.; Tanzi, R. E.; Cummings, J. L.; Herd, C. M.; Bush, A. I. *J. Alzheimer's Dis.,* **2010,** *20,* 509.

(36) DeToma, A. S.; Salamekh, S.; Ramamoorthy, A.; Lim, M. H. *Chem. Soc. Rev.,* **2012,** *41,* 608.

(37) Telpoukhovskaia, M. A.; Orvig, C. *Chem. Soc. Rev.,* **2013,** *42,* 1836.

(38) Pithadia, A. S.; Kochi, A.; Soper, M. T.; Beck, M. W.; Liu, Y.; Lee, S.; DeToma, A. S.; Ruotolo, B. T.; Lim, M. H. *Inorg. Chem.,* **2012,** *51,* 12959.

(39) Braymer, J. J.; Choi, J.-S.; DeToma, A. S.; Wang, C.; Nam, K.; Kampf, J. W.; Ramamoorthy, A.; Lim, M. H. *Inorg. Chem.,* **2011,** *50,* 10724.

(40) Liu, Y.; Kochi, A.; Pithadia, A. S.; Lee, S.; Nam, Y.; Beck, M. W.; He, X.; Lee D.; Lim, M. H. *Inorg. Chem.,* **2013,** *52,* 8121.

(41) Porter, M. R.; Kochi, A.; Karty, J. A.; Lim. M. H.; Zaleski. J. M. *Chem. Sci.,* **2015,** *6,* 1018.

(42) Rodríguez-Rodríguez, C.; Telpoukhovskaia, M.; Orvig, C. *Coord. Chem. Rev.* **2012,** *256,* 2308.

(43) DeToma, A. S.; Salamekh, S.; Ramamoorthy, A.; Lim, M. H. *Chem. Soc. Rev.* **2012,** *41,* 608.

(44) Braymer, J. J.; DeToma, A. S.; Choi, J.-S.; Ko, K. S.; Lim, M. H. *Int. J. Alzheimer's Dis.* **2011,** 623051.

(45) Scott, L. E.; Telpoukhovskaia, M.; Rodrıguez-Rodrıguez, C.; Merkel, M.; Bowen, M. L.; Page, B. D. G.; Green, D. E.; Storr, T.; Thomas, F.; Allen, D. D.; Lockman, P. R.; Patrick, B. O.; Adam, M. J.; Orvig. C. *Chem. Sci.,* **2011,** *2,* 642.

(46) Alies, B.; Sasaki, I.; Proux, O.; Sayen, S.; Guillon, E.; Faller, P.; Hureau, C. *Chem. Commun.* **2013,** *49,* 1214.

(47) Pramanik, D.; Dey, S. G. *J. Am. Chem. Soc.* **2011,** *133,* 81.

(48) Guilloreau, L.; Combalbert, S.; Sournia-Saquet, A.; Mazarguil, H.; Faller, P. *ChemBioChem* **2007,** *8,* 1317.

(49) Curtain, C. C.; Ali, F.; Volitakis, I.; Cherny, R. A.; Norton, R. S.; Beyreuther, K.; Barrow, C. J.; Masters, C. L.; Bush, A. I.; Barnham, K. J. *J. Biol. Chem.* **2001,** *276,* 20466.

(50) Smith, D. P.; Smith, D. G.; Curtain, C. C.; Boas, J. F.; Pilbrow, J. R.; Ciccotosto, G. D.; Lau, T.-L.; Tew, D. J.; Perez, K.; Wade, J. D.; Bush, A. I.; Drew, S. C.; Separovic, F.; Masters, C. L.; Cappai, R.; Barnham, K. J. *J. Biol. Chem.* **2006,** *281,* 15145.

(51) Smith, D. G.; Cappai, R.; Barnham, K. J. *Biochim. Biophys. Acta, Biomembr.* **2007,** *1768,* 1976.

(52) Galeazzi, L.; Ronchi, P.; Franceschi, C.; Giunta, S. *Amyloid* **1999,** *6,* 7.

(53) Giunta, S.; Ronchi, P.; Valli, B.; Franceschi, C.; Galeazzi, L. *Amyloid* **2000,** *7,* 189.

(54) Rolinski, O. J.; Amaro, M.; Birch, D. J. S. *Biosens Bioelectron.* **2010,** *25,* 2249.

(55) Amaro, M.; Birch, D. J. S.; Rolinski, O. J. *Phys. Chem. Chem. Phys.,* **2011,** *13,* 6434.

(56) Jensen, M.; Canning, A.; Chiha, S.; Bouquerel, P.; Pedersen, J. T.; Østergaard, J.; Cuvillier, O.; Sasaki, I.; Hureau, C.; Faller, P. *Chem. -Eur. J.* **2012,** *18,* 4836.

(57) Muthuraj, B.; Deshmukh, R.; Trivedi, V.; Iyer, P. K. *ACS Appl. Mater. Interfaces* **2014,** *6,* 6562.

(58) Maiti, N. C.; Jiang, D.; Wain, A. J.; Patel, S.; Dinh, K. L.; Zhou, F. *J. Phys. Chem. B* **2008,** *112,* 8406.

(59) Karr, J. W.; Akintoye, H.; Kaupp, L. J.; Szalai, V. A. *Biochemistry* **2005,** *44*, 5478.

(60) Syme, C. D.; Nadal, R. C.; Rigby, S. E. J.; Viles, J. H. *J. Biol. Chem.* **2004,** *279*, 18169.

(61) Ma, Q. F.; Hu, J.; Wu, W. H.; Liu, H. D.; Du, J. T.; Fu, Y.; Wu, Y. W.; Lei, P.; Zhao, Y. F.; Li, Y. M. *Biopolymers*, **2006,** *83*, 20.

(62) Atwood, C. S.; Perry, G.; Zeng, H.; Kato, Y.; Jones, W. D.; Ling, K. Q.; Huang, X.; Moir, R. D.; Wang, D.; Sayre, L. M.; Smith, M. A.; Chen, S. G.; Bush, A. I. *Biochemistry* **2004,** *43*, 560.

(63) Wu, W.; Lei, P.; Liu, Q.; Hu, J.; Gunn, A. P.; Chen, M.; Rui, Y.; Su, X.; Xie, Z.; Zhao, Y.; Bush, A. I.; Li, Y. *J. Biol. Chem.*, **2008,** *283*, 31657.

(64) Yu, M.; Ryan, T. M.; Ellis, S.; Bush, A. I.; Triccas, J. A.; Rutledge, P. J.; Todd, M. H. *Metallomics*, **2014,** *6*, 1931.

(65) Alies, B.; Renaglia, E.; Rózga, M.; Bal, W.; Faller, P.; Hureau, C. *Anal. Chem.* **2013,** *85*, 1501.

(66) Lincoln, K. M.; Gonzalez, P.; Richardson, T. E.; Julovich, D. A.; Saunders, R.; Simpkins, J. W.; Green, K. N. *Chem. Commun.*, **2013,** *49*, 2712.

(67) Scott, L. E.; Page, B. D. G.; Patrick, B. O.; Orvig, C. *Dalton Trans.*, **2008,** 6364.

(68) Chen, W.; Wang, X.; He, Y.; Zhang, C.; Wu, Z.; Liao, K.; Wang, J.; Guo, Z. *Inorg. Chem.*, **2009,** *48*, 5801.

(69) Faller, P.; Hureau, C.; Dorlet, P.; Hellwig, P.; Coppel, Y.; Collin, F.; Alies, B. *Coord. Chem. Rev.*, **2012,** *256*, 2381.

(70) Zhu, L.; Han, Y.; He, C.; Huang, X.; Wang, Y. *J. Phys. Chem. B* **2014,** *118*, 9298.

(71) Ma, Q.; Wei, G.; Yang, X. *Nanoscale* **2013,** *5*, 10397.

(72) Ban, T.; Hamada, D.; Hasegawa, K.; Naiki, H.; Goto, Y. *J. Biol. Chem.* **2003,** *278*, 16462.

(73) Anand, U.; Mukherjee, M. *Langmuir* **2013,** *29*, 2713.

(74) Pedersen, J. T.; Østergaard, J.; Rozlosnik, N.; Gammelgaard, B.; Heegaard, N. H. *J. Biol. Chem.* **2011,** *286*, 26952.

(75) Pedersen, J. T.; Teilum, K.; Heegaard, N. H.; Østergaard, J.; Adolph, H. W. Hemmingsen, L. *Angew. Chem. Int. Ed.* **2011,** *50*, 2532.

(76) Muthuraj, B.; Hussain, S.; Iyer, P. K. *Polym. Chem.* **2013,** *4*, 5096.

(77) Liu, L.; Zhang, L.; Mao, X.; Niu, L.; Yang, Y.; Wang, C. *Nano Lett.* **2009,** *9*, 4066.

(78) Liu, L.; Zhang, L.; Niu, L.; Xu, M.; Mao, X.; Yang, Y.; Wang, C. *ACS Nano* **2011,** *5*, 6001.

(79) Takai, E.; Uda, K.; Matsushita, S.; Shikiya, Y.; Yamada, Y.; Shiraki, K.; Zako, T.; Maeda, M. *Biotechnol. Prog.* **2014,** *30*, 470.

(80) Blennow, K.; Hampel, H. *Lancet Neurol.* **2003,** *2*, 605.

(81) Blennow, K.; Hampel, H.; Weiner, M.; Zetterberg, H. *Nat. Rev. Neurol.* **2010,** *6*, 131.

(82) Seubert, P.; Vigo-Pelfrey, C.; Esch, F.; Lee, M.; Dovey, H.; Davis, D.; Sinha, S.; Schlossmacher, M.; Whaley, J.; Swindlehurst, C.; McCormack, R.; Wolfert, R.; Selkoe, D.; Lieberburg, I.; Schenk, D. *Nature* **1992,** *359*, 325.

(83) Dwivedi, A. K.; Iyer, P. K. *Macromol. Biosci.* **2014,** *14***,** 508.

(84) Lee, J.; Culyba, E. K.; Powers, E. T.; Kelly, J. W. *Nat. Chem. Biol.* **2011,** *7*, 602.

(85) He, X.; Park, H. M.; Hyung, S. J.; DeToma, A. S.; Kim, C.; Ruotolo, B. T.; Lim, M. H. *Dalton Trans.* **2012,** *41*, 6558.

(86) Hindo, S. S.; Mancino, A. M.; Braymer, J. J.; Liu, Y.; Vivekanandan, S.; Ramamoorthy, A.; Lim, M. H. *J. Am. Chem. Soc.* **2009,** *131*, 16663.

(85) Jones, M. R.; Service, E. L.; Thompson, J, R.; Wang, M. C. P.; Kimsey, I. J.; DeToma, A. S.; Ramamoorthy, A.; Lim, M. H.; Storr, T. *Metallomics* **2012,** *4*, 910.

(88) Choi, J.; Braymer, J. J.; Nanga, R. P. R.; Ramamoorthy, A.; Lim, M. H. *Proc. Natl. Acad. Sci. U. S. A.* **2010,** *107*, 21990.

(89) Hickey, J. L.; Lim, S.; Hayne, D. J.; Paterson, B. M.; White, J. M.; Villemagne, V. L.; Roselt, P.; Binns, D.; Cullinane, C.; Jeffery, C. M.; Price, R. I.; Barnham, K. J.; Donnelly, P. S. *J. Am. Chem. Soc.* **2013,** *135*, 16120.

(90) Cabaleiro-Lago, C.; Quinlan-Pluck, F.; Lynch, I.; Lindman, S.; Minogue, A. M.; Thulin, E.; Walsh, D. M.; Dawson, K. A.; Linse, S. *J. Am. Chem. Soc.* **2008,** *130*, 15437.

(91) Cabaleiro-Lago, C.; Szczepankiewicz, O.; Linse, S. *Langmuir* **2012,** *28*, 1852.

(92) Choi, I.; Lee, L. P. *ACS Nano* **2013,** *7*, 6268.

(93) Ridgley, D. M.; Ebanks, K. C.; Barone, J. R. *Biomacromolecules* **2011,** *12*, 3770.

(94) Dehn, S.; Castelletto, V.; Hamley, I. W.; Perrier, S. *Biomacromolecules* **2012,** *13*, 2739.

(95) Nilsson, M. R.; Dobson, C. M. *Biochemistry* **2003,** *42*, 375.

(96) Mercato, L. L. D.; Maruccio, G.; Pompa, P. P.; Bochicchio, B.; Tamburro, A. M.; Cingolani, R.; Rinaldi, R. *Biomacromolecules* **2008,** *9*, 796.

(97) Sharpe, S.; Simonetti, K.; Yau, J.; Walsh, P. *Biomacromolecules* **2011,** *12*, 1546.

(98) Shirwany, N. A.; Payette, D.; Xie, J.; Guo, Q. *Dis. Treat.* **2007,** *3*, 597.

(99) Takuma, K.; Fang, F.; Zhang, W.; Yan, S.; Fukuzaki, E.; Du, H.; Sosunov, A.; McKhann, G.; Funatsu, Y.; Nakamichi, N.; Nagai, T.; Mizoguchi, H.; Ibi, D.; Hori, O.;

Ogawa, S.; Stern, D. M.; Yamada, K.; Yan, S. S. *Proc. Natl. Acad. Sci. U. S. A.* **2009,** *106*, 20021.

(100) Agarwal, A.; Covic, L.; Sevigny, L. M.; Kaneider, N. C.; Lazarides, K.; Azabdaftari, G.; Sharifi, S.; Kuliopulos, A. *Mol. Cancer Ther.* **2008,** 7, 2746.

(101) Rubin, L. L.; Hall, D. E.; Porter, S.; Barbu, K.; Cannon, C.; Horner, H. C.; Janatpour, M.; Liaw, C. W.; Manning, K.; Morales, J.; Tanner, L. I.; Tomaselli, K. J.; Bard, F. *J. Cell Biol.*, **1991,** *115*, 1725.

(102) Chen, S.; Wetzel, R. *Protein Sci.*, **2001,** *10*, 887.

(103) Hortschansky, P.; Schroeckh, V.; Christopeit, T.; Zandomeneghi, G.; Fändrich, M. **2005,** *Protein Sci.*, *14*, 1753.

(104) Mancino, A. M.; Hindo, S. S.; Kochi, A.; Lim, M. H. *Inorg. Chem.* **2009,** *48*, 9596.

(105) Hyung, S. J.; DeToma, A. S.; Brender, J. R.; Lee, S.; Vivekanandan, S.; Kochi, A.; Choi, J. S.; Ramamoorthy, A.; Ruotolo, B. T.; Lim, M. H. *Proc. Natl. Acad. Sci. U. S. A.* **2013,** *110,* 3743.

(106) Lee, S.; Zheng, X.; Krishnamoorthy, J.; Savelieff, M, G.; Park, H. M.; Brender, J. R.; Kim, J. H.; Derrick, J. S.; Kochi, A.; Lee, H. J.; Kim, C.; Ramamoorthy, A.; Bowers, M. T.; Lim, M. H. *J. Am. Chem. Soc.*, **2014,** 136, 299.

Appendix

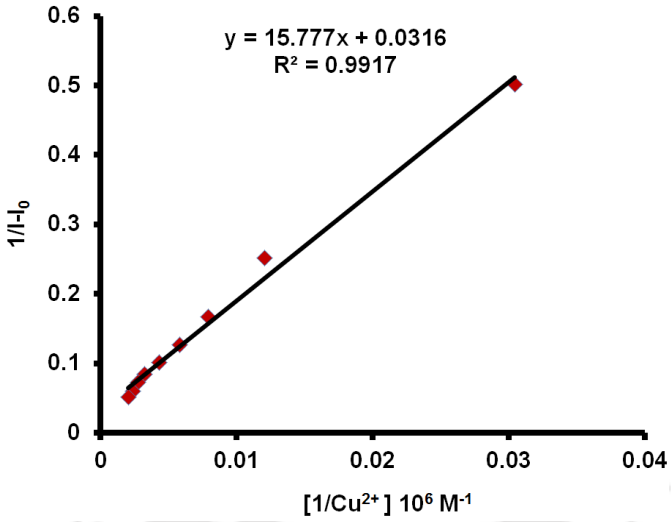

Figure A4b.1 Benesi-Hildebrand plot obtained from the emission spectra of FI+Cu complex by the chelation of copper from Aβ1–40+Cu^{2+} aggregates (Emission at 518 nm).

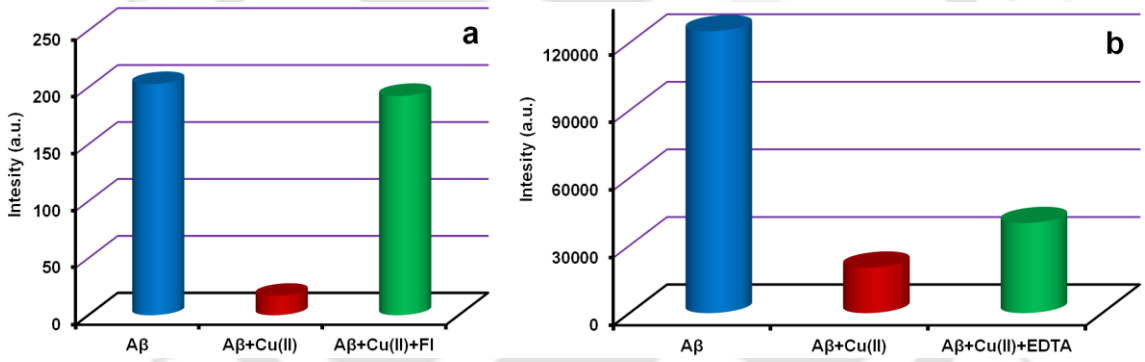

Figure A4b.2 (a) Tyr fluorescence quenching in Aβ1-40 (20 μM) observed upon the addition of 20 μM Cu^{2+} ion (in 10 mM HEPES buffer, pH 7.4); Tyr fluorescence dequenching observed rapidly upon addition of 20 μM FI into Aβ1-40-Cu^{2+} (1:1) in 10 mM HEPES buffer (10 mM, pH 7.4). (b) A control experiment performed with a nonfluorescent copper chelator EDTA: Tyr fluorescence quenching in Aβ1-40 (20 μM) observed upon the addition of 20 μM Cu^{2+} ion (in 10 mM HEPES buffer, pH 7.4); Tyr fluorescence dequenching observed after 48 h upon the addition of 40 μM EDTA into Aβ1-40-Cu^{2+} (1:1) in 10 mM HEPES buffer (10 mM, pH 7.4).

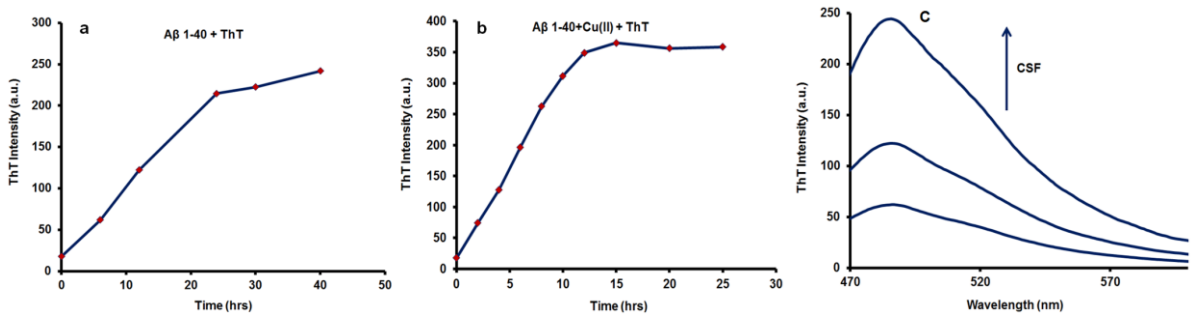

Figure A4b.3 (a) Aβ1–40 (20 μM) aggregated fibrils were monitored with different time incubations with ThT (20 μM) (pH 7.4 in 10 mM HEPES buffer) showed emission peak at λ_{em} 487 nm (λ_{ex} 440 nm). (b) Aβ1–40+Cu^{2+} aggregated fibrils were monitored with different time incubations in the presence of Cu^{2+} (20 μM) with ThT (20 μM) (pH 7.4 in 10 mM HEPES buffer) which showed emission peak at λ_{em} 487 nm (λ_{ex} 440 nm). (c) Presence of aggregated Aβ fibrils in CSF was confirmed with different volume of CSF (20, 50 and 100 μL) with ThT (pH 7.4 in 10 mM HEPES buffer), which showed emission peak at λ_{em} 487 nm (λ_{ex} 440 nm).

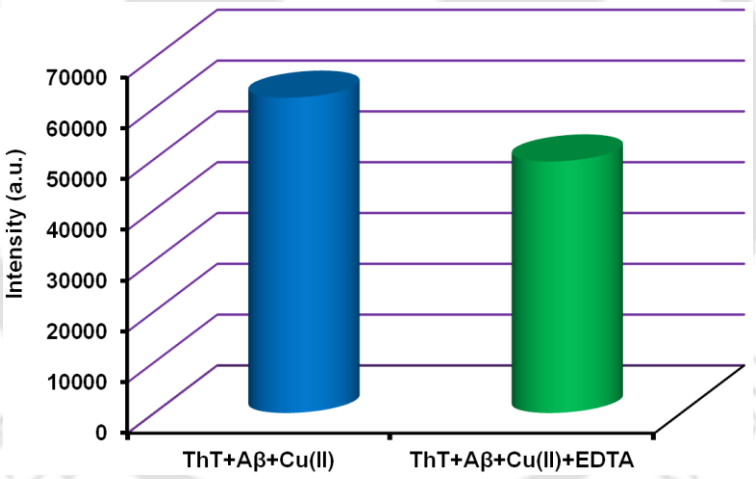

Figure A4b.4 Control study bar diagram for disaggregation of Aβ1-40 (20 μM) + Cu^{2+} (20 μM) aggregates in presence of nonfluorescent metal chelator EDTA (20 μM) in 10 mM HEPES buffer (pH 7.4).

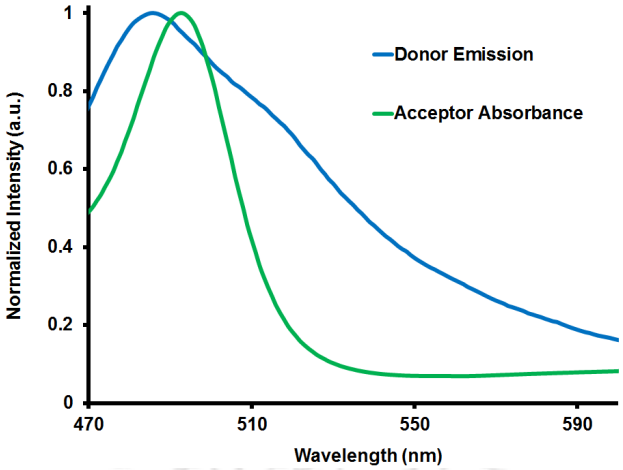

Figure A4b.5 Spectral overlap obtained between emission of ThT (blue curve) and absorbance of FI (green curve). The emission spectra at 487 nm (λ_{ex} 440 nm) obtained for the mixture of ThT (20 µM) in the presence of Aβ (20 µM) + Cu (20 µM) aggregates (pH 7.4 in 10 mM HEPES buffer). The absorption spectra obtained for the FI (20 µM) in 10 mM HEPES buffer solution (pH 7.4).

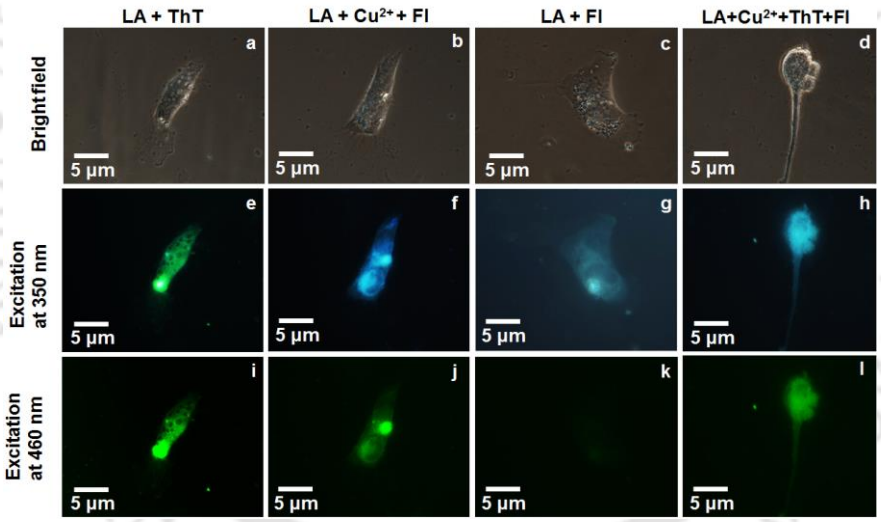

Figure A4b.6 Aggregation and disaggregation of Aβ LA was detected by fluorescence microscopy (excitation at 350 as well as 460 nm). (a, b, c and d) Bright field images of LA+ThT, LA+Cu^{2+}+FI, LA+FI and LA+Cu^{2+}+ThT+FI, after incubation for 2 h with U87 Mg Human astrocytes cells. (e, i) Cells treated β-sheet rich LA with ThT shows fluorescence after 2 h incubation. (f, j) The fluorescence was detected for the cells treated Aβ LA in the presence of Cu^{2+} with FI after incubation for 2 h. (h, i) ThT study of cells treated β-sheet rich LA shows fluorescence in the presence of Cu^{2+} after incubation for 2 h. (g, k) No significant fluorescence was observed for Aβ LA with FI in the absence of Cu^{2+} after 2 h incubation (Excitation at 350 as well as 460 nm).

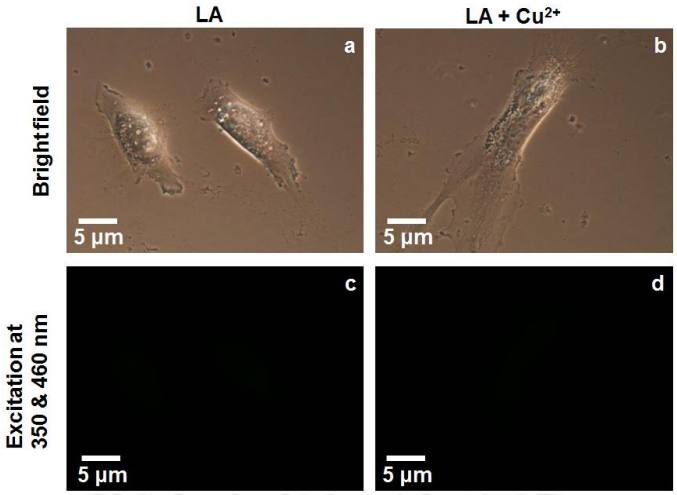

Figure A4b.7 (a, b) Bright field images of LA, LA+Cu^{2+} + FI after incubation for 2 h with U87 Mg Human astrocytes cells. (c, d) No significant fluorescence was observed for Aβ LA in the absence and presence of Cu^{2+} after 2 h incubation (Excitation at 350 and 460 nm).

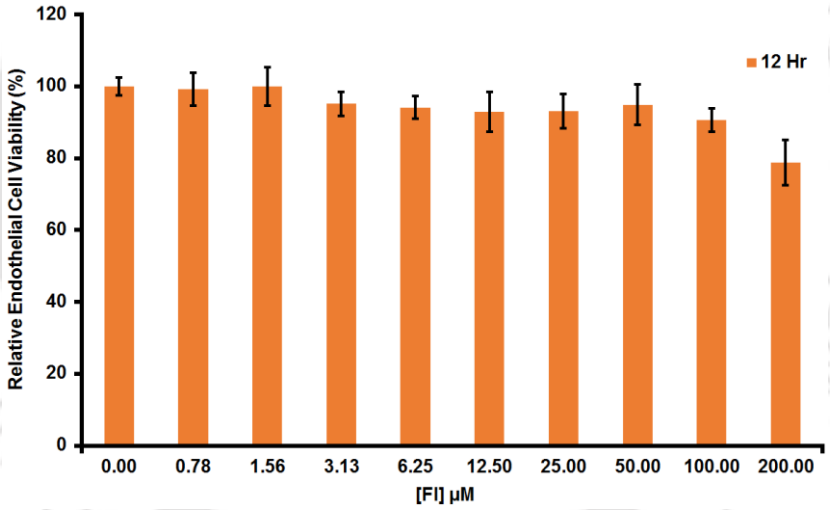

Figure A4b.8 FI treated endothelial cell viability: Endothelial cells were treated with 0 to 200 µM concentration of FI for 12 h.

Chapter: 5a

Aggregation Deaggregation Influenced Selective and Sensitive Detection of Cu^{2+} and ATP by Histidine Functionalized Water Soluble Fluorescent Perylene Diimide under Physiological Conditions and in Living Cells

Abstract

Highly fluorescent perylene diimide (PDI-HIS), functionalized with amino acid histidine is developed and utilized as a rapid "turn-off" fluorescence and colorimetric probe for the detection of Cu^{2+} and ATP under physiological conditions and in A549 cells. The emission of PDI-HIS gets completely quenched upon formation of Cu^{2+} complex, primarily caused by metal coordination induced molecular aggregation with a K_{SV} value of 7.1×10^6 M^{-1}. The PDI-HIS+Cu^{2+} complex was highly selective for ATP due to the disaggregation of this complex, with a very low limit of detection of 0.58×10^{-6} M. The low toxicity of PDI-HIS probe allowed its use for the detection and imaging of both Cu^{2+} and ATP in A549 living cells. The formation of PDI-HIS+Cu^{2+} complex aggregates was confirmed by the morphology changes as observed by AFM images and with dynamic light scattering (DLS) techniques, which strongly supported the aggregated form of PDI-HIS+Cu^{2+} complex (~120 nm diameter). The disaggregation of PDI-HIS+Cu^{2+} complex with ATP was also confirmed by AFM images and DLS techniques with the hydrodynamic particles diameter in the range of 200 ± 20 nm.

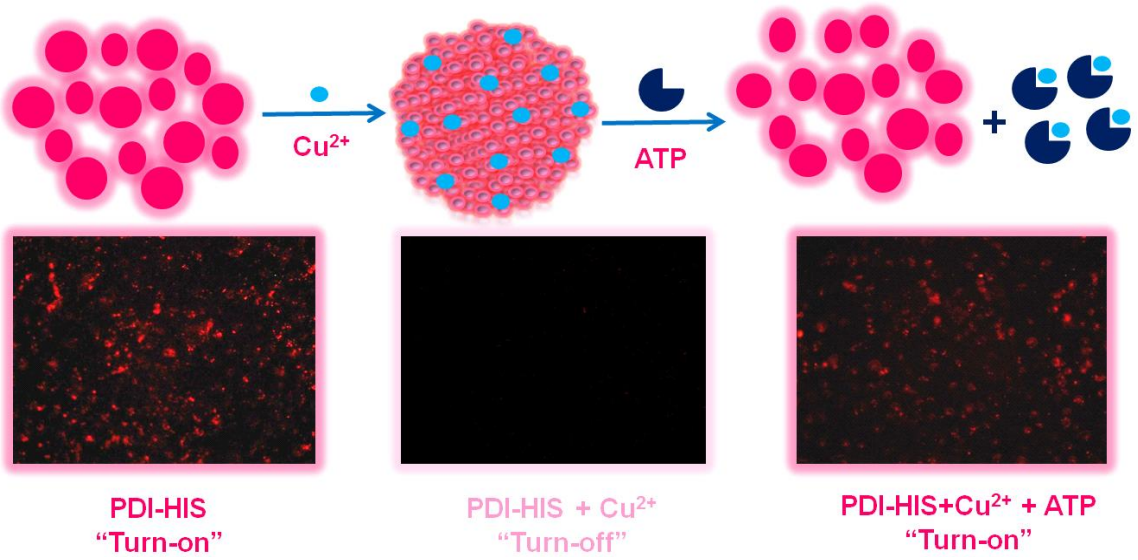

5a.1. Introduction

Innumerable anion sensors, including that for ATP, have been devised based on metal-ligand interactions.[1-4] A metal-ligand interaction is useful in the formulation of a sensitive anion sensor because the metal-anion interaction is very strong even in water and the metal cation exhibits preferred geometry towards particular anions with a selective binding tendency.[4,5] Phosphates have a prominent role in biological systems. Among all phosphates, ATP is the universal energy source in biology due to its energy production and storage functions in living cells.[6] ATP is involved in energy metabolism, DNA replication and transcription and other fundamental activities of life.[7,8] Subsequently, the real-time monitoring of ATP levels is imperative for the study of multiple cellular mechanisms, enzyme activity and other activities involving the production and consumption of ATP.[9-12] The excess amount of ATP consumed by creatine kinase causes particular diseases such as angiocardiopathy. Hence, there have been efforts to develop fluorescent or colorimetric sensors for ATP since the accurate detection and quantification of ATP is an important goal for both biochemical and clinical applications.[13,14] To this end, a variety of approaches or numerous metal complexes,[14,15-21] especially Zn^{2+} complexes have been developed for ATP detection.[22-27] However, the development of rapid, selective and highly sensitive probes for ATP detection in physiological conditions and in intracellular environment still remains a major challenge.

Copper is the third most abundant transition metal in the human body after iron and zinc, which plays vital roles in essential biological processes.[28-34] It's role as part of the catalytic centers of many proteins in various biological processes and chemical systems is very vital.[31,35] The over load or deficiency of copper leads to severe diseases, such as those closely associated with neurodegenerative diseases, namely, Alzheimer's disease, Parkinson's disease and amyotrophic lateral sclerosis (ALS).[36-47] The average normal copper concentration in blood is calculated to be 15.7–23.6 μM (100–150 μg dL^{-1}).[48] Fluorescence imaging is a powerful tool to visualize the metal ions in living systems[49-52] and the development of novel fluorescent molecules to image and detect Cu^{2+} ion is always attractive and promising due to their high sensitivity and the simplicity of equipment requirements.[53-56]

Water-soluble perylene diimide (PDI) based fluorescent chemosensors have recently received attention because of their outstanding photochemical stabilities and high fluorescence quantum yields.[57-63] The exceptional photostability of PDI derivatives provides the sensor system with additional credits in terms of enhanced sensitivity, sustainability, rapid optical signaling and reproducibility in real applications. One unique property of PDI molecules is

that the fluorescence of the individual molecule gets quenched dramatically when they aggregate in aqueous solution at higher concentration. The mechanism of sensing metal ion depends on this fluorescence quenching induced by molecular aggregation, which in turn is caused by the intermolecular coordination of the sensor molecules.[57,64] This efficient fluorescence quenching due to the strong intermolecular π-π interaction among the PDI molecules can be efficiently utilized as a platform for developing sensor assays. Despite these unique properties possessed by PDI derivatives and the vital requirement to develop efficient ATP sensor systems, the development of simple and easily synthesized PDI probes remains very rare.[57-62] So far, few reports on fluorescent probes for cations[53-55,65-71] and anions[59,62,69,72-77] (including few PDI based) have been reported using receptors like dipicolyl amine,[5a.59] 8-hydroxy quinoline,[66] amino acids,[62] etc. Herein, we report a novel histidine functionalized PDI probe as a "turn-on" fluorescent assay for ATP, which is based on the selective and sensitive binding of ATP with PDI-HIS+Cu^{2+} complex. This amino acid functionalized PDI-HIS derivative, is the first example demonstrating efficient sensing and discerning ATP in the presence of other competitive inorganic anions in physiological conditions and in living cells. PDI-HIS can form a complex with Cu^{2+} ion through metal−ligand interaction and was quenched efficiently on forming non-emitting aggregates with the forbidden low-energy excitonic transition.[57-62] Upon addition of ATP into the PDI-HIS+Cu^{2+} complex system, the competitive binding with the Cu^{2+} ion promotes the disassembly of PDI-HIS+Cu^{2+} complex. As a result, the PDI-HIS and Cu^{2+} complex formed in aqueous solution disaggregated and the disassembly process could be monitored efficiently by recording the fluorescence dequenching of PDI. Consequently, a rapid "turn-on" fluorescent and colorimetric method for the detection of ATP with exceptional sensitivity could be established using this novel PDI-HIS molecular probe.

5a.2. Results and discussion

5a.2.1. Synthesis of PDI-HIS

3, 4, 9, 10-Perylenetetracarboxylic acid bisanhydride (500 mg, 1.27 mmol), histidine (800 mg, 3.82 mmol) and 2.0 g of imidazole were heated at 140 °C for 8 h with stirring (Scheme 5a.1). The reaction mixture was allowed to cool to 90 °C, and then poured into water. The mixture was acidified with 2.0 M HCl, and the precipitate was washed with water and dried under vacuum at 80 °C to give the desired product PDI-HIS (800 mg, 94%). ^{1}H NMR (DMSO d_6, 600 MHz) δ (ppm) : 8.70 (broad, 4H), 8.54 (broad, 4H), 7.45 (broad, 2H), 6.75

(broad, 2H), 5.80 (broad, 2H), 3.69, 3.53 (broad, 4H), MS (m/z): 667.1475 [M+H$^+$], FT-IR (cm^{-1}) 3430, 2925, 2854, 1696, 1655, 1593, 1576, 1436, 1402, 1364. ^{13}C-NMR (DMSO d_6, 150 MHz) δ (ppm) : 29.18, 54.95, 116.72, 121.39, 124.49, 128.28, 131.50, 134.70, 135.09, 138.32, 154.99, 179.34.

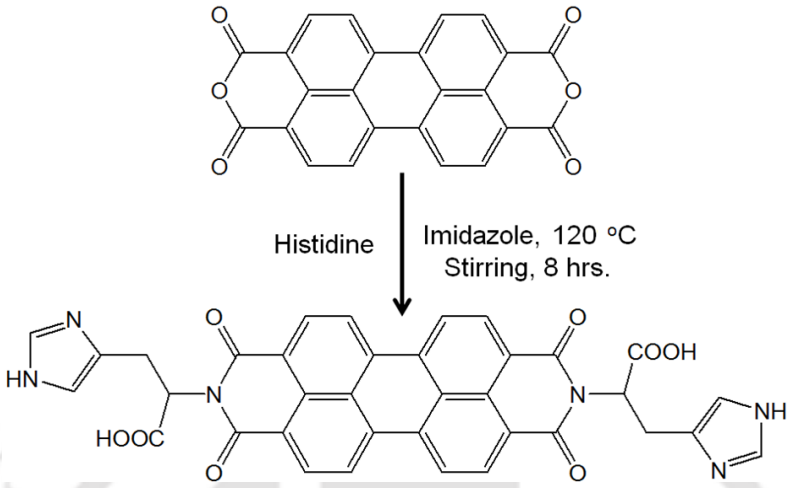

Scheme 5a.1 Synthesis of PDI-HIS. Histidine, imidazole, stirring at 120 ^{o}C, 8 h.

Herein, we exhibit the remarkable properties of a simple yet highly fluorescent molecule based on amino acid functionalized perylene diimide,[78,79] for the rapid and exceedingly sensitive detection of Cu^{2+} and ATP in physiological conditions and in A549 cells. The PDI-HIS probe demonstrated colorimetric and fluorescent "turn-off" and "turn-on" properties in the presence of Cu^{2+} and ATP selectively. The complex PDI-HIS+Cu^{2+}, displays a huge fluorescence enhancement exclusively with ATP, in presence of competitive and similar anions such as AMP, Pi and PPi. Most importantly, the PDI probe benefits from the straightforward one step synthesis from economical materials enabling its gram scale development and extending its utility in detecting ATP exclusively even in competitive cellular environment.

5a.2.2. UV-Visible study of PDI-HIS with copper and ATP

The influence of cations on PDI-HIS was carefully studied by absorption spectra. Figure 5a.1a illustrates that the PDI-HIS (2 µM) has two absorbance maximum peaks at 533 and 503 nm in HEPES buffer (10 mM, pH 7.4) solution. Upon addition of Cu^{2+} solution upto 0-2.5 equivalents (0-5 µM), the absorption bands of PDI-HIS decreases with red shift (of 508 nm) and a new broad shoulder appeared at ~556 nm due to the likely extended oligomer formation (Figure 5a.1a). These spectral changes reflect that the addition of Cu^{2+} ions intensifies the π–π stacking among perylene moieties and facilitates the formation of PDI-HIS

aggregates.[61,80-84] Excess addition of Cu^{2+} ions (50 equiv.), resulted in the PDI-HIS molecules being rapidly precipitated in the form of dark red flocs while rest of the solution became totally colorless. To disrupt the PDI-HIS+Cu^{2+} complex aggregates, we introduced a dilute solution of ATP from 0-150 equivalents into PDI-HIS+Cu^{2+} solution. As a result, the PDI-HIS monomer molecules separated, leading to the enhancement of 533 nm absorption bands. It is clearly evident that (Figure 5a.1b) on gradual addition of ATP (150 equiv.), the absorption bands associated with the PDI-HIS aggregates with the shoulder at 556 nm decreased in intensity and the 533 and 503 nm peaks regained gradually due to the development of ones related to 0−0 and 0−1 transitions.

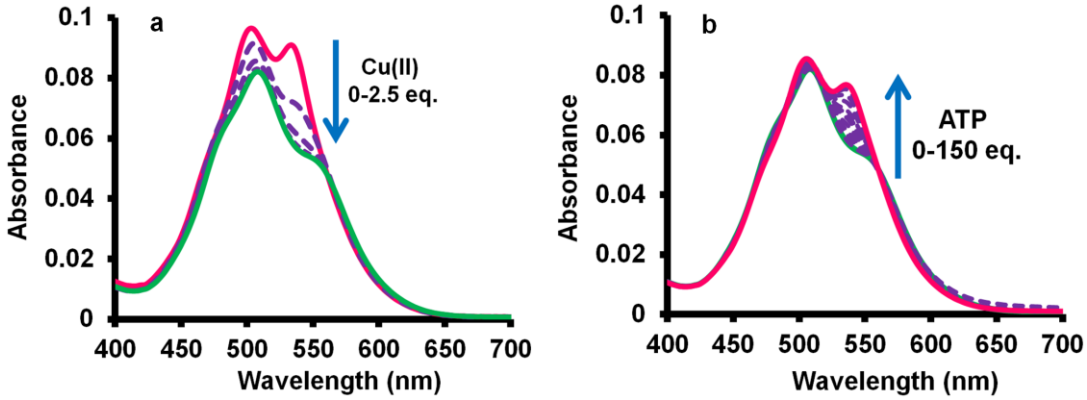

Figure 5a.1 (a) Absorption spectra of PDI-HIS (2 µM) was red shifted due to the aggregation upon the gradual addition of 5 µM (0-2.5 equiv.) of Cu^{2+} ions in HEPES buffer solution (10 mM, pH 7.4). (b) PDI-HIS+Cu^{2+} aggregated complex was disaggregated after the gradual addition of ATP (150 equiv.) in HEPES buffer (10 mM, pH 7.4).

5a.2.3. PDI-HIS aggregation study at different ratios of solvents

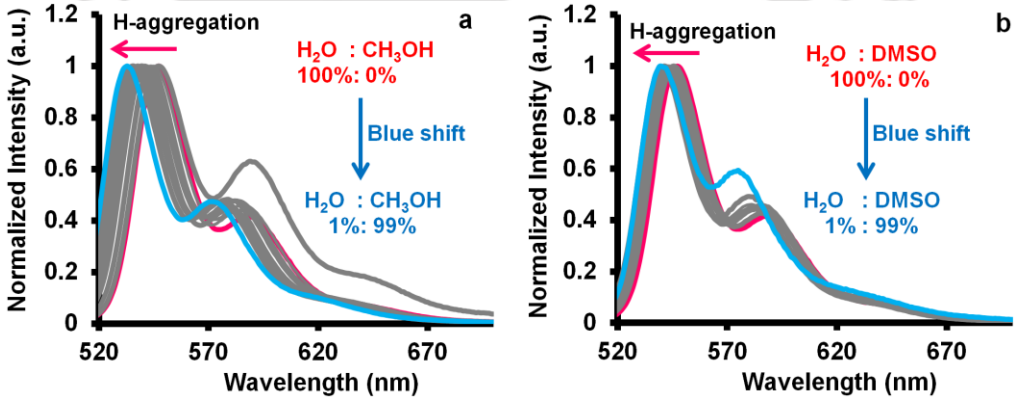

Figure 5a.2 (a, b) Fluorescence spectra of PDI-HIS (0.6 µM) at different ratios of water and methanol or DMSO solutions (100:0–1:99 v/v %).

To provide further evidence for the PDI-HIS aggregation, we performed the fluorescent experiments using a mixture of solvents comprising H_2O/CH_3OH and H_2O/DMSO (Figure 5a.2 and 5a.3). PDI-HIS exhibited a strong emission band at 547 and 588 nm due to the formation of J-aggregates when dissolved in pure H_2O (excitation wavelength = 508 nm). On the other hand, it was observed that in the mixture of H_2O:CH_3OH solution, the emission of PDI-HIS was blue shifted at 532 and 575 nm when the ratio of CH_3OH is higher in H_2O. As shown in Figure 5a.2 and 5a.3, the fluorescent properties of PDI-HIS were observed to vary at different ratios of H_2O:CH_3OH (100:0−1:99 v/v %) using HEPES buffer (10 mM, pH 7.4). When the H_2O:CH_3OH solution was at 90:10 v/v %, PDI-HIS showed intense fluorescence emission band at 547 nm and 588 nm due to the changes into monomeric species (Figure 5a.3). On the other hand, the intensity of the strong emission band of PDI-HIS dramatically decreased with the hypsochromic shift when the ratio of H_2O:CH_3OH was changed from 90:10 to 1:99 v/v %, due the formation of H-aggregates (Figure 5a.3).

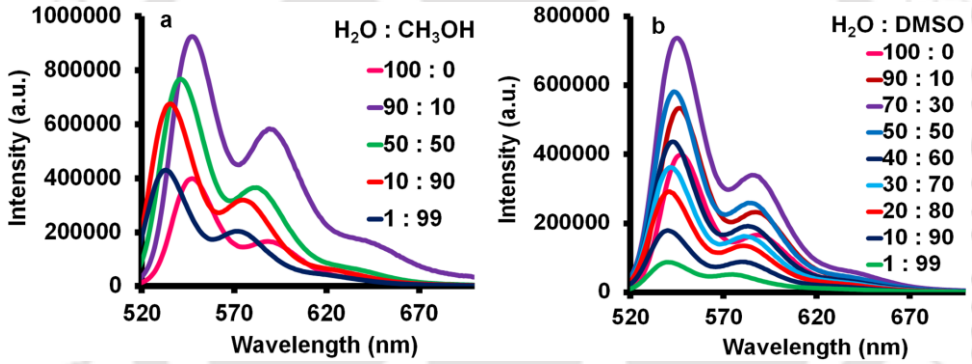

Figure 5a.3 (a, b) Fluorescence spectra of PDI-HIS (0.6 µM) at different ratios of water and methanol or DMSO solutions (100:0 – 1:99 v/v %).

As shown in figure 5a.3 at 99 % methanol, the emission band for PDI-HIS displayed hypsochromic shift of 15 nm from 547 nm and 13 nm from 588 nm due to H-aggregate formation.[85] Further, a similar experiment was performed to monitor the effect of other solvent ratios of H_2O:DMSO solutions (100:0 – 1:99 v/v %), where the emission of PDI-HIS changes were observed to be 7 nm red shifted from the 547 nm and 13 nm from 588 nm due to the formation of H-aggregates (Figure 5a.2 and 5a.3).

5a.2.4. Selective and sensitive detection of Cu^{2+} ion

Figure 5a.4 illustrates the fluorescence changes of PDI-HIS probe (0.33 µM) upon the addition of Cu^{2+} at pH 7.4, HEPES buffer. Since histidine pendants are very good receptors for binding metal ions, PDI-HIS (0.33 µM) was chosen for examining its sensing ability, in

which PDI-HIS exists primarily in the monomeric or dimeric form at very low concentrations. By adding Cu^{2+} to PDI-HIS aqueous solution, the fluorescence of PDI-HIS decreases gradually (Figure 5a.4a) due to the formation of larger non emitting aggregates with the forbidden low-energy exciton transition, and the observed emission is characteristic of PDI-HIS in the monomeric form.[61,84-87] These observations confirm that Cu^{2+} ion induces the aggregation of PDI-HIS effectively through the synergistic effect of Cu^{2+} coordination with histidine moieties and π-π stacking between PDI aromatic planes (Figures A5a.1 and A5a.2). The PDI-HIS is highly selective for Cu^{2+} with a LOD of 0.48 μM according to 3σ/k rule,[88] whereas no spectral changes occur in presence of other metal ions like Na^{+}, K^{+}, Ca^{2+}, Cr^{3+}, Mn^{2+}, Fe^{3+}, Fe^{2+}, Co^{2+}, Ni^{2+}, Zn^{2+}, Cd^{2+}, Hg^{2+}, Ag^{+} and Cu^{+} (Figure 5a.4b) even at higher concentrations. The quenching efficacy of Cu^{2+} for PDI-HIS is calculated to be $K_{SV} = 7.1 \times 10^{6}\ M^{-1}$.

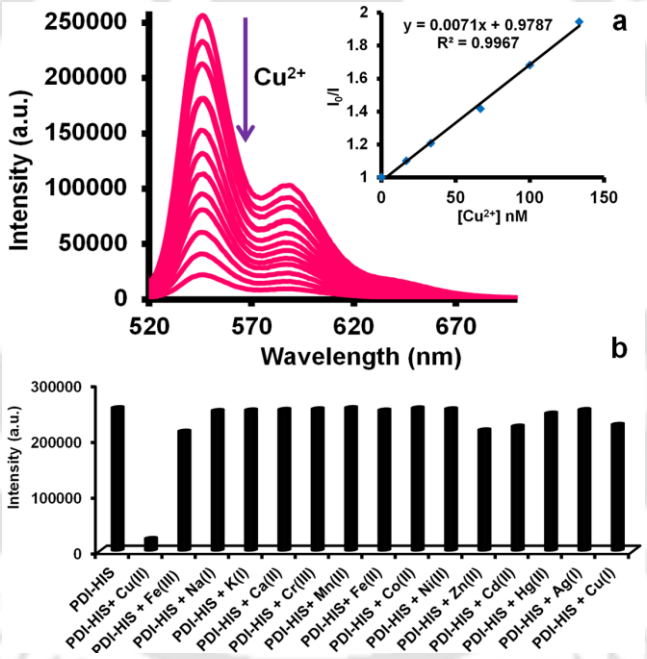

Figure 5a.4 (a) Emission spectra of PDI-HIS (0.33 μm) upon stepwise addition of Cu^{2+} ions in HEPES buffer (10 mM, pH 7.4). Excitation wavelength: 508 nm. (b) Bar diagram of fluorescence changes observed in the fluorescence peak of PDI-HIS at 546 nm in the presence of various metal ions. (except Cu^{2+} (1.3 μM), other metal concentrations are 10 μM). Inset in (a) Stern–Volmer plots for the fluorescence quenching of PDI-HIS by Cu^{2+}.

5a.2.5. Selective and sensitive detection of ATP

The fluorescent sensing of biologically important anions has generated considerable interest in recent years.[15,59,62] ATP has a strong affinity towards Cu^{2+} ion as compared to other multiple phosphates.[89,90] As expected, the introduction of ATP into the fluorescent quenched

PDI-HIS+Cu^{2+} solution, was found to be bind with Cu^{2+} ions, which disrupting the PDI-HIS–Cu^{2+} complex. As a result, free PDI-HIS molecules were separated from the complex leading to the fluorescent dequenching of PDI-HIS solution. To evaluate the selectivity of PDI-HIS+Cu^{2+} complex toward ATP, the fluorescence titration with other anions including PPi, GTP, CTP, TTP, Pi, AMP, F^-, Cl^-, Br^-, I^-, CN^-, CH_3COO^-, NO_3^-, NO_2^-, HSO_4^-, SO_4^{2-}, S^{2-}, N_3^-, ClO_4^- $H_2PO_4^{2-}$ and HPO_4^{2-} were performed under identical conditions. The selectivity of PDI-HIS+Cu^{2+} complex toward ATP suggests that PDI-HIS+Cu^{2+} has potential applications in sensing ATP in aqueous competitive solution. When the ATP concentration was increased, the maximum fluorescence intensity at 546 nm and 587 nm gradually increased (Figure 5a.5). On adding equimolar amount of ATP relative to Cu^{2+} into this solution, the fluorescence intensity recovered 100% of the initial intensity of free PDI-HIS and excess amount of ATP did not change the emission intensity further. These results indicate that the competitive binding of ATP to Cu^{2+} results in the dissociation of the PDI-HIS+Cu^{2+} complex, which is responsible for the fluorescence dequenching due to the equilibrium moving to the free PDI-HIS (Figure A5a.1 and A5a.2). The LOD was calculated to be 0.58 μM for ATP according to 3σ/k rule,[88,91] which confirms to be the highest sensitivity for ATP.[62] The percentage of dequenching towards PDI-HIS+Cu^{2+} complex was calculated to be ~99% for ATP and 65% for PPi. Other phosphates such as Pi, AMP and other anions showed negligible dequenching of <5% (Figure 5a.5b). The association/binding constant for Cu^{2+} and ATP were calculated to be 5.65×10^6 M^{-1} and 1.42×10^5 M^{-1} respectively (Figure A5a. 3).

The colorimetric sensing ability of PDI-HIS turn “on-off-on” was investigated under naked eye visualization and UV-lamp at 365 nm in aqueous solution (HEPES buffer at pH 7.4). When 2 equiv. of Cu^{2+} was added to the solution of PDI-HIS (10 μM), it responded with a dramatic color change from pink to nonfluorescent. The pink color is regained by the addition of 10 equiv. of ATP (Figure 5a.5b inset). The same study when investigated under UV-lamp illumination at 365 nm in the absence (yellowish orange) and presence (nonfluorescent) of Cu^{2+} with PDI-HIS, the yellowish orange color is regained for PDI-HIS+Cu^{2+} in presence of ATP by the decomplexation mechanism. Furthermore, it was confirmed that the sensitivity of PDI-HIS molecule was in the full pH range of 1−14 (Figure A5a. 4), thus extending the potential application of PDI-HIS in biosensor.

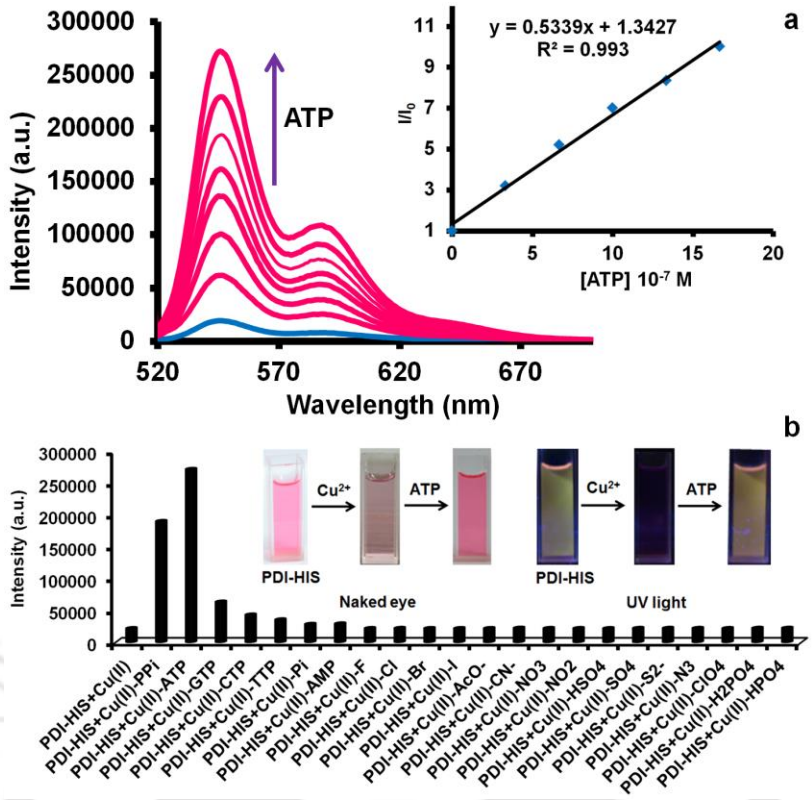

Figure 5a.5 (a) Dequenching emission spectra of PDI-HIS (0.33 μM) + Cu^{2+} (1.33 μM) upon the stepwise addition of different amounts of ATP (0-2.5 μM) in HEPES buffer (10 mM, pH 7.4). (b) Bar diagram of fluorescence changes observed in the fluorescence peak of PDI-HIS+Cu^{2+} in presence of various anions like PPi, ATP, GTP, CTP, TTP, Pi, AMP, F^-, Cl^-, Br^-, I^-, CN^-, CH_3COO^-, NO_3^-, NO_2^-, HSO_4^-, SO_4^{2-}, S^{2-}, N_3, ClO_4^- $H_2PO_4^{2-}$, and HPO_4^{2-}. (5 μM). Inset in (a) Linear plots for the fluorescence dequenching of PDI-HIS by ATP; Inset in (b) Colorimetric study of PDI-HIS in the absence (pink) and the presence (nonfluorescent) of Cu^{2+} and PDI-HIS+Cu^{2+} with ATP (Under naked eye and UV-lamp at 365 nm).

5a.2.6. AFM morphology study of PDI-HIS+Cu^{2+} complex with ATP

Further evidence for aggregation and disaggregation was confirmed from the morphological changes of PDI-HIS, PDI-HIS+Cu^{2+} complex and PDI-HIS+Cu^{2+} + ATP by atomic force microscopy (AFM) (Figure 5a.6). The AFM topography images of pure PDI-HIS was observed to be spherical with the diameter size of ~150-200 nm and 3 nm height (Figure 5a.6 (a-c)). The complex formation of PDI-HIS in the presence of Cu^{2+} was also observed and it induced the formation of aggregation with the height of ~40 nm which is higher than the height of free PDI-HIS monomers (Figure 5a.6 (d-f)). The aggregated PDI-HIS+Cu^{2+} complex was disaggregated rapidly in the presence of ATP, leading to regain the PDI-HIS monomer form with a height of ~10 nm which is less than the height of PDI-HIS+Cu^{2+}

complex (Figure 5a.6 (g-i)). Similarly, the above results were further confirmed by SEM images, which supported the formation of PDI-HIS+Cu^{2+} complex in flakes shape and disaggregated by ATP into spherical form (Figure A5a. 5).

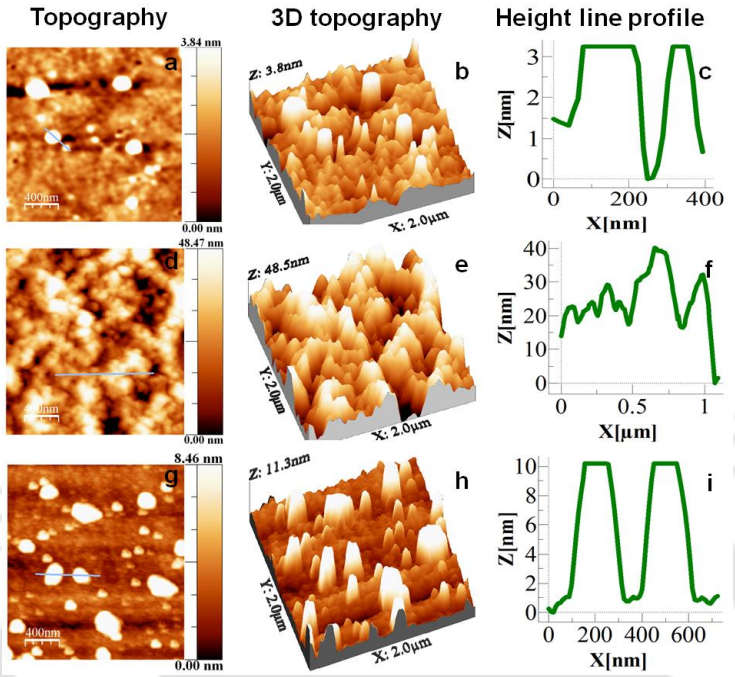

Figure 5a.6 (a, d, g) AFM topography images of PDI-HIS (monomer), PDI-HIS+Cu^{2+} (aggregated complex) and PDI-HIS+Cu^{2+}+ATP (disaggregated complex). (b, e, h) AFM 3D topography images of PDI-HIS, PDI-HIS+Cu^{2+} and PDI-HIS+Cu^{2+}+ATP. (c, f, i) AFM height line profiles of PDI-HIS, PDI-HIS+Cu^{2+} and PDI-HIS+Cu^{2+}+ATP (X = Distance, Z = Height).

The results of aggregation and disaggregation were further confirmed by other characterisation techniques such as, FT-IR spectroscopy (Figure. A5a. 6) and dynamic light scattering (DLS) (Figure A5a. 7). The observed results by FT-IR and DLS, indicates that the formation of PDI-HIS+Cu^{2+} complex was disturbed in presence of ATP by metal chelation method. The hydrodynamic particles diameter of PDI-HIS and PDI-HIS+Cu^{2+} aggregated complex was observed to be 220 and ~120 d. nm respectively. Further, the disaggregation of PDI-HIS+Cu^{2+} by ATP confirms that the hydrodynamic particles diameter at 220 (d. nm) are similar to that of free PDI-HIS (220 (d. nm)) (Figure A5a. 7). Finally, these studies strongly support the aggregation of PDI-HIS with Cu^{2+} ion and disaggregation of PDI-HIS+Cu^{2+} complex with ATP anions by "turn-on" metal chelation method.

5a.2.7. Cell viability of PDI-HIS by MTT assay

To utilize any compound for bio-sensing, diagnosis and therapeutic purpose it is vital to know its toxicity. To check the *in vitro* toxicity of PDI-HIS, normal (HUVEC and EA.hy926) and cancer cells (A549 and B16) were treated with PDI-HIS in a dose dependent manner (10 µg/ml - 750 µg/ml) for 24 h (Figure 5a.7). The results imply that upto ~500 µg/mL of PDI-HIS was biocompatible in nature and therefore, the PDI-HIS can be safely applied for imaging and cell studies.

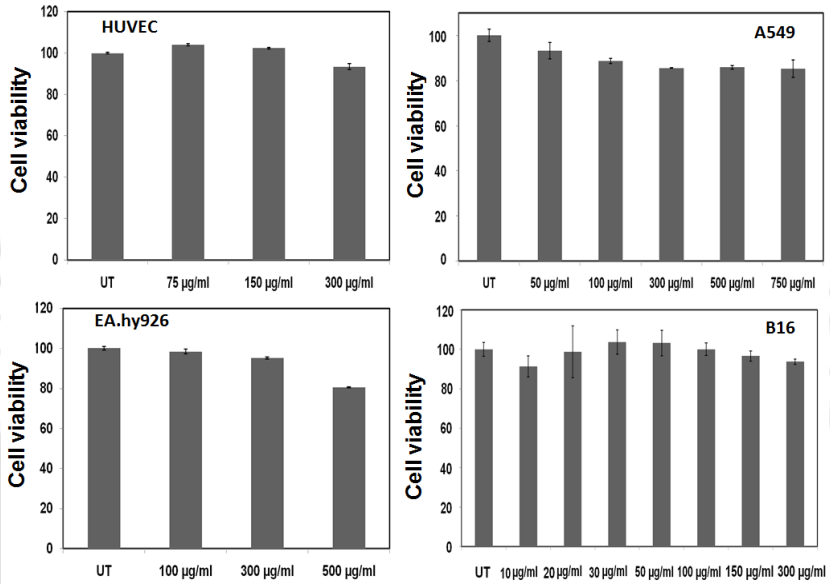

Figure 5a.7 Cell viability assay of PDI-HIS with different cell lines normal (HUVEC and EA.hy926) and cancer cells (A549 and B16) at different concentrations.

5a.2.8. Detection of Cu^{2+} ion and ATP in living cells

Further, A549 cells were seeded in each of the 24 well plates and incubated at 37 °C overnight in a CO_2 incubator prior to cell imaging studies. The next day, A549 cells were treated with 300 µg/mL of PDI-HIS and incubated for 24 h. A549 cells were washed atleast four times with PBS buffer and then were kept in HBSS buffer (pH 7.4) and finally the fluorescence images were recorded by fluorescence microscopy.[92,93] The A549 cells treated PDI-HIS probe alone showed a strong intracellular fluorescence images. All the images were collected with 10X (Figure 5a.8) and 20X (Figure A5a. 8) magnification. A549 cells were then treated with 1 mM of Cu^{2+} for 3 h and after washing 2-3 times with PBS buffer solutions the fluorescence gets quenched upon incubation with Cu^{2+} ions. Furthermore, the Cu^{2+} ion treated A549 cells were incubated with ATP (20 mM) for 1 h. The reappearance of fluorescence

was observed from A549 cells due to disaggregation of PDI-HIS-Cu^{2+} complex. This result validates that the PDI-HIS was able to detect intracellular Cu^{2+} ions via complex formation[88] and this complex detected intracellular ATP by "turn-on" mechanism due to the disaggregation of PDI-HIS-Cu complex.

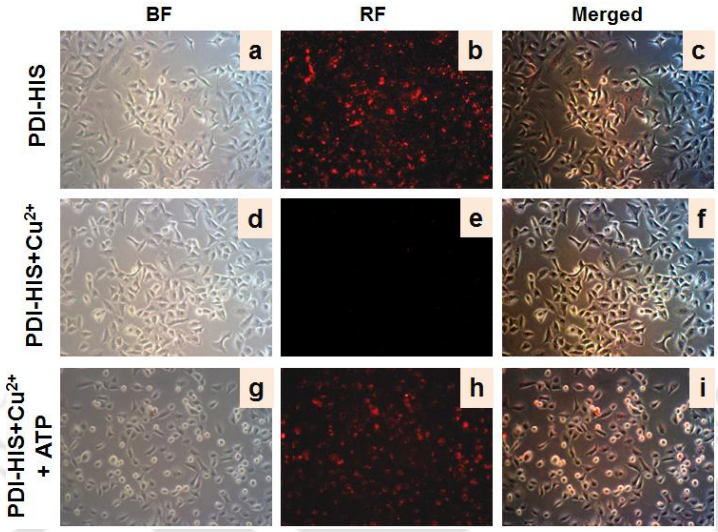

Figure 5a.8 (a, d, g) Bright-field images of A549 cells treated with PDI-HIS, PDI-HIS+Cu^{2+} and PDI-HIS+Cu^{2+}+ATP. (b) Fluorescence images of A549 cells incubated with 300 µg/mL PDI-HIS for 24 h. (e) PDI-HIS further incubated with 1 mM Cu^{2+} for 3 h. (h) PDI-HIS+Cu^{2+} complex further incubated with 20 mM ATP for 1 h. (c, f, i) Merged images of A549 cells treated with PDI-HIS, PDI-HIS+Cu^{2+} and PDI-HIS+Cu^{2+}+ATP. Excitation wavelength range λ_{ex} = 510-560 nm (green) and λ_{em} = 605 nm (red); 10X magnification).

5a.3. Conclusion

In summary, the synthesis of histidine functionalized water-soluble fluorescent perylene diimide derivative PDI-HIS and its ability as fluorescence "turn-off" and colorimetric Cu^{2+} sensor via metal coordination induced molecular aggregation is demonstrated in HEPES buffer solution (10 mM, pH 7.4). The highly efficient fluorescence quenching behavior of PDI-HIS molecule was possible due to the strong intermolecular π-π interaction among the PDI molecules allowing it to be utilized to detect Cu^{2+} at physiological conditions with a K_{SV} value of 7.1×10^6 M^{-1}. The PDI-HIS monomer fluorescence was quenched with high efficiency, primarily due to the formation of nonemitting aggregates with the forbidden low-energy exciton transition in the presence of Cu^{2+} in aqueous medium. The PDI-HIS-Cu^{2+} complex get disaggregated with rapid recovery of fluorescence on selectively binding ATP with a LOD of 0.58 µM in aqueous solution. PDI-HIS was nontoxic up to ~500 µg/mL levels and could be applied for cell studies and fluorescence imaging to detect Cu^{2+} and ATP in

A549 living cells. The detection ability and aggregation behavior of PDI-HIS was comprehensively monitored by a combination of spectroscopy methods such as UV-vis, fluorescence, FT-IR, atomic force microscopy and dynamic light scattering techniques in addition to the changes observed by UV-lamp and naked eye.

5a.4. Experimental Section

5a.4.1. Materials and methods

All reagents and solvents were purchased from commercial sources and the solvents used were of spectroscopic grade. UV-vis absorption spectra were recorded on a PerkinElmer Lambda-25 spectrometer. Fluorescence spectra were carried out on a FluoroMax-4 Spectrofluorometer-Horiba Scientific. A 10 × 10 mm quartz cuvette was used for solution spectra and emission was collected at 90° relative to the excitation beam. Deionized water was obtained from Milli-Q system (Millipore). ^{1}H NMR (400 and 600 MHz) spectra were obtained with a Varian-AS400NMR and Bruker spectrometer spectrometer. ^{13}C NMR (150 MHz) spectra were obtained by Bruker spectrometer. Mass spectra were recorded by Agilent Accurate-Mass Q-TOF LC/MS 6520, and peaks are given in m/z (% of basis peak). FT-IR was recorded in a PerkinElmer spectrometer with samples prepared with KBr pellets. Images were investigated by scanning electron microscopy (SEM) on a LEO 1430vp instrument operated at 8–10 kV. Atomic force microscopy images were taken by Agilent 5500-STM instrument. DLS were measured using a Zetasizer Nano series Nano-ZS90 instrument.

5a.4.2. Preparation of stock solutions

The PDI-HIS stock solution was prepared at a concentration of 1.0×10^{-3} mL^{-1} in 10 mL H_2O at pH 7-9. This stock solution was diluted to desired concentration for each titration in 3 mL cuvette having HEPES buffer at pH 7.4.

5a.4.3. Preparation of cation and anion stock solutions

Each inorganic metal salt and anions stock solutions were prepared at the concentration of 10.0×10^{-3} mL^{-1} in 5 mL Milli-Q water. The stock solutions were diluted to the desired concentrations with Milli-Q water when needed.

5a.4.4. Preparation of HEPES buffer solution

All the UV-visible and fluorescence titrations were performed in 10 mM HEPES buffer at pH 7.4 by using 4 M NaOH or 5 M HCl solution.

5a.4.5. Detection limit for Cu^{2+} ion

The detection limit was calculated on the basis of the fluorescence titration. The fluorescence emission spectrum of PDI-HIS was measured 10 times, and the standard deviation of blank measurement was achieved. To get the slope, the ratio of the emission intensity at 546 nm was plotted as a concentration of Cu^{2+}. The detection limit was calculated using the following equation

$$\text{Detection limit} = 3\sigma/k \quad (1)$$

Where σ is the standard deviation of blank measurement, and k is the slope between the ratios of emission intensity versus [Cu^{2+}].

5a.4.6. Aassociation or apparent binding constant calculation for Cu^{2+} and ATP

PDI-HIS is a highly selective "turn-off sensor" for copper ion and the association constants for the formation of PDI-HIS-Cu^{2+} complexes were evaluated using the fluorescence spectroscopy. The relative change in emission intensity of PDI-HIS at 546 nm was used to determine the binding constants.[94] The measured emission band ($I_0/\Delta I$) at 546 nm when plotted against the inverse of the concentration of Cu^{2+} solution fits almost a linear relationship. The ratio of the intercept versus slope gives the association constants of 5.65×10^6 M^{-1} for copper. Further, the apparent binding constant was evaluated using the Benesi−Hildebrand (B−H) plot by the fluorescence spectral changes at 546 nm for "turn-on" sensor for ATP with PDI-HIS-Cu complex and estimated to be 1.42×10^5 M^{-1}.

5a.4.7. Cell culture experiment

A549: human lung cancer, B16: mouse melanoma cell line, was purchased from ATCC and was cultured in DMEM (Dulbecco's Modified Eagle Medium) media supplemented with 5% L-glutamine, 10% fetal bovine serum (FBS) and 1% antibiotics (penicillin-streptomycin) in a humidified 5% CO_2 incubator at 37 °C for cell viability experiments, fluorescence imaging and bio-sensing studies. HUVECs: human umbilical vein endothelial cells were cultured in EBM complete media using 100 mm tissue culture plates at 37 °C and 5% CO_2 for 24 h. The human umbilical vein cell line (EA.hy926) was cultured in DMEM complete media. The cells were incubated with various concentrations of PDI-HIS (10 µg/ml - 750 µg/ml) for *in vitro* cytotoxicity experiments. PDI-HIS (2 µg/mL in water (pH 7.4)) was kept under UV irradiation inside the cell culture hood for 15-20 min before use.

5a.4.8. Cell viability of PDI-HIS by MTT assay

Viability of HUVEC, EA.hy926, A549 and B16 cells were checked by MTT assay according to the published protocol. Initially, 10,000 cells/ well were seeded in per well of 96 wells and various concentrations of PDI-HIS (10 µg/ml - 750 µg/ml) for cytotoxicity experiment for 24 h as a dose dependent manner. After 48 h of treatment 1 mL of MTT stock solution (concentration 5 mg/ mL) was diluted to 10 mL solution using DMEM media and 100 µL of this MTT solution (10 µL 5 mg/ mL MTT + 90 µL of corresponding media) was added to each well by replacing the media and allowed to incubate for 4 h. After 4 h, the media in each well was replaced by 100 µL of DMSO-methanol mixture (1:1 volume ratio) for solubilizing the violet crystal and kept the mixture on the shaker for homogeneous mixture. Finally, the absorbance of the mixture was measured at 570 nm using a microplate reader (Varioskan Flash). All the experiments were carried out in triplicate and the results are expressed as normalized viability = $\{1/Abs_{\lambda} = 570$ (untreated cells – blank)$\} \times \{Abs_{\lambda} = 570$ (treated cells – blank)$\}$.

5a.4.9. Fluorescence cell imaging study

2×10^4 numbers of A549 cells were seeded in each of the 24 well plates and incubated at 37 °C for overnight in a CO_2 incubator prior to cell imaging studies. On the next day A549 cells were treated with 300 µg/mL and 500 µg/mL of PDI-HIS and incubated for 24 h. Cells were washed with PBS (4-5 times) then the cells were kept in HBSS buffer (pH=7.4) and finally the fluorescence images were taken by fluorescence microscopy (Nikon Eclipse TE2000-E). The red fluorescence images were collected with a 10X and 20X microscope objective with excitation wavelength range λ_{Ex} = 510-560 nm (green) and λ_{Em} = 605 nm (red). A549 cells were then treated with 10^{-3} M (1 mM) of Cu^{2+} for 3 h. After 2-3 times PBS washing again the fluorescence images were taken in the red filter for copper sensing experiments. Further, the copper treated A549 cells were treated with ATP (20 mM) and incubated for 45 min. The reenhancement of fluorescence signals from A549 cells with the incubated ATP was observed under same excitation and emission filter (red).

References

(1) Rogers, C. W.; Wolf, M. O. *Coord. Chem. Rev.,* **2002,** *233-234,* 341.

(2) Martínez-Máñez, R. Sancenón, F. *Chem. Rev.* **2003,** *103,* 4419.

(3) Amendola, V.; Fabbrizzi, L.; Mangano, C.; Pallavicini, P.; Poggi, A.; Taglietti, A. *Coord. Chem. Rev.,* **2001,** *219-221,* 821.

(4) Fabbrizzi, L. Licchelli, M. Rabaioli, G. Taglietti, A. *Coord. Chem. Rev.,* **2000,** *205,* 85.

(5) Beer, D. P. *Acc. Chem. Res.,* **1998,** *31,* 71.

(6) Gourine, A. V.; Llaudet, E.; Dale, N. Spyer, K. M. *Nature* **2005,** *436,* 108.

(7) Shen, X.; Mizuguchi, G.; Hamiche, A. Wu, C. *Nature* **2000,** *406,* 541.

(8) Kornberg, A. *J. Biol. Chem.,* **1988,** *263,* 1.

(9) Beer, P. D. Gale, P. A. *Angew. Chem. Int. Ed.,* **2001,** *40,* 486.

(10) Spangler, C.; Schaeferling M.; Wolfbeis, O. S. *Microchim. Acta.,* **2008,** *161,* 1.

(11) Luk, C. K. *Biochemistry* **1971,** *10,* 2838.

(12) Hirose, J.; Fujiwara, H.; Magarifuchi, T.; Iguti, Y.; Iwamoto, H.; Kominami, S. Hiromi, K. *Biochim. Biophys. Acta.,* **1996,** *1296,* 103.

(13) Zhou, Y.; Xu, Z.; Yoon, J. *Chem. Soc. Rev.,* **2011,** *40,* 2222.

(14) Jeon, H.; Lee, S.; Li, Y.; Park, S.; Yoon, J. *J. Mater. Chem.,* **2012,** *22,* 3795.

(15) Yan, L.; Ye, Z.; Peng, C.; Zhang, S. *Tetrahedron* **2012,** *68,* 2725.

(16) Ojida, A.; Takashima, I.; Kohira, T.; Nonaka, H. Hamachi, I. *J. Am. Chem. Soc.* **2008,** *130,* 12095.

(17) Rao, A. S.; Kim, D.; Nam, H.; Jo, H.; Kim, K. H.; Ban, C.; Ahn, K. H. *Chem. Commun.,* **2012,** *48,* 3206.

(18) Swamy, K. M. K.; Kwon, S. K.; Lee, H. N.; Kumar, S. M. S.; Kim, J. S. Yoon, J. *Tetrahedron Lett.,* **2007,** *48,* 8683.

(19) Moro, A. J.; Cywinski, P. J.; Körsten, S.; Mohr, G. J. *Chem. Commun.,* **2010,** *46,* 1085.

(20) Jang, H. H.; Yi, S.; Kim, M. H.; Kim, S.; Lee, N. H.; Han, M. S. *Tetrahedron Lett.,* **2009,** *50,* 6241.

(21) Jose, D. A.; Mishra, S.; Ghosh, A.; Shrivastav, A.; Mishra, S. K. Das, A. *Org. Lett.,* **2007,** *9,* 1979.

(22) Imamura, H.; Nhat, K. P. H.; Togawa, H.; Saito, K.; Lino, R.; Kato-Yamada, Y.; Nagai, T. Noji, H. *Proc. Natl. Acad. Sci. USA* **2009,** *106,* 15651.

(23) Tsuboi, T.; Lippiat, J. D.; Ashcroft, F. M.; Rutter, G. A. *Proc. Natl. Acad. Sci. USA,* **2004,** *101,* 76.

(24) Berg, J.; Hung, Y. P.; Yellen, G. A. *Nat. Methods* **2009,** *6,* 161.

(25) Wang, W. U.; Chen, C.; Lin, K. H.; Fang, Y. Lieber, C. M. *Proc. Natl. Acad. Sci. USA,* **2005,** *102,* 3208.

(26) Bell, C. J.; Manfredi, G.; Griffiths, E. J.; Rutter, G. A. *Methods Cell Biol.,* **2007,** *80,* 341.

(27) Li, C.; Numata, M.; Takeuchi, M.; Shinkai, S. *Angew. Chem., Int. Ed.* **2005,** *44,* 6371.

(29) Que, E. L.; Domaille, D. W.; Chang, C. J. *Chem. Rev.* **2008,** *108,* 1517.

(29) Thiele, D. J.; Gitlin, J. D. *Nat. Chem. Biol.,* **2008,** *4,* 145.

(30) Davis, A. V.; O'Halloran, T. V. *Nat. Chem. Biol.,* **2008,** *4,* 148.

(31) Robinson, N. J.; Winge, D. R. *Annu. Rev. Biochem.,* **2010,** *79,* 537.

(32) Chen, X.; Tian, X.; Shin, I.; Yoon, J. *Chem. Soc. Rev.,* **2011,** *40,* 4783.

(33) Yanagida, T.; Ishii, Y. Single molecule dynamics in life science, John Wiley & Sons, **2008**.

(34) Sigel, A.; Sigel, H.; Sigel, R. K. O. Structural and catalytic roles of metal ions in RNA, *Royal Society of Chemistry,* **2011**.

(35) Li, P.; Duan, X.; Chen, Z.; Liu, Y.; Xie, T.; Fang, L.; Li, X.; Yin, M.; Tang, B. *Chem. Commun.,* **2011,** *47,* 7755.

(36) S. G. Kaler, *Nat. Rev. Neurol.,* **2011,** *7,* 15.

(37) Bertini, I.; Rosato, A. *Cell. Mol. Life Sci.,* **2008,** *65,* 89.

(38) Finkel, T.; Serrano, M.; Blasco, M. A. *Nature* **2007,** *448,* 767.

(39) Zou, Q.; Li, X.; Zhang, J.; Zhou, J.; Sun, B.; Tian, H. *Chem. Commun.,* **2012,** *48,* 2095.

(40) Guo, Z.-Q.; Chen, W.-Q.; Duan, X.-M. *Org. Lett.,* **2010,** *12,* 2202.

(41) Dalapati, S.; Jana, S.; Alam, M. A.; Guchhait, N. *Sens. Actuators, B,* **2011,** *160,* 1106.

(42) Shao, N.; Pang, G.-X.; Wang, X.-R.; Wu, R.-J.; Cheng, Y. *Tetrahedron* **2010,** *66,* 7302.

(43) Barceloux, D. G. *J. Toxicol. Clin. Toxicol.,* **1999,** *37,* 217.

(44) Strausak, D.; Mercer, J. F.; Dieter, H. H.; Stremmel, W.; Multhaup, G. *Brain Res. Bull.,* **2001,** *55,* 175.

(45) Gaggelli, E.; Kozlowski, H.; Valensin, D.; Valensin, G. *Chem. Rev.* **2006,** *106,* 1995.

(46) Valentine, J. S.; Hart, P. J. *Proc. Natl. Acad. Sci. USA,* **2003,** *100,* 3617.

(47) Barnham, K. J.; Masters, C. L.; Bush, A. I. *Nat. Rev. Drug Discovery* **2004,** *3,* 205.

(48) Tak, W. T. Yoon, S. C. *Korean J. Nephrol.,* **2001,** *20,* 863.

(49) Tour, O.; Adams, S. R.; Kerr, R. A.; Meijer, R. M.; Sejnowski, T. J.; Tsien, R. W.; Tsien, R. Y. *Nat. Chem. Biol.,* **2007,** *3,* 423.

(50) Komatsu, H.; Miki, T.; Citterio, D.; Kubota, T.; Shindo, Y.; Kitamura, Y.; Oka, K.; Suzuki, K. *J. Am. Chem. Soc.* **2005,** *127,* 10798.

(51) Burdette, S. C.; Lippard, S. J. *Proc. Natl. Acad. Sci. USA*, **2003,** *100,* 3605.

(52) Qian, F.; Zhang, C.; Zhang, Y.; He, W.; Gao, X.; Hu, P.; Guo, Z. *J. Am. Chem. Soc.* **2009,** *131,* 1460.

(53) Zhu, W.; Huang, X.; Guo, Z.; Wu, X.; Yu, H.; Tian, H. *Chem. Commun.*, **2012,** *48,* 1784.

(54) Kubo, Y.; Ishida, T.; Kobayashi, A.; James, T. D. *J. Mater. Chem.*, **2005,** *15,* 2889.

(55) Lee, Y. H.; Park, N.; Park, Y. B.; Hwang, Y. J.; Kang, C.; Kim, J. S. *Chem. Commun.*, **2014,** *50,* 3197.

(56) Shahid, M.; Razi, S. S.; Srivastava, P.; Ali, R.; Maiti, B.; Misra, A. *Tetrahedron* **2012,** *68,* 9076.

(57) Che, Y.; Yang, X.; Zang, L. *Chem. Commun.*, **2008,** 1413.

(58) Peneva, K.; Mihov, G.; Herrmann, A.; Zarrabi, N.; Börsch, M.; Duncan, M. T.; Müllen, K. *J. Am. Chem. Soc.* **2008,** *130,* 5398.

(59) Chen, X.; Jou, J. M.; Yoon, J. *Org. Lett.*, **2009,** *11,* 2181.

(60) Szelke, H.; Schübel, S.; Harenberg, J.; Krämer, R. *Chem. Commun.*, **2010,** *46,* 1667.

(61) Wang, B.; Yu, C. *Angew. Chem., Int. Ed.*, **2010,** *49,* 1485.

(62) Feng, X.; An, Y.; Yao, Z.; Li, C.; Shi, G. *ACS Appl. Mater. Interfaces* **2012,** *4,* 614.

(63) Pandeeswar, M.; Khare, H.; Ramakumar, S.; Govindaraju, T. *RSC Adv.* **2014,** *4,* 20154.

(64) Chan, Y. H.; Jin, Y.; Wu, C.; Chiu, D. T. *Chem. Commun.*, **2011,** *47,* 2820.

(65) Wang, Y.; Zhang, L.; Zhang, G.; Wu, Y.; Wu, S.; Yu, J.; Wang, L. *Tetrahedron Lett.*, **2014,** *55,* 3218.

(66) Singh, P.; Mittal, L. S.; Kumar, S.; Bhargava, G.; Kumar, S. *J Fluoresc.*, **2014,** *24,* 909.

(67) Liu, K.; Xu, Z.; Yin, M.; Yang, W.; He, B.; Wei, W.; Shen, J. *J. Mater. Chem. B,* **2014,** *2,* 2093.

(68) Geo, X.; Zhang, D.; Zhu, D. *Adv. Mater.*, **2004,** *16,* 125.

(69) Ge, S.; Zhang, C.; Zhu, Y.; Yu, J.; Zhanga, S. *Analyst* **2010,** *135,* 111.

(70) Muthuraj, B.; Hussain, S.; Iyer, P. K. *Polym. Chem.* **2013,** *4,* 5096.

(71) Saikia, G.; Dwivedi, A. K. Iyer, P. K. *Anal. Methods* **2012,** *4,* 3180.

(72) Chen, Z. J.; Wang, L. M.; Zou, G.; Zhang, L.; Zhang, G. J.; Cai, X. F.; Teng, M. S. *Dyes Pigments,* **2012,** *94,* 410.

(73) Singh, P.; Mittal, L. S.; Vanita, V.; Kumar, R.; Bhargava, G.; Walia, A.; Kumara, S. *Chem. Commun.,* **2014,** *50,* 13994.

(74) Ajayakumar, M. R.; Mukhopadhyay, P. *Org. lett.*, **2010,** *12*, 2646.

(75) Ge, S.; Zhang, C.; Yu, F.; Yan, M.; Yu, J. *Sens. Actuators B* **2011,** *156*, 222

(76) Xu, K-X.; Kong, H-J.; Li, P.; Yang, L.; Zhang, J-L.; Wang, C-J. *New J. Chem.*, **2014,** *38*, 1004.

(77) Fujimoto, K.; Yamada, S.; Inouye, M. *Chem. Commun.*, **2009,** 7164.

(78) Tuntiwechapikul, W.; Taka, T.; Béthencourt, M.; Makonkawkeyoon, L.; Lee, T. R. *Bioorg. Med. Chem. Lett.,* **2006,** *16*, 4120.

(79) Draper, E. R.; Walsh, J. J.; McDonald, T. O.; Zwijnenburg, M. A.; Cameron, P. J.; Cowan, A. J.; Adams, D. J. *J. Mater. Chem. C,* **2014,** *2*, 5570.

(80) Balakrishnan, K.; Datar, A.; Oitker, R.; Chen, H.; Zuo, J.; Zang, L. *J. Am. Chem. Soc.*, **2005,** *127,* 10496.

(81) Balakrishnan, K.; Datar, A.; Naddo, T.; Huang, J.; Oitker, R.; Yen, M.; Zhao, J.; Zang, L. *J. Am. Chem. Soc.*, **2006,** *128,* 7390.

(82) Herrikhuyzen, V.; Syamakumari, A.; Schenning, A. P. H. J.; Meijer, E. W. *J. Am. Chem. Soc.*, **2004,** *126,* 10021.

(83) Würthner, F. *Chem. Commun.*, **2004,** 1564.

(84) Rehm, S.; Stepanenko, V.; Zhang, X.; Rehm, T. H. Würthner, F. *Chem. -Eur. J.*, **2010,** *16,* 3372.

(85) Pescitelli, G.; Bari, L. D.; Berova. N. *Chem. Soc. Rev.*, **2014,** *43*, 5211.

(86) Ma, T.; Li C.; Shi, G. *Langmuir* **2007,** *24*, 43.

(87) Zhao, L.; Ma, T.; Bai, H.; Lu, G.; Li, C.; Shi, G. *Langmuir* **2008,** *24*, 4380.

(88) Muthuraj, B.; Deshmukh, R.; Trivedi, V.; Iyer, P. K. *ACS Appl. Mater. Interfaces* **2014,** *6*, 6562.

(89) Kataev, E.; Arnold, R.; Rüffer, T.; Lang, H.; *Inorg. Chem.*, **2012,** *51*, 7948.

(90) Almeida, B. L. D.; Versiani, O.; Sousa, M.; Mercê, A. L. R.; Mangrich, A. S.; Felcman, J.; *Inorg. Chim. Acta.*, **2009,** *362*, 2447.

(91) Guo, L.; Nie, D.; Qiu, C.; Zheng, Q.; Wu, H.; Ye, P.; Hao, Y.; Fu, F.; Chen, G. *Biosen. Bioelectron.,* **2012,** *35*, 123.

(92) Mukherjee, S.; Chowdhury, D.; Kotcherlakota, R.; Patra, S.; Vinothkumar, B.; Bhadra, M. P.; Sreedhar, B.; Patra, C. R. *Theranostics* **2014,** *4*, 316.

(93) Modak, A.; Barui, A. K.; Patra, C. R. Bhaumik, A. *Chem. Commun.*, **2013,** *49*, 7644.

(94) Chou, P. T.; Wu, G. R.; Wei, C. Y.; Cheng, C. C.; Chang, C. P.; Hung. F. T. *J. Phys. Chem. B.* **2000,** *104*, 7818.

Appendix

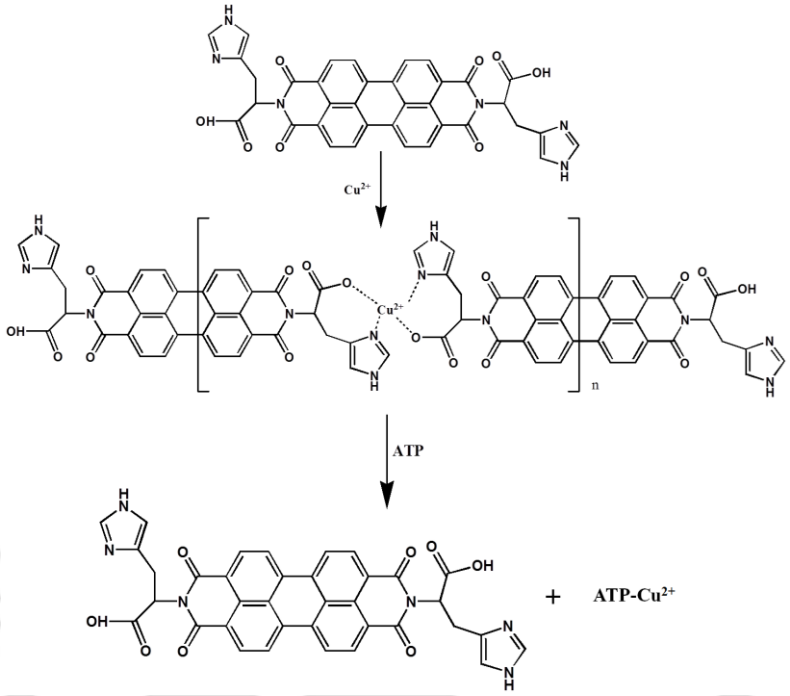

Figure A5a.1 Proposed mechanism for PDI-HIS aggregation with Cu^{2+} and disaggregation of PDI-HIS+ Cu^{2+} with ATP.

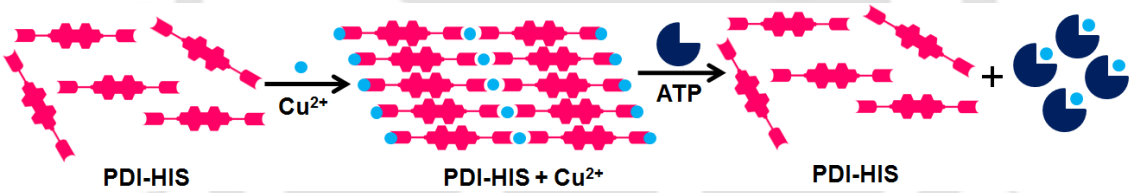

Figure A5a.2 Schematic representation of PDI-HIS aggregation with Cu^{2+} and disaggregation of PDI-HIS+ Cu^{2+} with ATP.

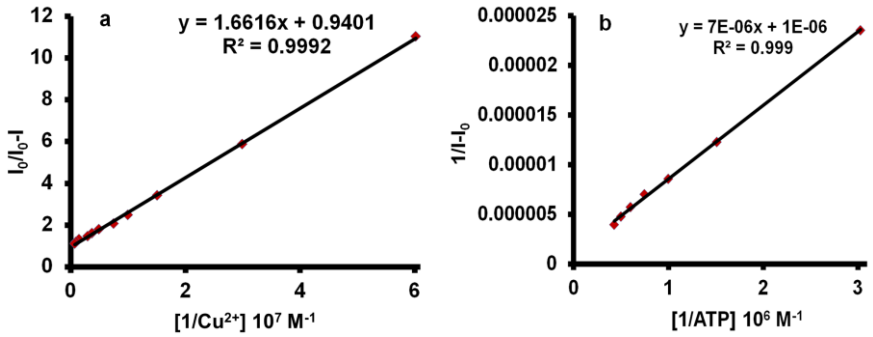

Figure A5a.3 (a) Binding constant curve for PDI-HIS with Cu^{2+} ion. (b) Benesi−Hildebrand (B−H) plot for the calculation of binding constant for ATP with PDI-HIS+Cu^{2+}.

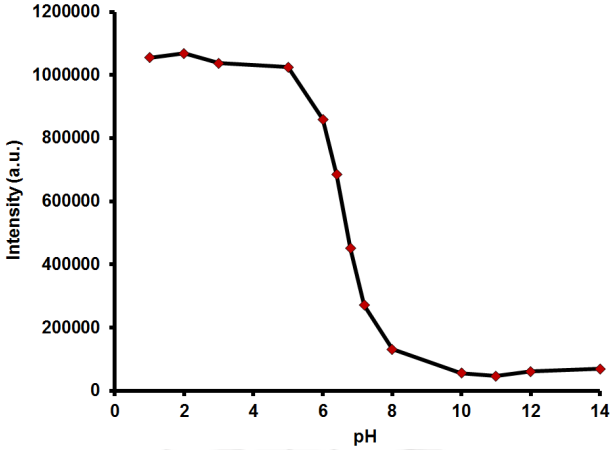

Figure A5a.4 pH sensitivity of PDI-HIS.

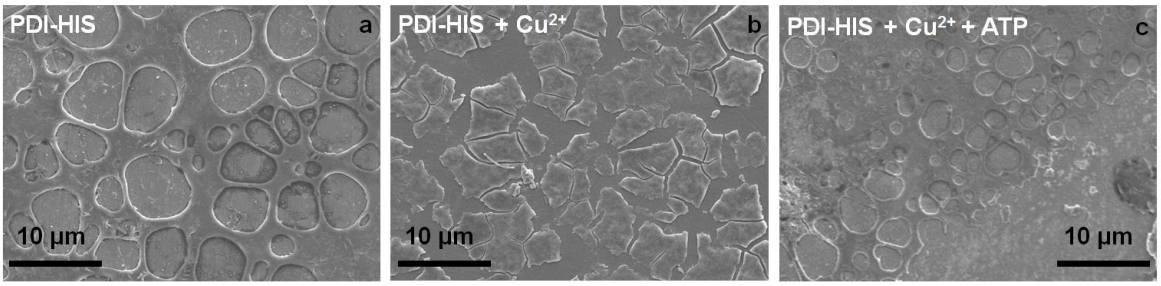

Figure A5a.5 SEM images of PDI-HIS, PDI-HIS+Cu^{2+} complex and PDI-HIS+Cu^{2+}+ATP.

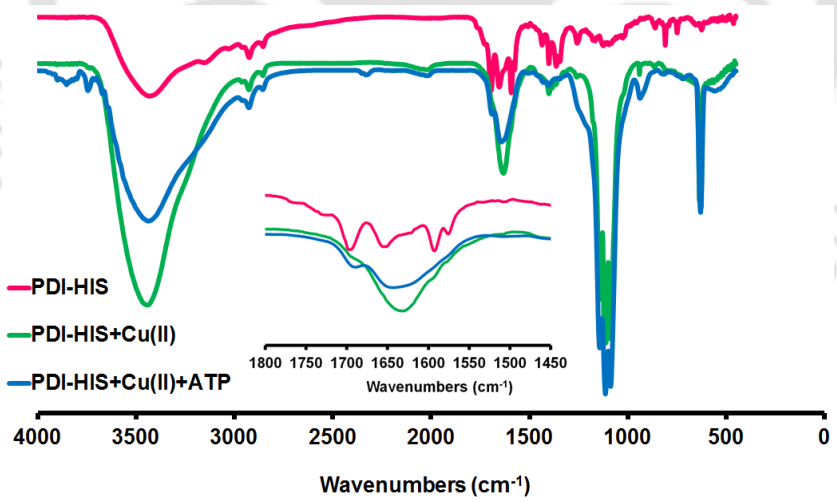

Figure A5a.6 FT-IR spectra of PDI-HIS, PDI-HIS+Cu^{2+} and PDI-HIS+Cu^{2+}+ATP.

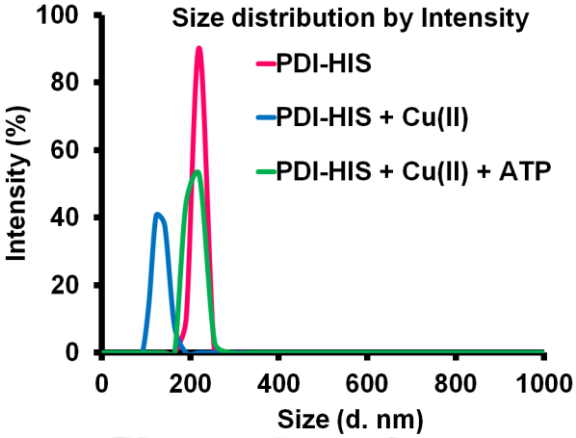

Figure A5a.7 Particle size analysis of PDI-HIS, PDI-HIS+Cu^{2+} and PDI-HIS+Cu^{2+}+ATP in HEPES buffer solution at pH 7.4 by DLS instrument.

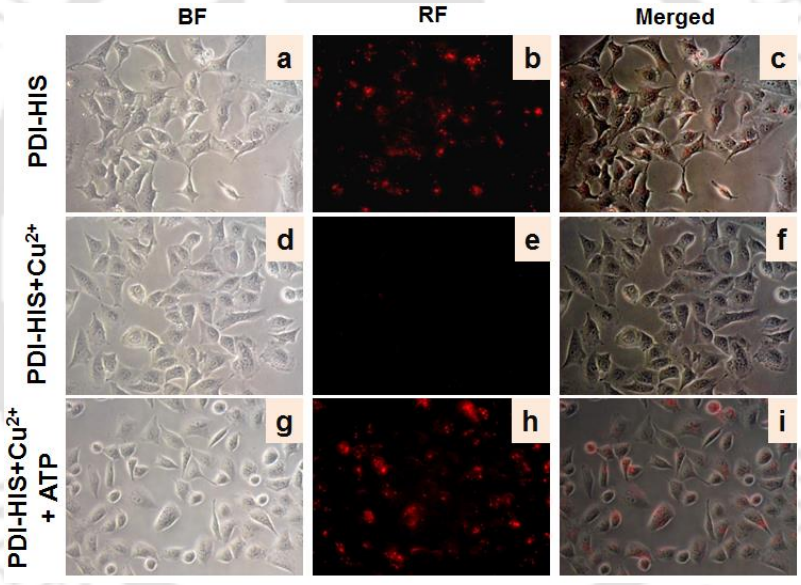

Figure A5a.8 (a, d, g) Bright-field image of A549 cells treated with PDI-HIS, PDI-HIS+Cu^{2+} and PDI-HIS+Cu^{2+} with ATP. (b) Fluorescence image of A549 cells incubated with 300 µg/mL of PDI-HIS for 24 h. (e) PDI-HIS further incubated with 1 mM Cu^{2+} ion for 3 h. (h) PDI-HIS+Cu^{2+} complex was further incubated with 20 mM ATP for 1 h. (c, f, i). Merged images of A549 cells treated with PDI-HIS, PDI-HIS+Cu^{2+} and PDI-HIS+Cu^{2+} with ATP. Excitation wavelength range λ_{ex} = 510-560 nm (green) and λ_{em} = 605 nm (red), (Nikon eclipse TE 2000-E, 20X magnification).

Chapter: 5b

An Efficient Strategy to Assemble Water Soluble Histidine–Perylene Diimide and Graphene Oxide for the Highly Selective and Sensitive Detection of PPi in Physiological Conditions and *in vitro*

Abstract

A strategy to self-assemble multiple dimension materials interconnected into aggregated networks resulted in the development of water soluble, biocompatible nanocomposite probe for the detection of pyrophosphate (PPi) in physiological conditions and in *in vitro* live melanoma cancer cells (B16F10). The self-assembled nanocomposite probe comprised of amino acid (histidine) functionalized perylenediimide (PDI-HIS) oligomer, copper metal salt and graphene oxide (GO) that was water soluble and could be utilized as a highly effective sensing platform in biological conditions and cellular environment via fluorescence "turn-on" for PPi detection. This controlled fabrication of metal organic self-assembled spheres along with GO proved very valuable for the detection of PPi with unprecedented sensitivity over other competing ions. The PDI-HIS-Cu-GO (PCG) nanocomposite sensor provides a unique platform for the fluorogenic detection of PPi having a very low limit of detection (LOD) of 0.60×10^{-7} M based on the strong affinity (1.0×10^{6} M^{-1}) between the copper complex of PDI-HIS receptor and PPi. The intracellular detection of PPi using PCG was also carried out in B16F10 cells where >10 times sensitively was observed as compared to the PDI-HIS+Cu^{2+} probe. This confirms the utility of the biocompatible nanocomposite for early cancer detection via PPi recognition in physiological conditions and in live cells. Furthermore, the fabrication of PDI-HIS and PCG with PVA hydrogel films and on thin layer chromatography plates demonstrated the practical utility for the detection of PPi anions by "off-on" response rapidly in a label free manner.

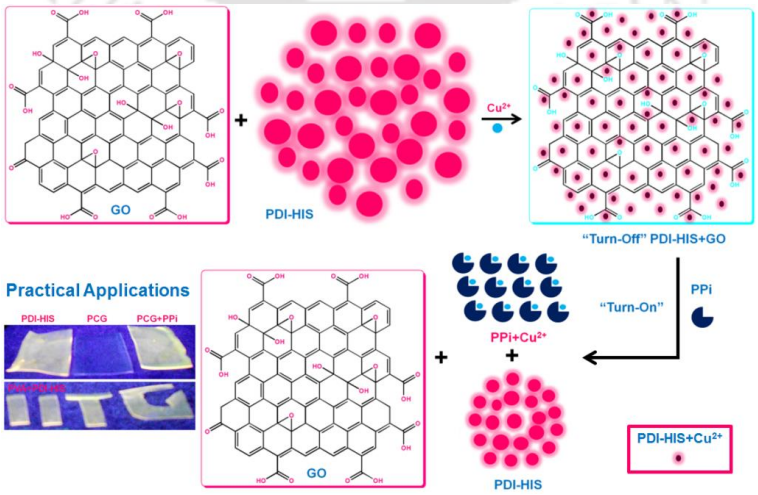

5b.1. Introduction

Detection of pyrophosphate anion (PPi) has become an important area of research due to its chemical and biological significance especially in early cancer diagnosis.[1-8] Among anions, pyrophosphate (PPi) is involved in numerous biological processes such as cellular metabolism,[9] DNA and RNA polymerization,[10] ATP hydrolysis[11] and enzymatic reactions.[10] Excess PPi is responsible for rheumatologic disorders such as chondrocalcinosis or calcium pyrophosphate dihydrate (CPPD) crystal deposition disease.[12,13] Therefore, monitoring the concentration of PPi in aqueous solutions at very low concentrations is vital for early cancer detection.[8,14] Till date, few sensors for PPi have been developed,[15-17] such as turn "off-on" or "on-off" sensor in physiological conditions,[18-35] indicator displacement approach,[36,37] competitive binding with metal ion,[38] metal-ligand interactions[39-41] and cancer diagnosis based on PPi detection.[8,14] It still remains one of the most attractive and challenging tasks to find new and smarter approaches that could improve the selectivity, sensitivity and simplicity of PPi detection *in vitro* and at physiological conditions.

Nanomaterials possess excellent optical, electrical, catalytic and magnetic properties compared to other bulk materials.[42,43] To this end, the construction of nanomaterials based platforms through a self-assembly method offers not just an alternative but a powerful strategy to address and develop important nanobiosensors which avoids and overcomes complicated synthesis steps.[44-46] Recently, graphene as an alternative material, has received immense attention in materials science, biotechnology and biosensors because of its unique two-dimensional nanostructure and high surface area.[47,48] The graphene-based biosensor and biochemical analysis were performed successfully by using the chemically modified graphene oxide nanomaterials.[49-58] Since, these chemically modified graphene oxide (GO)[47] has promising optical and electrical properties, good water solubility and low toxicity, they are prominent materials for the development of biocompatible sensors.[59-66] In particular, GO has been explored as a universal quencher for organic fluorescent probes.[60,67-70] Therefore, developing GO fluorescence-based optical biosensors for the selective detection of target analytes via "turn-on" analysis remains a tough task yet is of great interest. As a result, GO-based fluorescence "off-on" sensors for the detection of DNA, proteins and enzymes have been explored.[49,71-79] Recent reports demonstrate that two-dimensional GO nanomaterials are prime choice for the analysis of DNA rather than carbon nanotubes or gold nanoparticles.[80] Herein, we demonstrated that amino acid functionalized perylenediimide (PDI) in presence of copper and GO can be utilized for the selective detection of PPi via fluorescence "turn-on"

mechanism even in the presence of other competing phosphates and anions. By using GO we overcome the disadvantages of designing and developing newer synthetic probes that usually require tedious synthesis steps and in most cases are not selective enough for a particular analyte. We could overcome these challenges and observed that GO interacts with PDI-HIS backbone through noncovalent π-π stacking interaction which efficiently quenches the fluorescence of perylene diimide by energy transfer mechanism.[80,81]

5b.2 Results and discussion

5b.2.1. Synthesis of PDI-HIS

The synthesis of probe PDI-HIS was mentioned and discussed in previous chapter 5a (Scheme 5a.1), a reaction between 3,4,9,10-Perylenetetracarboxylic acid bisanhydride (500 mg, 1.27 mmol), histidine (800 mg, 3.82 mmol) and 2.0 g of imidazole which were heated at 140 °C for 8 h with stirring.[82] The reaction mixture was allowed to cool to 90 °C and poured into water. Then, the mixture was acidified with 2.0 M HCl, and the precipitate was washed with water and dried under vacuum at 80 °C to give the product PDI-HIS (800 mg, 94%).

5b.2.2. Characterizations of GO

The GO nano sheets were prepared by using a modified Hummer's method.[83] GO was obtained with a final concentration of 1 mg/mL in distilled water after sonicating the aqueous GO solutions. The characterization of GO was performed by fourier transform infrared (FT-IR), UV-Vis, Raman spectroscopy, atomic force microscopy and powder XRD (Figure 5b.1). The IR spectra indicate that it contains −COOH, epoxy, alkoxy and −OH groups, and all these oxygen based groups favour the aqueous sensor application of GO. In the FT-IR spectrum (Figure 5b.1a), the presence of different type of oxygen functionalities in GO was confirmed by the characteristic peaks located at 3430, 1740, 1631, 1220, and 1054 cm^{-1}, corresponding to the stretching vibrations of O–H, C=O, C=C, C–O bonds (epoxy) and C–O bonds (alkoxy), respectively.[83-85] As shown in Figure 5b.1b, the GO dispersion displays a maximum absorption at 234 nm which is due to the π-π* transition of aromatic C=C bonds and a shoulder at ~290-300 nm which corresponds to the n-π* transition of the C=O bond.[86,87] Raman spectra shows that the G band at 1600 cm^{-1} and a D band at 1354 cm^{-1} are detected (Figure 5b.1c), which is related to the characteristic carbon structure (I_D/I_G = 0.87).[88] The morphology of GO is characterized by AFM (Figure 5b.1d and 5b.1e), with the thickness of GO observed to be ~6.0 nm. Finally, the chemical oxidation of graphite into GO was

confirmed by powder XRD, (the 2θ peak shifted to 9.02), which indicates that the graphite was fully oxidized into GO (Figure 5b.1f).[88]

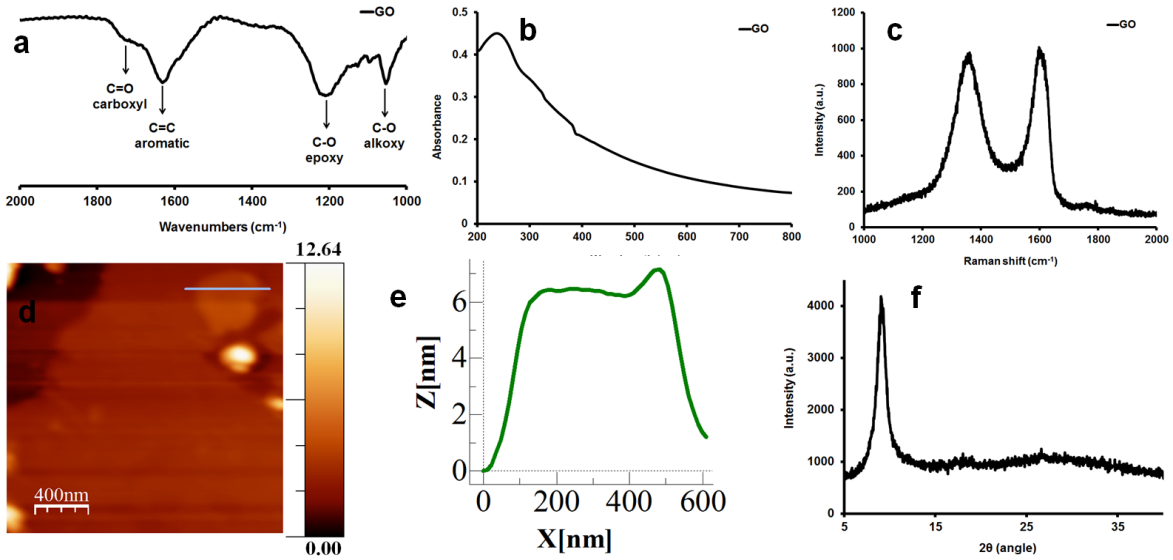

Figure 5b.1 (a-f) Analysis of GO by fourier transform infrared (FT-IR), UV-vis, raman spectroscopy, atomic force microscopy and powder XRD.

In the present work a simple strategy to self-assemble materials interconnected into aggregated networks that resulted in the development of water soluble, biocompatible nanocomposite probe for the exclusive detection of pyrophosphate (PPi) in physiological conditions and in *in vitro* live melanoma cancer cells (B16F10) is presented. This probe while performing PPi detection shows ~100% dequenching "turn-on" efficiency compared to ATP and other competing phosphates. The experiments confirm that the probe is selective towards PPi (~100%) and has negligible yet a partially positive response for ATP (~26%) but insignificant as compared to that of PPi. This difference in selectivity among PPi and ATP is also the highest for the detection difference of PPi over all other phosphates. The limit of detection (LOD) for PPi was calculated to be 0.60×10^{-7} M using the 3σ/k equation. Hence, the proposed PCG nanomaterial displays distinguishing and incredibly selective sensing ability for PPi over ATP with superior "turn-on" and limit of detection (LOD) of 0.58×10^{-6} M.[82] This is achieved by preparing an appropriate combination of GO with PDI-HIS instead of developing a new synthetic probe thereby avoiding the use of difficult synthetic and purification steps, yet achieving ~100 % "turn-on" selectivity for PPi via fluorescence responses which is very unique for GO based probes that rarely show dequenching properties. The dequenching sensing ability experiments for PPi were performed using PDI-HIS+Cu^{2+} complex without and with GO. The results confirm that the PDI-HIS fluorescence

reappears (~95 %) at 3.3 × 10^{-6} M of PPi concentration which is 10 times less efficient as compared with the PCG (LOD was 10.29 × 10^{-6} M). This difference of sensing for PPi using PDI-HIS+Cu^{2+} complex with GO may be due to the formation of homogeneous self-assembly process as compared to the PDI-HIS+Cu^{2+} complex without GO which forms an agglomeration. Therefore, to enhance the selectivity and sensitivity for PPi among other phosphates we utilized a unique fabrication strategy comprising amino acid (histidine) functionalized fluorescent probe with graphene oxide as discussed below to achieve unprecedented selectivity for PPi since it is a vital cancer biomarker.

5b.2.3. Quenching study of PDI-HIS with GO and Cu^{2+} ion

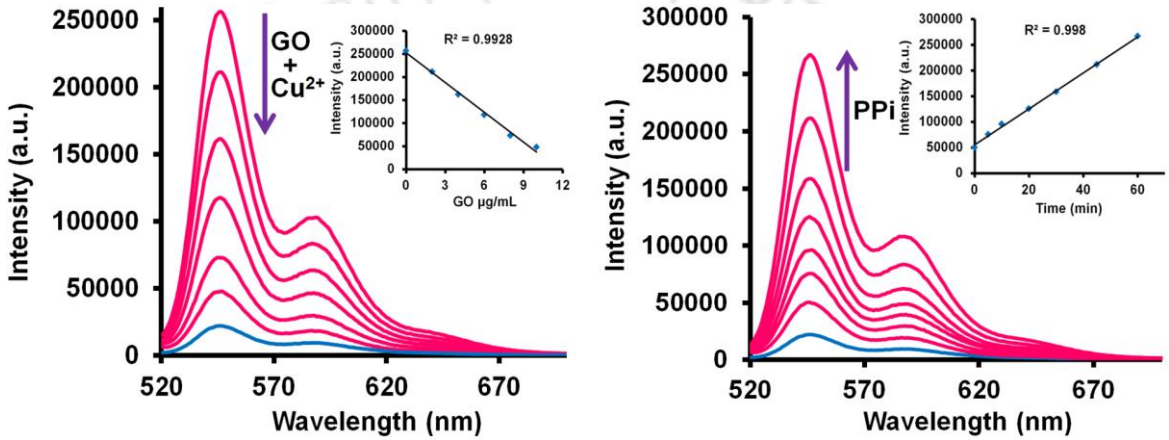

Figure 5b.2 (a) Emission spectra of PDI-HIS (0.33 µM) upon the stepwise addition of different amounts of GO (0-10 µg/mL) and single addition of 1.33 µM of Cu^{2+} (blue line) in HEPES buffer solution (10 mM, pH 7.4). Excitation wavelength: 508 nm. (b) Dequenching emission spectra of GO+PDI-HIS (0.33 µM) + Cu^{2+} (1.33 µM) upon the single addition of PPi (0.33 µM) at different time duration (0-60 min). Insets in (a) Linear response in the presence of GO for the fluorescence quenching of PDI-HIS. (b) Linear response in the presence of PPi for the fluorescence dequenching of PDI-HIS.

We evaluated the fluorescence quenching ability of GO with the histidine functionalized perylenediimide (PDI-HIS). Addition of 1-10 µg/mL GO into the highly fluorescent PDI-HIS, resulted in ~90% fluorescence quenching of PDI-HIS because of the strong π-π stacking between GO and PDI-HIS. This fluorescence quenching is assigned to the stacking of PDI-HIS over the surface of graphene sheet, where the photo-excited energy of the electron rich PDI-HIS is transferred from the PDI fluorophore to the GO acceptor.[60,77,81] Further, upon addition of 1.33 µM of Cu^{2+} into the PDI-HIS+GO solution, resulted in the complete fluorescence quenching of PDI-HIS due to the formation of PDI-HIS+Cu^{2+} complex on the surface of GO nano sheet. The quenching efficacy of PDI-HIS shows very good linear

response in the presence of GO (1-10 μg/mL) and was observed to be R^2 = 0.9928 (Figure 5b.2a). This optimized composition of PDI-HIS+Cu^{2+}+GO (PCG) was used as a platform for the selective detection of PPi in the present study.

5b.2.4. Selective and sensitive detection of PPi

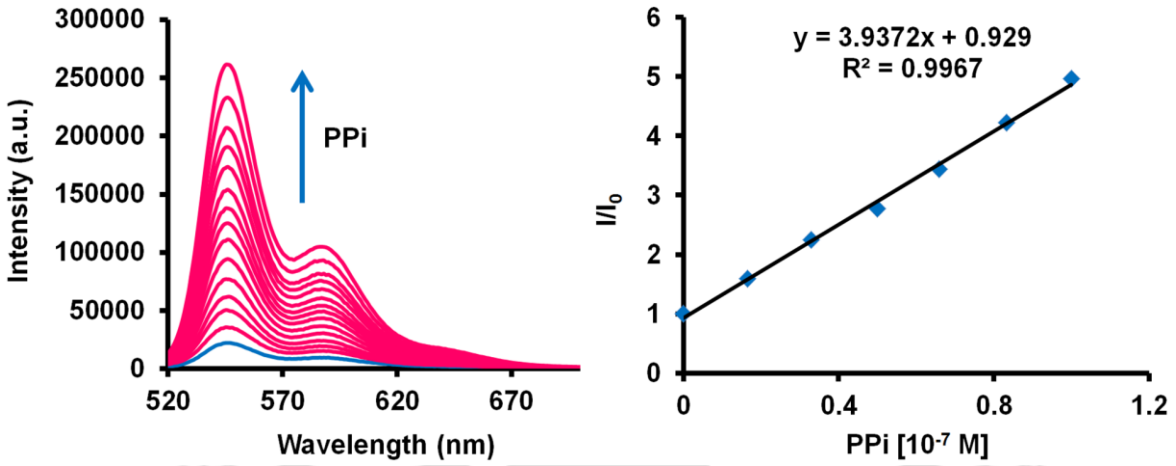

Figure 5b.3 (a) Dequenching emission spectra of GO+PDI-HIS (0.33 μM) + Cu^{2+} (1.33 μM) upon the addition of PPi (0-0.33 μM) in HEPES buffer (10 mM, pH 7.4). Excitation wavelength: 508 nm. (b) Linear response observed in the presence of PPi for the fluorescence dequenching of PDI-HIS.

In the presence of 0.33 μM concentration of PPi, the maximum fluorescence of PDI-HIS at 546 nm was recovered gradually with a complete recovery ratio of ~100% at time interval from 0-60 min. (Figure 5b.2b, the linear range of FL recovery is shown in Figure 5b.2b, R^2 = 0.998). We ascribe the "turn-on" response of the PCG nanocomposite to the specific interactions of PPi towards Cu^{2+} ions, which causes the complex to detach from the GO surface (weak π-π stacking). The release of the complex from the GO surface leads to the fluorescence recovery of the probe, since the fluorescence quenching of PDI-HIS by GO surface was now not possible. However, the complete fluorescence recovery of PDI-HIS indicates that PPi is very selective and sensitive to break the very strong π-π stacking of PCG. Therefore, it can be concluded that this fluorescence recovery is mainly due to the PDI-HIS desorption from GO nano sheet exclusively by PPi which demonstrates a powerful affinity for Cu^{2+} ions leading to the decomplexation of PDI-HIS+Cu^{2+} complex. Similarly, on performing the titration experiment at different concentrations of PPi with PCG nanocomposite, we confirmed that the fluorescence of PDI-HIS reappeared (Figure 5b.3). The limit of detection (LOD) for PPi was calculated to be 0.60 × 10^{-7} M using the 3σ/k equation.[82,89]

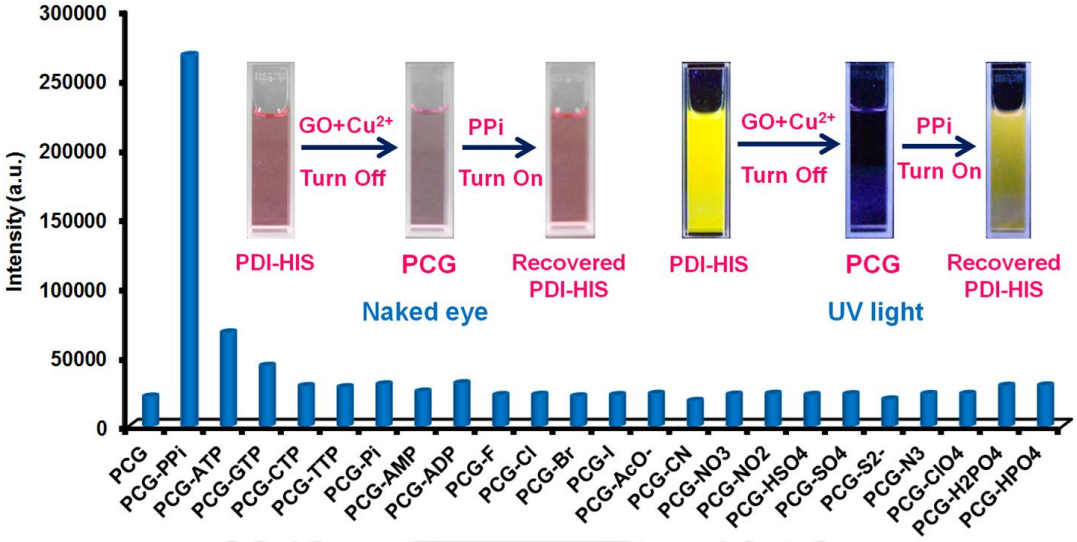

Figure 5b.4 Bar diagram of fluorescence changes observed in the fluorescence peak of PCG in presence of various anions like PPi, ATP, GTP, CTP, TTP, Pi, AMP, ADP, F^-, Cl^-, Br^-, I^-, CH_3COO^-, CN^-, NO_3^-, NO_2^-, HSO_4^-, SO_4^{2-}, S_2^-, N_3^-, ClO_4^-, $H_2PO_4^{2-}$, and HPO_4^{2-} (0.33 µM). Inset: Colorimetric study of PDI-HIS (10 µM) in the absence (pink color) and the presence (purple color) of Cu^{2+} (20 µM) with GO (10 µg/mL) and PDI-HIS+GO+Cu^{2+} with PPi (pink color) (under naked eye). Colorimetric study of PDI-HIS (10 µM) in the absence (yellowish orange color) and the presence (nonfluorescent purple color) of Cu^{2+} (20 µM) with GO (10 µg/mL) and PCG with PPi (yellowish orange color) (UV-lamp at 254 nm).

To evaluate the selectivity of PCG towards PPi, we carried out the fluorescence titration with other anions including F^-, Cl^-, Br^-, I^-, $CH_3CO_2^-$, CN^-, HPO_4^{2-}, NO_3^-, NO_2^-, SO_4^{2-}, S_2^-, HSO_4^-, Pi, AMP, ADP, ATP, GTP, CTP and TTP under identical conditions. Figure 5b.4 confirms that the probe is most selective towards PPi (>99 %) and has negligible yet a partially positive response for ATP (~26 %) but insignificant as compared to that of PPi. This difference in selectivity for PPi over ATP is highest for any existing probe and represents the example of "turn-on" detection of PPi (or any anions) using GO nanocomposites. In addition to the fluorometric detection of PPi, it was also possible to visualize the color changes of PDI-HIS in presence of GO, Cu^{2+} and PPi via naked eye observation and under a hand held UV lamp illumination. In presence of GO and Cu^{2+}, the pink color of PDI-HIS (yellow color under UV-lamp illumination at 254 nm) disappeared. However, the original color of PDI-HIS is regained in the presence of PPi (Inset figure 5b.4). The effect of dequenching on PCG observed with other anions and likely competing phosphates such as Pi, ADP, AMP, GTP, CTP, and TTP were insignificant and calculated to be <10 %. (Figure A5b.1 and A5b.2). For the control studies, we performed the dequenching sensing ability experiment by PPi without

GO (only with PDI-HIS+Cu^{2+} complex). The results confirm that the PDI-HIS fluorescence reappears (~95 %) at a PPi concentration of 3.3×10^{-6} M (10 times less efficient than PCG) and the LOD was found to be 10.29×10^{-6} M (Figure 5b.5).[82,89] Finally, the apparent binding constant was evaluated using Benesi−Hildebrand (B−H) plot by observing the fluorescence spectral changes at 546 nm for the "turn-on" detection of PPi with PDI-HIS-Cu^{2+} complex and PCG complex which are estimated to be 2.85×10^{5} M^{-1} and 1.0×10^{6} M^{-1} respectively (Figure A5b.3). These results confirm that PCG nanocomposite detects PPi with a very low LOD of 0.60×10^{-7} M and is more selective and efficient as compared to PDI-HIS-Cu^{2+} signifying the vital role of GO for the selectivity for PPi.

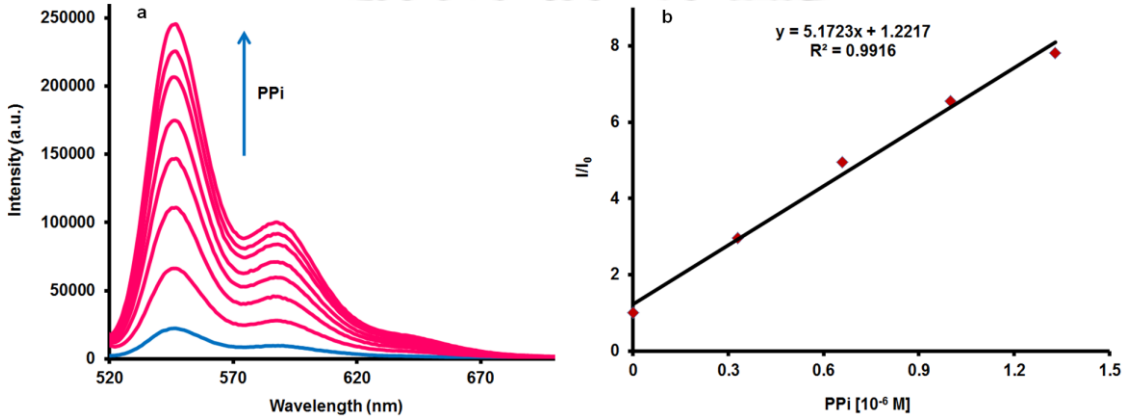

Figure 5b.5 (a) Dequenching emission spectra of PDI-HIS (0.33 µM) + Cu^{2+} (1.33 µM) upon the addition of PPi (0-3.3 µM) in HEPES buffer (10 mM, pH 7.4). Excitation wavelength: 508 nm. (b) Linear response observed in the presence of PPi for the fluorescence dequenching of PDI-HIS.

5b.2.5. UV-Visible studies of PDI-HIS

The self-assembly of the resultant PCG and its disassembly was examined and carefully studied from the absorption spectra. Figure 5b.6a, illustrates that the PDI-HIS (2.5 µM) has two absorbance maximum peaks at 535 and 504 nm in HEPES buffer (10 mM, pH 7.4) solution. Further, the absorbance peaks of PDI-HIS were enhanced at 534 and 502 nm after the addition of GO (10 µg/mL) due to the interactions of π electrons. On addition of Cu^{2+} solution into the PDI-HIS+GO mixtures the absorption band of PDI-HIS decreases with red shifted band at 508 nm and a new broad shoulder appeared at ~554 nm, indicating the formation of PCG nano aggregates. The PCG nano aggregates were disassembled on addition of PPi anions as seen from the changes in the absorption spectra (Figure 5b.6a). Further, we performed the concentration dependent UV-Visible study to understand the formation of nanoaggregates (PCG) and its disaggregation. Figure 5b.6b, shows that the absorption spectra

for GO (10 µg/mL) mixed PDI-HIS (1.5 µM) gives two enhanced absorbance bands at 533 and 502 nm in HEPES buffer (10 mM, pH 7.4) solution. On addition of Cu^{2+} solution up to 0-2 equivalents (0-3 µM), the absorption bands of PDI-HIS decreased with a red shifted to 508 nm and a new broad shoulder appeared at ~554 nm due to the formation of π–π stacking among perylene moieties over the GO and extended to the oligomer formations into the PCG nanoaggregates (Figure 5b.6b).[90-93] The PCG nanoaggregates became disassembled upon gradual addition of PPi anions and induces the reappearance of absorbance bands at 533 and 502 nm (Figure 5b.6c). This result indicates that formation of PDI-HIS monomer molecules leads to the enhancement of 533 nm absorption bands. It is clearly evident that on gradual addition of PPi (25eq.) (Figure 5b.6c), the shoulder at 554 nm absorption bands associated with the PCG nanoaggregates disappear and the ~533 nm and 502 nm peaks regained gradually due to the formation of free PDI-HIS molecules by metal chelation method which is depicted in a proposed mechanism (Scheme 5b.1).

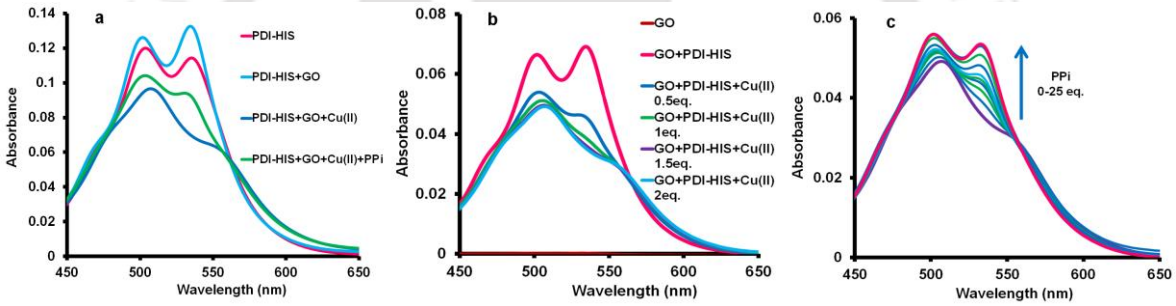

Figure 5b.6 (a) Absorption spectra of PDI-HIS, PCG aggregates and PCG with PPi anions in HEPES buffer solution (10 mM, pH 7.4). (b) Absorption spectra of PDI-HIS (1.5 µM) was red shifted due to the aggregation upon the addition of GO (10 µg/mL) with Cu^{2+} (3 µM) in HEPES buffer solution (10 mM, pH 7.4). (c) Absorption spectra for GO (10 µg/mL) mixed PDI-HIS (1.5 µM) with Cu^{2+} (3 µM) aggregated composites was disaggregated after the gradual addition of PPi (25 equiv.) in HEPES buffer solution (10 mM, pH 7.4).

5b.2.6. Dynamic light scattering studies of PDI-HIS

The higher order nano assembly of the resultant PCG and its disassembly was examined by dynamic light scattering (DLS) technique. Prior to metal complexation, the PDI-HIS solution (in HEPES buffer at pH 7.4) had a hydrodynamic diameter of 255 ± 40 nm (indicating single molecules) at an concentration of 0.33 µM (Figure 5b.7). The hydrodynamic diameter of PDI-HIS with GO is observed to be in the range of 400 to 615 nm. However, upon metal complexation the hydrodynamic diameter decreases significantly to 75 ± 5 nm for GO+PDI-HIS with 1.33 µM Cu^{2+} due to the complex formation of PDI-HIS+Cu^{2+} on the surface of

GO. The hydrodynamic particles diameter of the PCG nanocomposite complex was observed to be very less as compared to the formation of PDI-HIS+Cu^{2+} complex (110-160 nm) (Figure 5b.7). After the addition of PPi into this PCG nanocomposite, the PPi having strong affinity towards cupric ion induces the decomplexation. Hence, the PDI-HIS is detached from the surface of GO and the hydrodynamic particles diameter were large and in the range from 220 ± 30 nm. As a result, the analysis of the distribution of particle sizes confirms that relatively well-defined aggregates are formed during the nano self-assembly process in the presence of copper and the GO flakes.

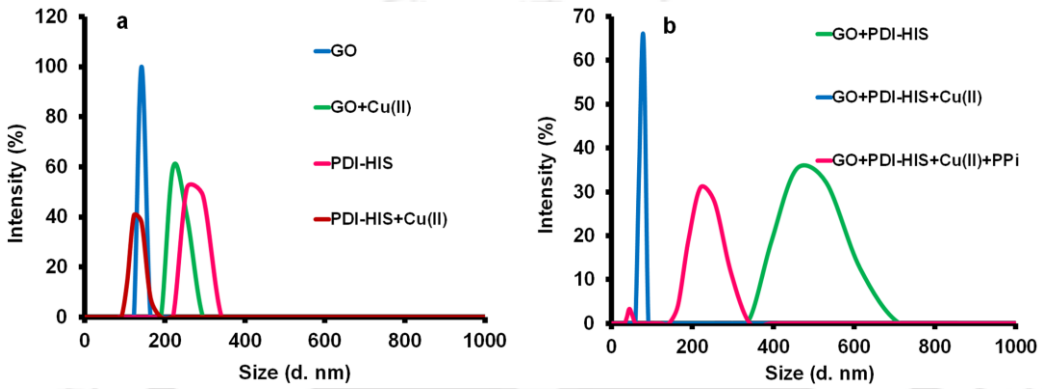

Figure 5b.7 (a) Particle size analysis of GO, GO+Cu^{2+}, PDI-HIS and PDI-HIS+Cu^{2+} in HEPES buffer at pH 7.4 by DLS. (b) Particle size analysis of GO+PDI-HIS, GO+PDI-HIS+Cu^{2+} and GO+PDI-HIS+Cu^{2+}+PPi in HEPES buffer at pH 7.4 by DLS.

Proposed mechanism for PCG nanoaggregates and disaggregation

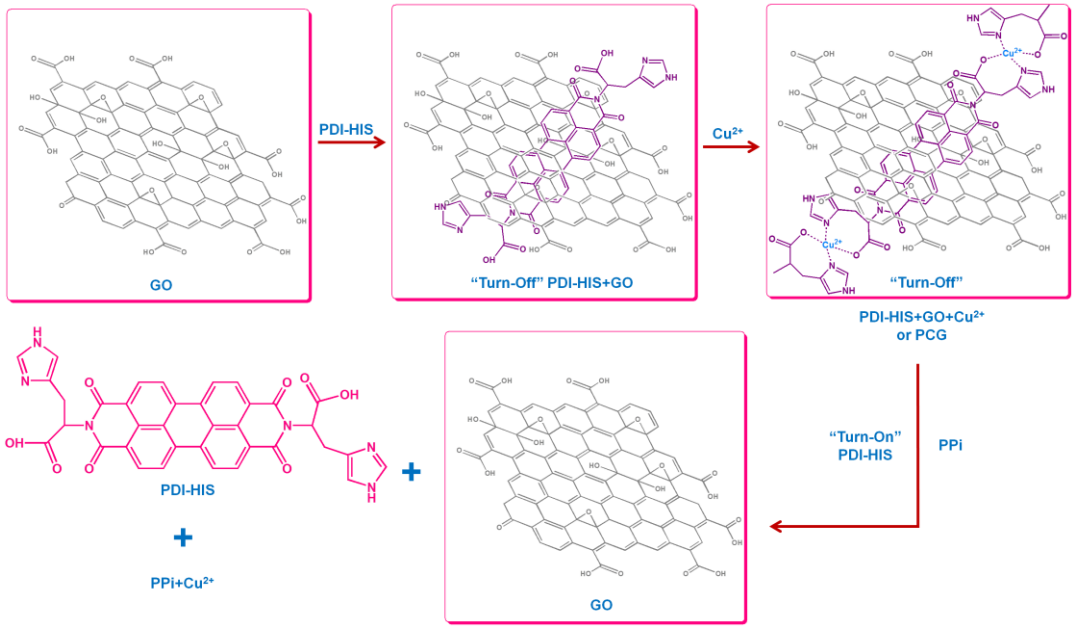

Scheme 5b.1 Proposed mechanism for the formation of PCG nanoaggregates from the mixture of PDI-HIS, GO and Cu^{2+} and disaggregation of PCG with PPi.

5b.2.7. AFM morphology study of PDI-HIS+Cu^{2+} with GO and PPi

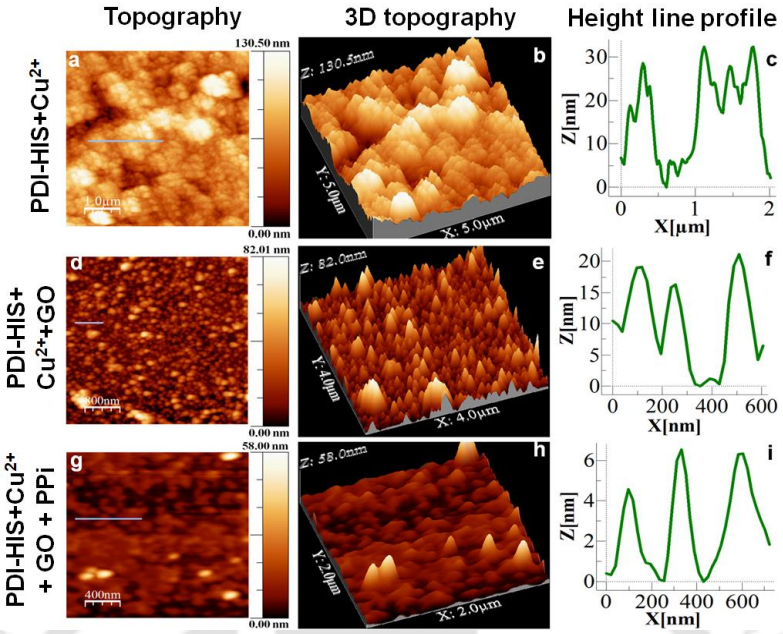

Figure 5b.8 (a, d, g) AFM topography images of PDI-HIS+Cu^{2+} (agglomerated complex), PCG (aggregated nanocomposite) and PCG+PPi (disaggregated complex). (b, e, h) AFM 3D topography images of PDI-HIS+Cu^{2+} (agglomerated complex), PCG (aggregated nanocomposite) and PDI-PCG+PPi (disaggregated complex). (c, f, i) AFM height line profiles of PDI-HIS+Cu^{2+} (agglomerated complex), PCG (aggregated nanocomposite) and PCG+PPi (disaggregated complex). (X = Distance and Z = Height).

As depicted in the AFM images, the morphological changes in the structural pattern of PDI-HIS differs from the in situ formed PDI-HIS+Cu^{2+} derivatives, indicating a Cu^{2+} induced agglomeration and homogenization of PDI-HIS (Figure 5b.8). The presence of Cu^{2+} ions gives the particles their spherical shape, but the average size of the particles increased (Figure 5b.8 (a-c)), as a result of the Cu^{2+}-induced agglomeration of PDI-HIS. When the same study was performed using GO as a quencher in the presence of Cu^{2+} and PDI-HIS, a homogeneous metal organic nano sphere is formed by ordered or randomly packed self-assembly process depending on the size dispersity and size ratios (Figure 5b.8 (d-f)). In figure 5b.8 (d-f), the self-assembled PCG was found to be the size of 75 ± 5 nm diameters and 15 ± 5 nm heights. The PPi mixed PCG complex image (Figure 5b.8 (g)) shows that the PPi induced the decomplexation or disaggregation of PCG due to the disruption of π-π stacking as well as the likely detachment of PDI-HIS from the surface of GO with a height profile found to be 4-8 nm (Figure 5b.8 (h-i)). Further, we have confirmed that the morphology of GO+PDI-

HIS samples showed no aggregation in the absence of Cu^{2+} ion and the average size of the particle diameter was found to be 900 ± 100 nm and 5 ± 1 nm height (Figure 5b.9 (a-c)). These morphological structural differences of PDI-HIS+Cu^{2+} complex formation in the absence and presence of GO, may be the reason to sense selectively PPi ions which shows Cu^{2+} induced homogeneous metal organic nano sphere by ordered self-assembly in presence of GO (Figure 5b.8 (d)). Hence, AFM images strongly support the fluorescence study results on the formation of self-assembled PDI-HIS+Cu^{2+} complex over the GO nano sheets which are decomplexed or disaggregated exclusively by PPi.

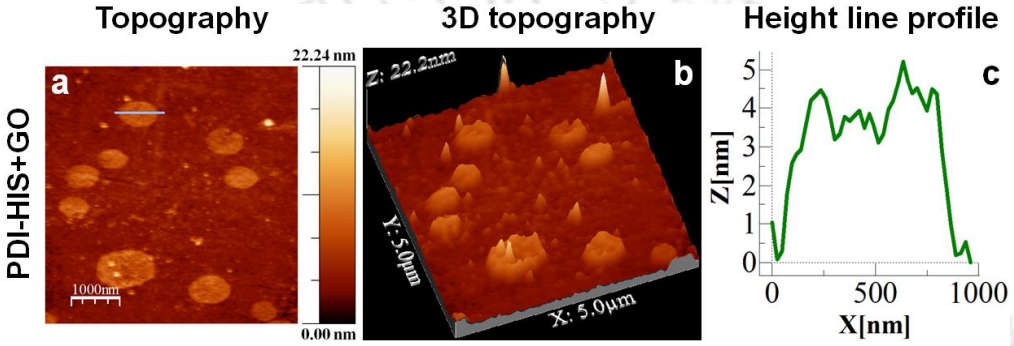

Figure 5b.9 (a) AFM topography images of GO+PDI-HIS. (b) AFM 3D topography images of GO+PDI-HIS. (c) AFM height line profiles of GO+PDI-HIS. (X = Distance and Z = Height).

5b.2.8. Cell viability assay

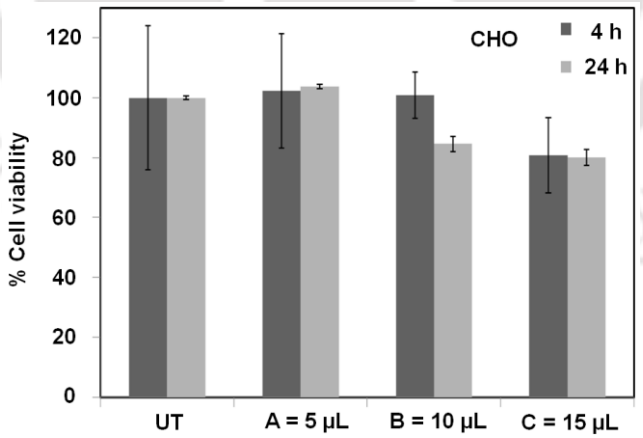

Figure 5b.10 Cell viability assay for PDI-HIS-GO+Cu^{2+} (PCG). A = 5µL is mixture of PDI-HIS (75 µg/mL) and Cu^{2+} (0.25 mM) in 10 mg/mL of GO. B = 10 µL is mixture of PDI-HIS (150 µg/mL) and Cu^{2+} (0.5 mM) in 10 mg/mL of GO. C = 15 µL is mixture of PDI-HIS (225 µg/mL) and Cu^{2+} (0.75 mM) in 10 mg/mL of GO.

Cell viability assay study performed for PDI-HIS-GO-Cu^{2+} (PCG) hybrid composites at various doses for 4 and 24 h exhibited negligible cytotoxicity for PCG hybrid composites (Figure 5b.10). Thus, PCG is biocompatible and can be used for biosensing PPi without any toxic side effects.

5b.2.9. Detection of PPi in living cells

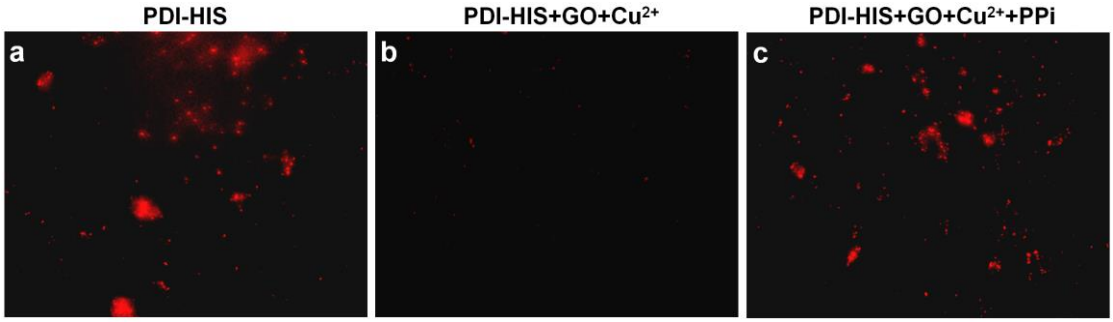

Figure 5b.11 (a) The fluorescence image of PDI-HIS observed where PDI-HIS (300 µg/mL) incubated with B16F10 cells for 24 h. (b) "Turn-off" fluorescence images observed for PCG where PDI-HIS further incubated with GO and 1 mM Cu^{2+} for 2 h. (c) "Turn-on" fluorescence images observed for PDI-HIS where PCG complex further incubated with 2 mM PPi for 45 min. Excitation wavelength range λ_{ex} = 510-560 nm (green) and λ_{em} = 605 nm (red). 20X magnification.

We further investigated the detection of PPi in B16F10 cells using PCG composites. The B16F10 cells were seeded in each of the 24 well plates and incubated at 37 °C overnight in a CO_2 incubator prior to cell imaging studies.[94,95] After 24 h, B16F10 cells were treated with 300 µg/mL of PDI-HIS and allowed to incubate overnight to observe the images (Figure 5b.11 and A5b.4). Fluorescence images of B16F10 cells treated with 300 µg/mL of PDI-HIS give bright red fluorescence on excitation which gets quenched upon incubation with GO+Cu^{2+} (1 mM) and Cu^{2+} (1 mM) (Figure 5b.11 and A5b.4, 5b.12 and A5b.5). The "turn-on" red fluorescence signals from the B16F10 cells reappeared upon the treatment of PPi (20 mM) in case of Cu^{2+} (1 mM) treated cells but in the case of GO+Cu^{2+} (1 mM) treated cells, only 2 mM PPi (10 times less than absence of GO) was enough to generate the red fluorescence. The fluorescence reappeared in the B16F10 cells due to the disaggregation and detachment of PDI-HIS-Cu^{2+} complex from GO flakes by PPi. This result confirms that the PCG was able to detect intracellular level PPi, with much higher sensitivity than only the PDI-HIS+Cu^{2+} complex by fluorescence "turn-on" mechanism due to the disaggregation and detachment of PDI-HIS-Cu complex. This is an exceptional study of intracellular

PPi detection using GO nanocomposites by "turn-on" fluorescence in the orange-red spectral region without interference of other competing phosphates, especially ATP.

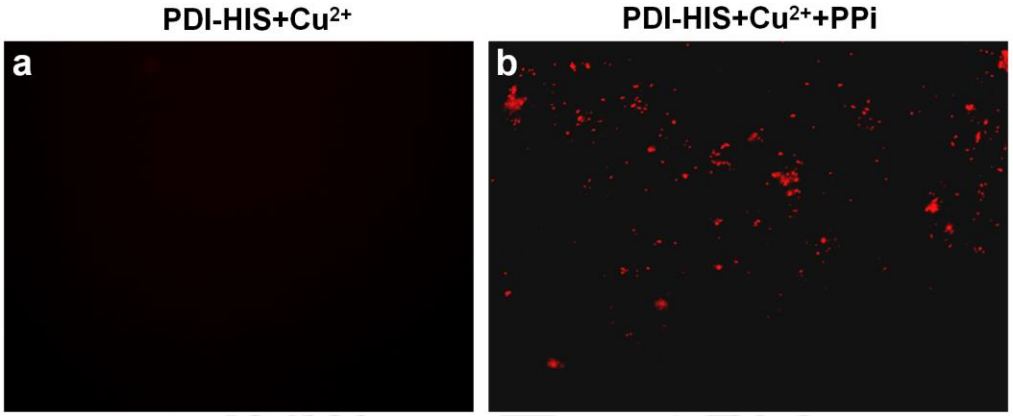

Figure 5b.12 (a) "Turn-off" fluorescence images observed for PDI-HIS+Cu^{2+} complex where B16F10 cells incubated with PDI-HIS (300 µg/mL) and 1 mM Cu^{2+} for 2 h. (b) "Turn-on" fluorescence images observed for PDI-HIS where PDI-HIS+Cu^{2+} complex further incubated with 20 mM PPi for 45 min. Excitation wavelength range λ_{ex} = 510-560 nm (green) and λ_{em} = 605 nm (red). 20X magnification.

5b.2.10. TLC and membrane based platforms for PPi detection

To realize practical applications with this PCG nanocomposite, we performed an experiment, where the PCG was loaded onto silica TLC plates to demonstrate the sensing of PPi anions on solid platform. The silica TLC plates show a distinct response to PPi anions when compared to other phosphate anions like AMP, ADP, ATP, GTP, CTP, TTP, $H_2PO_4^{2-}$, HPO_4^{2-}, PO_4^{3-} and PPi (25 equiv.). The fluorescence (color) of PDI-HIS (10 µM) on silica TLC plates changed from pink to nonfluorescent (Figure 5b.13) in presence of GO (10 µg/mL) with copper (2 equiv.) by turn "on−off" response. Further, when the nonfluorescent PCG materials were loaded on silica TLC plates it changed from nonfluorescent to pink in the presence of PPi by turn "off−on" response. Additionally, we prepared hydrogel films of desired shape and size comprising the mixtures of PVA [poly (vinyl alcohol)] and PCG to study the sensing of PPi anions. As shown in figure 5b.13, the bright yellowish orange fluorescence color was observed for PDI-HIS+PVA hydrogels that changes from bright orange to nonfluorescent in presence of GO and Cu^{2+} ions. The nonfluorescent hydrogels of PCG+PVA showed up as bright yellowish orange fluorescent color in the presence of PPi by turn "off−on" response. These results confirmed that PCG has excellent light transmittance properties even in the form of a highly flexible hydrogel films (PDI-HIS+PVA), which has potential to be used as a portable material to sense PPi anions.

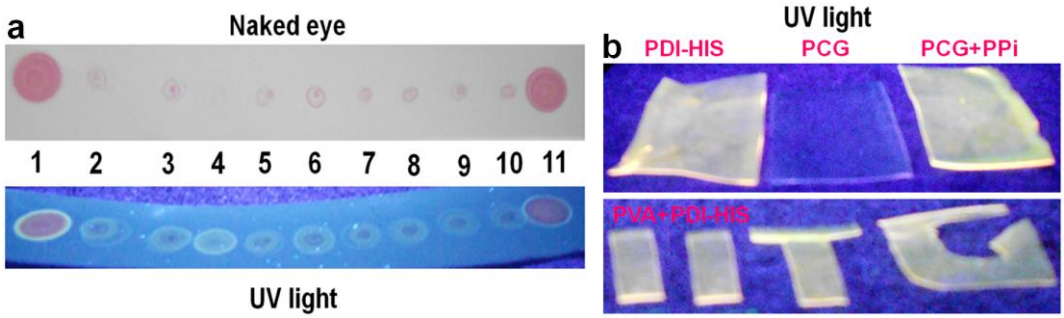

Figure 5b.13 (a) Fluorescence color changes observed for PDI-HIS (pink color) and PCG (purple or colorless) in the absence and presence of various phosphate anions on silica TLC plates observed by naked eye and UV Light at 254 nm. From left to right: 1: PDI-HIS, 2: PCG + AMP, 3: PCG + ADP, 4: PCG + ATP, 5: PCG + GTP, 6: PCG + CTP, 7: PCG + TTP, 8: PCG + $H_2PO_4^-$, 9: PCG + HPO_4^{2-}, 10: PCG + PO_4^{3-}, and 11: PCG + PPi. (b) The yellowish orange fluorescence color was observed for PDI-HIS+PVA hydrogel films (UV Light at 254 nm). A nonfluoresent hydrogel film was observed for PCG+PVA and the fluorescence color reappeared for PCG+PVA hydrogel film in presence of PPi anions (UV Light at 254 nm).

5b.3. Conclusion

In summary, we have developed an amino acid based PDI-HIS-Cu-GO nanocomposite probe for the fluorescence "turn-on" detection of PPi *in vitro* and in B16F10 cells. This nanocomposite platform shows remarkable sensitivity in *in vitro* conditions with a limit of detection of 0.60×10^{-7} M and can be used as a biomarker for early cancer diagnosis via PPi detection. The probe was found to be remarkably selective for PPi among all other biologically important phosphates including the highly interfering ATP, producing a fluorogenic "turn-on" signal response of ~100% thereby eliminating false and erroneous signals that are usually associated with assays operating on the fluorescence "turn-off" principle. This study sets the basis for the development of a new generation of probes for the detection of important markers for critical diseases such as cancer by using simple and economic graphene oxide composite materials and readily available biomolecules such as amino acids appended to signal amplifying molecules thereby avoiding tedious synthetic steps for the detection of specific biological analytes that have highly competing and similar molecules in the same environment. Moreover, this PDI-HIS-Cu-GO composite sensor represents a promising sensing strategy for the detection of the biologically important phosphates and "turn-on" fluorescence response with a good linear relationship towards PPi. In a broader context, this water-soluble platform can be directly used to monitor and detect

cancer and its progression via low level competitive detection of PPi. Furthermore, the fabrication of PDI-HIS and PCG with PVA hydrogel films and on TLC plates demonstrated the practical applications to detect PPi anions by "off-on" response on a solid platform.

5b.4. Experimental Section

5b.4.1. Materials and methods

All reagents and spectroscopic grade solvents were purchased from commercial sources and used as received. UV-vis absorption spectra were recorded on a PerkinElmer Lambda-25 spectrometer. Fluorescence spectra were recorded on a FluoroMax-4 Spectrofluorometer-Horiba Scientific. A 10 × 10 mm quartz cuvette was used for solution spectra and emission was collected at 90° relative to the excitation beam. Deionized water was obtained from Milli-Q system (Millipore). FT-IR was recorded on a PerkinElmer spectrometer with samples prepared as KBr pellets. Atomic force microscopy images were taken by on an Agilent 5500-STM instrument. DLS were measured by Zetasizer Nano series Nano-ZS90 instrument.

5b.4.2. Preparation of stock solutions

The PDI-HIS stock solution was prepared at a concentration of 1.0×10^{-3} mL^{-1} in 10 mL H_2O at pH 7-9. This stock solution was diluted to desired concentration for each titration in a 3 mL cuvette with HEPES buffer at pH 7.4.

5b.4.3. Preparation of cation and anion stock solutions

Each salt of anions stock solutions were prepared at the concentration of 10.0×10^{-3} mL^{-1} in 5 mL Milli-Q water. The stock solutions were diluted to the desired concentrations with Milli-Q water when needed.

5b.4.4. PPi detection on silica TLC plates

To demonstrate practical applications with the probe, we used silica TLC plates to show distinct responses of PPi anions as compared to other phosphate anions like AMP, ADP, ATP, GTP, CTP, TTP, $H_2PO_4^{2-}$, HPO_4^{2-}, PO_4^{3-} and PPi (25 equiv.). The fluorescence color of PDI-HIS (10 μM) on silica gel TLC plate changed from pink to nonfluorescent in presence of GO (10 μg/mL) and with copper (2 equiv.) by turn "on−off" response. Further, the nonfluorescent PCG loaded on silica gel TLC plates changed from nonfluorescent to pink in the presence of PPi by turn "off−on" response.

5b.4.5. Preparation of hydrogel films for PPi detection

2 g PVA [poly (vinyl alcohol)] was dissolved in Milli Q water (20 mL) and stirred at 95 °C until the PVA completely dissolved. Then, the solution of PDI-HIS (10 μM) was slowly

added to the PVA solution and stirred for complete mixing. After uniform mixing the mixture of solution was loaded onto a glass sheet and dried overnight. Similarly the hydrogels of PCG + PVA were formed in absence and the presence of PPi (25 equiv.) with the mixture of PDI-HIS (10 μM), GO (10 μg/mL) and copper (20 μM). After uniform mixing the mixture of hydrogels were loaded onto a glass sheet and dried overnight. Then the photographs were taken at 254 nm under UV lamp illumination for all the dried hydrogel films.

5b.4.6. Cell viability using MTT assay

Cell viability of CHO cells treated with different volumes of PDI-HIS-GO-Cu^{2+} (PCG) composites for 4 h and 24 h was carried out using MTT reagents according to standard protocol. Results were expressed as percent cell viability = {[A570 (treated cells) - background]/ [A570 (untreated cells) - background]} × 100. Cell viability assay study performed for PDI-HIS-GO-Cu^{2+} (PCG) hybrid at various doses for 4 and 24 h exhibited negligible cytotoxicity for PCG composites upto 24 h. Thus, PDI-HIS-GO-Cu^{2+} hybrid can be used for the biosensor for PPi without any toxic side effects.

5b.4.7. Cell culture experiments

2×10^4 numbers of melanoma cancer (B16F10) cells were seeded in each of the 24 well plates and incubated overnight at 37 °C in a CO_2 incubator before cell imaging experiments. After 24 h B16F10 cells were treated with 300 μg/mL of PDI-HIS and incubated overnight. Cells were washed with phosphate buffer saline (PBS, 4-5 times) and fluorescence images were taken by fluorescence microscopy (Nikon Eclipse TE2000-E). The red fluorescence images were observed with a 20X microscope objective with excitation wavelength range λ_{ex} = 510-560 nm (green) and λ_{em} = 605 nm (red). B16F10 cells were then treated with 10^{-3} M (1 mM) of Cu^{2+} for 3 h and GO+Cu^{2+} for 2 h, where concentration of Cu^{2+} is 1 mM. Here, we prepared 10 mg/mL of GO dispersion in tris-EDTA buffer (TE) and sonicated for 2 h in a bath sonicator. Then it was centrifuged at 5000 rpm for 10 mins at 10 °C and 50 μL of GO supernatant were used with 1 mM of Cu^{2+} for further study. After extensive washing with PBS (4-5 times), the fluorescence images of cells were taken in HBSS buffer (pH=7.4) using red filter for detection of copper ions. Furthermore, the PDI-HIS and copper treated B16F10 cells with or without GO were treated with 2 and 20 mM of PPi respectively and incubated for 45 min. After that the reenhancement of fluorescence signals were observed from B16F10 cells under same excitation and emission filter (red).

References

(1) Hargrove, A. E.; Nieto, S.; Zhang, T.; Sessler, J. L.; Anslyn, E. V. *Chem. Rev.* **2011**, *111*, 6603.

(2) Rurack, K.; Resch-Genger, U. *Chem. Soc. Rev.*, **2002**, *31*, 116.

(3) Beer, P. D.; Gale, P. A. *Angew. Chem., Int. Ed.* **2001**, *40*, 486.

(4) Martínez-Máñez, R.; Sancenón, F. *Chem. Rev.* **2003**, *103*, 4419.

(5) Hirose, M.; Abe-Hashimoto, J.; Ogura, K.; Tahara, H.; Ide, T.; Yoshimura, T. J. *Cancer Res. Clin. Oncol.* **1997**, *123*, 337.

(6) Ronaghi, M.; Uhlén, M.; Nyrén, P. *Science* **1998**, *281*, 363.

(7) Kim, J.-H.; Ahn, J.-H.; Barone, P. W.; Jin, H.; Zhang, J.; Heller, D. A.; Strano, M. S. *Angew. Chem., Int. Ed.* **2010**, *49*, 1456.

(8) Bhowmik, S.; Ghosh, B. N.; Marjomäki, V.; Rissanen, K. *J. Am. Chem. Soc*. **2014**, *136*, 5543.

(9) Farre, E. M.; Geigenberger, P.; Willmitzer, L.; Trethewey, R. N. *Plant Physiol.* **2000**, *123*, 681.

(10) Steinberg, K. M.; Okou, D. T.; Zwick, M. E. *Anal. Chem*. **2008**, *80*, 520.

(11) Heinonen, J. K. Biological role of inorganic pyrophosphate, Kluwer Academic Publishers, Norwell, **2001**.

(12) Wright, G. D. Doherty, M. *Ann. Rheum. Dis*. **1997**, *56*, 586.

(13) Tsui. F. W. L. *Curr. Rheumatol. Rep*. **2012**, *14*, 155.

(14) Zapata, F.; Caballero, A.; Espinosa, A.; Tárraga, A.; Molina, P. *J. Org. Chem*. **2008**, *73*, 4034.

(15) Zhu, W.; Huang, X.; Guo, Z.; Wu, X.; Yu, H.; Tian, H. *Chem. Commun.*, **2012**, *48*, 1784.

(16) Liu, X.; Ngo, H. T.; Ge, Z.; Butler, S. J.; Jolliffe, K. A. *Chem. Sci*. **2013**, *4*, 1680.

(17) Su, X.; Zhang, C.; Xiao, X.; Xu, A.; Xu, Z.; Zhao, M. *Chem. Commun.*, **2013**, *49*, 798.

(18) Lee, S.; Yuen, K. K. Y.; Jolliffe, K. A.; Yoon, J. *Chem. Soc. Rev.*, **2015**, *44*, 1749.

(19) Butler, S. J.; Jolliffe, K. A. *Chem. Asian J*. **2012,** *7*, 2621.

(20) Huang, X.; Guo, Z.; Zhu, W.; Xie, Y.; Tian, H. *Chem. Commun.*, **2008**, 5143.

(21) Feng, X.; An, Y.; Yao, Z.; Li, C.; Shi, G. *ACS Appl. Mater. Interfaces* **2012**, *4*, 614.

(22) Jiao, S.-Y.; Li, K.; Wang, X.; Huang, Z.; Pu, L.; Yu, X.-Q. *Analyst* **2015**, *140*, 174.

(23) Wang, J.; Liu, X.; Pang, Y. *J. Mater. Chem. B* **2014**, *2*, 6634.

(24) Sokkalingam, P.; Kim, D. S.; Hwang, H.; Sessler, J. L.; Lee, C.-H. *Chem. Sci*. **2012**, *3*, 1819.

(25) Chen, W.-H.; Xing, Y.; Pang, Y. *Org. Lett.* **2011**, *13*, 1362.

(26) Yu, C-J.; Wu, S.-M.; Tseng, W.-L. *Anal. Chem*. **2013**, *85*, 8559.

(27) Shao, N.; Wang, H.; Gao, X.; Yang, R.; Chan, W. *Anal. Chem.* **2010**, *82*, 4628.

(28) Hai, Z.; Bao, Y.; Miao, Q.; Yi, X.; Liang, G. *Anal. Chem.* **2015**, *87*, 2678.

(29) Das, P.; Bhattacharya, S.; Mishra, S.; Das, A. *Chem. Commun.*, **2011**, *47*, 8118.

(30) Zhang, J. F.; Park, M.; Ren, W. X.; Kim, Y.; Kim, S. J.; Jung, J. H.; Kim, J. S. *Chem. Commun.*, **2011**, *47*, 3568.

(31) Su, G.; Liu, Z.; Xie, Z.; Qian, F.; He, W.; Guo, Z. *Dalton Trans*. **2009**, 7888.

(32) Wen, J.; Geng, Z.; Yin, Y.; Zhang, Z.; Wang, Z. *Dalton Trans*. **2011**, *40*, 1984.

(33) Zhu, X.; Yang, J.; Schanze, K. S. *Photochem. Photobiol. Sci.* **2014**, *13*, 293.

(34) Pathak, R. K.; Tabbasum, K.; Rai, A.; Panda, D.; Rao, C. P. *Anal. Chem*. **2012**, *84*, 5117.

(35) Shin, I.-S.; Bae, S. W.; Kim, H.; Hong, J.-I. *Anal. Chem*. **2010**, *82*, 8259.

(36) Fabbrizzi, L.; Marcotte, N.; Stomeo, F. Taglietti, A. *Angew. Chem., Int. Ed*. **2002**, *41*, 3811.

(37) McDonough, M. J.; Reynolds, A. J.; Lee, W. Y. G.; Jolliffe, K. A. *Chem. Commun.*, **2006**, 2971.

(38) Zhao, X.; Liu, Y.; Schanze, K. S. *Chem. Commun.*, **2007**, 2914.

(39) Mizukami, S.; Nagano, T.; Urano, Y.; Odani, A.; Kikuchi, T. *J. Am. Chem. Soc.* **2002**, *124*, 3920.

(40) Lee, D. H.; Kim, S. Y.; Hong, J.-I. *Angew. Chem., Int. Ed.* **2004**, *43*, 4777.

(41) Kim, M. J.; Swamy, K. M. K.; Lee, K. M.; Jagdale, A. R.; Kim, Y.; Kim, S.-J.; Yoo, K. H.; Yoon, J. *Chem. Commun.*, **2009**, 7215.

(42) Pankhurst, Q. A.; Connolly, J.; Jones, S.; Dobson, J. *J. Phys. D: Appl. Phys.* **2003**, *36*, R167.

(43) Alivisatos, P. *Nat. Biotechnol*. **2004**, *22*, 47.

(44) Giljohann, D. A.; Mirkin, C. A. *Nature* **2009**, *462*, 461.

(45) Jin, R.; Cao, Y. C.; Hao, E.; Métraux, G. S.; Schatz, G. C.; Mirkin, C. A. *Nature* **2003**, *425*, 487.

(46) Liu, M.; Amro, N. A.; Chow, C. S.; Liu, G. *Nano Lett.* **2002**, *2*, 863.

(47) Novoselov, K. S.; Geim, A. K.; Morozov, S. V.; Jiang, D.; Zhang, Y.; Dubonos, S. V.; Grigorieva, I. V.; Firsov, A. A. *Science* **2004**, *306*, 666.

(48) Allen, M. J.; Tung, V. C.; Kaner, R. B. *Chem. Rev.* **2010**, *110*, 132.

(49) Geim, A. K. *Science* **2009**, *324*, 1530.

(50) Liu, X.; Aizen, R.; Freeman, R.; Yehezkeli, O.; Willner, I.; *ACS Nano* **2012**, *6*, 3553.

(51) Liu, B.; Sun, Z.; Zhang, X.; Liu, J. *Anal. Chem.* **2013**, *85*, 7987.

(52) Huang, P.-J. J.; Liu, J. *Anal. Chem*. **2012**, *84*, 4192.

(53) Chen, D.; Feng, H.; Li, J. *Chem. Rev*. **2012**, *112*, 6027.

(54) Wang, Y.; Li, Z.; Wang, J.; Li, J.; Lin, Y. *Trends Biotechnol*. **2011**, *29*, 205.

(55) Wang, Y.; Lu, J.; Tang, L.; Chang, H.; Li, J. *Anal. Chem*. **2009**, *81*, 9710.

(56) Liu, Z.; Robinson, J. T.; Sun, X.; Dai, H. *J. Am. Chem. Soc*. **2008**, *130*, 10876.

(57) Lu, C.-H.; Zhu, C.-L.; Li, J.; Liu, J.-J.; Chen, X.; Yang, H.-H. *Chem. Commun.*, **2010**, *46*, 3116.

(58) Chang, H.; Tang, L.; Wang, Y.; Jiang, J.; Li, J. *Anal. Chem*. **2010**, *82*, 2341.

(59) Georgakilas, V.; Otyepka, M.; Bourlinos, A. B.; Chandra, V.; Kim, N.; Kemp, K. C.; Hobza, P.; Zboril, R.; Kim, K. S. *Chem. Rev*. **2012**, *112*, 6156.

(60) Morales-Narváez, E.; Merkoçi, A. *Adv. Mater*. **2012**, *24*, 3298.

(61) Feng, L.; Wu, L.; Qu, X. *Adv. Mater*. **2013**, *25*, 168.

(62) Li, M.; Yang, X.; Ren, J.; Qu, K.; Qu, X. *Adv. Mater*. **2012**, *24*, 1722.

(63) Xu, J.-J.; Zhao, W-W.; Song, S.; Fan, C.; Chen, H.-Y. *Chem. Soc. Rev.*, **2014**, *43*, 1601.

(64) Pei, H.; Li, J.; Lv, M.; Wang, J.; Gao, J.; Lu, J.; Li, Y.; Huang, Q.; Hu, J.; Fan, C. *J. Am. Chem. Soc.* **2012**, *134*, 13843.

(65) Liu, X.; Wang, F.; Aizen, R.; Yehezkeli, O.; Willner, I. *J. Am. Chem. Soc*. **2013**, *135*, 11832.

(66) Xu, J.-J.; Zhao, W.-W.; Song, S.; Fan, C.; Chen, H.-Y. *Chem. Soc. Rev.*, **2014**, *43*, 1601.

(67) Lu, C.-H.; Yang, H.-H.; Zhu, C.-L.; Chen, X.; Chen, G.-N. *Angew. Chem., Int. Ed.* **2009**, *48*, 4785.

(68) Balapanuru, J.; Yang, J.-X.; Xiao, S.; Bao, Q.; Jahan, M.; Polavarapu, L.; Wei, J.; Xu, Q.-H.; Loh, K. P. *Angew. Chem., Int. Ed.* **2010**, *49*, 6549.

(69) Jang, H.; Kim, Y.-K.; Kwon, H.-M.; Yeo, W.-S.; Kim, D.-E.; Min, D.-H. *Angew. Chem., Int. Ed.* **2010**, *49*, 5703.

(70) Piao, Y.; Liu, F.; Seo, T. S. *Chem. Commun.*, **2011**, *47*, 12149.

(71) Nel, A. E.; Mädler, L.; Velegol, D.; Xia, T.; Hoek, E. M. V.; Somasundaran, P.; Klaessig, F.; Castranova, V.; Thompson, M. *Nat. Mat*. **2009**, *8*, 543.

(72) Wang, Y.; Li, Z.; Hu, D.; Lin, C.-T.; Li, J.; Lin, Y. *J. Am. Chem. Soc*. **2010**, *132*, 9274.

(73) Jung, J. H.; Cheon, D. S.; Liu, F.; Lee, K. B.; Seo, T. S. *Angew. Chem., Int. Ed.* **2010**, *49*, 5708.

(74) Wang, L.; Pu, K.-Y.; Li, J.; Qi, X.; Li, H.; Zhang, H.; Fan, C.; Liu, B. *Adv. Mater*. **2011**, *23*, 4386.

(75) Liu, Y.; Dong, X.; Chen, P. *Chem. Soc. Rev.*, **2012**, *41*, 2283.

(76) Li, Z.; Deng, S.-S.; Zang, Y.; Gu, Z.; He, X.-P.; Chen, G.-R.; Chen, K.; James, T. D.; Li, J.; Long, Y.-T. *Sci. Rep.* **2013**, *3*, 2293.

(75) Zhang, H.-L.; Wei, X.-L.; Zang, Y.; Cao, J.-Y.; Liu, S.; He, X.-P.; Chen, Q.; Long, Y.-T.; Li, J.; Chen, G.-R.; Chen, K. *Adv. Mater*. **2013**, *25*, 4097.

(78) He, X.-P.; Deng, Q.; Cai, L.; Wang, C.-Z.; Zang, Y.; Li, J.; Chen, G.-R.; Tian, H. *ACS Appl. Mater. Interfaces* **2014**, *6*, 5379.

(79) He, S.; Song, B.; Li, D.; Zhu, C.; Qi, W.; Wen, Y.; Wang, L.; Song, S.; Fang, H.; Fan, C. *Adv. Funct. Mater*. **2010**, *20*, 453.

(80) Fan, L.; Li, F.; Pei, H.; Wang, L.; Lu, J.; Gao, J.; Jiang, B.; Zhao, X.; Fan, C. *Adv. Funct. Mater*. **2013**, *23*, 4140.

(81) Kim, J.; Cote, L. J.; Kim, F.; Huang, J. *J. Am. Chem. Soc*. **2010**, *132*, 260.

(82) Muthuraj, B.; Chowdhury, S. R.; Mukherjee, S.; Patra, C.; Iyer, P. K. *RSC Adv*. **2015**, *5*, 28211.

(83) Marcano, D. C.; Kosynkin, D. V.; Berlin, J. M.; Sinitskii, A.; Sun, Z.; Slesarev, A.; Alemany, L. B.; Lu, W.; Tour, J. M. *ACS Nano*, **2010,** *4*, 4806.

(84) Liu, K.; Chen, L.; Chen, Y.; Wu, J.; Zhang, W.; Chen, F.; Fu, Q. *J. Mater. Chem*. **2011**, *21*, 8612.

(85) Hu, W.; He, G.; Chen, T.; Guo, C. X.; Lu, Z.; Selvaraj, J. N.; Liu, Y.; Li. C. M. *Chem. Commun.*, **2014**, *50*, 2133.

(86) Li, D.; Müller, M. B.; Gilje, S.; Kaner, R. B.; Wallace, G. G. *Nat. Nanotechnol.* **2008,** *3*, 101.

(87) Guo, Y.; Deng, L.; Li, J.; Guo, S.; Wang, E.; Dong. S. *ACS Nano*, **2011,** *5*, 1282.

(88) Cui, P.; Lee, J.; Hwang, E.; Lee, H. *Chem. Commun.*, **2011,** *47*, 12370.

(89) Muthuraj, B.; Deshmukh, R.; Trivedi, V.; Iyer, P. K. *ACS Appl. Mater. Interfaces* **2014**, *6*, 6562.

(90) Wang, B.; Yu, C. *Angew. Chem., Int. Ed.* **2010**, *49*, 1485.

(91) Balakrishnan, K.; Datar, A.; Oitker, R.; Chen, H.; Zuo, J.; Zang, L. *J. Am. Chem. Soc*. **2005**, *127*, 10496.

(92) Balakrishnan, K.; Datar, A.; Naddo, T.; Huang, J.; Oitker, R.; Yen, M.; Zhao, J.; Zang, L. *J. Am. Chem. Soc*. **2006**, *128*, 7390.

(93) Herrikhuyzen, J. V.; Syamakumari, A.; Schenning, A. P. H. J.; Meijer, E. W. *J. Am. Chem. Soc*. **2004**, *126*, 10021.

(94) Mukherjee, S.; Chowdhury, D.; Kotcherlakota, R.; Patra, S.; Vinothkumar, B.; Bhadra, M. P.; Sreedhar, B.; Patra, C. R. *Theranostics* **2014**, *4*, 316.

(95) Modak, A.; Barui, A. K.; Patra, C. R.; Bhaumik, A. *Chem. Commun.*, **2013**, *49*, 7644.

Appendix

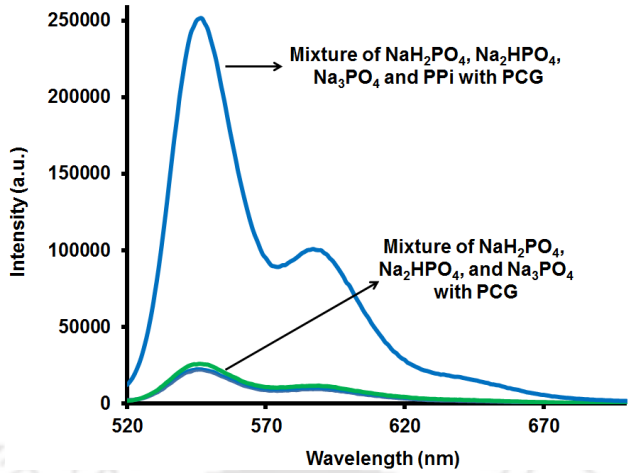

Figure A5b.1 Dequenching emission spectra of PDI-HIS (0.33 μM) + GO (10 μg/mL) + Cu^{2+} (1.33 μM) upon the addition of PPi (0-0.33μM) with other competing phosphates (0.33 μM) in HEPES buffer (10 mM, pH 7.4). Excitation wavelength: 508 nm.

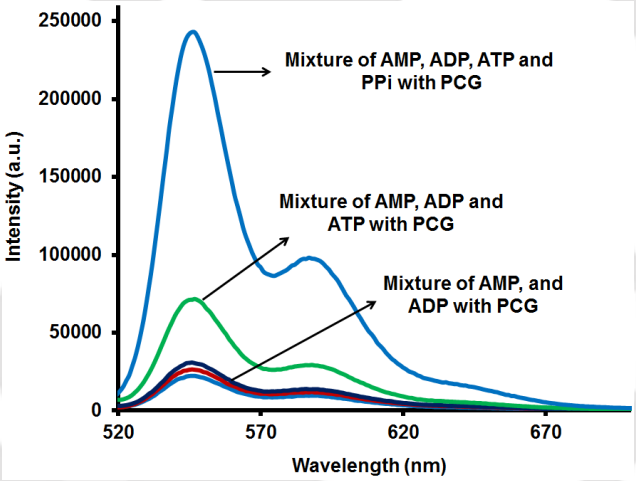

Figure A5b.2 Dequenching emission spectra of PDI-HIS (0.33 μM) + GO (10 μg/mL) + Cu^{2+} (1.33 μM) upon the addition of PPi (0.33μM) with other competing phosphates (0.33 μM) in HEPES buffer (10 mM, pH 7.4). Excitation wavelength: 508 nm.

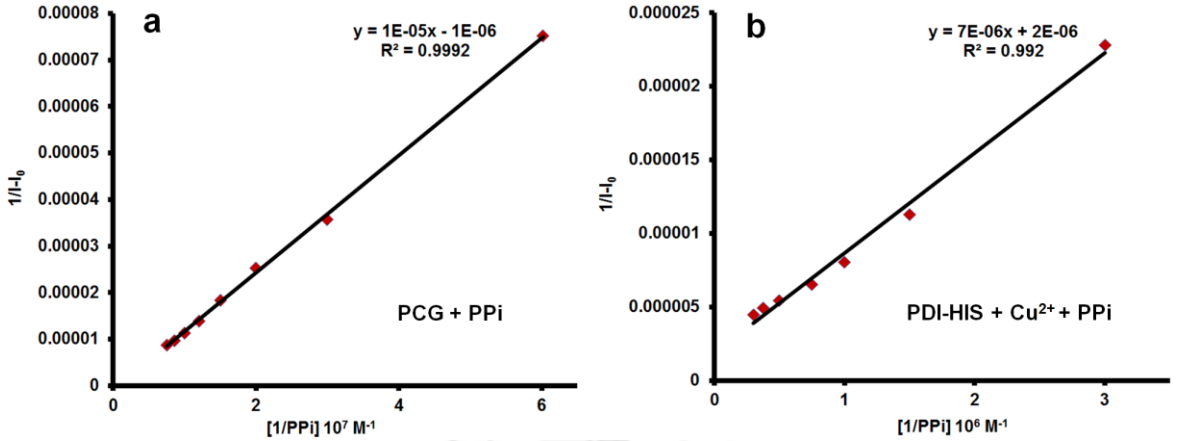

Figure A5b.3 The apparent binding constant was evaluated using Benesi−Hildebrand (B−H) plot by the fluorescence spectral changes at 546 nm for "turn-on" sensor for PPi with PDI-HIS-GO+Cu^{2+} (PCG) and PDI-HIS-Cu^{2+} complex.

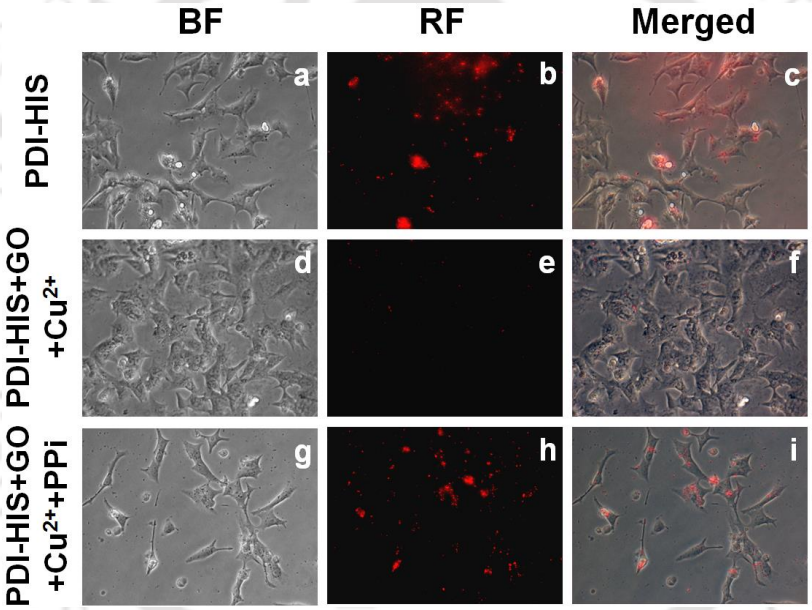

Figure A5b.4 (a, d, g) Bright-field images of B16F10 cells treated with PDI-HIS, PCG and PCG + PPi. (b) Fluorescence images of B16F10 cells incubated with 300 µg/mL PDI-HIS for 24 h (e) PDI-HIS further incubated with GO and 1 mM Cu^{2+} for 2 h. (h) PCG complex further incubated with 2 mM PPi for 45 min. (c, f, i) Merged images of B16F10 cells treated with PDI-HIS, PCG and PCG + PPi. Excitation wavelength range λ_{ex} = 510-560 nm (green) and λ_{em} = 605 nm (red). 20X magnification.

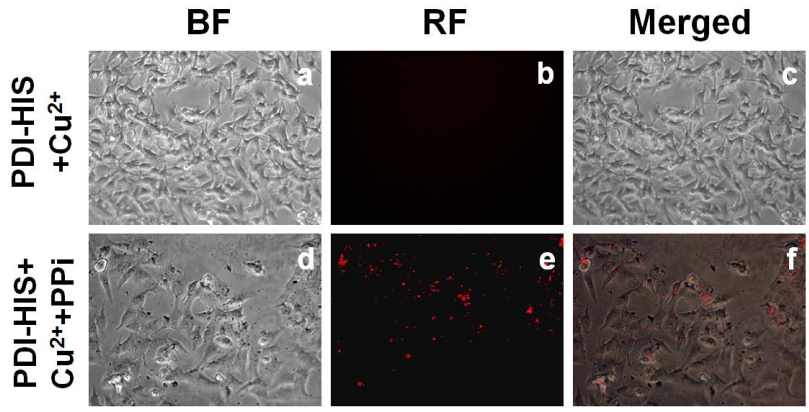

Figure A5b.5 (a, d) Bright-field images of B16F10 cells treated with PDI-HIS+Cu^{2+} and PDI-HIS + Cu^{2+} + PPi. (b) B16F10 cells further incubated with PDI-HIS (300 µg/mL) and 1 mM Cu^{2+} for 2 h. (e) Regained fluorescence images of PDI-HIS+Cu^{2+} complex further incubated with 20 mM PPi for 45 min. (c, f) Merged images of B16F10 cells treated with PDI-HIS, PDI-HIS + Cu^{2+} and PDI-HIS + Cu^{2+} + PPi. Excitation wavelength range λ_{ex} = 510-560 nm (green) and λ_{em} = 605 nm (red). 20X magnification.

Chapter: 5c

Modulation of Aβ Fibrils into Mature Micro Rod shaped Hybrid Structure by Histidine Functionalized Water soluble Perylene Diimide

Abstract

Alzheimer's disease (AD) is associated with different types of amyloid-β (Aβ) peptide aggregates including senile plaques, fibrils, protofibrils and oligomers. Due to these difficulties, a powerful strategy is needed for the disaggregation of Aβ aggregates by modulating their self-aggregation behavior. Herein, we reported a unique approach toward transforming the aggregated amyloidogenic peptides using an amino acid functionalized perylene diimide as a molecular modulator, which is a different and nondestructive approach as compared to inhibiting the aggregation of peptides. The histidine functionalized perylenediimide (PDI-HIS) molecule could co-assemble with Aβ peptides via hydrogen bonding that leads to the enhancement in the π-π interactions between Aβ and PDI-HIS moieties. The thioflavin T (ThT) assay and various spectroscopic and microscopic techniques establish that the PDI-HIS molecules accelerate the Aβ1-40 and the Aβ aggregates in CSF into micro size coassembled structures. These results give rise to a new and unique complementary approach for modulating the biological effects of the aggregates in amyloidogenic peptides.

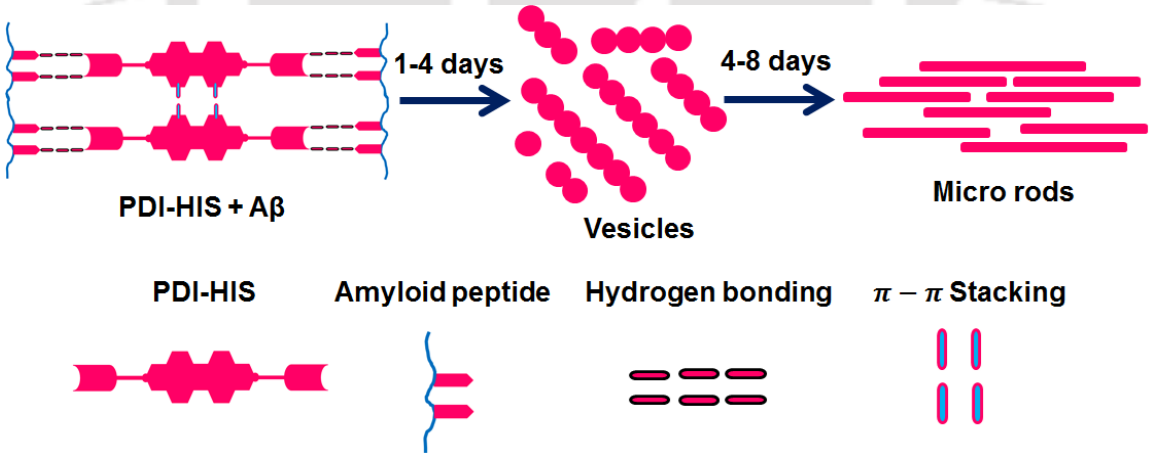

5c.1. Introduction

The aggregation of soluble Aβ monomer or oligomers into insoluble plaques or Aβ fibrils is a crucial step that drives Alzheimer's disease (AD) pathogenesis.[1-4] Based on this hypothesis several effective protocols have been attempted for modulating or inhibiting Aβ, such as peptides,[5,6] antibodies,[7,8] metal ion chelators,[9,10] small molecules[11,12] and nanoparticles,[13-16] which gave certain beneficial results toward AD treatment by preventing Aβ aggregate progression. Thus, an attractive therapeutic strategy for AD treatment remains the effective preservation mechanism of Aβ homeostasis by a combination of inhibiting Aβ aggregation and promoting Aβ aggregate clearance.

Small molecule based probes can self-assemble into well-arranged superstructures with multiple noncovalent interactions like hydrogen-bonding (H-bonding) and π-π interactions.[17,18] Notably, the noncovalent interactions are the driving forces for the peptide–organic molecule interaction and could lead to the efficient coassembly process.[18-22] Hence, the efficient coassembly between peptide and organic molecules is a vital structural characteristic of peptide assembly study for peptide induced diseases such as AD, Parkinson's and Prion diseases. Currently, smart self-assembling molecules have been identified that associate and promote the peptide–peptide and peptide–organic interactions converting the Aβ monomers and oligomers into nontoxic forms since the oligomeric forms of amyloidogenic peptides are reported to have higher toxicity as compared to the fibrillar aggregates.[11,12,23-29] In the present study, we establish a complementary approach to achieve a hybrid structure in the form of micro rods from aggregated Aβ fibrils, by the co-assembly between Aβ1–40 fibrils and histidine functionalized PDI molecule.[30-32]

5c.2. Results and discussion

5c.2.1. Synthesis of PDI-HIS

The synthesis of probe PDI-HIS was mentioned and discussed in previous chapter 5a (Scheme 5a.1), a reaction between 3,4,9,10-Perylenetetracarboxylic acid bisanhydride (500 mg, 1.27 mmol), histidine (800 mg, 3.82 mmol) and 2.0 g of imidazole which were heated at 140 °C for 8 h with stirring.[33] The reaction mixture was allowed to cool to 90 °C and poured into water. Then, the mixture was acidified with 2.0 M HCl, and the precipitate was washed with water and dried under vacuum at 80 °C to get the product PDI-HIS (800 mg, 94%.

Herein, we present a histidine functionalized biocompatible molecule PDI-HIS (λ_{em} = 546 nm) which is used as a modulator for Aβ aggregates (Figure 5c.1a and 5c.1b).[33] The

formation of coassembly with Aβ1-40 fibrils and Aβ aggregates in real cerebrospinal fluid (CSF), which is a vital biomarker for AD is presented using the water soluble PDI-HIS molecule. The modulating effects of PDI-HIS on Aβ aggregates were validated using AFM, FE-SEM, DLS, polarized optical microscopy (POM), optical spectroscopy, and Fourier transform infrared spectroscopy (FT-IR).

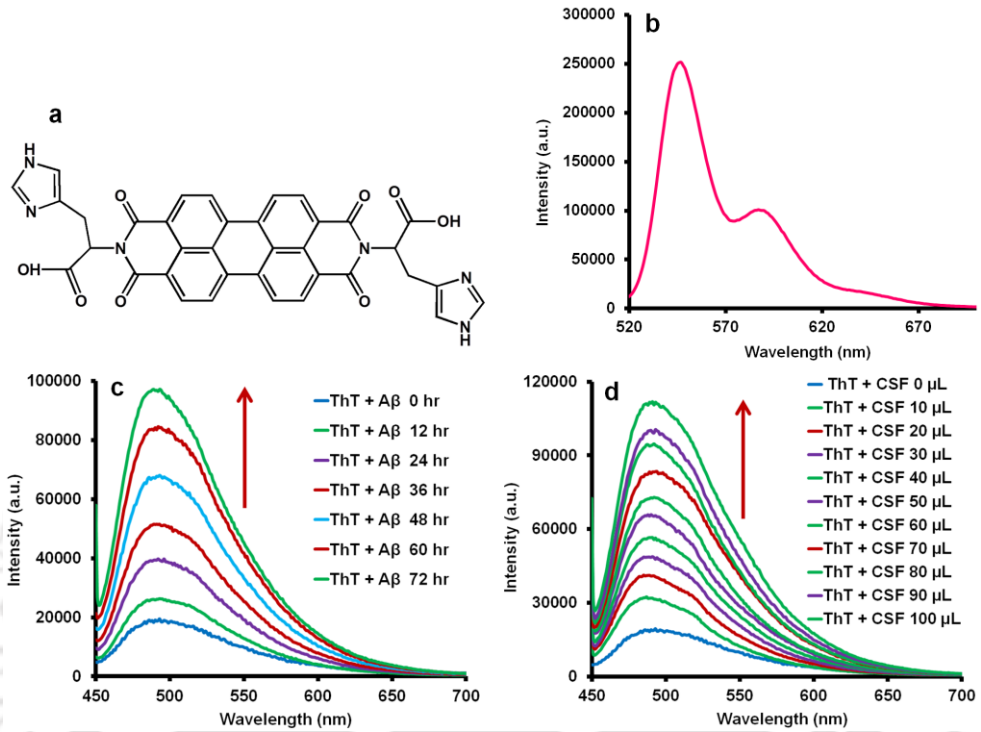

Figure 5c.1 (a) Structure of PDI-HIS. (b) Fluorescence spectra of PDI-HIS (0.33 µM) in HEPES buffer solution at pH 7.4. (c) Detection of Aβ fibrils using ThT assay: Fluorescence enhancement spectra (λ_{ex} = 440 nm, λ_{em} = 488 nm) of ThT (20 µM) (pH 7.4 in HEPES) mixed Aβ1-40 (25 µM) was measured every interval incubation time from 0-72 h. (d) Fluorescence enhancement (λ_{ex} = 440 nm, λ_{em} = 488 nm) of ThT (20 µM) (pH 7.4 in HEPES) was observed when the addition of CSF (0-100 µL).

5c.2.2. Confirmation study for the presence of Aβ peptide aggregates by ThT assay

Thioflavin T (ThT) assay is one of the most widely used methods to identify Aβ fibrils with high sensitivity.[34,35] The emission band at 488 nm is expected to be directly proportional to the amount of Aβ fibrils present, consequently, the formation of Aβ fibrils can be easily followed by measuring ThT fluorescence enhancement by time-dependent manner. Upon the addition of Aβ1-40 (25 µM) monomer into ThT (20 µM), a gradual enhancement of the emission peak at 488 nm is observed over 0-72 h incubation time (λ_{ex} – 440 nm) (Figure

5c.1c) which indicates the presence of Aβ fibrils. ThT enhanced fluorescence occurs due to the changes in the rotational freedom of the C-C bonds between the benzothiazole and dimethylanilino rings.[36] Furthermore, the presence of Aβ fibrils in CSF was also confirmed by the addition of upto 100 µL of the CSF sample into 20 µM solution of ThT (pH 7.4 in HEPES). After the addition of CSF sample we observed a gradual enhancement in the fluorescence intensity of ThT at 488 nm which validates strongly the existence of aggregated Aβ fibrils in the CSF sample (Figure 5c.1d).[37,38] Because, the Aβ fibrils formation from Aβ1-40 monomers and the existence of aggregated Aβ fibrils in the CSF sample was confirmed, we have further utilized these two samples for our studies.

5c.2.3. Confirmation of the presence of Aβ peptide aggregates by microscopic techniques

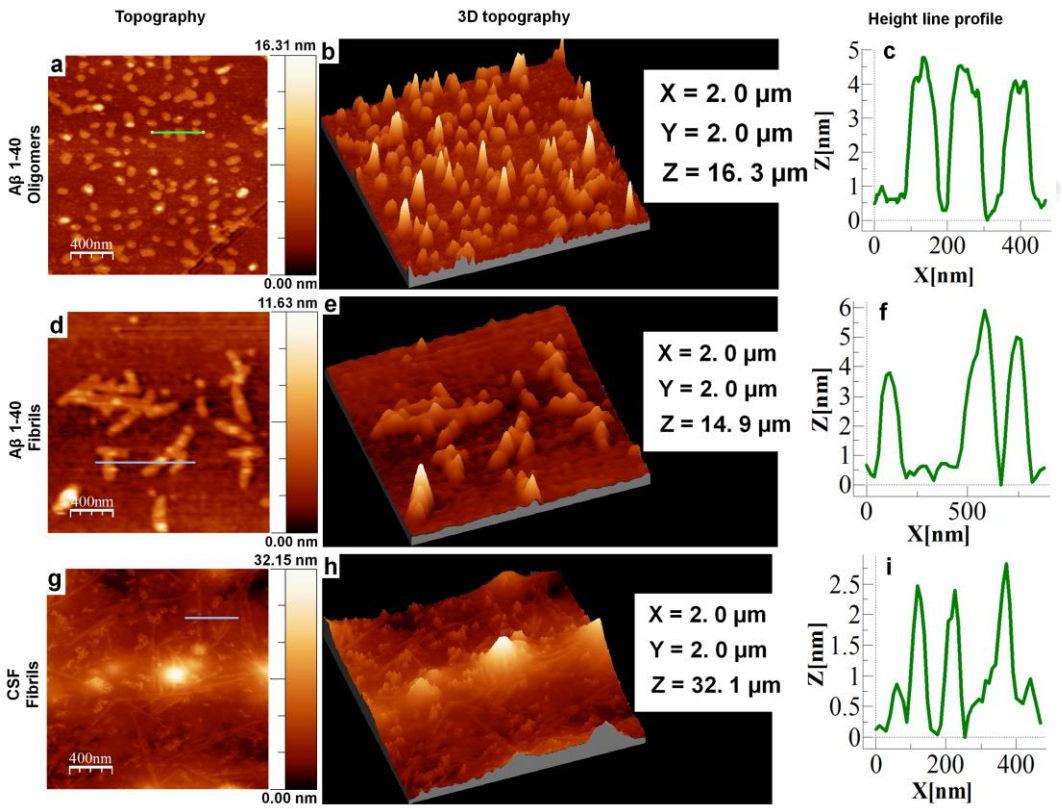

Figure 5c.2 Detection of Aβ fibrils using AFM analysis: (a) Aβ1-40 oligomers, (d) Aβ1-40 fibrils (from Aβ 1-40) and samples were analyzed after incubation times of (a) 24 h and (d) 72 h. (g) Detection of Aβ fibrils (from CSF). (b, e, h) 3D Topography images of Aβ1-40 oligomers, Aβ1-40 fibrils and CSF fibrils. (c, f, i) Height line profiles of Aβ1-40 oligomers, Aβ1-40 fibrils and CSF fibrils. (X = distance and Y = Height).

Several microscopy methods such as electron microscopy (EM) and atomic force microscopy (AFM) have been established to characterize the structural and morphological changes of noncrystalline protein fibrils.[39-41] The Aβ1–40 aggregates were monitored by AFM imaging at different incubation time (Figure 5c.2). The sample deposited with the freshly prepared solution, showed both small and large oligomers as observed in the topography image (Figure 5c.2a). The diameter of Aβ oligomers was observed to be ~100 ± 10 nm and ~5 nm height (Figure 5c.2b and 5c.2c). Further, these Aβ monomers and oligomers were incubated for 3 days, after that the AFM image showed a number of fibrils in the topography image (Figure 5c.2d) with ~80 ± 20 nm diameter and ~4-6 nm height (Figure 5c.2e and 5c.2f) confirming that the monomers and dimers continue to form aggregated oligomers that further assemble to form protofibrils and then into fibrils. The images of the real CSF sample (Figure 5c.2g-5c.2i) showed large number of mature fibrils. The diameter of Aβ fibrils in CSF was observed to be ~50 ± 20 nm and ~2.5 nm height (Figure 5c.2h and 5c.2i). Consequently, these morphological results confirm that formation of aggregated Aβ fibrils from Aβ1–40 monomers and existence of Aβ fibrils in CSF could be used for further characterization.

5c.2.4. Modulating effect of PDI-HIS on amyloid aggregates monitored by fluorescence spectroscopy

Further, the binding and modulating ability of PDI-HIS were ascertained by the changes in the fluorescence spectra in the presence of Aβ1–40 fibrils and CSF Aβ fibrils. When PDI-HIS (0.33 μM) solution was excited at 508 nm we observed an emission peak at 546 nm (Figure 5c.3a and 5c.3b blue curve). Upon separate addition of Aβ1–40 fibrils (0.76 μM) and CSF Aβ fibrils (50 μL) into the PDI-HIS solution, only slight fluorescence changes were observed in the PDI-HIS+Aβ1–40 fibrils and PDI-HIS+CSF aggregate mixtures. However, after the samples were incubated for 0−90 h at 37 °C (pH 7.4), we observed gradual fluorescence enhancement in the PDI-HIS+Aβ1–40 fibrils and PDI-HIS+CSF solutions respectively. The fluorescence enhancement occurred due to the formation of well-ordered supramolecular coassembly structures of Aβ1-40 and CSF aggregates with PDI-HIS via noncovalent interactions like H-bonding and π-π stacking. The coassembly between PDI-HIS and Aβ aggregates likely occur via the H-bonding between the hydrophilic ends of PDI-HIS with the Aβ peptide containing amide and carboxylic groups which further induces the formation of π-π stacking between perylene hydrophobic interfaces. These noncovalent interactions promote the interconversion of the fibrillar structures into micro rod like

structures (Scheme 5c.1) as visualized and confirmed via other techniques (AFM, FE-SEM and POM images).

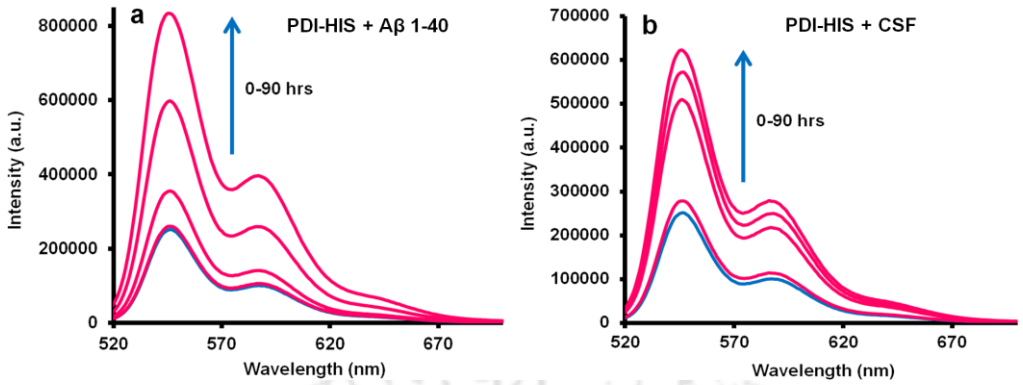

Figure 5c.3 (a, b) Fluorescence enhanced emission spectra measured for PDI-HIS (0.33 μM) with Aβ 1–40 (0.76 μM) aggregates and PDI-HIS (0.33 μM) with CSF (50 μL) aggregates from 0-90 h incubation in HEPES (10 mM) buffer at pH 7.4. Excitation of PDI-HIS is 508 nm and emission at 546 nm maximum.

Schematic representation of micro rods formations by coassembly

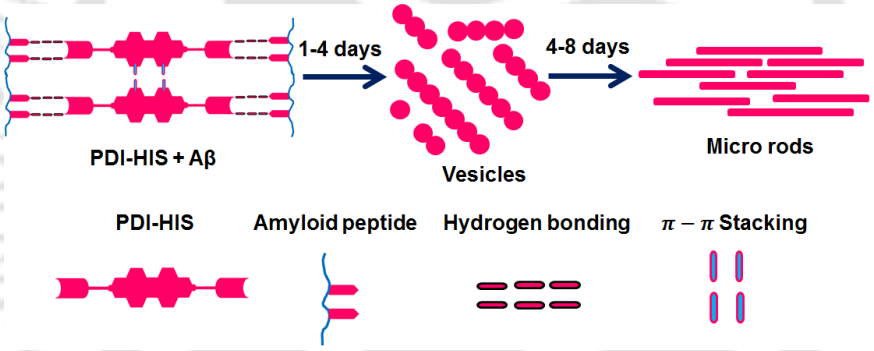

Scheme 5c.1 Schematic representation of micro rods formations from aggregated Aβ fibrils with PDI-HIS.

5c.2.5. Modulating effect on amyloid peptide aggregates monitored by FT-IR spectra and DLS study

To validate the results obtained from fluorescence study, we examined the secondary structure of Aβ1–40 fibrils alone and the coassembly structures of PDI-HIS + Aβ1–40 fibrils and PDI-HIS + CSF aggregates by using FT-IR spectroscopy.[42-44] The FT-IR spectrum of Aβ1–40 fibrils and CSF Aβ fibrils showed a major band at 1630±2 cm^{-1} which indicates the parallel β-sheet conformation of Aβ1–40 aggregates (Figure 5c.4a, blue curve and A5c.1). The parallel β-sheet conformation of Aβ1–40 fibrils were transformed into the random coil conformation due to the formation of co-assembly structures with PDI-HIS (PDI-HIS+Aβ1–40 fibrils and PDI-HIS+CSF Aβ fibrils), as illustrated by a major band at 1646±2 cm^{-1}

(Figure 5c.4a, green and pink). This result confirms that PDI-HIS has the ability to modulate preformed Aβ1–40 fibrils as well as the Aβ aggregates in CSF.

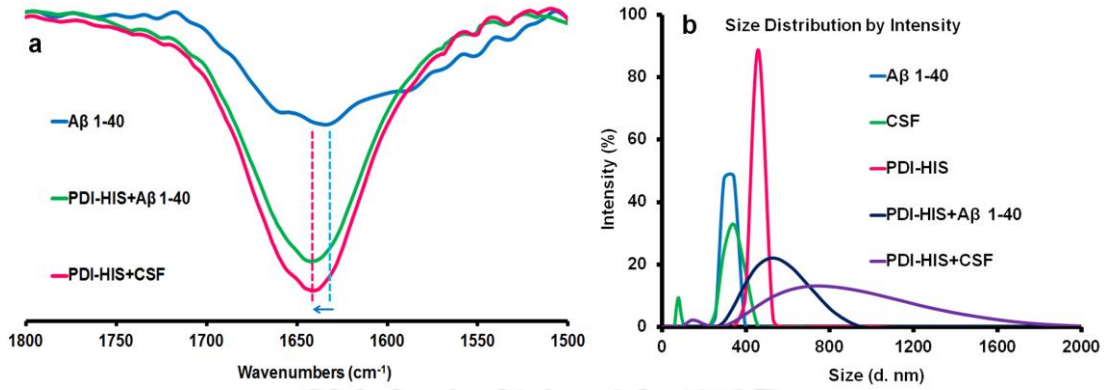

Figure 5c.4 (a) Modulation effects of PDI-HIS on Aβ 1-40 fibrils and CSF Aβ fibrils were measured by FT-IR spectroscopy. (b) Modulation effects of PDI-HIS on Aβ 1-40 fibrils and CSF Aβ fibrils were measured by dynamic light scattering (DLS) in HEPES buffer solution at pH 7.4.

Further, we examined the size distribution of PDI-HIS and the formation of coassembly structure between PDI-HIS and Aβ aggregates (Aβ1–40, CSF) in aqueous HEPES buffer (pH 7.4) solution by DLS experiments (Figure 5c.4b). It could be established that the PDI-HIS could accelerate the formation of co-assembly structure via aggregation process with Aβ1–40 fibrils as well as CSF Aβ fibrils (Figure 5c.4b). The control experiments demonstrated that Aβ1–40 fibrils (295-341 d. nm), CSF Aβ fibrils (295-396 d. nm) and PDI-HIS (458 d. nm) are lower in size independently as compared to the co-assembly structures of PDI-HIS+Aβ1–40 fibrils (342-825 d. nm) and PDI-HIS+CSF Aβ fibrils (342-1718 d. nm). Therefore, the mechanism of the accelerated aggregation during modulation could be attributed to the formation of co-assembly by noncovalent interactions linking peptide stripes with the PDI-HIS molecules (Scheme 5c.1). Therefore, it is feasible to change the Aβ aggregates (Aβ1–40, CSF) into co-assembly structure in the presence of PDI-HIS. This result also strongly confirms that PDI-HIS modulates the aggregation behavior of Aβ1–40 fibrils and CSF Aβ fibrils, which would possibly reduce the effective concentration of Aβ self-aggregates.

5c.2.6. Modulating effect on amyloid peptide aggregates monitored by morphology images

Furthermore, AFM and FE-SEM studies were also used to visualize the morphological images of the coassembly structure formation (Figure 5c.5 and 5c.6). As expected, Aβ1–40 monomers form Aβ1–40 fibrils and existence of Aβ1–40 fibril in CSF were also confirmed

by AFM and FE-SEM images as mentioned earlier in figure 5c.2d and 5c.2g. In 3 mL of HEPES buffer (10 mM, pH 7.4) the prepared solutions of PDI-HIS (0.33 μM) + Aβ1-40 (0.76 μM) and PDI-HIS (0.33 μM) + CSF (50 μL) aggregates were kept for 0-90 h incubation at 37 °C in water bath. These solutions were further utilized to monitor the AFM morphology images. Both the solutions were separately diluted by 10 times and then from the diluted solutions 5 μL of the PDI-HIS + Aβ1-40 as well as PDI-HIS + CSF samples were dropped onto the freshly cleaned glass slide, dried at room temperature overnight and the morphology studied by AFM. Appreciably, micro rod type morphology image developed when PDI-HIS assembled with Aβ1–40 and CSF fibrils, rather than the formation of oligomer or fibrils (Figure 5c.5 and 5c.6), which is an exceptional observation. The discrepancies in aggregate morphologies of Aβ1–40 and Aβ1–40 + PDI-HIS are very unique, which are assigned to the modulating effect on the assembly structures of Aβ1–40 peptides on a molecular level. The diameter of coassembled Aβ1–40 + PDI-HIS micro rods were observed to be 550 ± 20 nm with ~25 nm height and 6 ± 1 μm length (Figure 5c.5a-5c.5c), which are much bigger in size as compared to the free Aβ fibrils of amyloidogenic peptides. Similarly, the coassembled morphologies of CSF + PDI-HIS mature micro rod diameter was observed to be 500 ± 10 nm with a height of ~13 nm and length of 4 ± 1 μm (Figure 5c.5d-5c.5f).

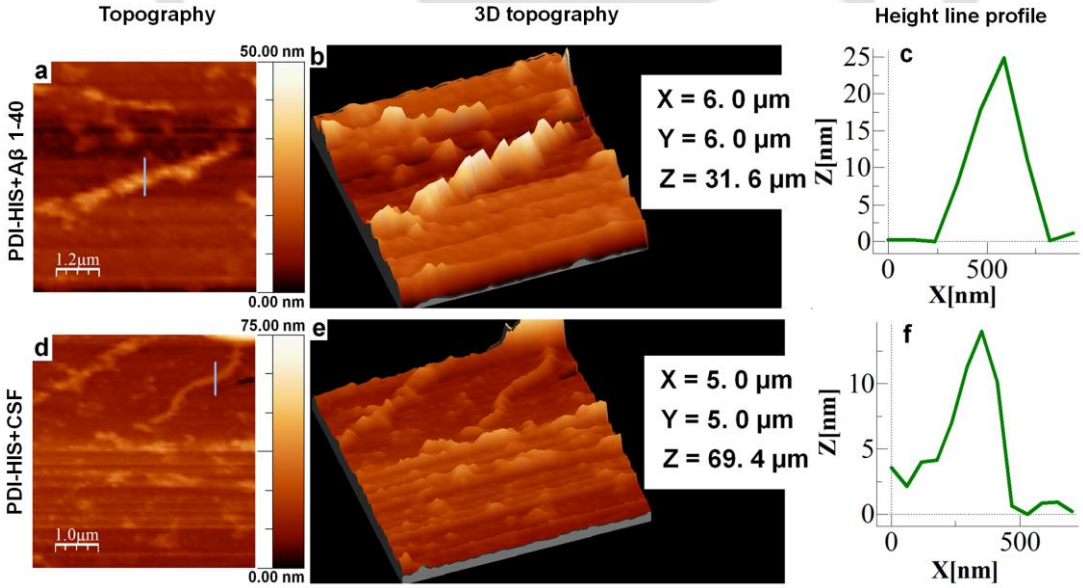

Figure 5c.5 Detection of Aβ 1–40 fibrils into the formation of coassembled mature rod-shaped structure using PDI-HIS: (a) PDI-HIS + Aβ 1–40 fibrils (d) PDI-HIS with CSF Aβ fibrils after 8 days incubation. (b, e) 3D Topography images of PDI-HIS + Aβ 1–40 fibrils and PDI-HIS + CSF Aβ fibrils. (c, f) Height line profiles of PDI-HIS + Aβ 1–40 fibrils and PDI-HIS + CSF Aβ fibrils. (X = distance and Y = Height).

Additionally, FE-SEM also strongly supported the formation of coassembled mature micro rod structures in presence of PDI-HIS with Aβ1–40 and CSF aggregates respectively (Figure 5c.6). These results validate that PDI-HIS is an effective modulator for Aβ1–40 fibrils and amyloid aggregates in CSF by the interconversion of amyloid aggregates into coassembled mature micro rod like structures that are completely different from the free Aβ fibrils.

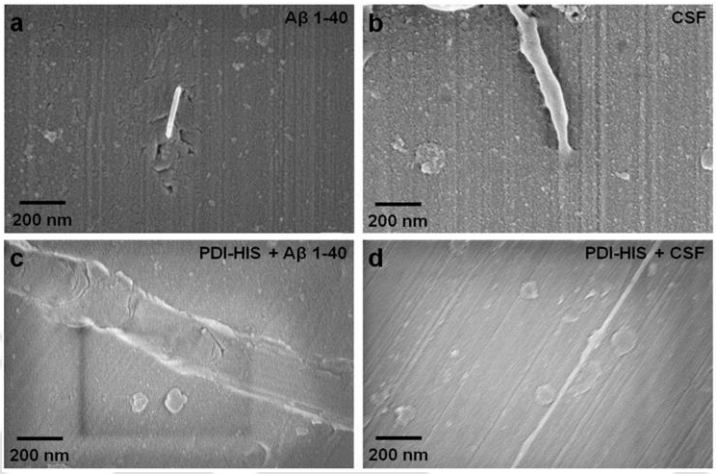

Figure 5c.6 FE-SEM images demonstrate that modulating effect on Aβ1–40 and CSF aggregates into mature rod-shaped coassembly structure: (a, b) Aβ1–40 and CSF aggregates. (c, d) Co-assembly structures of PDI-HIS + Aβ1–40 fibrils and PDI-HIS + CSF Aβ fibrils.

5c.2.7. Modulating effect on Aβ peptide aggregates monitored by Polarized optical microscopy (POM)

The modulating effect of PDI-HIS on the assembly of Aβ1-40 and aggregated fibrils in CSF were also investigated by polarized optical microscopy (POM) (Figure 5c.7). The POM images of Aβ1–40 and CSF aggregates depicted typical spherical shape (Figure 5c.7a and 5c.7e). Aβ1–40 aggregates (0.76 μM) were incubated with PDI-HIS (0.33 μM) in 3 mL HEPES buffer solution (10 mM, pH 7.4) at 37 ^{o}C for 0-90 h. Similarly, CSF aggregates (50 μL) were also incubated with PDI-HIS (0.33 μM) in 3 mL HEPES buffer solution (10 mM, pH 7.4) at 37 ^{o}C for 0-90 h. Further, from the above solutions the samples were prepared separately by spreading 30 μL of each solution on glass slide and the images were observed for both the samples at different time of incubation under a microscope. After 2 days incubation with PDI-HIS, the mixture of PDI-HIS+Aβ1–40 aggregates and PDI-HIS+CSF aggregates showed the formation of coassembled vesicles (Figure 5c.7b and 5c.7f) due to the noncovalent interactions between the hydrophilic ends of the PDI-HIS with Aβ peptide containing amide and carboxylic groups (as discussed earlier). This noncovalent interaction

comprising π-π stacking of PDI induces the formation of young micro rod like structure after 4 days incubation at pH 7.4 in HEPES buffer solution (Figure 5c.7c and 5c.7g).

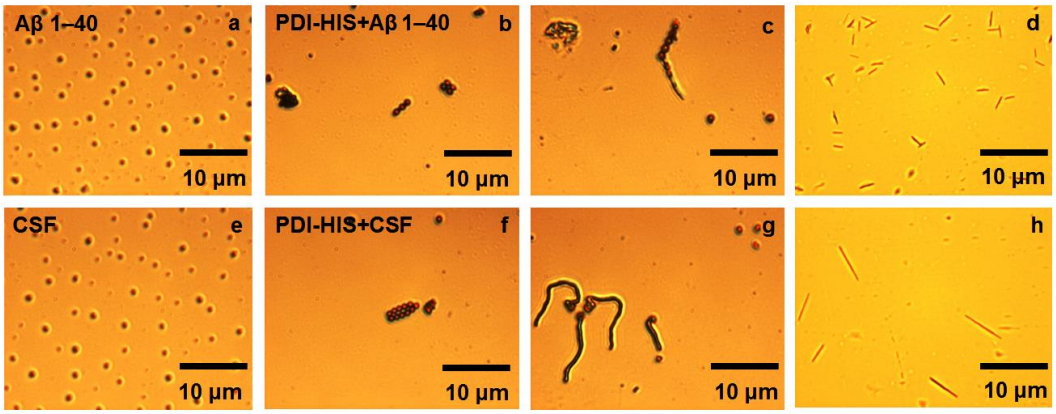

Figure 5c.7 Detection of Aβ 1–40 fibrils into rod shaped coassembly structure using PDI-HIS: (a) Optical microscopic image clearly shows the formation of aggregated Aβ 1–40 spheres. (b, c) The formation of coassembled vesicles and immature rod-shaped structures were observed in presence of PDI-HIS (0.33 µM) with Aβ 1–40 (0.76 µM) after 2 and 4 days incubation. (d) Formation of coassembled mature rod-shape structure was observed from vesicles structure by PDI-HIS with Aβ 1–40 fibrils after 8 days incubation. (e) Optical microscopic image clearly shows that existence of aggregated Aβ spheres in CSF. (f, g) Formation of coassembled vesicles and immature rod-shape structures were observed in presence of PDI-HIS (0.33 µM) with CSF Aβ fibrils (50 µL) after 2 and 4 days incubation. (h) Formation of coassembled mature rod-shape structure was observed from vesicles by PDI-HIS with CSF after 8 days incubation.

However, when the same sample was incubated for 8 days the young and immature micro rod structures are totally converted into mature micro rod co-assembled structures (Figure 5c.7d and 5c.7h) which are in agreement with the AFM and FE-SEM images. Finally, the obtained POM images confirm the modulation of Aβ1–40 and aggregates in CSF into co-assembled mature micro rod structure which are entirely different from the Aβ self-aggregates. For control studies, we performed similar experiments to confirm the formation of coassembled vesicles and mature rod-shaped structures in the absence of PDI-HIS with Aβ 1–40 fibrils (0.76 µM) and CSF Aβ fibrils (50 µL). The obtained images confirm that mature rod-shape structures were not observed in the absence of PDI-HIS with Aβ1–40 fibrils and CSF Aβ fibrils even after 4 and 8 days incubation (Figure A5c.2).

5c.2.8. Modulating effect of PDI-HIS confirmed by FRET study

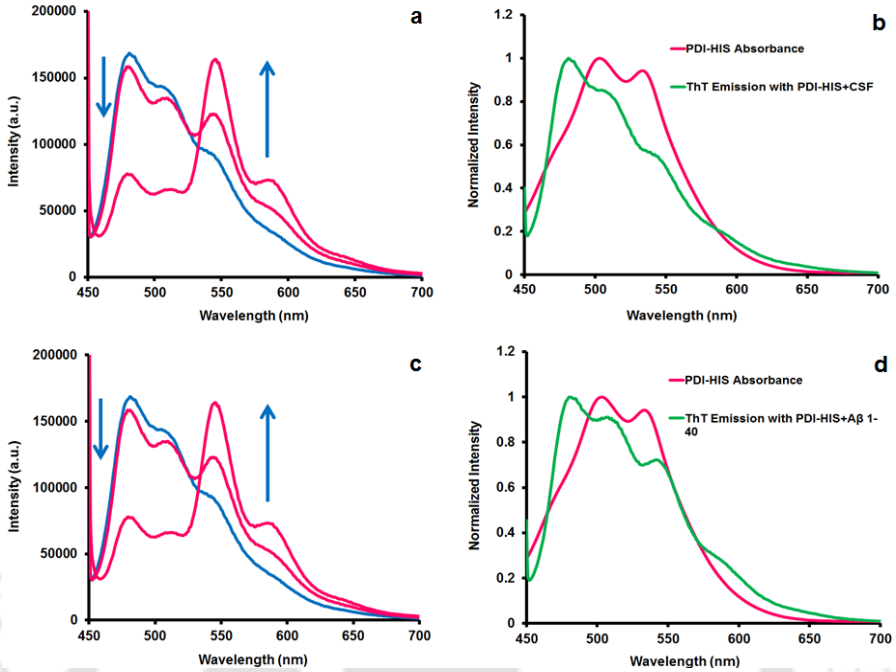

Figure 5c.8 Monitoring Aβ1–40 aggregation by fluorescence resonance energy transfer (FRET) from ThT to PDI-HIS: (a, c) Emission spectra (excitation wavelength, 440 nm) of CSF and Aβ1–40 (0.76 μM) incubated at 37 °C from 0-72 h with PDI-HIS (0.33 μM) and ThT (20 μM). ThT emission λ_{max} = 488 nm and PDI-HIS emission λ_{max} = 546 nm. (b, d) FRET spectra obtained from donor ThT to PDI-HIS.

The interaction of PDI-HIS with specific Aβ aggregates were examined by assessing the amount of Aβ aggregates from the fluorescence intensity of ThT fluorescence assay (0-72 h) (Figure 5c.8). ThT does not bind with Aβ1-40 and Aβ1-42 monomers but ThT is a common fluorescent probe that could be used to quantify Aβ aggregates. Initially, the PDI-HIS (0.33 μM) was added into aggregated Aβ1-40 fibrils (0.76 μM) and CSF Aβ fibrils (50 μL) in the presence of ThT (20 μM) and kept for incubation (0-72 h) to monitor the fluorescence changes at 488 nm. The mixtures of both the solutions were excited at 440 nm and the emission peaks appeared at 488 nm predominantly at 0 h confirming that no significant interaction occurred between PDI-HIS and Aβ fibrils. After the samples were incubated (0-72 h), we screened ThT fluorescence changes at 488 nm for both the samples. Subsequently, we observed that PDI-HIS significantly quenched the fluorescence of ThT after interacting with Aβ fibrils and a new enhanced emission peak appeared at 546 nm at different time intervals (0-72 h) which strongly confirms that PDI-HIS modulates the Aβ fibrils.

To determine the mechanism of PDI-HIS binding and its influence on the Aβ1–40 aggregation, we monitored the Aβ1–40 aggregation over time in the presence of ThT fluorescence with PDI-HIS. Increase in ThT fluorescence suggests that the compound may induce Aβ aggregation, while decrease in ThT fluorescence suggests that the compound modulates Aβ aggregation. Notably, the ThT emission band at 488 nm with PDI-HIS in presence of Aβ1–40 fibril is much lower than in the absence of PDI-HIS, due to nonradiative energy transfer from ThT to PDI-HIS. When we incubated PDI-HIS in presence of CSF Aβ fibrils and Aβ1–40 fibrils with ThT and excited them at 440 nm, we observed the ThT emission maximum at 488 nm (with lower fluorescence intensity) but the significant emission band appeared at 546 nm (Figure 5c.8a and 5c.8c) due to the consistent energy transfer from the donor ThT into the acceptor PDI-HIS (FRET).[45] Consequently, the emission spectra of ThT with CSF aggregates and/or Aβ1–40 fibrils overlapped with the excitation spectra of PDI-HIS (Figure 5c.8b and 5c.8d), which confirmed the mechanism of nonradiative transfer of ThT excited-state energy to PDI-HIS (FRET). Finally, this result strongly confirms that PDI-HIS could recognize and modulate the Aβ1–40 fibrils and aggregated fibrils in CSF by the noncovalent interaction induced co-assembly mechanism.[46]

5c.3. Conclusion

In summary, we presented an extremely effective and complementary approach toward the modulation of amyloidogenic peptides by accelerating the aggregation process using a biocompatible fluorescent PDI-HIS molecule, which is different from inhibiting the aggregation of Aβ peptides. The formation of hybrid micro rods in aqueous solution by the process of coassembly between Aβ1-40 fibrils and Aβ aggregates of CSF with PDI-HIS, was predominantly driven by noncovalent interactions. However, the modulating effect on Aβ1-40 and CSF aggregates were validated by the experiments like ThT assay, FT-IR, fluorescence spectroscopy, DLS, FE-SEM, POM and AFM which establishes that the histidine functionalized perylene diimide molecule accelerates the Aβ1-40 and the aggregates of CSF into micro size coassembled structures. Therefore, we could confirm that PDI-HIS possesses a significant targeted modulating effect on Aβ1-40 fibrils and the Aβ fibrils of CSF by forming coassembled PDI-HIS+Aβ hybrids structure. Consequently, this could lead to potential design and development of drugs targeted toward AD.

5c.4. Experimental Section

5c.4.1. Materials and methods

All the reagents and chemicals were purchased from Aldrich Chemicals, Merck or Ranbaxy (India) and used as received. Milli-Q water and HPLC grade solvents were used in all the experiments. Solvents were degassed using three freeze thaw cycles or flushed with nitrogen for at least 1 h prior to use when necessary. β-Amyloid (1-40), human was purchased from GL Biochem Ltd., Shanghai, China. The cerebrospinal fluid (CSF) samples were gifted by Guwahati Neurological Research Center and Hospital, Guwahati, India and were obtained as part of routine care from patients. Nonetheless, information explaining the purpose of this study was specified at the time of sample collection adhering to the bioethics policy of the hospital.

Fluorescence spectra were carried out on a FluoroMax-4 Spectrofluorometer-Horiba Scientific. A 10 × 10 mm quartz cuvette was used for solution spectra and emission was collected at 90° relative to the excitation beam. Leica polarizable optical microscope was used to image the aggregation and disruption studies. FT–IR spectra were recorded on a PerkinElmer spectrometer with samples prepared as KBr pellets. A fresh glass slide was used for every experiment. Deionized water was obtained from Milli–Q system (Millipore). Field emission scanning electron microscopy (FE-SEM) measurements were made on a Carl Zeiss, SIGMA VP instrument. Atomic force microscopy (AFM) was recorded on an Agilent instrument, model 5500 series with noncontact mode. DLS were measured by Zetasizer Nano series Nano-ZS90 instrument. The POM images were obtained on a Leica DM 2500P microscope.

5c.4.2. Preparation of stock solutions

The PDI-HIS stock solution was prepared at a concentration of 1.0×10^{-3} mL^{-1} in 10 mL H_2O at pH 7-9. This stock solution was diluted to desired concentration for each titration in a 3 mL cuvette with 10 mM HEPES buffer at pH 7.4.

5c.4.3. Preparation of HEPES buffer solutions

The fluorescence titrations and all other experiments were performed in 10 mM HEPES buffer solution and pH 7.4 was maintained by using 4 M NaOH or 5 M HCl solution.

5c.4.4. Cell viability assay (MTT)

Viability of HUVEC, EA.hy926, A549 and B16 cells were checked by MTT assay as per published protocol.[33] Initially, 10,000 cells/ well were seeded in per well of 96 well and

different concentrations of probe PDI-HIS (10 µg/mL - 750 µg/mL) for cytotoxicity experiment for 24 h as a dose dependent manner. After 48 h treatment, 1 mL MTT stock solution (concentration 5 mg/ mL) was diluted to 10 mL solution using DMEM media and 100 µL of this MTT solution (10 µL 5 mg/ mL MTT + 90 µL of corresponding media) was added to each well by replacing the media and further allowed to incubate for 4 h. After 4 h, the media in each well was replaced by 100 µL of DMSO-methanol mixture (1:1 volume ratio) for solubilizing the violet crystal and kept the mixture on the shaker for homogeneous mixture. Finally, the absorbance of the mixture was measured at 570 nm using a microplate reader (Varioskan Flash). All the experiments were carried out in triplicate and the results are expressed as normalized viability = $\{1/Abs_{\lambda} = 570 \text{ (untreated cells} - \text{blank)}\} \times \{Abs_{\lambda} = 570 \text{ (treated cells} - \text{blank)}\}$.

5c.4.5. TFA/HFIP treatment of Aβ1–40 peptides

Aβ1–40 was disaggregated using trifluoroacetic acid/1,1,1,3,3,3-hexafluuor-2-propanol (TFA/HFIP) by an established method.[37,47,48] 0.5 mg of Aβ1–40 was added to a 2.5 mL Eppendorf tube and dissolved in TFA to obtain a homogeneous solution free of aggregates. TFA was then evaporated using argon gas. Any left-over TFA was further removed by adding HFIP followed by evaporation using an argon gas flow to obtain a film like material. This process was repeated twice. To the Eppendorf tube, 2.5 mL of HEPES (10 mM, pH 7.4) was added followed by sonication and vortexing to obtain a final concentration of 4.6×10^{-4} M. Fibril formation was monitored using a ThT binding assay.

5c.4.6. Preparation of Aβ1–40 aggregates and ThT Binding Assay

For the preparation of amyloid peptide aggregates,[37,47-49] after the TFA/HFIP treatment for amyloid peptide, the Aβ1–40 (25 µM) was initially incubated with ThT (20 µM) at 37 °C for 0-72 h in 10 mM HEPES buffer at pH 7.4 with steady agitation. Further, Aβ1–40 aggregated amyloid fibrils were monitored with different time incubations by monitoring ThT (20 µM) fluorescence enhancement peak at λ_{em} - 488 nm while exciting at λ_{ex} - 440 nm.

5c.4.7. Confirmation of CSF Aβ aggregates using ThT Binding Assay

The presence of Aβ fibrils in CSF was confirmed by the gradual addition of CSF sample up to 100 µL solution (each addition 10 µL) into ThT (20 µM) solution (pH 7.4 in HEPES) to observe a gradual enhancement in the fluorescence intensity of ThT at 488 nm validating strongly the existence of aggregated Aβ fibrils in the CSF sample.

5c.4.8. Modulating experiment for Aβ1–40 and CSF aggregates

The modulating ability of PDI-HIS was examined by the changes in the fluorescence spectra in the presence of Aβ1–40 fibrils and CSF Aβ fibrils. The samples were prepared in the final volume of 3000 μL in HEPES buffer (10 mM, pH 7.4). First, when PDI-HIS (0.33 μM) solution was excited at 508 nm we observed an emission peak at 546 nm. Further, upon addition of Aβ1–40 fibrils (0.76 μM) and CSF Aβ fibrils (50 μL) into the PDI-HIS solution, the fluorescence changes observed instantly in PDI-HIS+Aβ1–40 and PDI-HIS+CSF aggregate mixtures were minimum. However, after incubation (0-90 h) at 37 °C (pH 7.4), we observed gradual fluorescence enhancement in the PDI-HIS+Aβ1–40 and PDI-HIS+CSF solutions respectively.

5c.4.9. AFM sample preparation

As prepared solutions of PDI−HIS (0.33 μM) + Aβ1−40 (0.76 μM) and PDI−HIS (0.33 μM) + CSF (50 μL) aggregates were kept in 3 mL of HEPES buffer (10 mM, pH7.4) for 0−90 h incubation at 37 °C in water bath. These solutions were further utilized to monitor the AFM morphology. Both the solutions were separately diluted by 10 times and then from the diluted solutions 5 μL of the PDI−HIS + Aβ1−40 and PDI−HIS + CSF samples were dropped onto freshly cleaned glass slide and dried at room temperature overnight and recorded by atomic force microscopy (AFM) on an Agilent instrument, model 5500 series with noncontact mode.

5c.4.10. FE-SEM sample preparation

As prepared solutions of PDI−HIS (0.33 μM) + Aβ1−40 (0.76 μM) and PDI−HIS (0.33 μM) + CSF (50 μL) aggregates were kept in 3 mL of HEPES buffer (10 mM, pH7.4) for 0−90 h incubation at 37 °C in water bath. These solutions were further utilized to monitor the FE-SEM morphology. Both solutions were separately diluted by 10 times, and then, from the diluted solutions, 5 μL of the PDI−HIS + Aβ1−40 and PDI−HIS + CSF samples was dropped onto the aluminum foil covered freshly cleaned glass slide and dried at room temperature overnight and recorded by field emission scanning electron microscopy (FE-SEM) on a Carl Zeiss, SIGMA VP instrument.

5c.4.11. FT-IR spectra sample preparation

As prepared solutions of PDI−HIS (0.33 μM) + Aβ1−40 (0.76 μM) and PDI−HIS (0.33 μM) + CSF (50 μL) aggregates were kept in 3 mL of HEPES buffer (10 mM, pH 7.4) for 0−90 h incubation at 37 °C in water bath. These solutions were further utilized to monitor the FT-IR spectra. 30−50 μL of PDI− HIS + Aβ1−40 fibrils and PDI−HIS + CSF samples were dropped

onto the freshly cleaned glass slide and dried at room temperature overnight and FT−IR spectra recorded on a PerkinElmer spectrometer with samples prepared as KBr pellets.

5c.4.12. Dynamic Light Scattering study

As prepared solutions of PDI−HIS (0.33 μM) + Aβ1−40 (0.76 μM) and PDI−HIS (0.33 μM) + CSF (50 μL) aggregates were kept in 3 mL of HEPES buffer (10 mM, pH7.4) for 90 h incubation at 37 °C in water bath. These solutions were further utilized to monitor the hydrodynamic particle diameter by DLS. Both the solutions were separately diluted by 10 times, and then, from the diluted solution, 500 μL of the PDI–HIS + Aβ1–40 and PDI–HIS + CSF samples were used to record DLS measurements by Zetasizer Nano series Nano-ZS90 instrument.

5c.4.13. Polarized optical microscopy study

Images of Aβ1–40 and CSF aggregates were detected by polarized optical microscopy. Aβ1–40 aggregates (0.76 μM) were incubated with PDI-HIS (0.33 μM) in 3 mL HEPES buffer solution (10 mM, pH 7.4) at 37 ^{o}C for 0-90 h. Similarly, CSF aggregates (50 μL) also incubated with PDI-HIS (0.33 μM) in 3 mL HEPES buffer solution (10 mM, pH 7.4) at 37 ^{o}C for 0-90 h. Further, from the above solutions the samples were prepared separately by spreading 30 μL of each solution on glass slide then the images were observed for both the samples at different time of incubation under Leica DM 2500P microscope. For control study, we performed similar experiments to confirm the formation of coassembled vesicles and mature rod-shaped structures in the absence of PDI-HIS with Aβ 1–40 fibrils (0.76 μM) and CSF Aβ fibrils (50 μL) after 4 and 8 days incubation. The obtained images shows that the mature rod-shape structures were not observed in the absence of PDI-HIS with Aβ 1–40 fibrils as well as with CSF Aβ fibrils even after 4 and 8 days incubation.

References

(1) Chiti, F.; Dobson, C. M. *Annu. Rev. Biochem.* **2006,** *75*, 333.

(2) LaFerla, F. M.; Green, K. N.; Oddo, S. *Nat. Rev. Neurosci.* **2007,** *8*, 499.

(3) Roychaudhuri, R.; Yang, M., Hoshi, M. M.; Teplow, D. B. *J. Biol. Chem.* **2009,** *284*, 4749.

(4) Hamley, I. W. *Chem. Rev.* **2012,** *112*, 5147.

(5) Takahashi, T.; Mihara, H. *Acc. Chem. Res.* **2008,** *41*, 1309.

(6) Gordon, D. J.; Sciarretta, K. L.; Meredith, S. C. *Biochemistry* **2001,** *40*, 8237.

(7) Bard, F.; Cannon, C.; Barbour, R.; Burke, R.; Games, D.; Grajeda, H.; Guido, T.; Hu, K.; Huang, J.; Johnson-Wood, K.; Khan, K.; Kholodenko, D.; Lee, M.; Lieberburg, I.; Motter, R.; Nguyen, M.; Soriano, F.; Vasquez, N.; Weiss, K.; Welch, B.; Seubert, P.; Schenk, D.; Yednock, T. *Nat. Med.* **2000,** *6*, 916.

(8) McLaurin, J.; Cecal, R.; Kierstead, M. E.; Tian, X.; Phinney, A. L.; Manea, M.; French, J. E.; Lambermon, M. H. L.; Darabie, A. A.; Brown, M. E.; Janus, C.; Chishti, M. A.; Horne, P.; Westaway, D.; Fraser, P. E.; Mount, H. T. J.; Przybylski, M.; St George-Hyslop, P. *Nat. Med.* **2002,** *8*, 1263.

(9) Crouch, P. J.; Barnham, K. J. *Acc. Chem. Res.* **2012,** *45*, 1604.

(10) Hindo, S. S.; Mancino, A. M.; Braymer, J. J.; Liu, Y.; Vivekanandan, S.; Ramamoorthy, A.; Lim, M. H. *J. Am. Chem. Soc.* **2009,** *131*, 16663.

(11) Yang, F.; Lim, G. P.; Begum, A. N.; Ubeda, O. J.; Simmons, M. R.; Ambegaokar, S. S.; Chen, P. P.; Kayed, R.; Glabe, C. G.; Frautschy, S. A.; Cole, G. M. *J. Biol. Chem.* **2005,** *280*, 5892.

(12) Cavalli, A.; Bolognesi, M. L.; Capsoni, S., Andrisano, V.; Bartolini, M.; Margotti, E.; Cattaneo, A.; Recanatini, M.; Melchiorre, C. *Angew. Chem. Int. Ed.* **2007,** *46*, 3689.

(13) Cabaleiro-Lago, C.; Quinlan-Pluck, F.; Lynch, I., Lindman, S.; Minogue, A. M.; Thulin, E.; Walsh, D. M.; Dawson, K. A.; Linse, S. *J. Am. Chem. Soc.* **2008,** *130*, 15437.

(14) Yoo, S. I.; Yang, M.; Brender, J. R.; Subramanian, V.; Sun, K.; Joo, N. E.; Jeong, S.; Ramamoorthy, A.; Kotov, N. A. *Angew. Chem., Int. Ed.* **2011,** *50*, 5110.

(15) Geng, J.; Li, M.; Ren, J.; Wang, E.; Qu, X. *Angew. Chem., Int. Ed.* **2011,** *50*, 4184.

(16) Le Droumaguet, B.; Nicolas, J.; Brambilla, D.; Mura, S.; Maksimenko, A.; De Kimpe, L.; Salvati, E.; Zona, C.; Airoldi, C.; Canovi, M.; Gobbi, M.; Magali, N.; La Ferla, B.; Nicotra, F.; Scheper, W.; Flores, O.; Masserini, M.; Andrieux, K.; Couvreur, P. *ACS Nano* **2012,** *6*, 5866.

(17) Würthner, F.; Thalacker, C.; Sautter, A. *Adv. Mater.* **1999,** *11,* 754.

(18) Hirschberg, J. H. K. K.; Brunsveld, L.; Ramzi, A.; Vekemans, J. A. J. M.; Sijbesma, R. P.; Meijer, E. W. *Nature* **2000,** *407,* 167.

(19) Yang, D. S.; Yip, C. M.; Huang, T. H. J.; Chakrabartty, A.; Fraser, P. E. *J. Biol. Chem.* **1999,** *274,* 32970.

(20) Urbanc, B.; Cruz, L.; Le, R.; Sanders, J.; Ashe, K. H.; Duff, K.; Stanley, H. E.; Irizarry, M. C.; Hyman, B. T. *Proc. Natl. Acad. Sci. U. S. A.* **2002,** *99,* 13990.

(21) Alavez, S.; Vantipalli, M. C.; Zucker, D. J. S.; Klang, I. M.; Lithgow, G. J. *Nature* **2011,** *472,* 226.

(22) Salomon, A. R.; Marcinowski, K. J.; Friedland, R. P.; Zagorski, M. G. *Biochemistry* **1996,** *35,* 13568.

(23) Claridge, S. A.; Thomas, J. C.; Silverman, M. A.; Schwartz, J. J.; Yang, Y.; Wang, C.; Weiss, P. S. *J. Am. Chem. Soc.* **2013,** *135,* 18528.

(24) Kalashnyk, N.; Nielsen, J. T.; Nielsen, E. H.; Skrydstrup, T.; Otzen, D. E.; Laegsgaard, E.; Wang, C., Besenbacher, F., Nielsen, N. C., Linderoth, T. R. *ACS Nano* **2012,** *6,* 6882.

(25) Mao, X.; Guo, Y.; Luo, Y.; Niu, L.; Liu, L.; Ma, X.; Wang, H.; Yang, Y.; Wei, G.; Wang, C. *J. Am. Chem. Soc.* **2013,** *135,* 2181.

(26) Ma, X. J.; Liu, L.; Mao, X. B.; Niu, L.; Deng, K.; Wu, W. H.; Li, Y. M.; Yang, Y. L.; Wang, C. *J. Mol. Biol.* **2009,** *388,* 894.

(27) Mao, X. B.; Wang, C. X.; Wu, X. K.; Ma, X. J.; Liu, L.; Zhang, L.; Niu, L.; Guo, Y. Y.; Li, D. H.; Yang, Y. L.; Wang, C. *Proc. Natl. Acad. Sci. U. S. A.* **2011,** *108,* 19605-19610.

(28) Liu, L.; Zhang, L.; Mao, X.; Niu, L.; Yang, Y.; Wang, C. *Nano Lett.* **2009,** *9,* 4066.

(29) Liu, L.; Zhang, L.; Niu, L.; Xu, M.; Mao, X.; Yang, Y.; Wang, C. *ACS Nano* **2011,** *5,* 6001.

(30) Hard, T.; Lendel, C. *J. Mol. Biol.* **2012,** *421,* 441.

(31) Necula, M.; Kayed, R.; Milton, S.; Glabe, C. G. *J. Biol. Chem.* **2007,** *282,* 10311.

(32) Bucciantini, M.; Giannoni, E.; Chiti, F.; Baroni, F.; Formigli, L.; Zurdo, J. S.; Taddei, N.; Ramponi, G.; Dobson, C. M.; Stefani, M. *Nature* **2002,** *416,* 507.

(33) Muthuraj, B.; Chowdhury, S. R.; Mukherjee, S.; Patra, C. R.; Iyer, P. K. *RSC Adv.* **2015,** *5,* 28211.

(34) Ma, Q.; Wei, G.; Yang, X. *Nanoscale* **2013,** *5,* 10397.

(35) Ban, T.; Hamada, D.; Hasegawa, K.; Naiki, H.; Goto, Y. *J. Biol. Chem.* **2003,** *278,* 16462.

(36) D'Amico, M.; Schiro, G.; Cupane, A.; D'Alfonso, L.; Leone, M.; Militello, V.; Vetri, V. *Langmuir*, **2013**, *29*, 10238.

(37) Muthuraj, B.; Hussain, S.; Iyer, P. K. *Polym. Chem.* **2013,** *4*, 5096.

(38) Dwivedi, A. K.; Iyer, P. K. *Macromol. Biosci.* **2014,** *14*, 508.

(39) Chen, B.; Thurber, K. R.; Shewmaker, F.; Wickner, R. B.; Tycko, R. *Proc. Natl. Acad. Sci. U. S. A.* **2009,** *106*, 14339.

(40) Campioni, S.; Carret, G.; Jordens, S.; Nicoud, L.; Mezzenga, R.; Riek, R. *J. Am. Chem. Soc.* **2014,** *136*, 2866.

(41) Jansen, R.; Dzwolak, W.; Winter, R. *Biophys. J.* **2005,** *88*, 1344.

(42) Ridgley, D. M.; Ebanks, K. C.; Barone, J. R. *Biomacromolecules* **2011,** *12*, 3770.

(43) Dehn, S.; Castelletto, V.; Hamley, I. W.; Perrier, S. *Biomacromolecules* **2012,** *13*, 2739.

(44) Nilsson, M. R.; Dobson, C. M. *Biochemistry* **2003,** *42*, 375.

(45) Lee, J.; Culyba, E. K.; Powers, E. T.; Kelly, J. W. *Nat. Chem. Biol.* **2011,** *7*, 602.

(46) Tagliavini, F.; Forloni, G.; Colombo, L.; Rossi, G.; Girola, L.; Canciani, B.; Angeretti, N.; Giampaolo, L.; Peressini, E.; Awan, T.; De Gioia, L.; Ragg, E.; Bugiani, O.; Salmona, M. *J. Mol. Biol.* **2000,** *300*, 1309.

(47) Chen, S.; Wetzel, R. *Protein Sci.* **2001,** *10*, 887.

(48) Hortschansky, P.; Schroeckh, V.; Christopeit, T.; Zandomeneghi, G.; Fändrich, M. *Protein Sci.* **2005,** *14*, 1753.

(49) Hindo, S. S.; Mancino, A. M.; Braymer, J. J.; Liu, Y.; Vivekanandan, S.; Ramamoorthy, A.; Lim, M. H. *J. Am. Chem. Soc.* **2009,** *131*, 16663.

Appendix

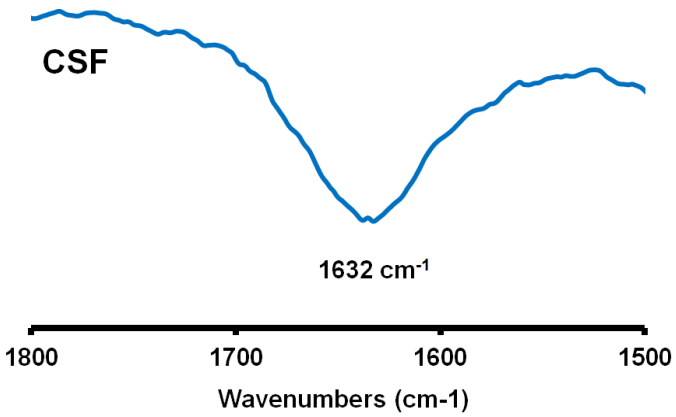

Figure A5c.1 FT-IR spectra of CSF aggregates show a major band at 1632 cm^{-1} which indicates the parallel β-sheet conformation of Aβ aggregates.

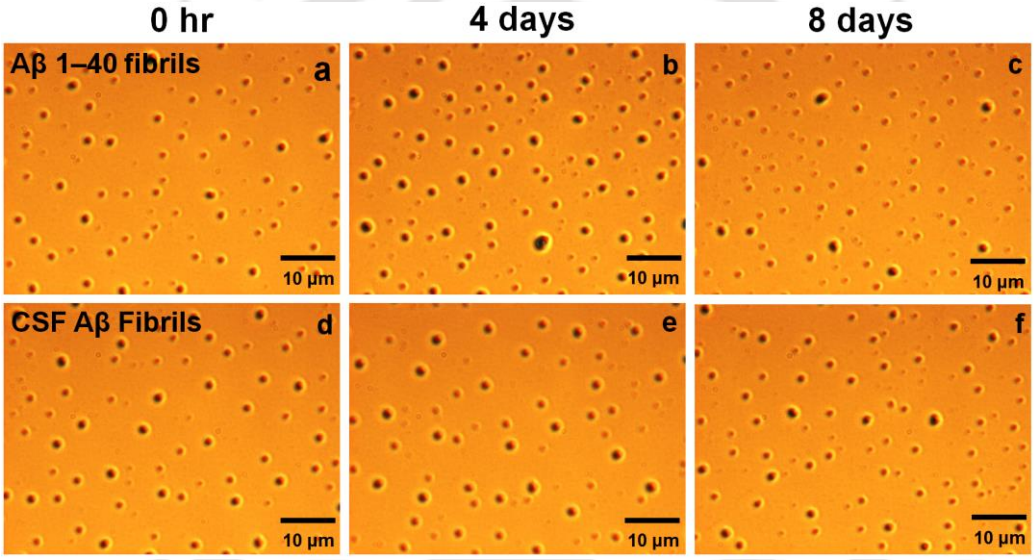

Figure A5c.2 (a) Optical microscopic image shows that the formation of aggregated Aβ 1–40 spheres. (b, c) The formation of coassembled vesicles and mature rod-shaped structures were not observed in the absence of PDI-HIS with Aβ 1–40 (0.76 µM) even after 4 and 8 days incubation. (d) Optical microscopic image clearly shows that existence of aggregated Aβ spheres in CSF. (e, f) Formation of coassembled vesicles and mature rod-shape structures were not observed in the absence of PDI-HIS with CSF (50 µL) even after 4 and 8 days incubation.

Conclusion and Thesis overview

In conclusion, we designed and synthesized new fluorescent conjugated polymers (PHQ and PF–DPA) and small molecules (FI and PDI–HIS) and successfully utilized them for various applications in sensors to detect cations (Fe^{2+}/Fe^{3+}, Co^{2+} and Cu^{2+}) and anions (ATP, PPi and NO) respectively. Furthermore, the same conjugated polymers (PHQ and PF–DPA) and small molecules (FI and PDI–HIS) were also successfully utilized for modulating Aβ fibrils and metal–associated Aβ aggregates by different mechanisms.

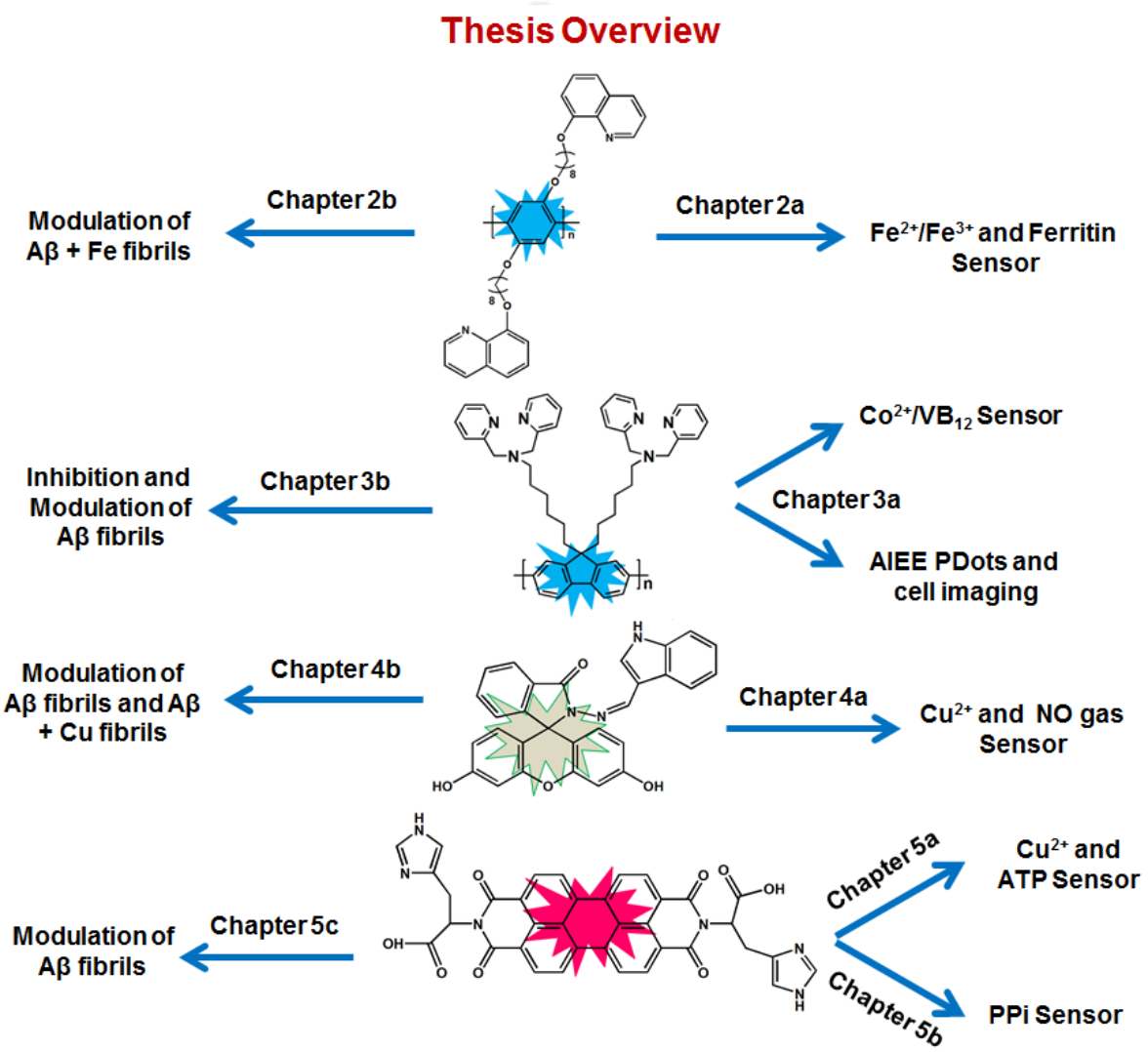

Publications

1. **Muthuraj, B.;** Hussain, S.; Iyer, P. K. A Rapid and Sensitive Detection of Ferritin at a Nanomolar Level and Disruption of Amyloid Beta Fibrils Using Fluorescent Conjugated Polymer. *Polym. Chem.* **2013,** *4*, 5096-5107. (Selected as author of the week and paper of the week).

2. **Muthuraj, B.;** Deshmukh, R.; Trivedi, V.; Iyer, P. K. Highly Selective Probe Detects Cu^{2+} and Endogenous NO Gas in Living Cell. *ACS Appl. Mater. Interfaces,* **2014,** *6,* 6562–6569.

3. **Muthuraj, B.;** Chowdhury, S. R.; Mukherjee, S.; Patra, C.; Iyer, P. K. Aggregation Deaggregation Influenced Ultrasensitive detection of Cu^{2+} and ATP by Histidine Functionalized Water–Soluble Fluorescent Perylene Diimide under Physiological Conditions and in Living Cells. *RSC Adv.* **2015,** *5,* 28211–28218.

4. **Muthuraj, B.;** Layek, S.; Balaji, S. N.; Trivedi, V.; Iyer, P. K. Multiple Function Fluorescein Probe Performs Metal Chelation, Disaggregation, and Modulation of Aggregated Aβ and Aβ-Cu Complex. *ACS Chem. Neurosci.* **2015,** 6, 1880–1891.

5. **Muthuraj, B.;** Chowdhury, S. R.; Iyer, P. K. Modulation of Amyloid-β Fibrils into Mature Microrod-Shaped Structure by Histidine Functionalized Water-Soluble Perylene Diimide. *ACS Appl. Mater. Interfaces,* **2015,** *7,* 21226-21234.

6. **Muthuraj, B.;** Mukherjee, S.; Chowdhury, S. R.; Patra, C. R.; Iyer, P. K. An Efficient Strategy to Assemble Water Soluble Histidine–Perylene Diimide and Graphene Oxide for the Highly Selective and Sensitive Detection of PPi in Physiological Conditions and in vitro. *Biosens. Bioelectron.* **2016,** Doi:10.1016/j.bios.2015.12.036.

7. **Muthuraj, B.;** Mukherjee, S.; Patra, C.; Iyer, P. K. Aggregation Induced Enhanced Emission from Polyfluorene Nanoparticles for Simultaneous Live Cell Imaging and Targeted Cancer Therapy (Revision).

8. **Muthuraj, B.;** Iyer, P. K. Inhibition of Amyloid–β Fibrillation and Modulation Effect on Preformed Aβ Oligomers and Fibrils by an Influence of Aggregation Induced Enhanced Emission Luminogen of PF–DPA PDots (Communicated).

9. **Muthuraj, B.;** Iyer, P. K. Multifunctional Role as Cobalt, Vitamin B_{12} Sensor and Aggregation–Induced Enhanced Emission Luminogen of Polyfluorene Nanoparticles for TNT Sensor (Under preparation).

Conferences

Conferences attended

1. Participated and presented in "FICS–2010 –National Conference on Frontiers in Chemical Sciences" held at IIT Guwahati (3, 4 Dec. 2010).

2. Participated and presented in "8th J–NOST Conference for Research Scholar" held at IIT Guwahati (15–17 Dec. 2012).

3. Participated and presented in "Indo–US Symposium on Molecular Materials" held at Indian Institute of Science, Bangalore, India (15–17 July, 2013).

4. Participated in "Workshop on Sensors and its Application" held at Institute of Advanced Study in Science and Technology, Guwahati, Assam (November 15th in 2013).

5. Participated in "ICANN–2013 –International Conference on Advanced Nanomaterials and Nanotechnology" held at IIT Guwahati (1–3 Dec. 2013).

6. Participated and presented in "ICCB–2014 International Conference on Chemical Biology: Disease Mechanisms and Therapeutics" held at Indian Institute of Chemical Technology, Hyderabad, India (6–8 Feb, 2014).

7. Participated and presented oral lecture in India-Sweden bilateral workshop/seminar on Advanced Materials with a focus in the area of health and energy held on 29-31 August 2014 at IIT Guwahati.